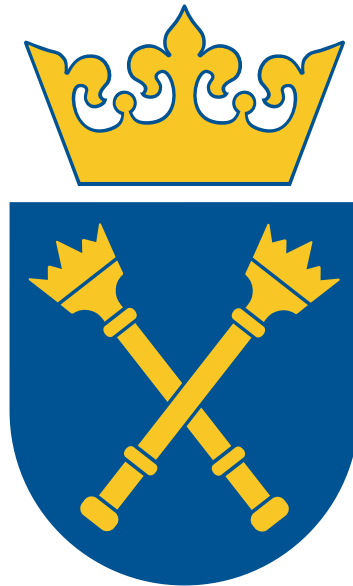


Relativistic charge and energy transport phenomena in graphene nanostructures

Dominik Suszalski

Rozprawa doktorska

Promotor: prof. dr hab. Adam Rycerz
Promotor pomocniczy: dr Grzegorz Rut



Uniwersytet Jagielloński
Instytut Fizyki im. Mariana Smoluchowskiego
Zakład Teorii Materii Skondensowanej i Nanofizyki

Kraków, lipiec 2020

Wydział Fizyki, Astronomii i Informatyki Stosowanej
Uniwersytet Jagielloński

Oświadczenie

Ja niżej podpisany Dominik Suszalski (nr indeksu: 1079343) doktorant Wydziału Fizyki, Astronomii i Informatyki Stosowanej Uniwersytetu Jagiellońskiego oświadczam, że przedłożona przeze mnie rozprawa doktorska pt. „Relativistic quasiparticles in charge and energy transport through graphene nanostructures” jest oryginalna i przedstawia wyniki badań wykonanych przeze mnie osobiście, pod kierunkiem prof. dr hab. Adama Rycerza. Pracę napisałem samodzielnie.

Oświadczam, że moja rozprawa doktorska została opracowana zgodnie z Ustawą o prawie autorskim i prawach pokrewnych z dnia 4 lutego 1994 r. (Dziennik Ustaw 1994 nr 24 poz. 83 wraz z późniejszymi zmianami).

Jestem świadom, że niezgodność niniejszego oświadczenia z prawdą ujawniona w dowolnym czasie, niezależnie od skutków prawnych wynikających z ww. ustawy, może spowodować unieważnienie stopnia nabytego na podstawie tej rozprawy.

Kraków, dnia 29.07.2020

.....

podpis doktoranta

Contents

1	Introduction	11
1.1	Aim and scope of this thesis	11
2	Graphene structure	13
2.1	Crystal structure of graphene	13
2.2	Electronic structure of graphene	13
2.3	Crystal structure of bilayer graphene	14
2.4	Electronic structure of bilayer graphene	15
2.5	The 2-band approximation for bilayer graphene	15
2.6	The Peierls substitution	16
2.7	Local density of states	16
3	Scattering matrix formalism	18
3.1	The concept of leads	18
3.2	Scattering matrix	18
3.3	Transport characteristics at constant temperature	19
3.4	Thermoelectric properties	20
3.5	Adiabatic pumping	20
4	Investigating graphene	21
4.1	Pursuing the trigonal warping strength	21
4.1.1	Motivation	21
4.1.2	Seebeck coefficient: the simple approach	21
4.1.3	Temperature dependent analysis	24
4.2	Thermoelectric properties in the presence of the bandgap	27
4.2.1	Introduction	27
4.2.2	Seebeck coefficient and $T^{(\alpha)}$ models	27
4.2.3	Thermoelectric figure of merit (ZT)	30
4.3	Conductivity of the large sample of bilayer graphene	31
4.3.1	Introduction	31
4.3.2	Zero-temperature results	31
4.3.3	Finite temperature effects	34
4.3.4	Spontaneous symmetry breaking in bilayer graphene	36
5	Selected devices made out of graphene	37
5.1	Aharonov-Bohm effect without two slits	37
5.1.1	Introduction	37
5.1.2	Earlier work	37
5.1.3	Magnetoconductance at non-zero chemical potential	38
5.1.4	Magnetoconductance in the absence of cylindrical symmetry	38
5.2	Mesoscopic valley filter	41
5.2.1	Concept of valleytronics	41

5.2.2	The setup	41
5.2.3	Role of electrostatic potential	42
5.2.4	Role of the mass term	42
5.2.5	Operating the valley filter	45
5.3	Adiabatic quantum pumping with mechanical kinks in graphene	49
5.3.1	Aim of the section	49
5.3.2	Simple kink model	50
5.4	Dynamics in the simple kink model	50
5.4.1	The SSH kink model	54
5.4.2	Results for the SSH kink model	55
6	Conclusions	60

Publications constituting the thesis

1. D. Suszalski, G. Rut and A. Rycerz, *Lifshitz transition and thermoelectric properties of bilayer graphene*, Physical Review B 97, 125403 (2018).
2. D. Suszalski, G. Rut and A. Rycerz, *Thermoelectric properties of gapped bilayer graphene*, Journal of Physics: Condensed Matter 31, 415501 (2019).
3. D. Suszalski, G. Rut and A. Rycerz, *Mesoscopic valley filter in graphene Corbino disk containing a p-n junction*, Journal of Physics: Materials 3, 015006 (2019).
4. D. Suszalski, G. Rut and A. Rycerz, *Conductivity scaling and the effects of symmetry-breaking terms in bilayer graphene Hamiltonian*, Physical Review B 101, 125425 (2020).
5. R. Adam and D. Suszalski, *Graphene disk in a solenoid magnetic potential: Aharonov-Bohm effect without a two-slit-like setup*, Physical Review B 101, 245429 (2020).
6. D. Suszalski and A. Rycerz, *Adiabatic quantum pumping in buckled graphene nanoribbon driven by a kink*, <http://arxiv.org/abs/2002.08507>, accepted to Acta Physica Polonica B.

Supplement:

7. D. Suszalski and A. Rycerz, *Adiabatic pumping driven by moving kink and quantum standard ampere in buckled graphene nanoribbon*, <http://arxiv.org/abs/2007.11145>, (unpublished).

Acknowledgments

I would like to express my deep gratitude to my supervisor, Prof. Adam Rycerz for his time and guidance. I am also very grateful for his critical reading of this Thesis.

My deep thanks are extended to my supporting supervisor, Dr. Grzegorz Rut, for his presence and all the friendly advice given.

I thank Prof. Anton Akhmerov for hospitality in his research group and introduction to Kwant package.

Many thanks go to Dr. Maciej Fidrysiak, Dr. Danuta Goc-Jagło, Dr. Andrzej Kapanowski, Dr. Andrzej Kądziaława, Prof. Józef Spałek, Krzysztof Nowakowski, Wojciech Tarnowski, Franciszek Sobczuk, Dr Bas Nijholt, Dr Kim Pöyhönen, Dr Piotr Rożek, Dr Daniel Varjas, Dr Adriaan Vuik for fruitful conversations and all help received.

Special thanks go to my wife for her love, support and ongoing presence, and my parents for all the effort they put in raising me.

Last but not least, I would like to thank the Lord for life, love and all the beautiful world to investigate.

The work was supported by the National Science Centre of Poland (NCN) via Grant No. 2014/14/E/ST3/00256. The financial support from dotation KNOW from Krakowskie Konsorcjum “Materia-EnergiaPrzyszłość” im. Mariana Smoluchowskiego is acknowledged.

Abstract

This thesis is concentrated on quantum transport properties of mono- and bilayer graphene systems in ballistic regime. The Landauer–Büttiker formalism is utilised to analyse transport properties of ultraclean samples. The aims of this work are twofold. The first one is concerned in analysing the properties of graphene itself, both mono- and bilayer. The second one is concentrated on novel electronic devices that might be constructed thanks to extraordinary properties of graphene. The particular systems are chosen weighting the theoretical interest, experimental feasibility and possible future applications.

The first part addresses three main questions. The first one *How one may reliably measure the trigonal warping strength in bilayer graphene?* is replied with vast analysis of thermoelectric properties of bilayer graphene. Two experimentally accessible ways has been proposed. The first one requires measurement of carrier concentration corresponding to the secondary maximum of the Seebeck coefficient, while the other requires measurement of temperature at which the Seebeck coefficient reaches its global maximum on the doping – temperature plane.

The second question: *How appearance of a bandgap will modify the thermoelectric properties?* is followed by analysis of two system geometries. The traditional lead-sample-lead geometry and the sharp potential step geometry allowing to pinpoint the crucial properties of the system in idealised case. The thermoelectric properties occur to be defined dominantly by the presence of the bandgap. The special attention is put to unusual behaviour of figure of merit (ZT).

The third question: *What is a conductivity of large piece of bilayer graphene?* considers the impact of non-leading terms in effective bilayer graphene Hamiltonian on the conductance of the large system at zero doping. The three different behaviours of conductivity (diverging, levelling off or decaying) with growing system length are recognized and interpreted. The analysis includes the finite temperature effects and comparison with available experimental results.

The second part is also naturally divided into three parts. The first one concentrates on possibility of *pinpointing the Aharonov-Bohm effect without two slit setup* in the Corbino disk made out of graphene. It occurred that pseudodiffusive transport in bilayer graphene is affected by magnetic flux piercing the central electrode and sufficiently strong to allow its experimental measurement. The robustness of the effect is analysed in terms of non-zero doping and breaking of rotational symmetry of the system.

The second system is a proposition of *a mesoscopic valley filter* – the first device in valleytronics being the modification of electronics that takes advantage of valley polarised currents in graphene. As proposition does not require use of experimentally problematic single atom precise sample forming or application of strain-induced pseudomagnetic fields, we believe it allows experimental construction of the first valley filter – a milestone in development of valleytronics.

The last system consists of buckled nanoribbon with mechanical kink generator. Such a system has been analysed before, by other authors, and proved to be controllable via gentle shaking of one of its ends, taking advantage of unusual negative radiation

pressure effect. Our central question: *Does buckled graphene nanoribbon might be used as an electric pump?* is addressed and analysed in terms of SSH model. The surprising result show it should be possible not only to construct such a pump, but also to use it as a standard current device (ampere prototype).

Streszczenie

Dysertacja jest skoncentrowana na kwantowych cechach przewodnictwa w ballistycznych układach grafenu i dwuwarstwy grafenowej. Do analizy przewodnictwa wykorzystano formalizm Landauera–Büttikera. Cele niniejszej pracy dzielą się na dwie ogólne grupy. Pierwsza grupa koncentruje się na analizie własności monowarstwy i dwuwarstwy grafenowej. Druga natomiast rozważa własności konkretnych układów wykonanych z grafenu. Wybór układów jest podyktowany interesującą fizyką, realizowalnością oraz możliwymi, przyszłymi zastosowaniami.

Pierwsza część pracy zadaje trzy główne pytania. Po pierwsze, *Jak wiarygodnie zmierzyć wartość tunelowania skośnego w dwuwarstwie?* pytanie to jest analizowane w świetle własności termoelektrycznych dwuwarstwy grafenowej. Dwie dostępne eksperymentalnie procedury są zaproponowane. Pierwsza wymaga pomiaru koncentracji nośników ładunku odpowiadającej pobocznemu maksimum współczynnika Seebecka, podczas gdy druga wymaga pomiaru temperatury odpowiadającej najwyższej wartości współczynnika Seebecka w przestrzeni parametrów domieszkowanie – temperatura.

Drugie pytanie *Jak obecność przerwy energetycznej wpływa na własności termoelektryczne?* jest analizowane dla dwóch różnych geometrii układu. Tradycyjnej geometrii złącze-próbka-złącze oraz geometrii z gwałtownym skokiem potencjału, która umożliwi analizę kluczowych własności dwuwarstwy w sytuacji uproszczonej. Analizowane własności termoelektryczne okazują się być w dominującym stopniu zdeterminowane przez obecność przerwy energetycznej. Szczególny nacisk jest położony na analizę współczynnika wydajności (ZT).

Trzecie pytanie *Jaka jest przewodność dużego fragmentu dwuwarstwy grafenowej?* dotyczy kwestii wpływu niewiodących wyrazów Hamiltonianu na przewodnictwo dużych układów niedomieszkowanej dwuwarstwy grafenowej. Trzy istotnie różne zachowania przewodnictwa (rozbieżne, stabilizujące się oraz zanikające) zostały zaobserwowane przy wzroście długości układu w zależności od obecności/braku poszczególnych wyrazów. Analiza uwzględnia również efekty skończonej temperatury oraz porównanie z wynikami eksperymentalnymi.

Druga część pracy również naturalnie dzieli się na trzy części. Pierwsza koncentruje się na możliwości *obserwacji efektu Aharonova-Bohma bez tradycyjnej geometrii dwuszczeniowej* w dysku Corbino wykonanym z grafenu. Okazuje się, że strumień pola magnetycznego przechodzący przez centralną elektrodę wpływa na pseudodyfuzyjny transfer ładunku w stopniu umożliwiającym eksperymentalną obserwację. Trwałość efektu jest analizowana ze względu zmienne domieszkowanie i złamanie symetrii obrotowej układu.

Drugi z rozważanych systemów jest propozycją *konstrukcji mezoskopowego filtra dolinowego* – pierwszego z urządzeń postulowanych w ramach dolinotroniki, będącej wersją elektroniki wykorzystującą możliwość dolinowego polaryzowania prądu w grafenie. Jako że proponowany układ nie wymaga przygotowania z precyzją sięgającą pojedynczych atomów, ani wykorzystania pochodzących z naprężeń pól pseudomagnetycznych, mamy nadzieję, że pozwoli on na realistyczną eksperymentalnie konstrukcję pierwszego filtra dolinowego – kamienia milowego rozwoju dolinotroniki.

Ostatni z rozważanych systemów składa się ze ściśniętego paska grafenu połączonego

z generatorem mechanicznych kinków. Taki układ był niedawno analizowany przez innych autorów ze względu na możliwość kontroli ruchu solitonów (kinków) poprzez delikatne potrząsanie jednym z końców paska. Mechanizm kontroli wykorzystuje niecodzienne zjawisko ujemnego ciśnienia promieniowania. Nasze pytanie *Czy ściśnięty pasek grafenowy może posłużyć jako pompa elektronowa?* jest analizowane w ramach modelu SSH (Su-Schrieffer-Heeger). Dość nieoczekiwane wyniki wskazują na możliwość wykorzystania takiego układu jako wzorca ampera.

1 Introduction

Mastering new materials has been one of key ingredients driving human development. Starting from ancient times and mastering the stone and brass, through mastering the iron and steel up to nowadays. Understanding the electron behaviour gun fired electricity revolution. Last century resulted in mastering semiconductors, liquid crystals, optical fibres and many other materials. The possibilities opened by those breakthroughs do not need to be enlisted for a modern man. To say that we achieved a lot would be an understatement, yet it seems we are still at the beginning of the journey.

Many researchers struggle in order to understand high temperature superconductors, that are already used in medical tomography. The fascinating world of topological insulators and Majorana edge modes is now opening, holding the hope for realisation of scalable quantum computers. Single atom manipulation via Scanning Tunnelling Microscope is already achievable in almost every nanoscale laboratory. *There's Plenty of Room at the Bottom*[1] and there are probably wonders that not a man has ever dreamed about. Down there, among many others, there is graphene – a unique material holding very special place.

Graphene is a stable, self-standing, two-dimensional material of thickness of a single carbon atom. Such materials were long thought to be non-existing and even impossible to exist due to reasons connected with mechanical stability of in-plane vibrations [2]. In finite temperatures its mechanical properties are exceptional making it one of the strongest material ever tested [3]. Graphene is a great and promising thermal conductor [4]. It has unusually high carrier mobility making it a great current conductor [5]. Its phenomenal electronic feasibility has drawn interest of many researchers investigating graphene devices in areas like unconventional superconductivity [6], spintronics [7], valleytronics or physics of Quantum Hall Effect [8]. Despite purely laboratory character of first graphene production method (2004) it has already found first applications and is available in commercial products including cars [9], earphones [10], helmets [11], tires [12], lubricants [13], conducting ink [14], conducting packing foil for electronics [15] and photodetectors [16]. Graphene allowed also to relax operating conditions of Quantum Hall resistance standards from $T_{\max} \approx 1.3$ K, $B_{\min} \approx 10$ T, and $I_{\max} \approx 30 \mu\text{A}$ to $T_{\max} \approx 10$ K, $B_{\min} \approx 3.5$ T, and $I_{\max} \approx 0.5$ mA significantly reducing their size, cost and complexity [17].

1.1 Aim and scope of this thesis

Among different interests and hopes concerning graphene this thesis is devoted to its electronic properties in ballistic regime. The Landauer–Büttiker formalism is used throughout the thesis. Despite all the research done, there are still some questions concerning properties of graphene itself. This thesis addresses some of them

- What is a value of trigonal warping strength in bilayer graphene?
- How does it affect thermoelectric properties?

- How thermoelectric properties are going to change if the bandgap appear?
- What is the conductivity of infinite sample of ultraclean bilayer graphene?

The first question is one of few elementary questions about electronic structure of bilayer graphene that is still open. The second one is a consequence of approach taken to the first one. The third one is a natural extension and a complementary research. The fourth question, probably the most complex one, is devoted to the analysis of effective low energy Hamiltonian and significance of terms appearing in it for conductivity of large samples.

To understand graphene well may yet be only a temporary goal. The real value of graphene lies in possibilities opened by its understanding and mastering of its fabrication. Among enormous number of graphene applications considered in contemporary discussion this thesis concentrates on three special cases

- realisation of Aharonov-Bohm effect in Corbino geometry (without two slit setup),
- construction of a mesoscopic valley filter,
- construction of an electric pump in graphene nanoribbon.

The first task is an interesting possibility to realise Aharonov-Bohm effect without standard two slit setup. Such a realisation would also allow to show the magnetoconductance oscillations in graphene Corbino disk that are not experimentally available in constant magnetic field situation [18]. The second task is a new proposition of construction of mesoscopic valley filter - the device that might be use to valley polarise current flowing through graphene. The basic idea of valley polarised current has given rise to the valleytronics - the modern electronics, yet to be implemented due to experimental difficulties. The mesoscopic nature of proposed filter should help to overcome some of them. The third task has brought interesting result, showing possibility of constructing mechanically driven electric pump that transports a quantum value of charge per cycle. Such a pump might be then used to construct a device serving as a current standard. The author believes that two last system might lead to construction of devices that push further limits of the human development.

2 Graphene structure

2.1 Crystal structure of graphene

Graphene is one of crystalline carbon allotropes. It is 2-dimensional honeycomb crystal of carbon atoms. The primitive lattice vectors are

$$\mathbf{a}_1 = \left(\frac{a}{2}, \frac{\sqrt{3}a}{2} \right), \quad \mathbf{a}_2 = (a, 0), \quad (1)$$

with lattice constant of graphene $a = 0.246 \text{ nm}$ [19]. Within the unit cell there are two atoms located at positions

$$\mathbf{d}_A = (0, 0), \quad \mathbf{d}_B = \left(\frac{a}{\sqrt{3}}, 0 \right), \quad (2)$$

leading to presence of two triangular sublattices, often referred to as A and B sublattices (or atoms).

The reciprocal lattice of a triangular lattice is also a triangular lattice leading to hexagon shape of Wigner-Seitz cell being the first Brillouin zone. Its primitive vectors are defined as

$$\mathbf{b}_1 = \left(\frac{2\pi}{a}, \frac{2\pi}{\sqrt{3}a} \right), \quad \mathbf{b}_2 = \left(\frac{2\pi}{a}, -\frac{2\pi}{\sqrt{3}a} \right). \quad (3)$$

It is important to note that out of six corners of the Brillouin three may be connected by inverse lattice vectors. Thus there exists two inequivalent corners called K and K' points. Hereinafter, the following convention is chosen

$$\mathbf{K} = \left(\frac{4\pi}{3a}, 0 \right) \quad \text{and} \quad \mathbf{K}' = \left(-\frac{4\pi}{3a}, 0 \right). \quad (4)$$

2.2 Electronic structure of graphene

The band structure of graphene crosses the zero-energy level at K and K' points [20]. In the vicinity of each of them (called also valleys) there is a conical structure that resembles dispersion relation of relativistic, massless particles. Around the K and K' points the effective Hamiltonian may be written as:

$$H_\xi = v_0 \mathbf{p} \cdot (\xi \sigma^x, \sigma^y) + V(\mathbf{x}) + M(\mathbf{x}) \sigma^z, \quad (5)$$

where $\xi = 1(-1)$ corresponds to $K(K')$ valley, $v_0 \approx 10^6 \text{ m/s}$ is the Fermi velocity, $\mathbf{p} = -i\hbar\nabla$ is a 2-dimensional momentum operator, $V(\mathbf{x})$ is a potential that has the same value on both sublattices and $M(\mathbf{x})$ is a staggered potential. The above Hamiltonian is equivalent to the 2-dimensional Dirac Hamiltonian, where $V(\mathbf{x})$ plays the role of external potential and $M(\mathbf{x})$ plays a role of a mass term. It is also worth to note that second nearest neighbour tunnelling within a graphene lattice does not introduce terms linear

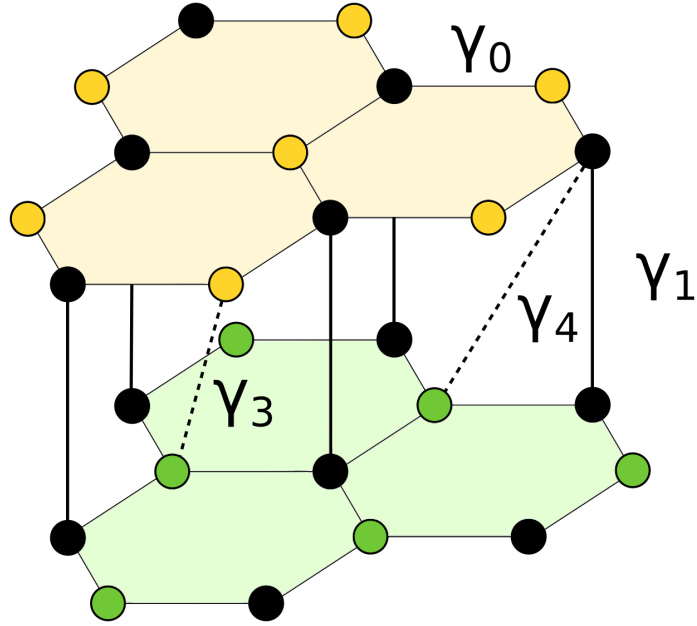


Figure 1: Structure of tight-binding parameters in bilayer graphene. The matrix elements γ_3 and γ_4 are displayed only once for clarity of the figure. The $B(A)$ sublattice in upper(lower) lattice are marked with black dots. They are vertically aligned and connected with the biggest interlayer matrix element γ_1 . The other sublattices are marked by coloured dots.

in momentum to the Hamiltonian. The peculiar Hamiltonian structure is the source of bizarre behaviour of electrons in graphene, such as spinor transformation rules for the wavefunction, Klein tunnelling or lack of backscattering for normal incidence.

2.3 Crystal structure of bilayer graphene

Bilayer graphene consists of two graphene layers based on top of one another. In order to minimize energy of such system the second lattices needs to be shifted with respect to the first one forming so-called Bernard stacking [21]. In this stacking atoms from one sublattice in the lower sheet are positioned directly under the atoms from the second sublattice in the sheet above. Such pairs of vertically aligned atoms are called dimers, while the other atoms will be referred to as non-dimer ones. Both real and reciprocal primitive cells are the same as in the case of graphene. The $K(K')$ points are inherited from their definition in monolayer graphene. Infinite self-standing bilayer graphene is an energetically stable system.

2.4 Electronic structure of bilayer graphene

The electronic properties of bilayer graphene are more complicated than those of single layer graphene. This is not surprising as in addition to intra-layer tunnellings one need to include interlayer ones. The tight binding Hamiltonian including three dominant interlayer tunnellings takes a form:

$$H_b = \begin{pmatrix} \delta_{AB}/2 - U/2 & v_0\pi & \gamma_1 & -v_4\pi^\dagger \\ v_0\pi^\dagger & -\delta_{AB}/2 - U/2 & -v_4\pi^\dagger & v_3\pi \\ \gamma_1 & -v_4\pi & -\delta_{AB}/2 + U/2 & v_0\pi^\dagger \\ -v_4\pi & v_3\pi^\dagger & v_0\pi & \delta_{AB}/2 + U/2 \end{pmatrix}, \quad (6)$$

where $\pi = e^{-i\theta}(\xi p_x + i p_y)$, $\pi^\dagger = e^{-i\theta}(\xi p_x - i p_y)$, θ is the angle between armchair direction and the x -axis, ξ equals $+1(-1)$ for $K(K')$ valley, $v_3 = v_0\gamma_3/\gamma_0$, $v_4 = v_0\gamma_4/\gamma_0$, U is the electrostatic bias between layers and δ_{AB} is the staggered potential describing irreducible part of spontaneous bandgap in bilayer graphene. One might also add additional potential (Δ') introducing energy difference between dimer and non-dimer sites. Such a term introduces electron-hole asymmetry to the system, similarly to the γ_4 tunnelling. As γ_4 is present in model considered Δ' may be skipped as redundant clarifying interpretation of γ_4 .

The values of $\gamma_0 = 3.16$ eV and $\gamma_1 = 0.38$ eV are widely accepted[22]. The value of $\gamma_4 \approx 0.15$ eV is known with reasonable precision, while γ_3 remains somehow a mystery with values reported from 0.1 eV to 0.4 eV. Experiments report no presence of spontaneous bandgap in bilayer graphene based on semiconductor. The value of interlayer energy offset U is defined by external out of plane electric field. Provided values are used throughout the thesis unless stated otherwise.

The difference in band structure of bilayer and monolayer graphene comes predominantly from γ_1 term. Its presence changes the graphene band structure around $K(K')$ points significantly. It is no longer linear and become quadratic in momentum. Moreover, bands split leading to appearance of low energy conductance band (that touches highest valence band) and high energy conductance band (and corresponding lower valence band). It may be also interpreted as giving mass to electron pseudoparticles.

2.5 The 2-band approximation for bilayer graphene

In the low energy limit the electronic properties of the bilayer graphene origins almost entirely from the lowest conductance band and the highest valence band. It is thus possible to catch them in the 2-band approximation [21]

$$\hat{H}_2 = \hat{h}_0 + \hat{h}_3 + \hat{h}_4 + \hat{h}_U + \hat{h}_{AB}, \quad (7)$$

$$\hat{h}_0 = -\frac{1}{2m} \begin{pmatrix} 0 & (\pi^\dagger)^2 \\ \pi^2 & 0 \end{pmatrix}, \quad (8)$$

$$\hat{h}_3 = v_3 \begin{pmatrix} 0 & \pi \\ \pi^\dagger & 0 \end{pmatrix} - \frac{v_3 a}{4\sqrt{3}\hbar} \begin{pmatrix} 0 & (\pi^\dagger)^2 \\ \pi^2 & 0 \end{pmatrix}, \quad (9)$$

$$\hat{h}_4 = \frac{2vv_4}{\gamma_1} \begin{pmatrix} \pi^\dagger\pi & 0 \\ 0 & \pi\pi^\dagger \end{pmatrix}, \quad (10)$$

$$\hat{h}_U = -\frac{U}{2} \left[\begin{pmatrix} 1 & 0 \\ 0 & -1 \end{pmatrix} - \frac{2v^2}{\gamma_1^2} \begin{pmatrix} \pi^\dagger\pi & 0 \\ 0 & -\pi\pi^\dagger \end{pmatrix} \right], \quad (11)$$

$$\hat{h}_{AB} = \frac{\delta_{AB}}{2} \begin{pmatrix} 1 & 0 \\ 0 & -1 \end{pmatrix}, \quad (12)$$

with \hat{H}_2 being the 2-band approximate Hamiltonian. The \hat{h}_0 term dominates in low energy limit, thus other terms might be considered a correction to it. It is worth noting that second part of \hat{h}_3 term is only a renormalization of effective electron mass and the unique role of γ_3 comes from the first part.

2.6 The Peierls substitution

The inclusion of magnetic field is somehow unique among many different physical effects. Usually inclusion of additional effects correspond to addition of a new term to effective Hamiltonian. In the case of magnetic field it is rather modification of existing terms. The exact formula is given by the Peierls substitution

$$\mathbf{p} \rightarrow \mathbf{p} + e\mathbf{A}, \quad (13)$$

where e is electron charge and \mathbf{A} is the vector potential corresponding to magnetic field considered $\mathbf{B} = \nabla \times \mathbf{A}$. The vector potential is a gauge field giving one some freedom in parametrization of the problem. Throughout this thesis, the symmetric gauges will be chosen.

2.7 Local density of states

Density of states is a useful quantity giving insight into the quantum system considered. It describes the number of quantum states present in given energy range. Formally, it is defined as

$$\rho(E) = \sum_n \delta(E - E_n), \quad (14)$$

where $\delta(x)$ is Dirac delta, E_n is energy of state n and sum is performed over all eigenstates of Hamiltonian. Analysis of density of states reveals presence or lack of valence/conduction band and the bandgap, that is crucial for electronic properties of the

system. In some cases additional, useful information may be obtained from its local version. It is unsurprisingly called the local density of states and in the lattice models is defined as

$$\rho_{\text{loc}}(\mathbf{R}_j, E) = \sum_n |\psi_n^{(j)}|^2 \delta(E - E_n), \quad (15)$$

where \mathbf{R}_j is a position of site j and $\psi_n^{(j)}$ is the value of n -th Hamiltonian eigenstate wavefunction at site j . Local density of states gives information where are localized states corresponding to given energy. For practical reasons, usually in order to obtain better looking plots, both density of states and local density of states is smeared by substituting

$$\delta(x) \rightarrow \frac{1}{\pi} \frac{\epsilon}{x^2 + \epsilon^2}, \quad (16)$$

where ϵ defines (small) energy scale over which the densities are smeared.

3 Scattering matrix formalism

3.1 The concept of leads

One of the main difficulties in the domain of quantum transport is connecting the macroscopic circuits (batteries, amperometers, voltmeters or probes in general) with the investigated nanostructure. Due to the quantum nature of such systems the measurement rules known from macroscopic world do not longer apply. The theoretical object allowing modelling of macroscopic probes connected to the true quantum system is a lead. The lead is a thermodynamic reservoir of electrons occupying delocalized states. Connecting two or more of such leads to the quantum nanostructure allows one to characterise transport properties of the structure. The electrons coming from an incoming lead may be reflected back from a nanostructure or transmitted to a second lead giving rise to the flow of the electric current through the nanostructure. If a number of open channels - quantum delocalized states allowing to deliver or pick up electrons - in the leads is much bigger than the number of open channels in the nanostructure the current flowing through the system does not usually depend on the microscopic details of the leads and may be solely predicted by the details of nanostructure and thermodynamic properties of the leads (the temperature and chemical potential for electrons).

It is striking that transport properties of the nanostructure are described most conveniently solely in terms of states in the leads being at once independent on the specific choice of the leads¹.

3.2 Scattering matrix

The quantum system may be then described by so called scattering matrix ($\hat{S}(E)$) connecting the incoming electron states in the leads ($\Psi_{\text{in}}(E)$) with outgoing electron states in the leads ($\Psi_{\text{out}}(E)$):

$$\Psi_{\text{out}}(E) = \hat{S}(E)\Psi_{\text{in}}(E), \quad (17)$$

or explicitly specifying states from left (L) and right (R) leads (the dependence on chemical potential is omitted for clarity):

$$\begin{pmatrix} \Psi_{L,\text{out}} \\ \Psi_{R,\text{out}} \end{pmatrix} = \begin{pmatrix} \hat{s}_{LL} & \hat{s}_{LR} \\ \hat{s}_{RL} & \hat{s}_{RR} \end{pmatrix} \begin{pmatrix} \Psi_{L,\text{in}} \\ \Psi_{R,\text{in}} \end{pmatrix}. \quad (18)$$

Traditionally, the blocks building the scattering matrix are renamed into transmission (t and t') and reflection (r and r') parts of scattering matrix:

$$\hat{S} = \begin{pmatrix} \hat{s}_{LL} & \hat{s}_{LR} \\ \hat{s}_{RL} & \hat{s}_{RR} \end{pmatrix} \equiv \begin{pmatrix} \hat{r} & \hat{t}' \\ \hat{t} & \hat{r}' \end{pmatrix}. \quad (19)$$

¹The transmission amplitudes and form of scattering matrix blocks may (and will) of course depend on the exact choice of the leads, yet the set of transmission eigenvalues will approximately not.

Of great theoretical interest are probabilities of electron incoming in channel n being transmitted through (or reflected by) the nanostructure. These probabilities are given by diagonal values formed by transmission and reflection matrices:

$$T_n = (\hat{t}^\dagger \hat{t})_{nn}, \quad (20)$$

$$R_n = (\hat{r}^\dagger \hat{r})_{nn}. \quad (21)$$

3.3 Transport characteristics at constant temperature

The most straightforward transport characteristic of a quantum nanosystem is conductance (G) being the inverse of the electric resistance. To obtain a formula for the conductance of a system it is convenient to start with formula for the current flowing through the system [23]:

$$I = 2_s e \sum_n \left\{ \int_0^\infty \frac{dk_x}{2\pi} v_x(k_x) f_L(E) \right. \quad (22)$$

$$\left. + \int_{-\infty}^0 \frac{dk_x}{2\pi} v_x(k_x) [R_n(E) f_L(E) + (1 - R'_n(E)) f_R(E)] \right\} \quad (23)$$

$$= \frac{2_s e}{h} \sum_n \int_0^\infty (1 - R_n(E)) [f_L(E) - f_R(E)] dE \quad (24)$$

$$= \frac{2_s e}{h} \int_0^\infty \left(\sum_n T_n(E) \right) [f_L(E) - f_R(E)] dE \quad (25)$$

$$\approx \frac{2_s e^2}{h} U \left(\sum_n T_n(E) \right), \quad (26)$$

obtaining desire formula for the system conductance:

$$G(E) = 2_s G_0 \sum_n T_n(E), \quad (27)$$

where $G_0 = e^2/h$ is conductance quantum, $f_{L(R)}(E)$ is the Fermi-Dirac distribution of electrons in the left (right) lead, U is the (small) voltage and 2_s stands for spin degeneracy. In the derivation, identities $\sum_n 1 - R'_n = \sum_n 1 - R_n = \sum_n T_n$ following from the unitarity of the scattering matrix have been used. In the final approximation the assumption that transmission coefficients does not significantly depend on chemical potential in the scales defined by voltage U and temperature $k_b T$ has been made.

3.4 Thermoelectric properties

Despite a fact that electric current is *the current* that drives electronic and informatic revolutions the thermoelectric properties of materials are also of significant importance. The electronic part of thermal current (and thermal properties of a material) may be easily represented in Landauer–Büttiker formalism. Starting from formulas for electrical and thermal currents [24]:

$$I = -\frac{ge}{h} \int T(E)[f_L(E) - f_R(E)]dE,$$

$$I_Q = \frac{g}{h} \int T(E)[f_L(E) - f_R(E)](E - \mu)dE,$$

where g is the degeneracy factor, μ is the (average) chemical potential in the leads and $T(E)$ is shorthand notation for $\sum_n T_n(E)$. In the linear response regime (infinitesimal potential and temperature differences) the Seebeck (S) coefficient and the thermal conductance K_{el} are given by:

$$S = -\frac{V}{\Delta T} \Big|_{I=0} = \frac{L_1}{eTL_0}, \quad (28)$$

$$K_{el} = \frac{I_Q}{\Delta T} \Big|_{I=0} = \frac{L_0L_2 - L_1^2}{TL_0}, \quad (29)$$

where

$$L_n = \frac{g}{h} \int T(E) \left(-\frac{\partial f}{\partial E} \right) (E - \mu)^n, \quad (30)$$

with f being the Fermi Dirac distribution with thermodynamic parameters (chemical potential and temperature) taken as mean values between the leads.

3.5 Adiabatic pumping

The analysis of transport properties of a nanostructure up to now assumed that the nanostructure itself does not change during the time of experiment. When it does, this process may generate the current between the leads even in the absence of voltage and temperature difference between the leads. Assuming that typical time corresponding to change of the scatterer is much larger than time of flight of electron through the scatterer one may write adiabatic formula for a charge transferred [23]

$$\Delta Q_\alpha = -\frac{ie}{2\pi} \int Tr_\alpha \left(\frac{d\hat{S}}{dt} \hat{S}^\dagger \right) dt \quad (31)$$

where ΔQ_α is charge transferred to a lead α and trace is taken over elements corresponding to states originating from the lead α .

4 Investigating graphene

4.1 Pursuing the trigonal warping strength

4.1.1 Motivation

Trigonal warping is the common name for γ_3 tunnelling - arguably the second most important interlayer tunnelling in bilayer graphene. This term breaks the rotational symmetry of the approximate band structure in the vicinity of the K and K' points. Moreover it leads to the splitting of each of two Dirac cones into 4 new cones (see Fig. 2 (a)). A single cone out of 4 new cones is centred exactly at the K (K') point, while 3 remaining cones are centred at momentum $p = \gamma_1 v_3 / v^2$ at three different directions. The central cone is approximately circular, while the satellite cones are approximately elliptical with ratio of major- an minor-semi axes equal 3.

The splitting of Dirac cones leads to enhancement of minimal conductivity of bilayer graphene by (approximately) factor of 3 [25] being the possible explanation for experimentally measured value [26]. The splitting of the Fermi surface does not survive to higher chemical potentials. This has obvious consequence of appearance of the Lifshitz phase transition reconnecting the splitted Fermi surface. The Lifshitz transition appears at Lifshitz energy

$$E_L = \frac{\gamma_1}{4} \left(\frac{\gamma_3}{\gamma_0} \right)^2 \quad (32)$$

and is accompanied by the presence of van Hove singularity in bulk density of states (see Fig. 2 (b)) [27].

Despite being profound in its consequences the Lifshitz transition has till now been avoiding precise experimental determination. The available experimental results cover the range of $E_L \sim 0.1 - 1$ meV [29, 30, 22]. The motivation of this work was to propose an experimentally convenient way to measure trigonal warping strength with satisfying precision.

4.1.2 Seebeck coefficient: the simple approach

For the clarity of reasoning and in order to concentrate on the influence of trigonal warping strength the simplest possible model has been chosen. Explicitly, our model is equivalent to setting $v_4 = U = \delta_{AB} = 0$ in Hamiltonian (6).

The Lifshitz transition is accompanied by van Hove singularity in density of states. One may thus expect abrupt behaviour of conductance of the system in the vicinity of the Lifshitz energy. Unfortunately there are too small to smoke gun the transition in experiment. The well-known Mott formula for metals² [31] states that Seebeck coefficient is proportional to logarithmic derivative of transmission with respect to chemical potential. One may thus expect that due to low conductance at the vicinity of Lifshitz

² $S = (\pi^2/3)e^{-1}k_B^2 T [\partial \ln T(E) / \partial E]_{E=\mu}$

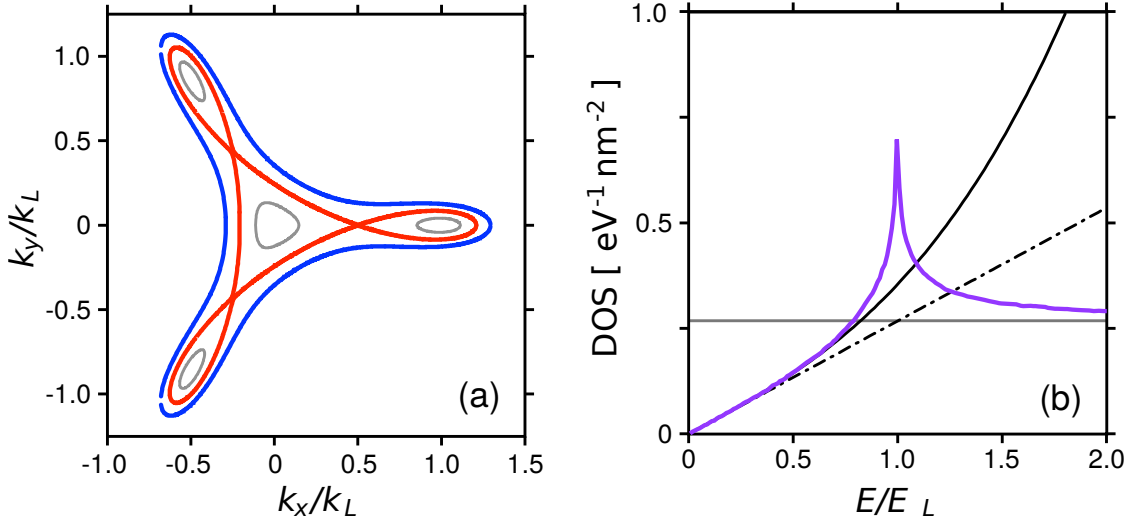


Figure 2: (a) The Fermi surface for $E = 0.5E_L$, $E = E_L$, $E = 1.5E_L$ depicted by grey solid lines, red solid lines and blue dashed lines respectively. (b) Density of states (purple solid lines) with the case $\gamma_3 = 0$ (grey solid line) and linear approximation for $\gamma_3 \neq 0$ (black dash dotted line, see eq. (33)). Adapted from [28].

transition and the presence of derivative in the Mott formula the abrupt changes originating from van Hove singularity will be magnified in dependence of Seebeck coefficient on chemical potential.

The analysis starts with simplified 2-band Hamiltonian for bilayer graphene (7). Treating each Dirac cone separately and expanding the Hamiltonian to linear terms in momentum leads to simple formula for bulk density of states:

$$\rho(E) \approx \rho_0 \frac{|E|}{E_L}, \quad (33)$$

where ρ_0 is the bulk density of states of bilayer graphene in the absence of trigonal warping. One may thus expect linear dependence of conductance of the system as the function of chemical potential. Mode matching numerical analysis confirms these suspicion for chemical potential $E \leq E_L/2$ (see Fig. 3).

Unfortunately for a system with linear dependence of conductance on chemical potential the Seebeck coefficient is uniquely defined by temperature and holds no information about the slope of conductance vs chemical potential dependence. Moreover one may not simply apply Mott formula to numerical analysis due to significant contribution from Fabry-Pérot resonances. One is forced to use non-simplified equation (28).

Fortunately enough, the full numerical calculation of Seebeck coefficient shows anomaly - the additional maximum at the vicinity of Lifshitz energy (E_L) for appropriate temperature range (see Fig. 4). When the temperature is too large, it average out all details connected to Lifshitz transition. When it is too small, the Fabry-Pérot oscillations give

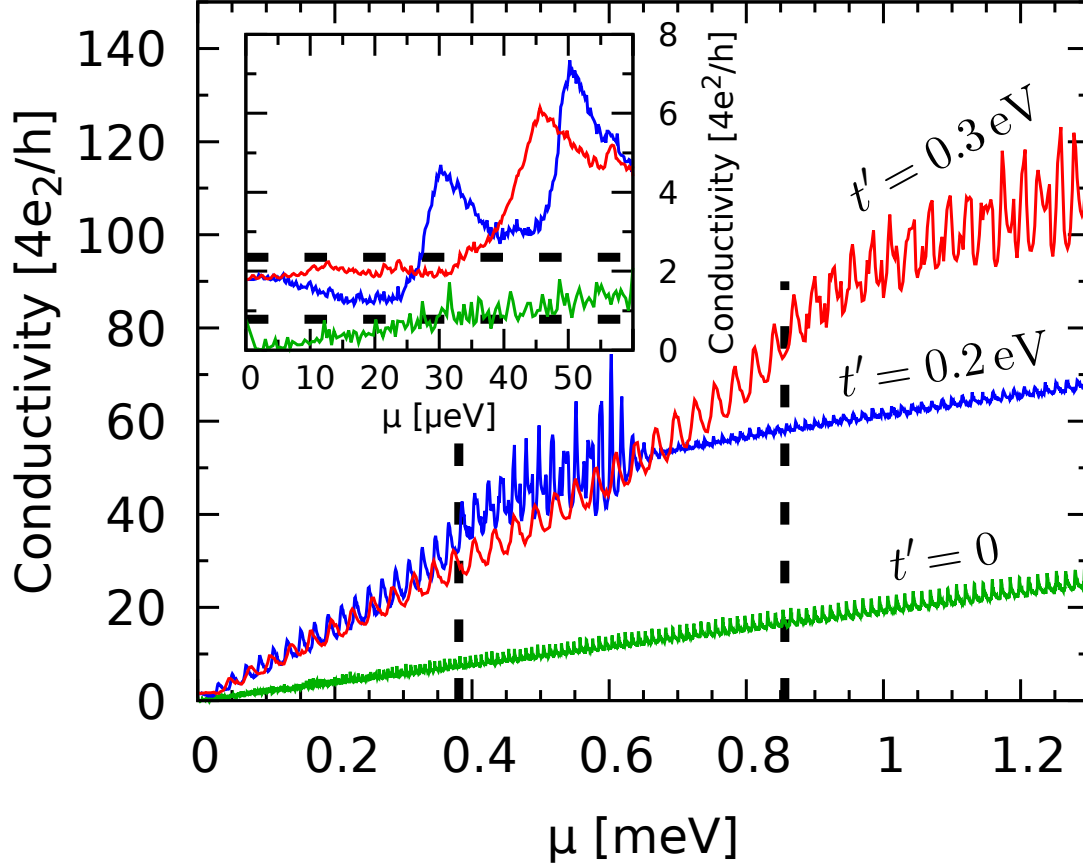


Figure 3: The zero temperature conductivity of bilayer graphene for 3 distinct values of trigonal warping (marked on picture). The vertical dashed lines corresponds to Lifshitz energies for considered values of trigonal warping (compare eq. 32). The inset is a zoom-in close to charge neutrality point. The horizontal lines corresponds to conductivities $\sigma = 2\sigma_{\text{MLG}} = (8/\pi)e^2/h$ and $\sigma = 6\sigma_{\text{MLG}}$. Reprinted from [28].

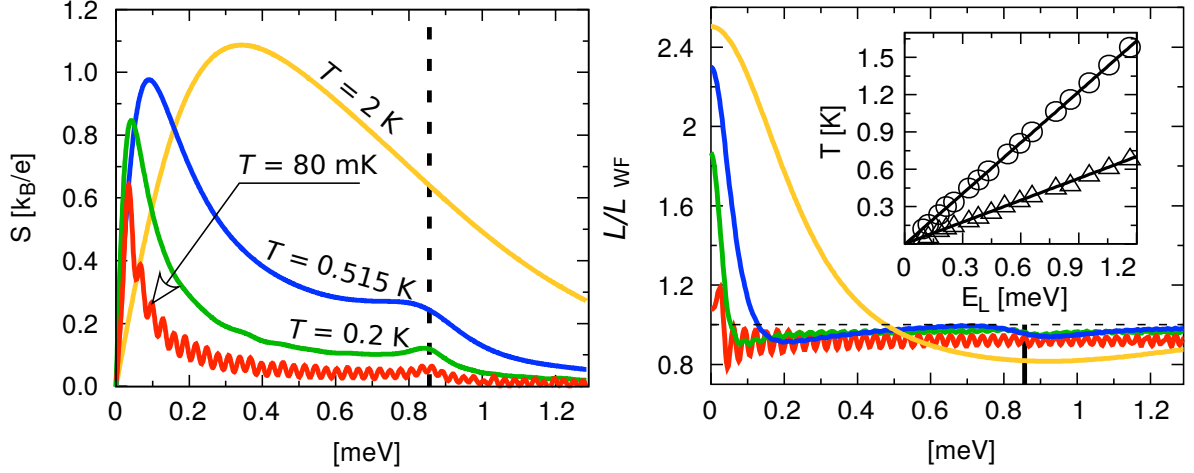


Figure 4: Left: The Seebeck coefficient for $\gamma_3 = 0.3$ eV for 4 different temperatures (see the picture). The dashed vertical line marks the Lifshitz energy. Right: The Lorentz number with respect to the value provided by Wiedemann-Franz law. The temperatures are the same as in the left panel. Inset shows the crossover temperature corresponding to disappearance of second maximum of Seebeck coefficient (triangles) and second minimum of Lorentz number (triangles) with respect to Lifshitz energy. Reprinted from [28].

higher contribution than the anomaly.

Similar anomaly is present in the Lorentz number being the ratio of electronic part of thermal conductance to the conductance $\mathcal{L} = K_{el}/TG$ though this time it represents itself as an additional minimum (see Fig. 4) below the value given by Wiedemann-Franz law ($\mathcal{L}_{WF} = (\pi^2/3)(k_B/e)^2$), obeyed by the standard Fermi gas (with constant DOS).

Measuring thus the Seebeck coefficient or the Lorentz number as a function of chemical potential allows to find a value of Lifshitz energy. One may be worried about possibility of measuring the electronic part of thermal conductance, yet such worries would be misplaced. The electronic part of thermal conductance may be measured as a difference between the total thermal conductance and the phonon thermal conductance. Measuring the phonon thermal conductance is possible by electrostatically opening the energy gap, reducing the electronic contribution of thermal conductance to negligible value.

The real inconvenience of such measurement comes from the need to measure values considered as a function of chemical potential, while most of experiments provides them rather as the function of carrier concentration. This difficulty might however be overcome.

4.1.3 Temperature dependent analysis

In order to avoid measurement of chemical potential one may measure global properties of the dependence of Seebeck coefficient on the chemical potential. The procedure proposed is to find (for a given temperature) the global maximum of Seebeck coefficient

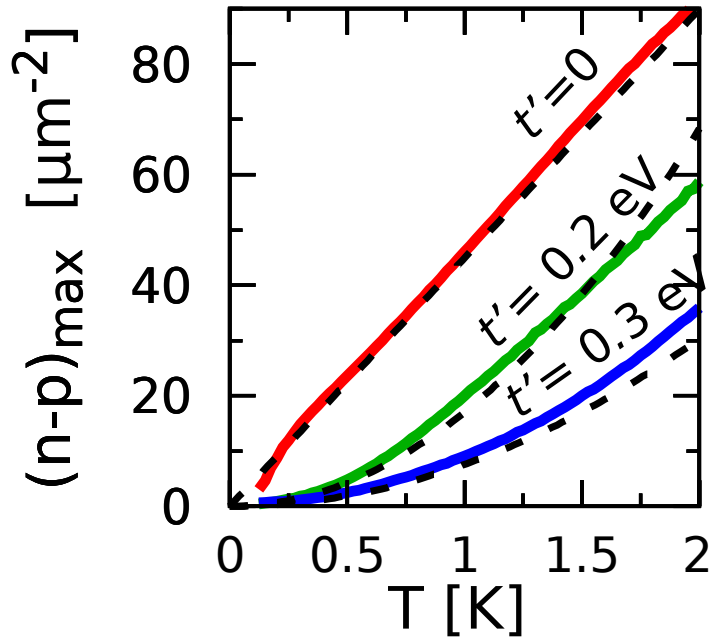


Figure 5: The carrier concentration corresponding to the maximal Seebeck coefficient as a function of temperature for three different values of trigonal warping. Reprinted from [28].

as a function of chemical potential (controlled by the bias gate voltage). Then for the bias gate voltage corresponding to the maximal value of Seebeck coefficient one should measure the carrier concentration. Such a measurement should be repeated for different values of temperature. From measured temperature dependence of carrier concentration corresponding to the maximal Seebeck coefficient one may obtain the value of trigonal warping strength (compare Fig. 5). It should be stressed, that despite of finding the maximum of Seebeck coefficient as a function of chemical potential, the chemical potential need *not* to be measured. The corresponding bias gate potential is fully capable of controlling the measurement process.

During the investigation of system properties another method has been found. It is based on the observation that the maximal value of Seebeck coefficient (as the function of chemical potential) grows up to some temperature and than starts to fall down. It occurred that the temperature corresponding to the maximal value of Seebeck coefficient depends linearly on the Lifschitz energy. It is thus enough to measure temperature corresponding to global maximum of the Seebeck coefficient as the function of both chemical potential *and* temperature (compare Fig. 6). Once again, the chemical potential does not need to be measure, even once.

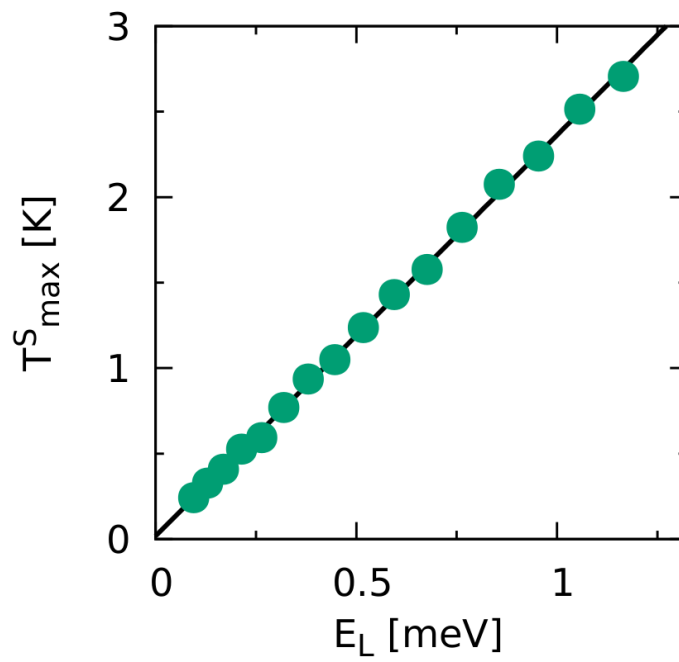


Figure 6: Temperature corresponding to global maximum of the Seebeck coefficient (on the chemical potential vs temperature plane) as a function of Lifshitz energy. Adapted from [28].

4.2 Thermoelectric properties in the presence of the bandgap

4.2.1 Introduction

Previous analysis has been restricted to situation, where there is no bandgap in the system. It is valuable to include in the analysis also the case with the bandgap present. Such gap may be easily realised experimentally by applying out of plane electric field.³ In order to do so, one needs to include U term from Hamiltonian (6) on top of all parameters considered till now. In the absence of trigonal warping, the bandgap is equal to $\Delta = |U|t_{\perp}/\sqrt{U^2 + t_{\perp}^2}$. The presence of trigonal warping leads to minor correction, that usually might be ignored.

As the presence of the bandgap suppress the minimal conductance via evanescent modes and the bandgap influence is of primary interest one may get rid of the Fabry-Pérot oscillations by considering the sharp potential step geometry instead of usual lead-sample-lead geometry. Such sharp potential step geometry might be understood as a geometry joining two regions (weakly- and heavily-doped) at an abrupt line. Unfortunately despite producing nice looking, qualitatively correct predictions it also overestimates the conductance by the approximate factor of 2 (due to lack of backscattering at the second interface). All the analysis is then performed for two system geometries - the abrupt potential step one and the traditional lead-sample-lead one. The first gives clear view, while the second gives results easier to realize in typical experiments.

4.2.2 Seebeck coefficient and $T^{(\alpha)}$ models

As one might expect opening the bandgap leads to strong suppression of the conductance in the bandgap regime followed by rapid increase just after the bottom of the conduction band (see Fig. 7). Following the Mott formula one would expect the appearance of the maximum of Seebeck coefficient at the bottom of conduction band. That is not the case for finite temperatures. Instead it appears at the vicinity of the Goldsmid-Sharp value $|S|_{\max}^{\text{GS}} = \Delta/(2eT)$ derived for wide semiconductors.

In order to understand that behaviour one might apply the family of simple models quantifying the transmission of the system

$$T^{(\alpha)} = C(\Delta) \times \begin{cases} \delta(E - \frac{1}{2}\Delta) + \delta(E + \frac{1}{2}\Delta) & \text{if } \alpha = 0 \\ \Theta(|E| - \frac{1}{2}\Delta) (|E| - \frac{1}{2}\Delta)^{\alpha-1} & \text{if } \alpha > 0 \end{cases} \quad (34)$$

where $C(\Delta)$ is parameter controlling the value of transmission, $\delta(x)$ is the Dirac delta function and $\Theta(x)$ is Heaviside step function.

Applying the above family of models to the calculation of Seebeck coefficient leads to the asymptotic ($u = \Delta/(2k_B T) \gg 1$) formula for the maximum of the Seebeck coefficient

$$|S|_{\max}^{(\alpha)} \approx \frac{k_B}{e} \left(u - \frac{1}{2} \ln(u) + \alpha - \frac{1}{2} + \mathcal{O}(u^{-1}) \right), \quad (35)$$

³Some experiments report appearance of spontaneous bandgap in the suspended graphene of the order of 2.5 meV [32, 33]. Such a bandgap is much smaller than the gaps analysed in this work and is not found in the graphene placed on semiconductor, thus it is of little importance for this analysis.

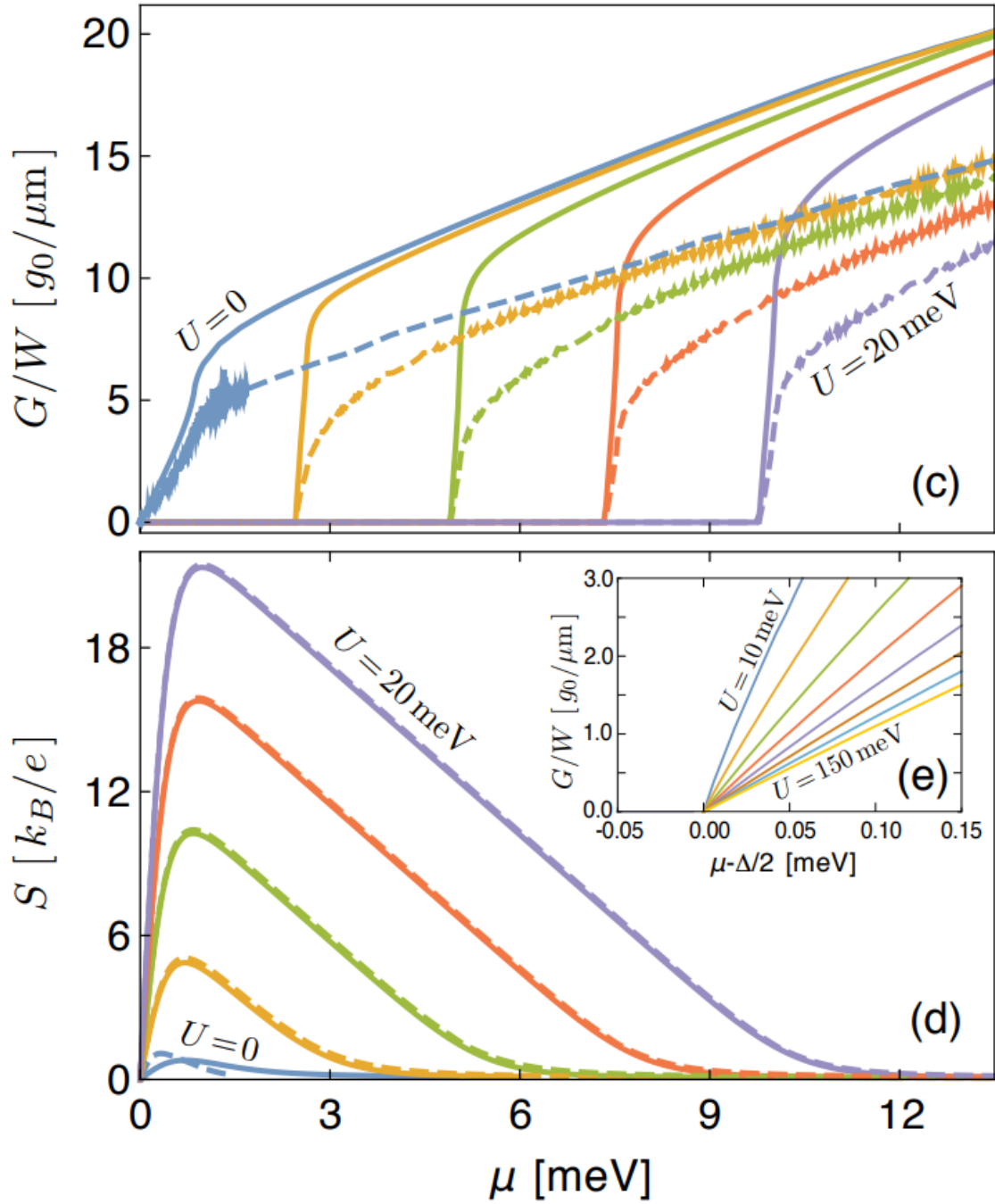


Figure 7: Conductance and Seebeck coefficient as a function of chemical potential for different values of the bandgap (from 0 meV to 20 meV every 5 meV). Solid lines correspond to potential step geometry, while dashed lines correspond to lead-sample-lead geometry. The inset shows zoom-in of conductance around the bottom of the conductance band (the curves where appropriately shifted). Reprinted from [34].

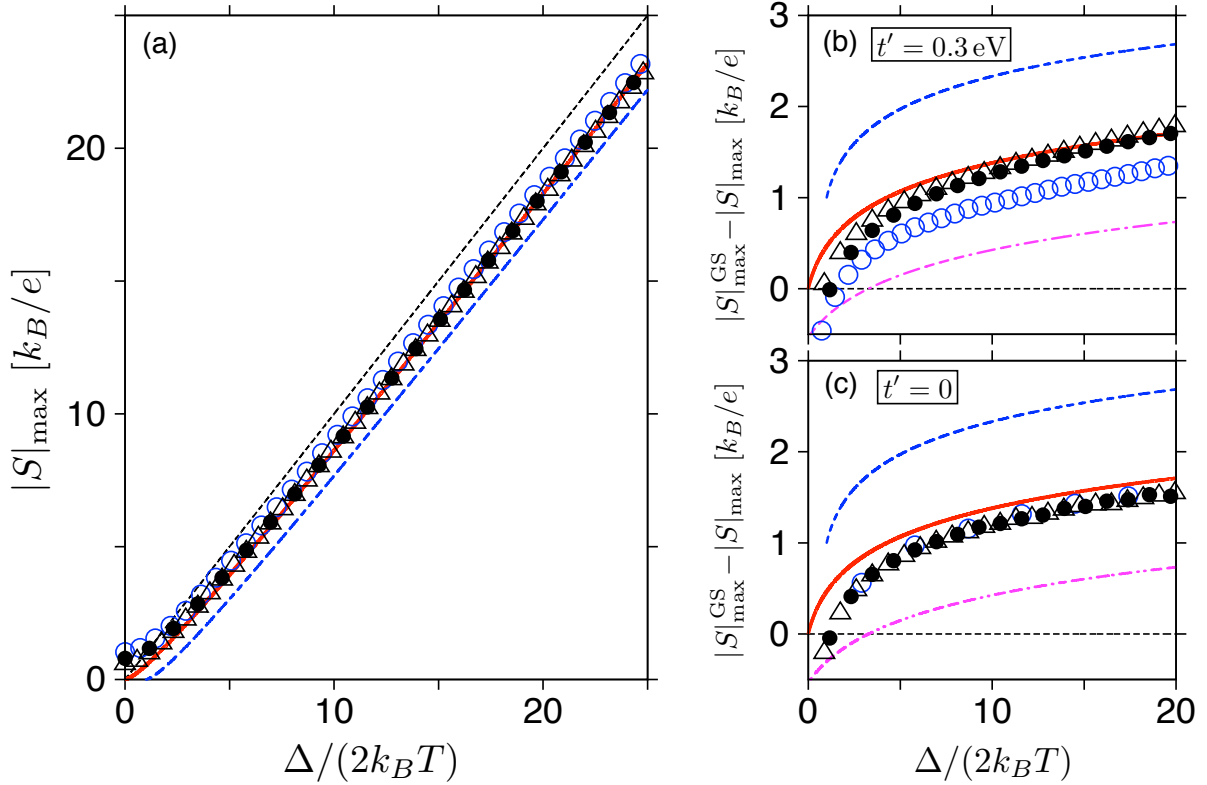


Figure 8: (a) Maximal value of the Seebeck coefficient as a function of $\Delta/(2k_B T)$ for sharp potential step geometry. (b,c) Deviation from Goldsmid-Sharp value in the presence (absence) of trigonal warping. Points show numerical calculations for $T = 1\text{K}$ (open circles), $T = 5\text{K}$ (full circles) and $T = 10\text{K}$ (triangles). Lines shows predictions of $T^{(\alpha)}$ models for $\alpha = 0$ (blue dashed), $\alpha = 1$ (red solid) and $\alpha = 2$ (magenta dash dotted). Reprinted from [34].

which clearly reproduces Goldsmid-Sharp value in the leading term. Moreover it predicts this maximum to appear at the chemical potential

$$\mu_{\max}^{|S|} \approx \frac{k_B T}{2} \ln \left(\frac{2\Delta}{k_B T} \right) \quad (36)$$

that is much lower value than the one expected by naive implementation of Mott formula ($\mu_{\text{expected}} = \Delta/2$). This lead to conclusion that the properties of Seebeck coefficient (at sufficiently low temperatures) are predominantly determined by the presence of bandgap and the details of band structure or transmission give just minor corrections. Indeed, the comparison of numerical calculations with predictions of $T^{(\alpha)}$ models gives great agreement (see Fig. 8). One should though stress that influence of trigonal warping strength is still visible in low temperature data (see Fig. 8 (b,c)).

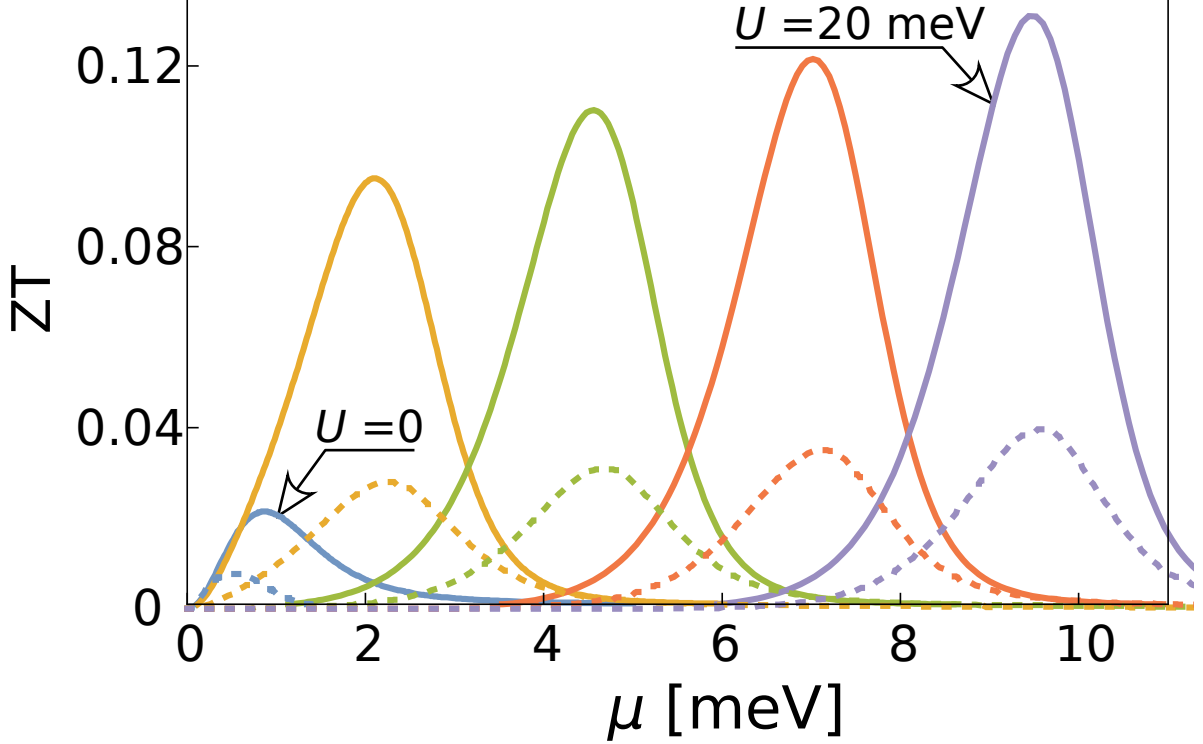


Figure 9: The figure of merit (ZT) as a function of chemical potential for different values of the gap. The temperature is set to 5 K. The color and solid/dashed encoding of lines is the same as in Fig. 7. Reprinted from [34].

4.2.3 Thermoelectric figure of merit (ZT)

Having analysed the Seebeck coefficient one may now wonder how the thermoelectric figure of merit (ZT) will behave in such a system. Usually, the maximum of ZT corresponds to the maximum of the Seebeck coefficient due to its square dependence on it. However, in the system considered that is no longer the truth. The reason for that lies in a strong suppression of the figure of merit in the gap regime due to almost negligible conductance. One might have expected that the ratio of electronic to thermal electron conductance would still remain almost constant and thus the suppression of conductance should not diminish the figure of merit. Such reasoning would yet be misplaced, as the figure of merit does depend on total thermal conductivity and the phonon thermal conductance is almost unaffected by electric field opening the gap.

In gapped bilayer graphene the maximum of figure of merit corresponds to the bottom of the conduction band (and top of the valence band), see Fig. 9. This is the result of interplay between energies with disappearing conductance and regions with disappearing Seebeck coefficient. Again the results for finite sample system are qualitatively the same as the results for potential step geometry, being just diminished by some numerical factor.

Once again, the T^α models (see Eq.(34)) are capable of both describing the figure of

merit and predicting the maximum of it with satisfying precision (especially for $\alpha = 1$, see Fig. 10). Just like in the case of the Seebeck coefficient one may conclude that the properties of the figure of merit are determined by the presence of the bandgap, while the other properties of band structure play at most secondary role.

Phonons play dominant role in thermal conductance during the determination of figure of merit for bilayer graphene. Among different degrees of freedom, the dominant contribution to phonon thermal conductance comes from out of plane modes (ZA phonons). Thus suppressing them by placing bilayer graphene on rigid substrate may open practical possibility to enhance the maximal value of the figure of merit, approximated by a factor of 3.

4.3 Conductivity of the large sample of bilayer graphene

4.3.1 Introduction

Bilayer graphene is a crystal characterized by several non-equivalent parameters. Researchers included different sets of them, appropriately to the goal chosen. Here the following question is addressed

What is the D.C. conductance of large piece of ultra-clean bilayer graphene and which microscopic parameters are crucial for appropriate description of it?

In order to pursue crucial model parameters the symmetry driven approach, ennobled in long history of physics, has been taken. Among different parameters in Eq.(6) only U is omitted, as the interest lies in intrinsic properties of bilayer graphene, not the ones originating from external fields. Parameters γ_0 and γ_1 describes the nearest neighbour hoppings within the layers and between them respectively. There are thus unavoidable and form a minimal model of bilayer graphene. The trigonal warping strength γ_3 introduces the breaking of rotational symmetry, while γ_4 breaks the electron-hole symmetry. The δ_{AB} term represents the irreducible part of bandgap that may not be closed by external electric field. Such a gap may spontaneously appear due to electron-electron interaction [35], that are otherwise ignored in this work.

For the simplicity and clarity of discussion unique, non-zero values has been chosen for each parameter according to reported experimental results [21]. Namely $\gamma_3 = 0.3$ eV, $\gamma_4 = 0.15$ eV and $\delta_{AB} = 1.5$ meV has been chosen.

4.3.2 Zero-temperature results

The zero temperature results in the presence of a gap are not surprising. The bilayer graphene becomes an insulator, while for short samples ($L < 100l_{\perp}$ with $l_{\perp} = \sqrt{3}a\gamma_0/(2\gamma_1) \approx 1.77$ nm being the effective length appearing in bilayer graphene transport analysis that originates from coupling between the layers) it preserves some transmission via evanescent modes (see Fig. 11 (c,d)).

The physics becomes more rich in gapless scenarios. In absence of both skew inter-layer tunnellings the conductance of the system is just twice the conductance of single

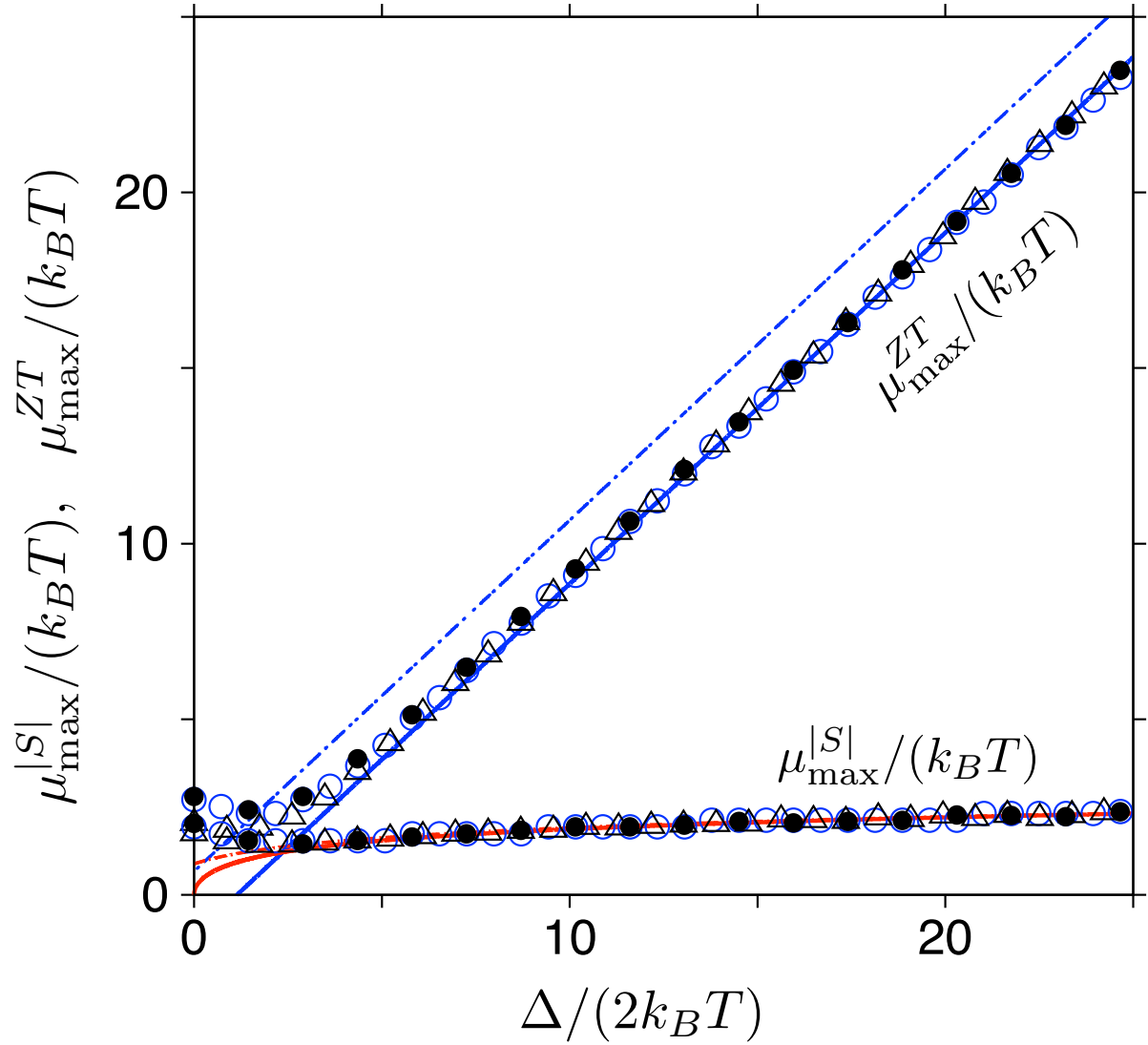


Figure 10: Chemical potential corresponding to maximal values of Seebeck coefficient ($\mu_{\max}^{|S|}$) and figure of merit (μ_{\max}^{ZT}) as a function of Goldsmid-Sharp value. Point symbol encoding is the same as in Fig. 8. Lines correspond to $T^{(\alpha)}$ model predictions for $\alpha = 1$ (solid) and $\alpha = 2$ (dash dotted). Reprinted from [34].

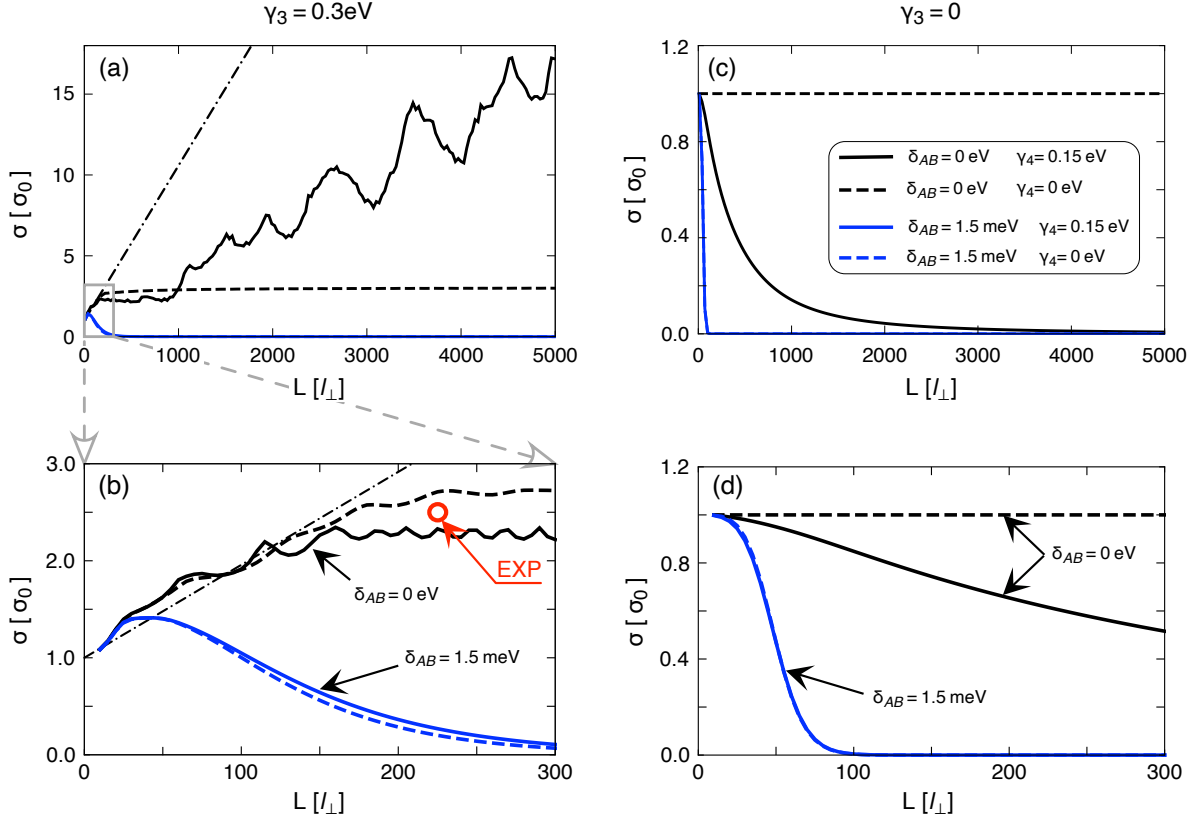


Figure 11: Conductivity of the bilayer graphene as a function of sample length ($\sigma_0 = (8/\pi)e^2/h$ is the conductance at charge neutrality point). Systems with presence/lack of trigonal warping strength are presented at panel (a,b)/(c,d). Bottom panels are zoom-ins of the upper ones for short system lengths. The red circle represents the experimental result [26]. Reprinted from [36].

layer graphene, despite presence of the coupling (it is a non-trivial result, see Ref.[37]). Introduction of trigonal warping (and thus breaking of the rotational symmetry) slowly increases the conductance up to the value of $3\sigma_0$, with σ_0 being the conductance of two decoupled graphene layers. Introduction of γ_4 term in place of trigonal warping leads in opposite to slow, power law decrease of conductance with the system length ($\sigma \propto L^{-2.0}$). One would expect the situation with presence of both trigonal warping and γ_4 term to be a competition between two opposite forces. Instead, presence of both skew tunnelling terms leads to unbounded increase of conductance with the system length (see Fig. 11 (a)). The reason of this approximately linear increase is the presence of propagating modes at zero energy (or any other energy). The propagating modes originate from elevation of three of secondary Dirac cones. The secondary cones are introduced by trigonal warping, yet elevated by γ_4 term. Thus only presence of both terms may introduce conducting states at zero energy to the bilayer graphene. This situation where interplay of two factors leads to appearance of qualitatively new phenomenon is a beautiful example of the rich structure of quantum mechanics and physics in general.

It is worth to note, that Fano factor does not significantly differ from the pseudodiffusive value ($F = 1/3$), except for the regimes of vanishing conductance, when unsurprisingly it approaches value of 1.

4.3.3 Finite temperature effects

At the beginning of discussion of influence of temperature on conductance properties of the system one should note that interaction induced gap depends on temperature and disappears for a critical value of temperature. In order to reproduce reported temperature dependence [38] the gap will be than modelled as

$$\delta_{AB}(T) = \delta_{AB}(0) \begin{cases} \tanh\left(1.74\sqrt{\frac{T_C}{T} - 1}\right) & \text{if } T \leq T_C \\ 0 & \text{if } T > T_C \end{cases}, \quad (37)$$

with $T_C = 12$ K and $\delta_{AB}(0) = 1.5$ meV.

One of the most striking features of finite temperature conductance is that it almost does not depend on γ_4 term, that becomes irrelevant. One may thus conclude that electron-hole symmetry does not play important role in finite temperature conductance of bilayer graphene (see Fig. 12).

Unsurprisingly, $T > 0$ leads to increase of conductance with higher temperature leading to higher increase of conductance. The increase seems unlimited with system length for any finite temperature considered. The presence of thermally reduced gap leads to diminished increase of conductance, with effect disappearing altogether with gap closing.

The most interesting part of conductance is probably the regime of sufficiently short, gapless systems where the effects of finite temperature are almost negligible. In this regime the quantum properties of conductance via evanescent states are the most important and dominate the finite temperature effects.

The electronic noise for finite temperature is dominated by Nyquist-Johnson noise, making the Fano factor irrelevant.

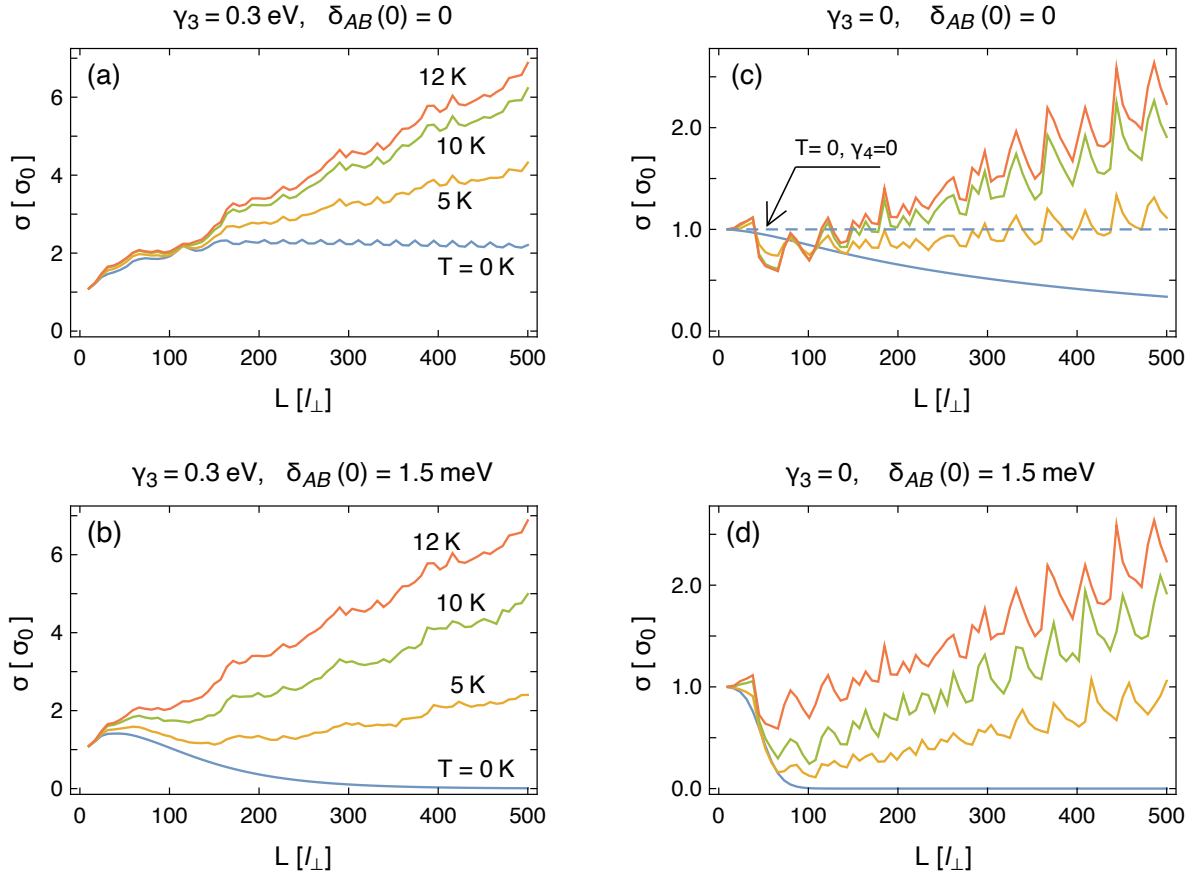


Figure 12: Conductivity of the bilayer graphene as a function of sample length ($\sigma_0 = (8/\pi)e^2/h$ is the conductance at charge neutrality point) for $T = 0 \text{ K}$, 5 K , 10 K and $T_C = 12 \text{ K}$. As influence of γ_4 occurred to be almost negligible, γ_4 is set to 0.15 eV for all lines with single exception in panel (c). Reprinted from [36].

4.3.4 Spontaneous symmetry breaking in bilayer graphene

Another interesting property of conductance of bilayer graphene is the fact that it may be used as an example of spontaneous symmetry breaking system with three possible scenarios. Considering $\sigma(L)$ being the order parameter the spontaneous symmetry breaking is gun-smoked by non-commuting order of limits

$$\lim_{L \rightarrow \infty} [...] \sigma = \sigma_0, \quad (38)$$

$$\lim_{d \rightarrow \infty} \lim_{L \rightarrow \infty} \lim_{\delta_{AB} \rightarrow 0} \sigma = \infty, \quad (39)$$

$$\lim_{d \rightarrow \infty} \lim_{\delta_{AB} \rightarrow 0} \lim_{L \rightarrow \infty} \sigma = \lim_{\delta_{AB} \rightarrow 0} \sigma = 0, \quad (40)$$

where limit of infinite interlayer distance d ($d \rightarrow \infty$) correspond to simultaneous limits $\gamma_3 \rightarrow 0$, $\gamma_4 \rightarrow 0$ and $\gamma_1 \rightarrow 0$ (the last limit being irrelevant for the final result). One may than conclude that in bilayer graphene breaking of the rotational symmetry, breaking of electron-hole symmetry and breaking of sublattice equivalence (due to $\gamma_1 \neq 0$) may appear spontaneously.

5 Selected devices made out of graphene

5.1 Aharonov-Bohm effect without two slits

5.1.1 Introduction

Aharonov-Bohm effect is a bizarre quantum effect that has no analogue in classical mechanics. It is unique in the sense that it allows to influence time evolution of charged particles by the magnetic field that is never met by particles wavefunctions. Despite many experimental realizations [39, 40] its existence in orthodox version presented here has been long questioned and the effect was attributed to residual Lorentz force (originating from e.g. leakage fields) acting on the electron wavefunction [41, 42]. Nowadays the discussion is settled, by beautiful experimental realization [43] exploiting shielding of the magnetic field with superconductor.

In vast majority of experimental realizations of Aharonov-Bohm effect the trajectories encircling the magnetic field flux are considered as they provide most straightforward interpretations. In this work an alternative approach is taken. Instead of electron current encircling the magnetic field, the electron wavefunctions themselves encircle magnetic field flux at each moment of experiment and electron current flows radially according to rotational symmetry of the system.

5.1.2 Earlier work

The functional form of transmission coefficient for Corbino disk in uniform magnetic field at charge neutrality point is long since known [44]

$$T_j = \frac{1}{\cosh^2 [\ln(R_o/R_i)(j + \phi_d/\phi_0)]}, \quad (41)$$

where j corresponds to total angular momentum ($J_z = \hbar j$, $j = \pm 1/2, \pm 3/2, \dots$), $\phi_d = \pi (R_o^2 - R_i^2) B$ is the magnetic flux piercing the disk, $\phi_0 = 2(h/e) \ln(R_o/R_i)$ being period of conductance oscillations, B standing for magnetic field, $R_o(R_i)$ for outer (inner) disk radius. Unfortunately, the uniform magnetic field setup occurred to be unsuitable to measure oscillations of magnetoconductance, leaving space for more subtle approach involving Aharonov-Bohm effect.

The picture is even more simple in the case of Aharonov-Bohm effect, when all the magnetic field flows through the hole in the inner lead and does not flow through the disk itself. In such a situation above formula holds, but with simplified substitution [45]

$$\phi_d \equiv \phi_i, \quad (42)$$

$$\phi_0 \equiv \phi_{AB} = h/e, \quad (43)$$

where ϕ_i stands for total magnetic flux piercing the inner lead. Nonetheless, the analysis for non-zero chemical potentials were missing.

5.1.3 Magnetoconductance at non-zero chemical potential

The magnetoconductance of the system has been derived using mode matching analysis. The closed form solution for the transmission coefficients has been derived [18] and used to analyse the magnetoconductance. The total conductance of the system grows almost linearly starting from charge neutrality conductance via evanescent modes (see Fig. 13 (a)). The magnetoconductance is perfectly periodic with a period given by Aharonov-Bohm flux (ϕ_{AB}) (see Fig. 13 (b)). Notably enough, the magnetoconductance oscillations are quite large (of the order of $0.15 \phi_{AB}$ for chosen $R_o/R_i = 5$). Moreover the oscillations appear at almost all energies (see Fig. 13 (d)) with contraposition to the uniform magnetic field case, where they appear only in the vicinity of Landau levels [44]. The further analysis shows that similarly high magnetoconductance oscillations appear also for different ratios of disk radii (see Fig. 13 (c)), yet they might be shifted toward higher chemical potential.

5.1.4 Magnetoconductance in the absence of cylindrical symmetry

In experimental reality the perfect cylindrical symmetry might be hard to achieve. Almost all imperfections leads to mode mixing and many to local charge density fluctuations (i.e. *p-n puddles*). The natural question arises, whether results of the previous section survive in lower symmetry reality. In order to investigate this issue lets consider application of in plane electric field leading to addition of linear potential

$$U(r, \varphi) = -\frac{U_0 r}{R_o} \sin(\varphi), \quad (44)$$

where U_0 stands for maximal value of potential at the edge of the system. Such a term introduces mode mixing to the system removing possibility of finding compact closed form solution for transmission coefficients. The numerical analysis has been then applied, following the standard procedure. The results are compactly summarised in Fig. 14. As expected, presence of in-plane electric field enhanced the zero-energy transmission (via conducting states formed in heavily doped regions). The change in total conductance is almost negligible for the higher chemical potentials, as one may consider the uniformly doped sample as being 'averaged' version of a sample with linear potential. The interest lies though in the magnetoconductance. At the charge neutrality point the amplitude of magnetoconductance oscillations is strongly diminished. This may be understood, provided the additional conducting states are roughly localized *either* in upper or lower half circle. Such states does not encircle the magnetic field flux and there is no reason to believe they should be significantly influenced by its change. Fortunately, the amplitude of magnetoconductance oscillations is preserved even for U_0 values being higher than p-n puddle potential variations (being of the order of 10 meV [47]) provided than one not restrict the analysis to charge neutrality point (see Fig. 14). This proves both the robustness of results obtained and importance of non-zero chemical potential analysis.

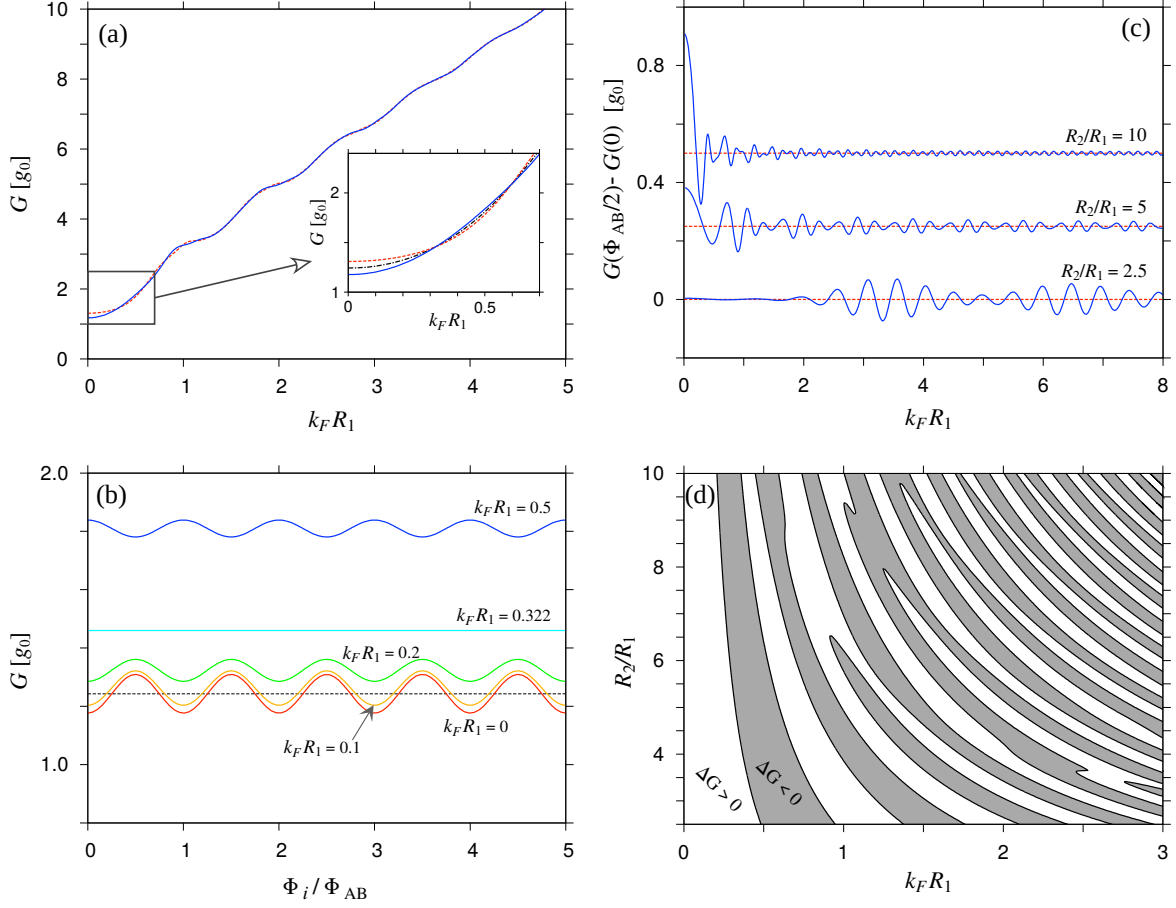


Figure 13: (a) The conductance of the system as a function of doping for the ratio $R_o/R_i = 5$. Lines depict $\phi_i = 0$ (blue solid) and $\phi_i = \phi_{AB}/2$ (red dashed). Black dash dotted line in the inset is the average over ϕ_i . (b) The magnetoconductance for different doping. Dashed line marks pseudodiffusive conductance $G_{\text{diff}} = 2g_0 / \ln(R_o/R_i)$ with $g_0 = 4e^2/h$. (c) Magnitude of magnetoconductance oscillations as a function of doping for different radii ratio. The lines for $R_o/R_i = 5$ ($R_o/R_i = 10$) are shifted by $0.25 g_0$ ($0.5 g_0$). (d) 2-dimensional map of nodal lines marking conductance unaffected by magnetic field on the radii ratio - doping plane. $\Delta G = G(\phi_{AB}/2) - G(0)$. Reprinted from [46].

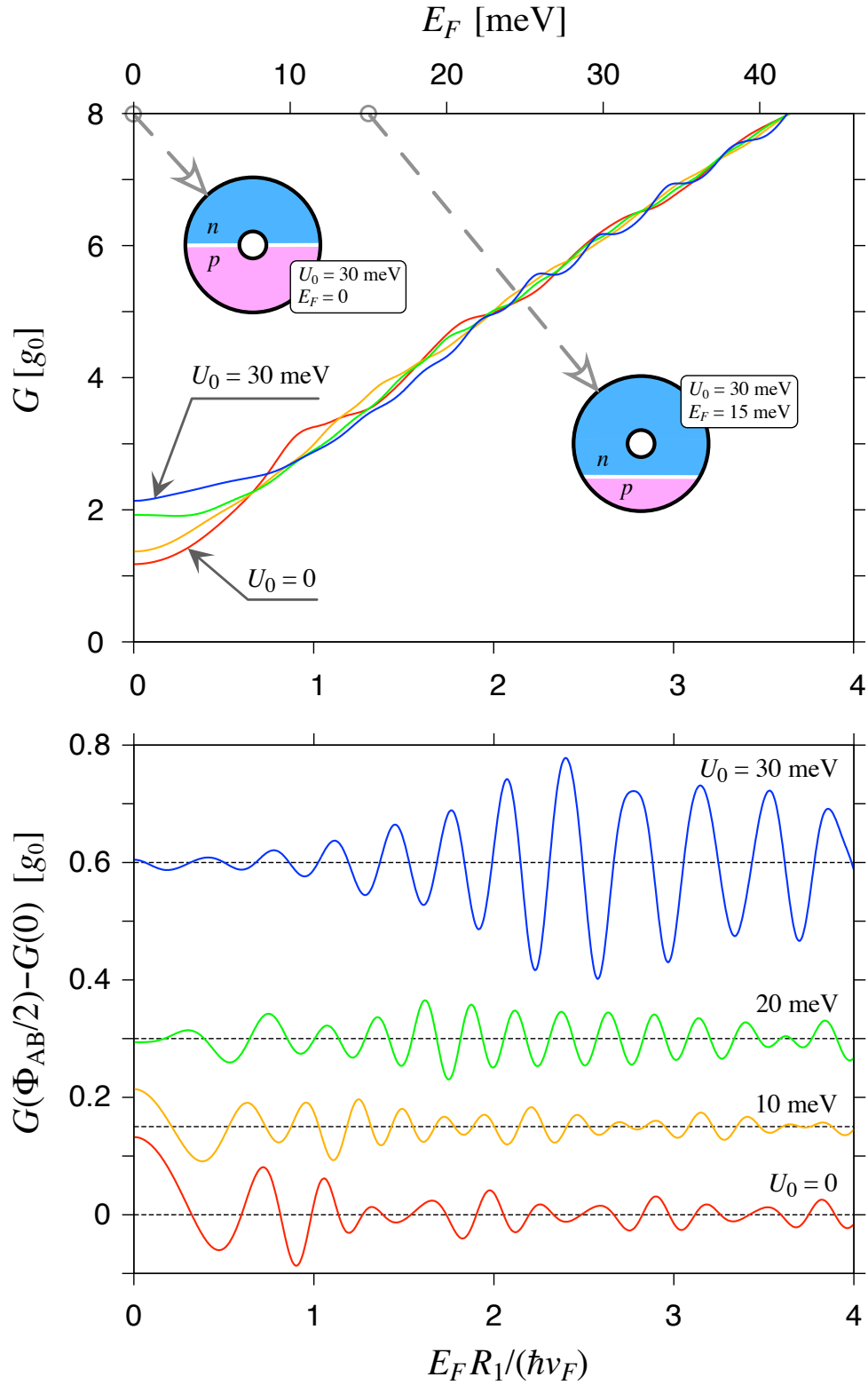


Figure 14: Conductance of the system as the function of doping (upper) and magnitude of conductance oscillations (lower) for 4 different values of U_0 from 0 meV to 30 meV every 10 meV. At the bottom figure the lines corresponding to $U_0 > 0$ are subjected to vertical shifts. Reprinted from [46].

5.2 Mesoscopic valley filter

5.2.1 Concept of valleytronics

The presence of two Dirac cones (valleys) in a dispersion relation of graphene does usually manifest itself as an additional (to spin) two-fold degeneracy of electron states. This follows from equivalence of valleys - there are exchanged under combined action of time reversal and charge conjugation operators. As long as this symmetry holds and there is no coupling between layers the degeneracy of states is be preserved. Breaking those symmetries may lead however to more complex behaviour.

Valleytronic is probably most far going idea of utilizing the valley inequivalence [48]. It postulates to physically separate the currents originating from both graphene valleys in analogy to spintronics postulating separation of currents with respect to spin polarization. Such valley polarized current might be than used to store information and give rise to new type of electronics — the valleytronics itself.

The valley polarization is defined as

$$\mathcal{P} = \frac{Tr\mathbf{T}_{\xi=1} - Tr\mathbf{T}_{\xi=-1}}{Tr\mathbf{T}_{\xi=1} + Tr\mathbf{T}_{\xi=-1}}, \quad (45)$$

with T_ξ being the transmission matrix for valley ξ ($\xi = 1, -1$ corresponds to K, K' valley).

The first valleytronic device, crucial for the whole idea, would be then the valley filter (or polariser) of the current. There are many propositions of constructing such devices, all employing either system preparation with single-atom precision, or presence of strained induced pseudomagnetic fields, both being problematic for experimental realisation. In opposition to them this work tries to propose construction of mesoscopic valley filter - the valley filter that operation will not depend on single-atom details, but rather on mesoscopic properties without experimental difficulties of strain induced pseudomagnetic fields.

5.2.2 The setup

In order to achieve the goal lets concentrate on effective graphene Hamiltonian with two additional potentials

$$(\xi\pi_x\sigma_x + \pi_y\sigma_y) \psi(r, \phi) = [E - \mathcal{V}(r, \phi) - \mathcal{M}(r, \phi)\sigma_z] \psi(r, \phi) \quad (46)$$

with $\mathcal{V}(r, \phi)$ being the electrostatic potential and $\mathcal{M}(r, \phi)$ being the position dependent mass term. The system in Corbino geometry has been chosen due to clarity of picture following from the lack of edge states. The electrostatic potential is assumed to origin from in-plane electric field leading to form of

$$\mathcal{V}(r, \phi) = -e\mathcal{E}r \sin(\phi - \phi_V), \quad (47)$$

where \mathcal{E} stands for electric field and ϕ_V defines orientation of direction of electric field. For further use define $V = e\mathcal{E}R_o$ with R_i, R_o being respectively the internal and external

Corbino disk radii. The ratio $R_o/R_i = 4$ has been chosen throughout all section. For the sake of simplicity, the step profile of mass term has been incorporated

$$\mathcal{M}(r, \phi) = M\Theta(\phi - \phi_M)\Theta(\pi + \phi_M - \phi), \quad (48)$$

with M quantifying the mass potential strength and ϕ_M defining the mass orientation. Such a mass term may originate from chemical functionalization [49] or the adsorption of hexagonal boron nitride [50]. Throughout the whole paper $\phi_V = \pi/2$ and $\phi_M = 0$ has been preserved. The filter is designed in such a way, that after system fabrication it might be fully controlled by gate voltages adjusting the in-plane electric field and chemical potential. It is worth noting that fully functioning filters has been modelled also for continuous change in spatial mass distribution following very similar procedure to the one described here.

5.2.3 Role of electrostatic potential

The analysis of system behaviour starts with the case of zero mass ($M = 0$). In the case of lack of external electric field and zero chemical potential the system is in pseudodiffusive limit and the conductance of the system slightly oscillates around the approximate value of $6g_0$, with $g_0 = e^2/h$ (see Fig. 16). For small electric field the behaviour of the system does not differ significantly up to some threshold value of magnetic field, where the conductance drops to the value of $4g_0$. The stronger the electric field, the lower the threshold magnetic field. Above that magnetic field the current flows along the p-n interface through so-called snake states, with single snake state per valley explaining the additional factor of 2 (on top on spin degeneracy). The snake states are most intuitively described via the semi-classical picture involving Klein tunnelling. In that picture travelling electron is subjected to classical cyclotron trajectories and consecutive changes into and from a hole at the moment of traversing the p-n interface (see Fig. 15). Despite easily understandable picture the quantum mechanical states themselves does not exhibit 'snake shape' structure and usually are evenly distributed around the interface preserving the translational symmetry along the (straight) p-n interface. Nonetheless, the formation of snake states, being just special kind of Quantum Hall states, is well understood and will be of primary interest of this work.

The crucial property of this snake states used in construction of valley filter is their appearance on only single side of the system for a given voltage polarization between the leads (see Fig. 17). It is enforced by their Quantum Hall nature, that allows them to traverse the interface in exactly one direction. At the end of this paragraph I would like to note that up to know the currents originating from both valleys behave exactly in the same way. In order to construct a working valley filter one needs additional tool.

5.2.4 Role of the mass term

The primary role of the mass term is to break the valley symmetry. It is possible, because mass term breaks the symplectic symmetry that gives rise to effective time-reversal symmetry in each of the valleys. Combined with magnetic field that breaks

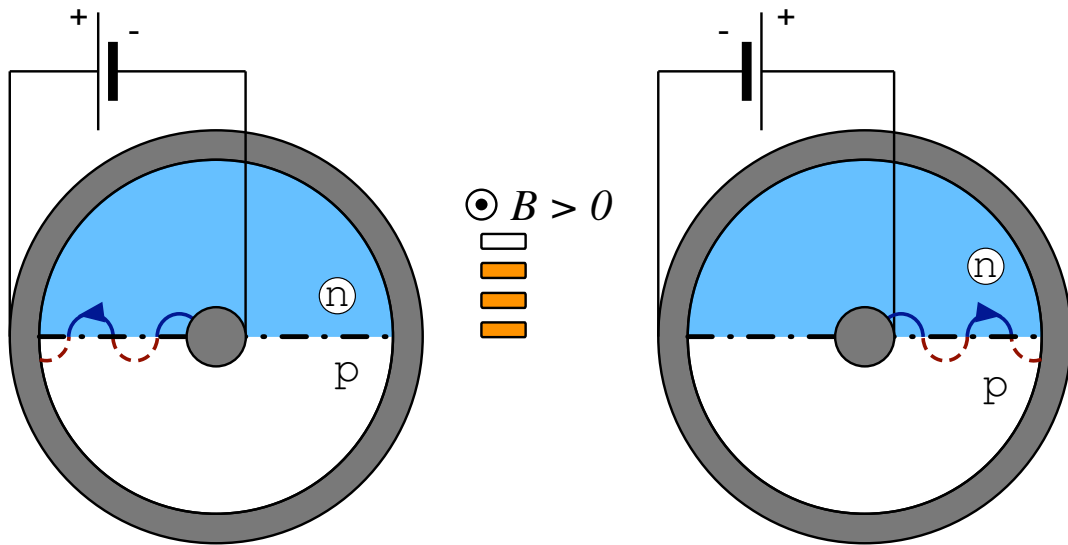


Figure 15: Quasi-classical picture of snake states. The electron (in n -doped region) traversing p-n junction changes into a hole (in p -doped region). This change is accompanied by change of sign of curvature radius. Reprinted from [51].

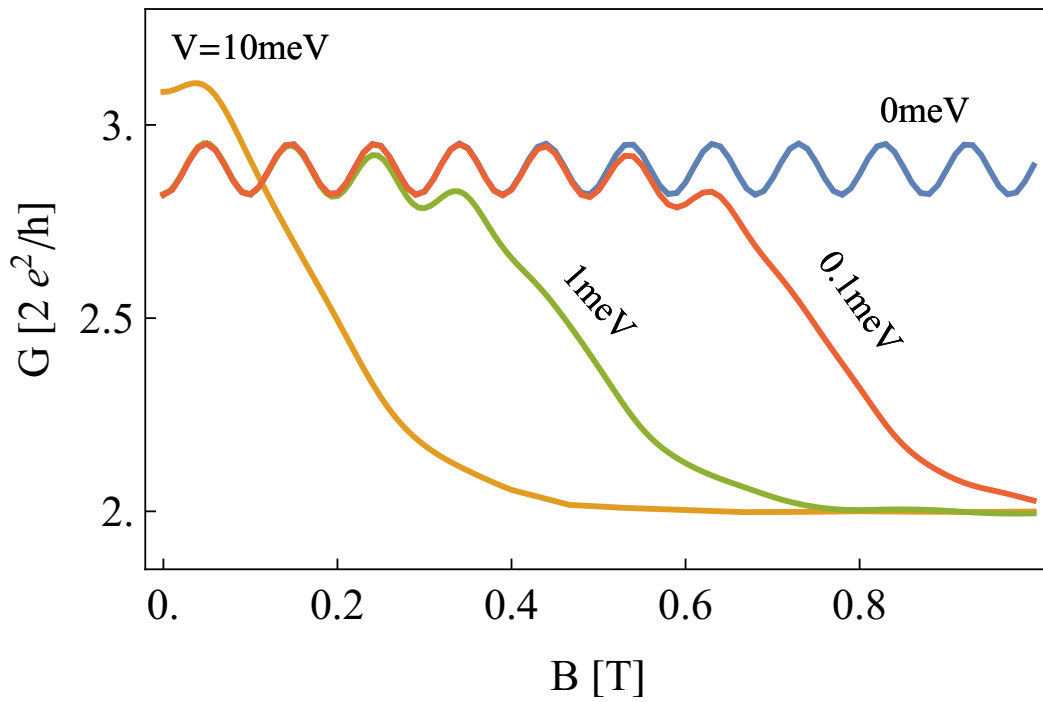


Figure 16: Magnetoconductance of the Corbino disk at the charge neutrality point for different values of electric field \mathcal{E} (represented by $V = e\mathcal{E}R_o$). Reprinted from [51].

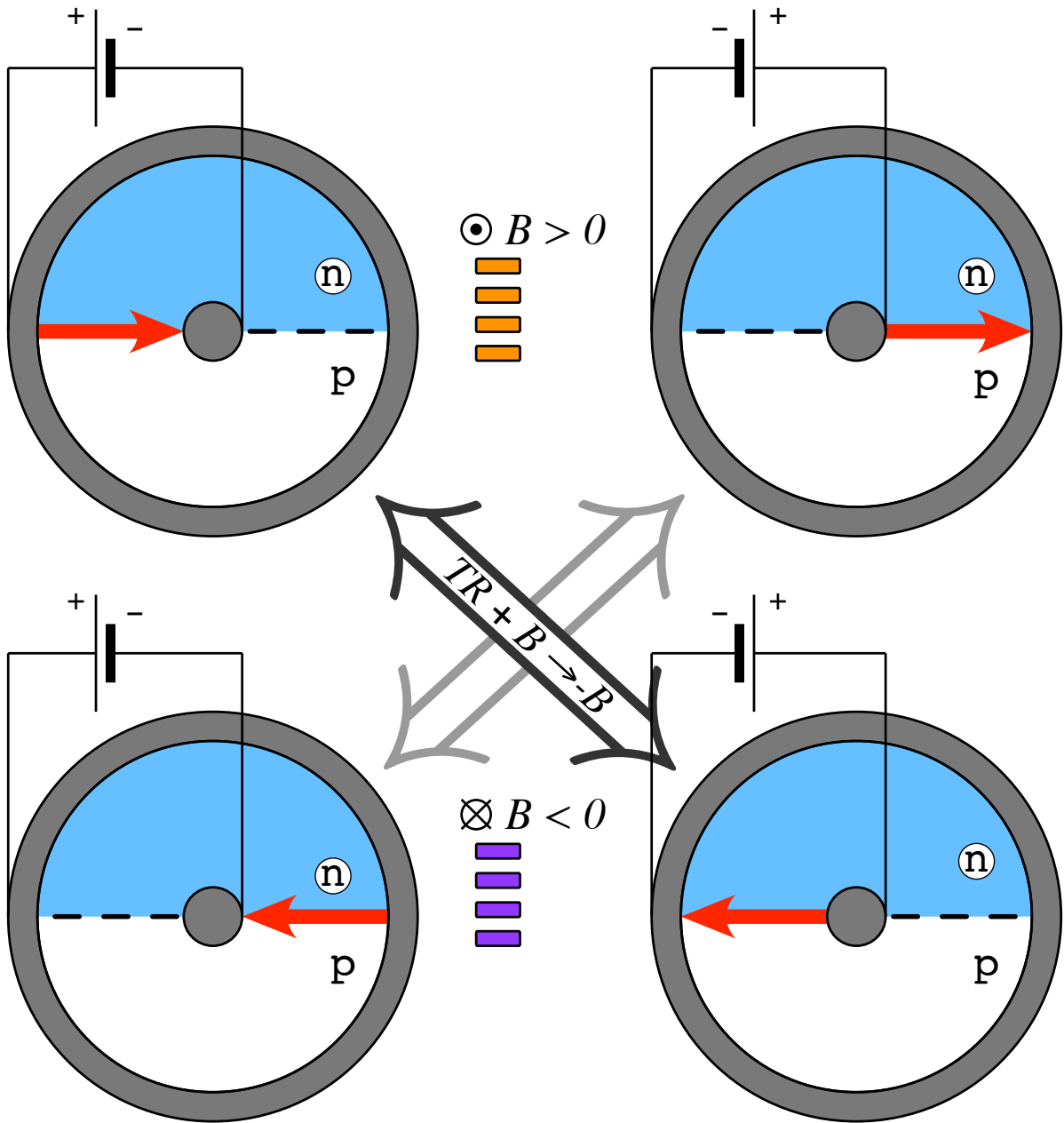


Figure 17: The symmetry of Quantum Hall states in the Corbino disk in external electric field. The current propagates along p-n junction each time using only half of it. The top (bottom) panels correspond to $B > 0$ ($B < 0$) case. The direction of electric field is defined by p - and n -doped regions. Reprinted from [51].

$V=0\text{meV}, M=10\text{meV}$

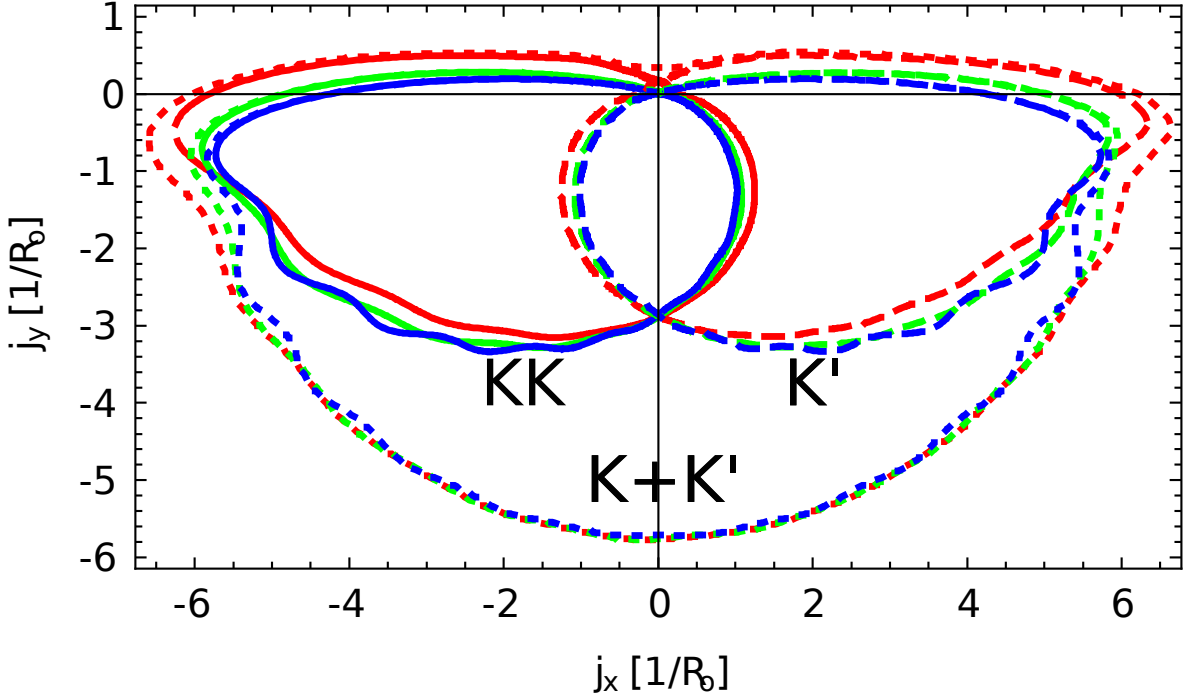


Figure 18: Radial plot of radial density of current for K (solid line) and K' valleys (dashed line). Dotted line represents the total current. The numerical values correspond to magnetic field $B = 0\text{ T}$ (red), $B = 1/2\text{ T}$ (green) and $B = 1\text{ T}$ (blue). Reprinted from [51].

the true time-reversal symmetry (involved in symmetry between valleys) it should be capable of allowing the existence of valley filter.

Lets start with the case of zero magnetic and electric fields. Oddly enough, in configuration considered the valley currents are already well separated (see Fig. 18). One may relate it to forming of the zero doping edge states formation, with mass step playing the role of effective edge of the system. Unlike in true edge case, in mass step setup there is no reason to enforce sharpness of the step. In addition to the cases considered here, the systems with regularised step profile has been considered, all of them leading to same qualitatively results.

5.2.5 Operating the valley filter

Having described influence of both electric field and mass term it is time to combine them in a valley filter. The spatial orientation of potentials is the same as in the examples above. The electric potential V is set to 1 meV and magnetic field is set to large value of $B = 1\text{ T}$. Large value means here that the magnetic length $l_B = \sqrt{\hbar/eB}$ and cyclotron radius are significantly smaller than distance between leads. Note however that such

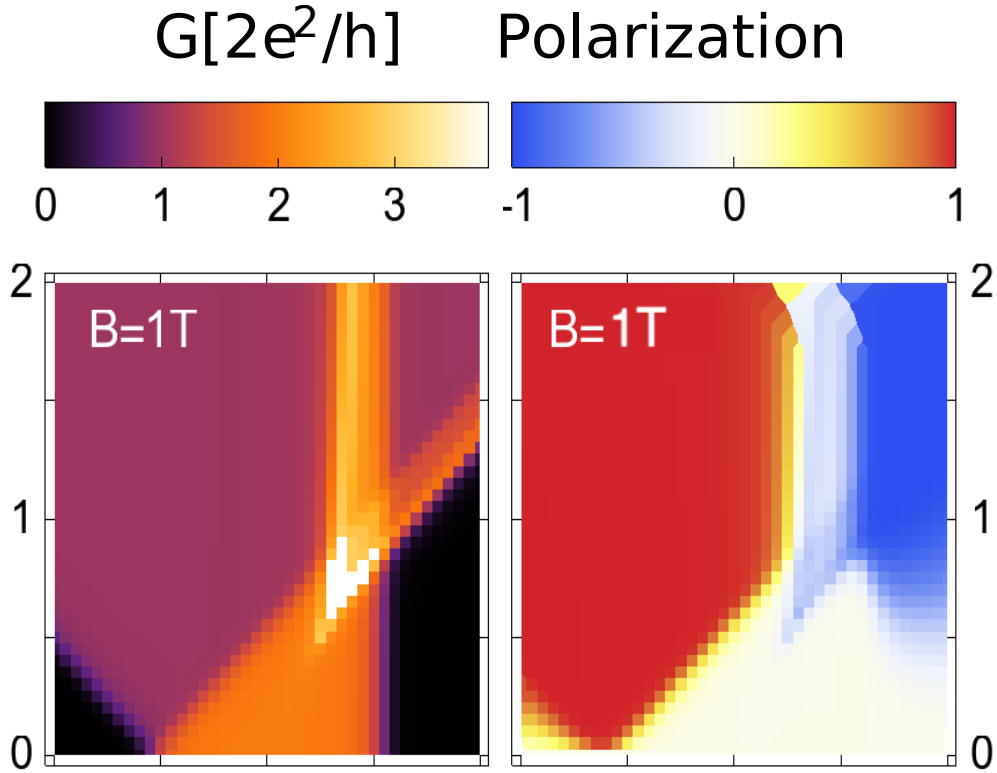


Figure 19: Conductance (left) and valley polarization (right) of the current flowing through the valley filter. The electric field is set to 1 meV. As it may be seen even for small values of mass term almost perfect polarization of the current is achieved. Reprinted from [51].

value describes moderate magnetic fields and is easily achievable in laboratory with use of permanent magnets. The main result of this part of work – the working diagram of the filter – is presented at Fig. 19.

The diagram may be easily understood in idealized case ($B \rightarrow \infty$, $\mathcal{E}R_i \ll E, M$) depicted on Fig. 20. The analysis is based on assumption that effective potentials experienced by currents originating from both valleys might be approximated by effective potentials for lower and upper component of pseudospin wavefunction (see Fig. 21). Such an approximation is valid for the case of strong electric potential [52] and seems to survive to the range of parameters considered here.

Having made the assumption about effective potentials one should only add that the each effective p-n junction within single valley will provide one conducting state. The role of the chemical potential is restricted to shifting the p-n junctions. As long as effective p-n junction crosses the internal lead the conducting state provided by it increases the conductance by g_0 . The situation is especially clear for the $M = 0$ case, where the conductance is equal to $2g_0$ as long as p-n junction crosses the internal lead and 0 when it does not. The appearance of small mass leads in the first place to the splitting of the p-n junction as long as its original position stay within the upper halfcircle (being

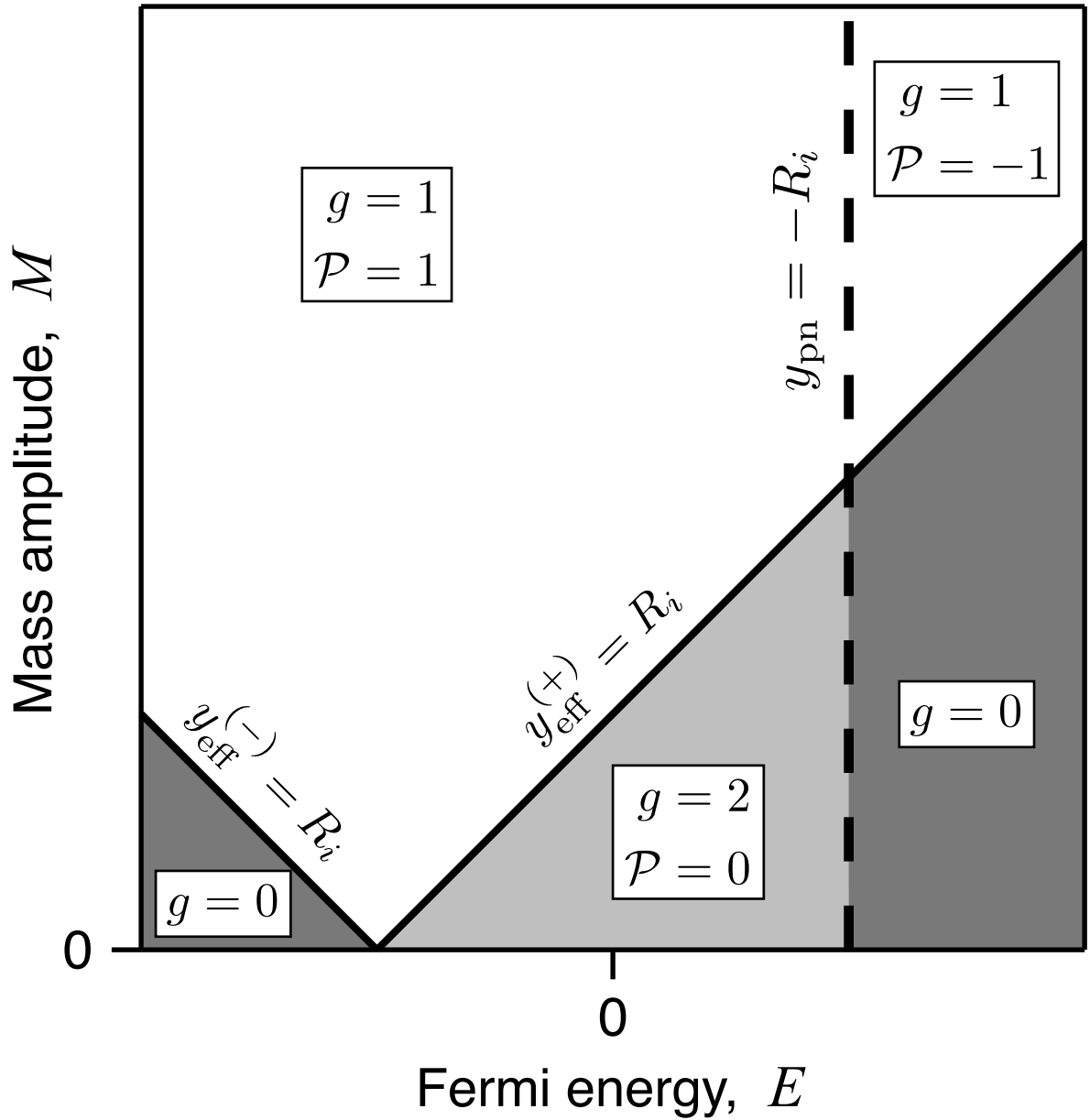


Figure 20: The schematic working diagram of strong magnetic field valley filter. The black solid lines correspond to effective p-n junctions splitted by mass, while dashed line correspond to p-n junction crossing the bottom of the Corbino disk. Reprinted from [51].

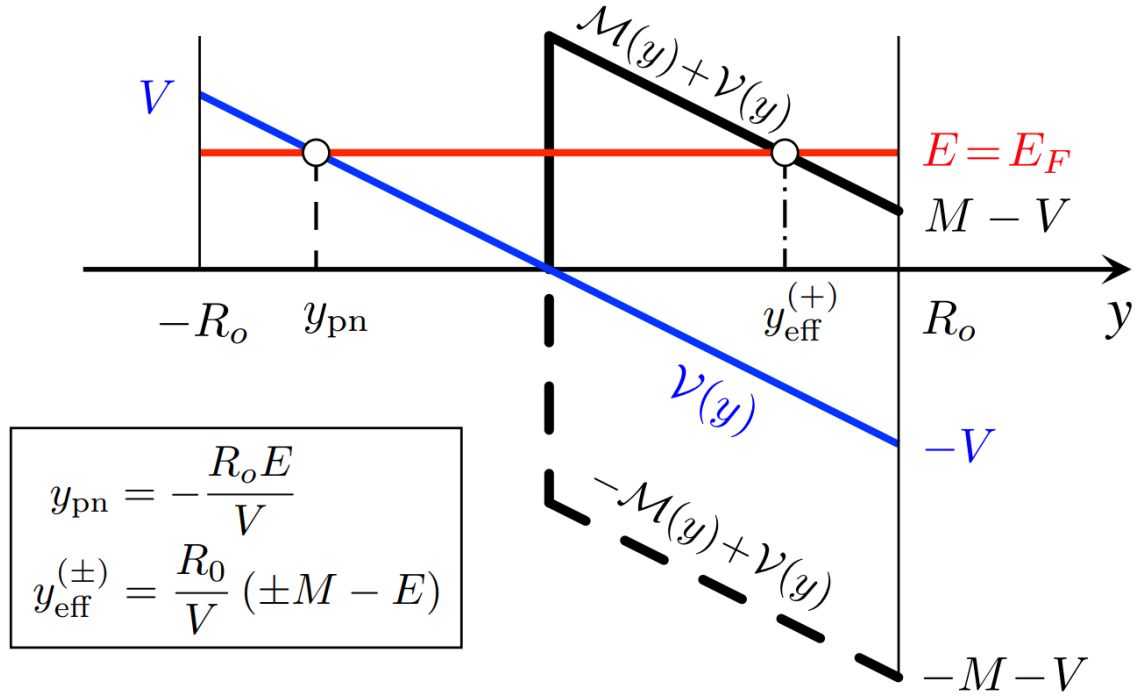


Figure 21: The electrostatic potential (blue line) and the effective potentials $\mathcal{V}(y) \pm \mathcal{M}(y)$ (black lines). The conducting states appear at the effective p-n interfaces corresponding to electrostatic potential (for $y < 0$) or the effective potential (for $y > 0$) crossing the Fermi energy E_F . Additional interface may appear at $y = 0$ due to existence of step of effective potential. Reprinted from [51].

the region of $M \neq 0$). As long as exactly one effective p-n junction crosses the internal lead the conduction is equal g_0 and all the current is fully valley polarized. In the high mass limit the upper half circle effective potential is dominated by the mass effective potential (but of opposite signs for different valleys). The appearance of the effective p-n junction will thus depend on the polarization of lower half circle (ruled by the chemical potential). If the polarizations are the same there is no p-n junction and no current, if there are opposite there is the single conducting state. Following the fact of dominant contribution of mass term being opposite for different valleys, there is always just single conducting state and the current is always fully polarized.

In the case of finite fields there are two main corrections. The first one is coming from finite width of the conducting states, leading to increase of effective radius of the inner lead by approximately l_B . The second one is connected to finite value of V , which leads to formation of additional, not fully developed conducting states at the edges of $\mathcal{P} = -1$ domain. Those additional states may be easily pinpointed by more detailed analysis of exact form of effective potentials (see Fig. 21). As they brought no additional insight into the physics of the system nor influence the interior of well developed domains of fully polarized current they detailed analysis will be omitted here.

Having understood the physics of working valley filter two possible ways of switching the polarization of the current may be proposed. The first one assumes changing the chemical potential (via the bias gate potential) at given value of in-plane electric field, while the second assumes changing the in-plane electric field at constant and close to zero chemical potential. Both propositions require only changing the gate potentials, while keeping the mass term and magnetic field constant.

The author believe that proposed here scheme of valley filter is experimentally realizable and may lead to breakthrough in realization of valleytronic devices.

5.3 Adiabatic quantum pumping with mechanical kinks in graphene

5.3.1 Aim of the section

Recently, very interesting study of buckled graphene nanoribbon as a mechanical realisation of ϕ^4 model has appeared [53]. The formation, reflection and annihilation of solitons (kinks and antikinks) has been predicted. Moreover, it has been shown that one may control the kink movement by periodically shaking one of the edges of the nanoribbon. Such shaking produces phonons that may either push the kink away from this end either *pull it toward* the source of phonons (being the realization of radiation within the model) resulting in straightforward realization of striking negative radiation pressure effect.

Having such mechanical system described one may ask about characterization of its electronic properties, crowned with question

May such a system be used as an electric pump?

What really is a pump? Pump is a device working in a periodic cycle that produces the net flow. Usually, we encounter pumps that enforce flow of liquid or gas using electrical or combustion engines (with human heart being noticeable exception). Here, electric pump means the pump that produces flow of electrons (the electric current) out of mechanical motion of the nanoribbon (ignoring the source of mechanical force). It is worth to note, that usually electricity is produced using Faraday's law or by chemical reaction. Here the interest lies in none of them. Electric pump understood in this way has been already proposed taking advantage of laser irradiation [54], strain fields [55], tunable magnetic barriers [56], Landau quantization [57], or sliding the Moiré pattern in twisted bilayer graphene [58].

Despite differences in details, the general system geometry will be the same throughout the whole section. The nanoribbon considered is long (along y -dimension) and narrow (along x -dimension). Near both ends of the nanoribbon there are 2 electrodes connected to the opposite edges of the nanoribbon (see Fig. 22). The leads are made out of flat graphene. The energy offset in the leads is assumed to be $U_\infty = -0.5 t_0$ throughout all section.

5.3.2 Simple kink model

Lets consider simple model of kink, by defining elevation of atoms as

$$z = H \tanh\left(\frac{y - y_0}{\lambda}\right) \sin^2\left(\frac{\pi x}{W}\right), \quad (49)$$

here W is the nanoribbon width, y_0 is a position of a center of the kink, H is the maximal elevation of atoms in graphene buckled nanoribbon in the absence of kink and λ is the parameter describing kink profile. The $\lambda = 3a$ has been set throughout the work in order to resemble the kink profile obtained from molecular dynamics simulations [53].

Having defined atom positions the standard modification of tunnellings is applied to tight binding model of electrons in graphene [60]

$$t_{ij} = -t_0 \exp\left(-\beta \frac{\delta d_{ij}}{d_0}\right), \quad (50)$$

where t_{ij} is the tunnelling between the atoms i and j , t_0 is the nearest neighbour tunnelling value for the relaxed graphene, $\beta = 3$ is the dimensionless electron-phonon coupling, δd_{ij} is the elongation of the bond length and $d_0 = a/\sqrt{3}$ is the equilibrium bond length.

Such a system obviously lacks relaxation, as it may only extend interlayer bond length. It may be then at most the first step in this journey, yet it is capable of catching few key concepts.

5.4 Dynamics in the simple kink model

We start the analysis of the system dynamics by calculating the conductance of the nanoribbon in the absence of the kink, in the buckled nanoribbon (being the case of

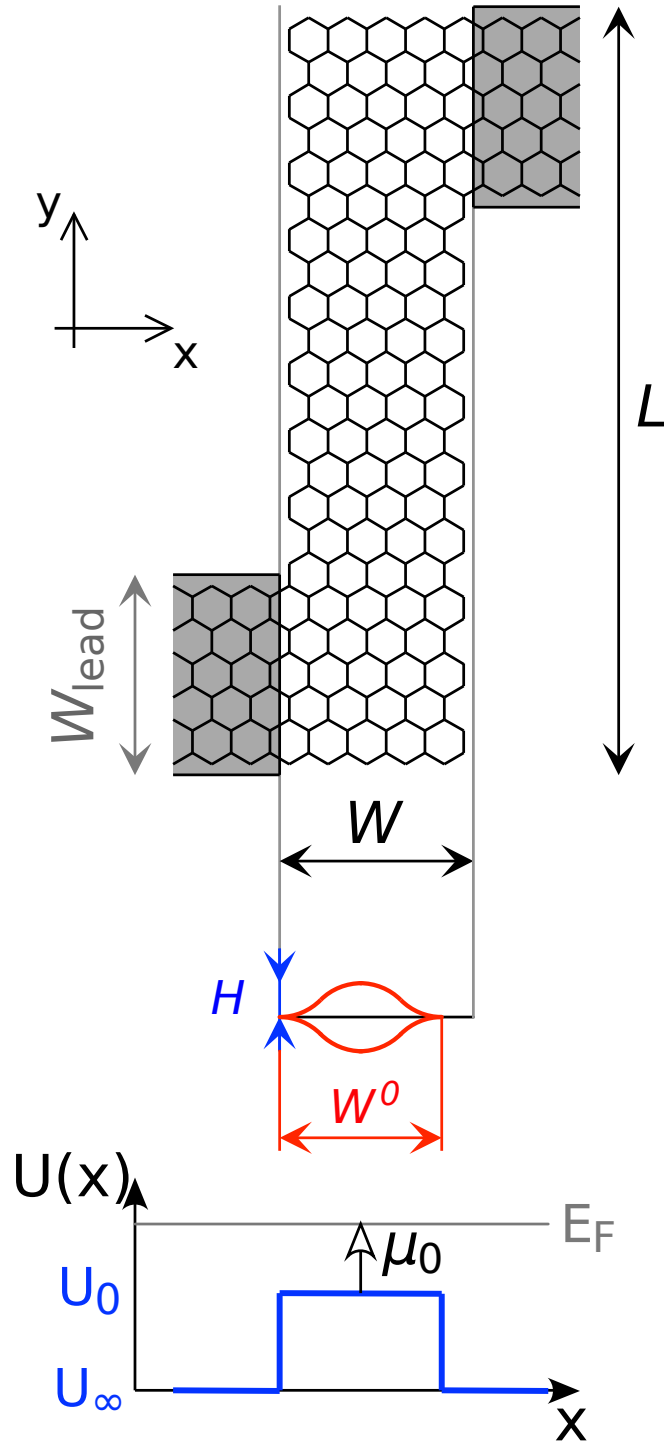


Figure 22: The scheme of the system with length ($L = 11.5\sqrt{3}a$) and width ($W = 5a$) reduced for clarity of the picture. W' marks reduced width of the buckled graphene on the cross-section diagram altogether with buckle height H . The schematic plot of chemical potential is also provided. Reprinted from [59].

$y_0 \rightarrow \infty$) and in the presence of the kink at the center of the system. The results are depicted in the Fig. 23. The conducting nanoribbon ($W = 10a$) has been chosen. As it may be easily seen the conductance of buckled nanoribbon does not significantly differ from the case of flat nanoribbon with exception of the charge neutrality point. There is a wide region ($\mu_0 \in [-0.2t_0, 0.2t_0]$) where conductance is close to $2e^2/h$. The 2 degeneracy factor originates from the spin degeneracy. Outside of that region the conductance becomes heavily noisy, thus the analysis will be restricted to the region itself. The behaviour of the system becomes very different in the presence of the kink. The nanoribbon stops to conduct, with the exception of two very narrow resonances, that disappear, when the kink is shifted from the center of the nanoribbon ($y_0 \neq L/2$ with L being the nanoribbon length).

Described behaviour of the system is very promising. The kink seems to play the role of impenetrable barrier for electrons. One may thus hope, that moving it through the system will sweep the electrons from the ribbon to the (second) lead. The working mechanism would be then very simple and similar to the working mechanism of the snow plow.

The calculations seem to confirm the thesis above (see Fig. 24). For purpose of calculating the charge transferred the kink has been moved from effective $-\infty$ position to the effective $+\infty$. The charge has been calculated with use of the formula (31). As one may see the pumping efficiency is approximately linear with the chemical potential and grow with kink height. The results may be understood in terms of mechanism proposed. In the regime considered the band structure of unbuckled nanoribbon consists of two states with linear dispersion relation $E = \pm \hbar v_F k_y$. Thus, the total pumpable charge present in the nanoribbon at given chemical potential is

$$\frac{Q_{\text{tot}}}{e} \approx \frac{|\mu_0|}{\hbar v_F} \frac{L_{\text{eff}}}{\pi} = 35.3 \frac{|\mu_0|}{t_0} \quad (51)$$

where $L_{\text{eff}} = L - W_{\text{lead}}$. As one may see, the moderate kink height $H = 2a$ already corresponds to almost maximal theoretical pumping efficiency. It suggests that buckling of the nanoribbon has not significantly changed corresponding density of electrons. It is worth to note that system has Z_2 symmetry corresponding to the reflection of z -axis. Due to that the scattering matrix does not change under $z \rightarrow -z$ transformation. Thus full pumping cycle, corresponding to transport of two kinks through the system, that restores the original mechanical state of the system corresponds to two identical cycles of its electronic properties. Having that in mind, the term cycle will correspond to the full mechanical cycle of the pump, while all the charge will be referenced for half-cycle or in other words per kink.

Summing up the results, buckling nanoribbon has little influence on its electronic properties, the kink may play a role of impenetrable barrier for electrons and it may sweep them through the system. The problem posses the Z_2 symmetry corresponding to halving the electronic cycle length with respect to mechanical cycle length. Now it is time to verify, if those findings appear in more realistic model of graphene nanoribbon.

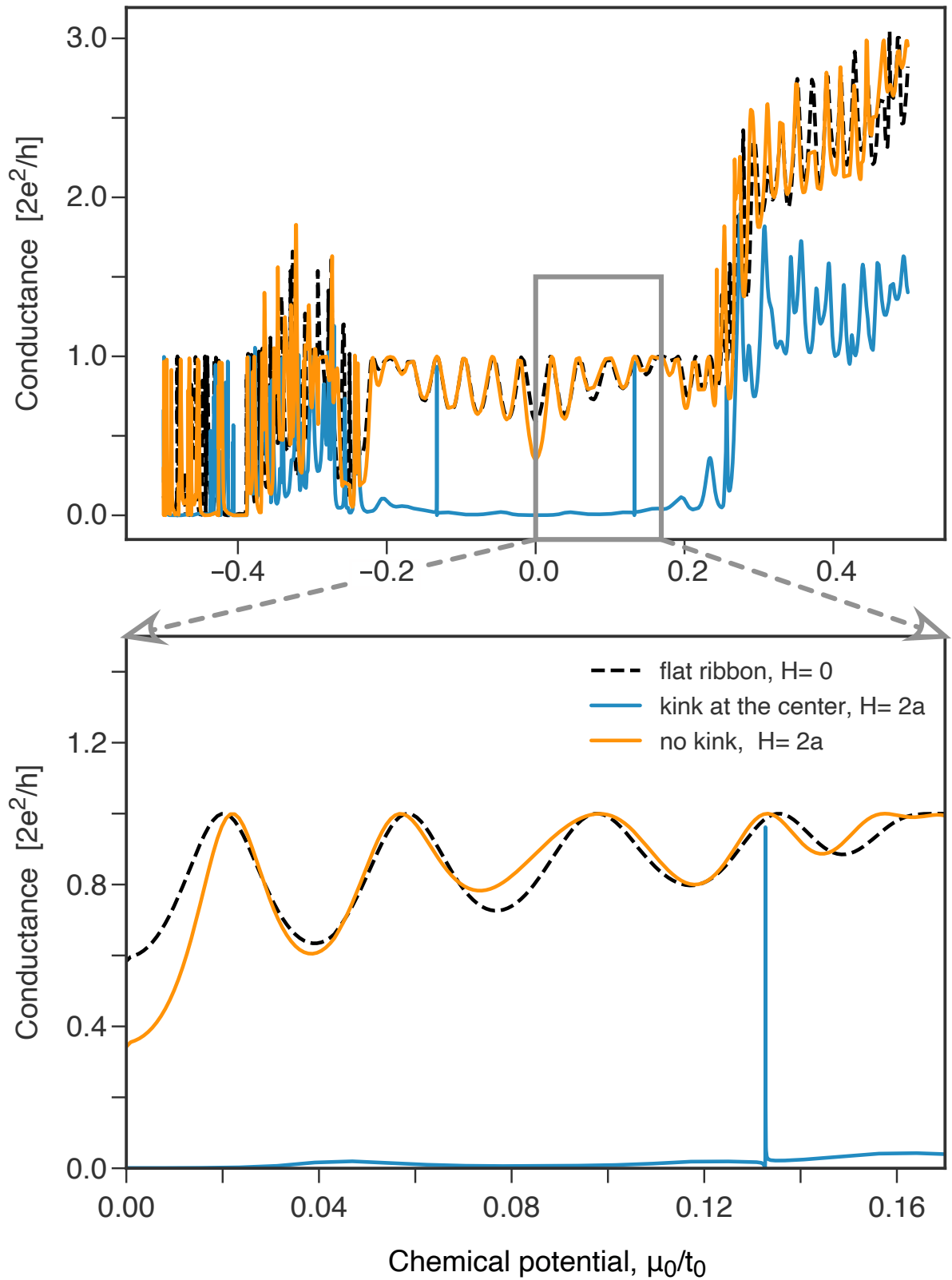


Figure 23: Conductance of the flat nanoribbon and buckled nanoribbon with (and without) presence of the kink. Reprinted from [59].

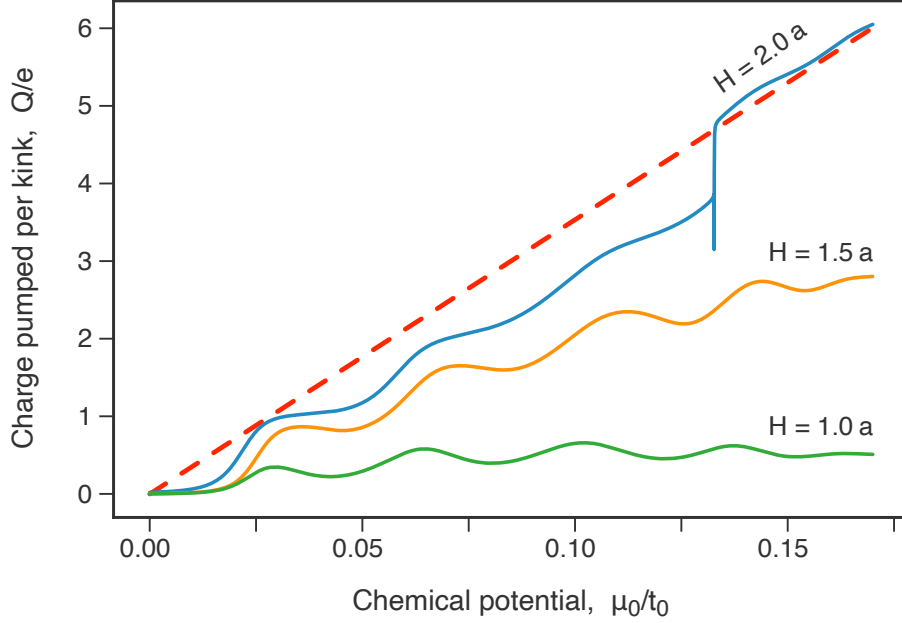


Figure 24: Charge pumped through the system by a traversing kink for three different kink height H . The red dashed line depict approximation (51). Reprinted from [59].

5.4.1 The SSH kink model

In order to validate results obtained with simple kink model the Su-Shrieffer-Heeger (SSH) Hamiltonian has been adopted [60]. It takes a form

$$\begin{aligned}
\mathcal{H}_{\text{SSH}} = & -t_0 \sum_{\langle ij \rangle, s} \exp\left(-\beta \frac{\delta d_{ij}}{d_0}\right) \left(c_{i,s}^\dagger c_{j,s} + c_{j,s}^\dagger c_{i,s}\right) \\
& + \frac{1}{2} K_d \sum_{\langle ij \rangle} (d_{ij} - d_0)^2 \\
& + \frac{1}{2} K_\theta \sum_j \sum_{\{\langle(j)\}} (\theta_{\langle(j)} - \theta_0)^2 \\
& + V_\delta \sum_j \left(2\pi - \sum_{\{\langle(j)\}} \theta_{\langle(j)}\right),
\end{aligned} \tag{52}$$

with a constrain

$$\sum_{\langle ij \rangle} (d_{ij} - d_0) = 0. \tag{53}$$

The modified tunnellings are the same as in the equation 50, K_d quantizes the energy corresponding to change of the bond length, K_θ parametrizes the resistance to angle

bending, V_δ describes the influence of out of plane deformations and $\theta_0 = 120^\circ$. The sum over set of angles $\{\angle(j)\}$ is sum of 3 angles with the common vertex (j). Its value is equal to full angle (2π) in flat graphene.

The minimization procedure requires simultaneous minimization of both electron and phonon parts of the Hamiltonian. The minimum is obtained by standard iterative procedure. Within the model considered the configuration of atoms and bond lengths depends on the chemical potential. However for the range of chemical potentials analysed here the difference is negligible and will be omitted. The results are provided for $\mu = 0$ being the charge neutrality point with number of electrons equal to number of atoms. Two systems are considered, the metallic armchair nanoribbon ($W = 10a$, $L = 90\sqrt{3}a$) and for insulating armchair nanoribbon ($W = 11a$, $L = 90\sqrt{3}a$).

5.4.2 Results for the SSH kink model

The case of metallic armchair is quite similar to the one described previously. The charge pumped per kink grows approximately linearly with the chemical potential and for $W'/W = 0.90$ is close to the total charge available in the conduction band (see Fig. 25). The hypothesis about sweeping the electrons by kink is supported by analysis of local density of states. For illustrative purposes, we take $\mu = 0.04t_0$, the local density of states is calculated according to formula (15) with smearing (16), $\epsilon = 5 \cdot 10^{-3}t_0$. The results are presented on the figure 26. As one may see, there is no electron density in the vicinity of the kink. The kink forms an impenetrable barrier for electrons, what explains the pumping mechanism.

The case of insulating armchair is more interesting. For sufficiently strong buckling, already of the order of $W' = 0.96W$, the charge pumped per kink levels at the value of $2e$ for significant range of chemical potential (see Fig. 25). This is the pumped charge quantization. In order to understand its origin once again the local density of states will be proved useful. As one may see on Figure 26 the local density of states is concentrated in the vicinity of the kink itself. It represents electron bound state that accompanies the mechanical kink. The single bound state (though with a twofold spin degeneracy) located in the bandgap is easily visible in the density of states, see figure 27 d). Such bound state is absent in the metallic nanoribbon, as there is no bandgap and all states are delocalized.

In the case of insulating armchair the pumping mechanism is thus very different. The kink and accompanying electron bound state are formed at the beginning of the nanoribbon. As the nanoribbon is insulating the bound state is initially unoccupied. As kink adiabatically traverses the system, the bound state is following it. Passing the first electrode the bound state is filled by electron (2 electrons counting the spin degeneracy). Later the connection to the first electrode is broken by insulating nanoribbon. At the end of the system the kink is annihilated and there is no place for the electron occupying till now the bound state. The electron(s) is thus forced to leave the system by second electrode located near the system end. In opposition to the case of metallic armchair the kink does not sweep electrons in front of itself, it rather loads them on itself and carry them between the electrodes.

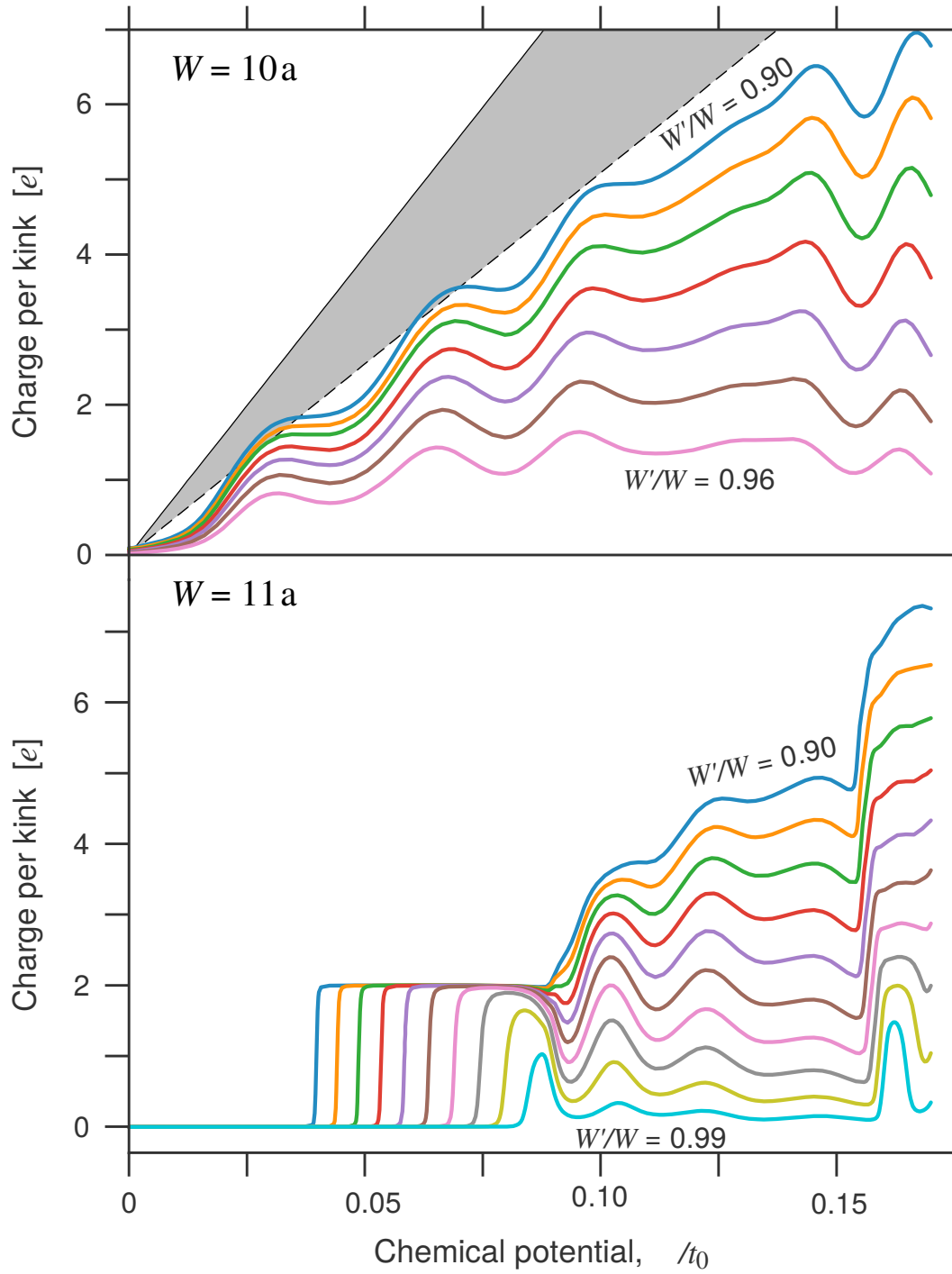


Figure 25: Charge pumped per kink (or antikink) traversing the system for the metallic ($W = 10a$) and insulating ($W = 11a$) nanoribbons. The shaded area corresponds to approximation (51) with L_{eff} varying from the distance between the leads to the value higher by the the lead width. In the lower panel the pumped charge quantization is well visible. Adapted from [61].

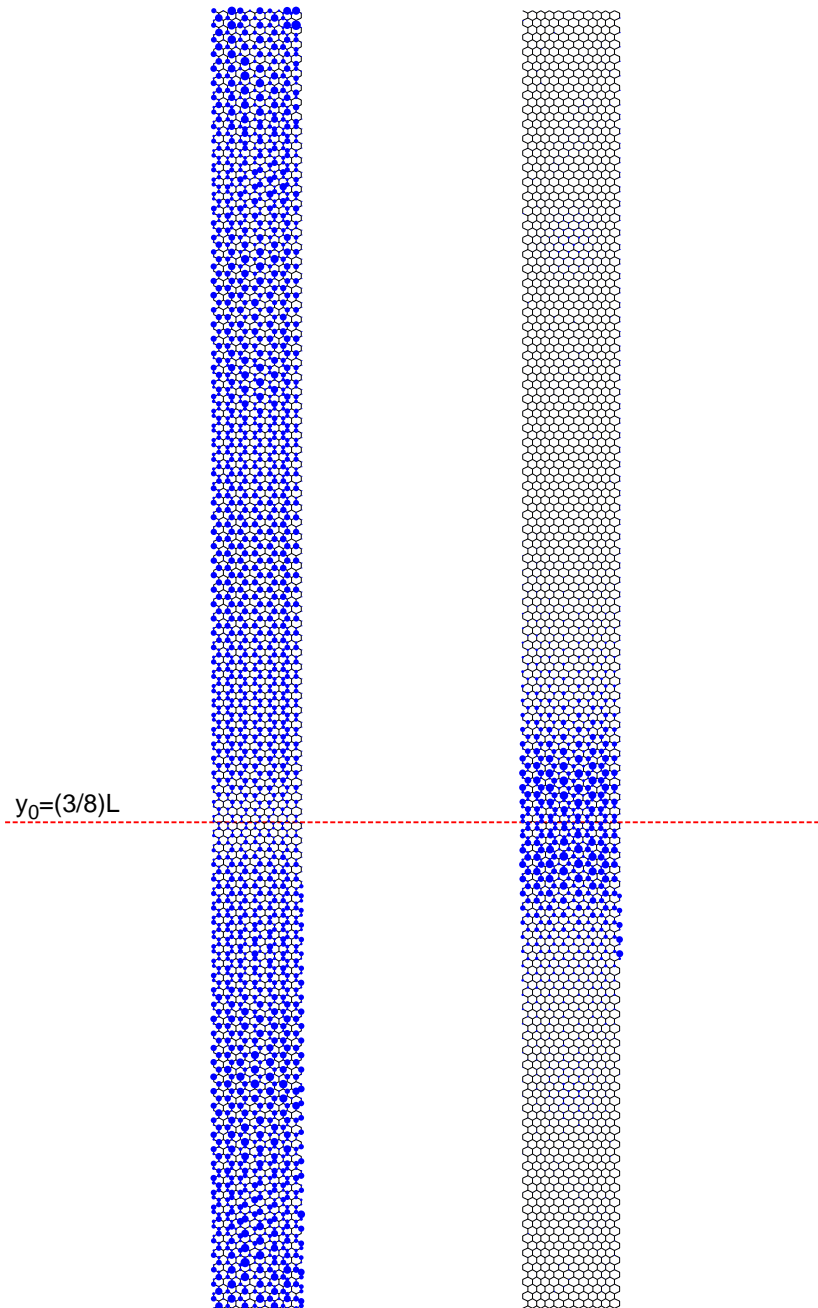


Figure 26: The local density of states for metallic (left) and insulating (right) nanoribbons. The chemical potential is set to $\mu = 0.04 t_0$, level smearing is $\epsilon = 5 \cdot 10^{-4} t_0$. The electron phonon coupling $\beta = 3$ was present during the bond length optimization for buckling $W'/W = 0.90$. Reprinted from [61].

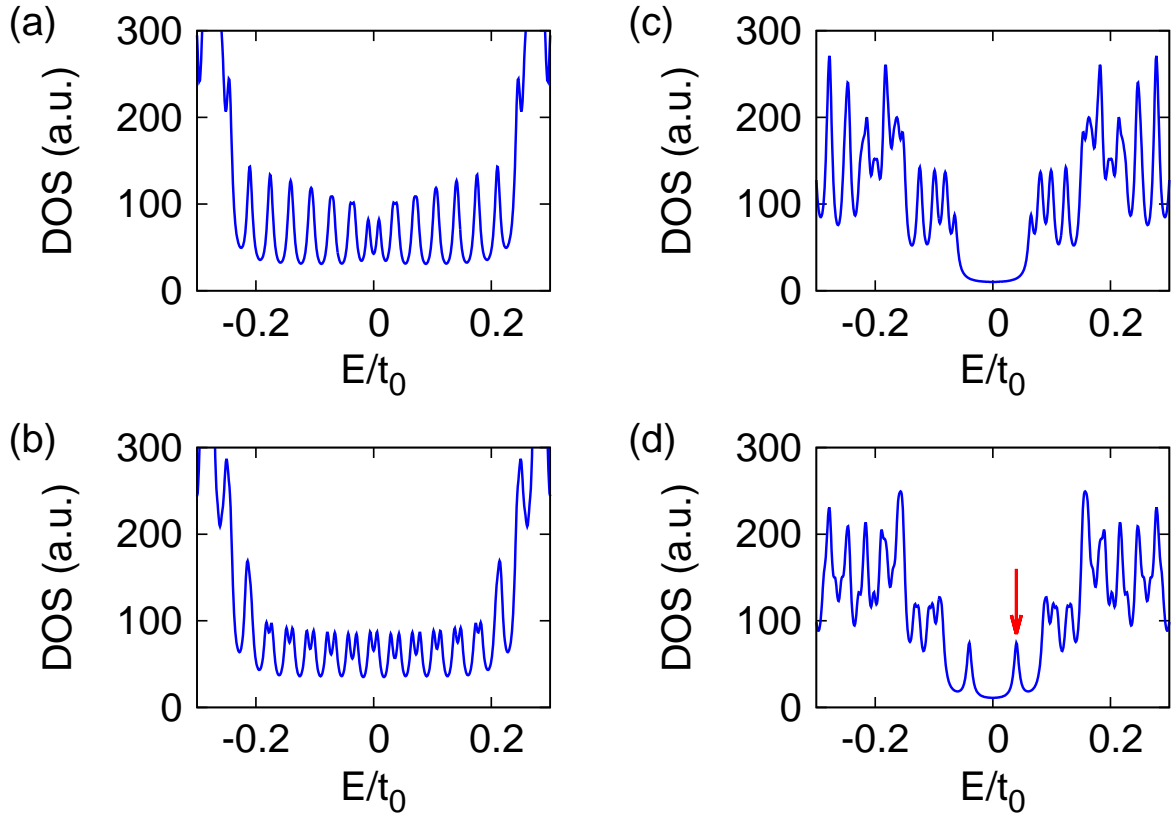


Figure 27: Electron density of states as the function of chemical potential for metallic (a,b) and insulating (c,d) armchair nanoribbons. The $\beta = 0(3)$ was set respectively in (a,c) and (b,d) panels. Arrow marks position of localized bound state at $E = 0.04t_0$ located in the band gap. Smearing and buckling are the same as in Fig. 26. Reprinted from [61].

The important note is needed to be made. The density of states corresponding to systems optimized with and without electron phonon coupling (corresponding to $\beta = 3$ or $\beta = 0$) are quite similar, yet without the electron phonon coupling the bound state localized crucial for quantization of charge pumped does not appear (see Fig. 27). Thus in order to properly describe pumping in the insulating nanoribbon one has to include electron density impact on the bond lengths.

Concluding results of this section, the metallic armchair nanoribbon behaves similarly to the system described by simple kink model, efficiently sweeping electron density on front of itself. On the other hand the description of insulating armchair nanoribbon is more involved and requires full SSH model. The charge pumped per kink in the insulating armchair is quantized, opening the possibility of using it as a quantum standard of ampere.

6 Conclusions

The transport properties of both mono- and bilayer graphene has been studied. The special attention has been put on the analysis of thermoelectric properties and conductivity scaling for bilayer graphene systems. Moreover, three graphene devices has been proposed and analysed. The purposes of those devices are: visualisation of Aharonov-Bohm effect, valley polarization of electric current, and serving as a current standard.

Our initial motivation of analysing the thermoelectric properties of bilayer graphene was to find a suitable way to determine the value of trigonal warping strength. This task results with three propositions: (i) to measure the anomaly of thermoelectric properties in sub-Kelvin temperatures, (ii) to measure the carrier concentration corresponding to the maximal Seebeck coefficient, and (iii) to measure temperature corresponding to global maximum of the Seebeck coefficient on the doping-temperature plane. The last two propositions do not need to be performed at sub-Kelvin temperatures, the approximate temperature of 1 K should be sufficient. It is worth to stress that proposed measurements does not require neither strong magnetic fields nor measurement of conductivity scaling with the systems length. All of them might be performed at a single sample.

The thermoelectric properties of the bilayer graphene has been analysed with respect to varying doping, temperature and external electric field opening the bandgap. The Seebeck coefficient, Lorentz number and figure of merit has been studied numerically. Observed behaviour of discussed quantities has been rationalised in term of simple effective models. The violation of Wiedemann-Franz law in the pseudodiffusive regime has been found and reported. Among different results, the dominant role of bandgap in forming the thermoelectric characteristic should be marked.

The influence of trigonal warping strength γ_3 , γ_4 term and the bandgap on conductivity of long sample at zero doping point has been studied. The four different behaviour has been identified. The semiconductor behaviour characterises all systems with the bandgap. For the systems without a gap three regimes appear, the well known pseudodiffusive regime for $\gamma_3 = \gamma_4 = 0$, the asymptotic pseudodiffusive regime $\gamma_3 \neq 0, \gamma_4 = 0$ and divergent pseudodiffusive regime for $\gamma_3 \neq 0$ and $\gamma_4 \neq 0$. The available experimental data allow to conclude that the conductivity of bilayer graphene may not be properly described without γ_3 . The role of γ_4 is revealed only in samples much longer than the ones experimentally achievable so far.

Use of graphene Corbino disk to measure the Aharonov-Bohm effect has been proposed. This proposition avoids use of two slit setup typical for magnetic Aharonov-Bohm effect. Instead it presents that properties of the wavefunction propagating away from central solenoid in any direction on xy plane might be significantly affected by magnetic flux flowing through the center of the system. As in standard Aharonov-Bohm setup the wavefunction is affected, despite never seeing the magnetic field itself. The amplitude of the effect has been investigated with respect to system geometry, doping, magnetic field and in-plane electric field being a measure of system imperfections. The effect has been found to be robust and possibly measurable over wide range of parameters considered.

Taking advantage of the presence of two Dirac cones in graphene dispersion relation

the construction of mesoscopic valley filter has been proposed. The construction has been based on functionalization of graphene Corbino disk in a preparation phase, constant magnetic field, and gates providing control over the doping and the in-plane electric field. The system has been designed to be controllable and switchable between current polarisation solely by means of gate potentials. Almost perfect filtering efficiency exceeding 99% has been observed even in the scenarios with lowered assumptions about system manufacturing precision. The device is believed to be scalable and robust against long range manufacturing imperfections.

Turning recently considered mechanical kink representation of $1 - D$ field theory in graphene into electric pump serving as a current standard device has been proposed. The construction is based on clamped and buckled graphene nanoribbon and the control is performed by mechanical shaking of one of the system edges. The mechanical solitons are found to be efficient pumps pushing out almost all available electrons in their way. The special case of soliton is accompanied by the electron bound state that might be used to deliver quantum charge per pump cycle, potentially serving as the current standard device.

References

- [1] *Miniaturization*. Reinhold Publishing Corporation, 1961.
- [2] N. D. Mermin. Crystalline order in two dimensions. *Phys. Rev.*, 176:250–254, Dec 1968.
- [3] Ke Cao, Shizhe Feng, Ying Han, Libo Gao, Thuc Hue Ly, Zhiping Xu, and Yang Lu. Elastic straining of free-standing monolayer graphene. *Nature Communications*, 11(1):284, Jan 2020.
- [4] Jae-Ung Lee, Duhee Yoon, Hakseong Kim, Sang Wook Lee, and Hyeonsik Cheong. Thermal conductivity of suspended pristine graphene measured by raman spectroscopy. *Phys. Rev. B*, 83:081419, Feb 2011.
- [5] Luca Banszerus, Michael Schmitz, Stephan Engels, Jan Dauber, Martin Oellers, Federica Haupt, Kenji Watanabe, Takashi Taniguchi, Bernd Beschoten, and Christoph Stampfer. Ultrahigh-mobility graphene devices from chemical vapor deposition on reusable copper. *Science Advances*, 1(6), 2015.
- [6] Yuan Cao, Valla Fatemi, Shiang Fang, Kenji Watanabe, Takashi Taniguchi, Efthimios Kaxiras, and Pablo Jarillo-Herrero. Unconventional superconductivity in magic-angle graphene superlattices. *Nature*, 556(7699):43–50, Apr 2018.
- [7] Wei Han, Roland K. Kawakami, Martin Gmitra, and Jaroslav Fabian. Graphene spintronics. *Nature Nanotechnology*, 9(10):794–807, Oct 2014.

- [8] Yuanbo Zhang, Yan-Wen Tan, Horst L. Stormer, and Philip Kim. Experimental observation of the quantum hall effect and berry's phase in graphene. *Nature*, 438(7065):201–204, Nov 2005.
- [9] Graphene Flagship. <https://graphene-flagship.eu/news/Pages/Graphene-for-Composites-Applications2.aspx>. Accessed: 18.06.2020.
- [10] MediaDevil. <https://mediadevil.com/products/artisanphonics-cb-01-nanene-graphene-wood-earphones>. Accessed: 18.06.2020.
- [11] MomoDesign. <https://en.momodesign.com/products/fgtr-graphene-1-0>. Accessed: 18.06.2020.
- [12] Vittoria. <https://www.vittoria.com/eu/corsa-competition-race.html>. Accessed: 18.06.2020.
- [13] Graphene-XT. <https://www.graphene-xt.com/en/gxt-lubricant-2/>. Accessed: 18.06.2020.
- [14] S. GrapheneTech. <http://www.graphene-tech.net/product/conductive-ink/>. Accessed: 18.06.2020.
- [15] Graphene-XT. <https://www.graphene-xt.com/en/gxt-esd-2/>. Accessed: 18.06.2020.
- [16] Emberion. <https://www.emberion.com/products/vis-swir/>. Accessed: 18.06.2020.
- [17] R. Ribeiro-Palau, F. Lafont, J. Brun-Picard, D. Kazazis, A. Michon, F. Cheynis, O. Couturaud, C. Consejo, B. Jouault, W. Poirier, and F. Schopfer. Quantum hall resistance standard in graphene devices under relaxed experimental conditions. *Nature Nanotechnology*, 10(11):965–971, Nov 2015.
- [18] Dominik Suszalski and Adam Rycerz. Adiabatic quantum pumping in buckled graphene nanoribbon driven by a kink, 2020.
- [19] R Saito, G Dresselhaus, and M S Dresselhaus. *Physical Properties of Carbon Nanotubes*. published by Imperial College Press and Distributed by World Scientific Publishing Co., 1998.
- [20] Michael Wimmer. Quantum transport in nanostructures: From computational concepts to spintronics in graphene and magnetic tunnel junctions, December 2009.
- [21] Edward McCann and Mikito Koshino. The electronic properties of bilayer graphene. *Reports on Progress in Physics*, 76(5):056503, Apr 2013.
- [22] A. B. Kuzmenko, I. Crassee, D. van der Marel, P. Blake, and K. S. Novoselov. Determination of the gate-tunable band gap and tight-binding parameters in bilayer graphene using infrared spectroscopy. *Phys. Rev. B*, 80:165406, Oct 2009.

- [23] Yuli V. Nazarov and Yaroslav M. Blanter. *Quantum Transport: Introduction to Nanoscience*. Cambridge University Press, 2009.
- [24] Keivan Esfarjani, Mona Zebarjadi, and Yoshiyuki Kawazoe. Thermoelectric properties of a nanocontact made of two-capped single-wall carbon nanotubes calculated within the tight-binding approximation. *Phys. Rev. B*, 73:085406, Feb 2006.
- [25] József Cserti, András Csordás, and Gyula Dávid. Role of the trigonal warping on the minimal conductivity of bilayer graphene. *Phys. Rev. Lett.*, 99:066802, Aug 2007.
- [26] A. S. Mayorov, D. C. Elias, M. Mucha-Kruczynski, R. V. Gorbachev, T. Tudorovskiy, A. Zhukov, S. V. Morozov, M. I. Katsnelson, V.I. Falkó, A. K. Geim, and K. S. Novoselov. Interaction-driven spectrum reconstruction in bilayer graphene. *Science*, 333(6044):860–863, 2011.
- [27] Francisco Guinea, Antonio Castro Neto, and Nuno Peres. Electronic states and Landau levels in graphene stacks. *Physical Review B*, 73, 04 2006.
- [28] Dominik Suszalski, Grzegorz Rut, and Adam Rycerz. Lifshitz transition and thermoelectric properties of bilayer graphene. *Phys. Rev. B*, 97:125403, Mar 2018.
- [29] L. M. Malard, J. Nilsson, D. C. Elias, J. C. Brant, F. Plentz, E. S. Alves, A. H. Castro Neto, and M. A. Pimenta. Probing the electronic structure of bilayer graphene by Raman scattering. *Phys. Rev. B*, 76:201401, Nov 2007.
- [30] L. M. Zhang, Z. Q. Li, D. N. Basov, M. M. Fogler, Z. Hao, and M. C. Martin. Determination of the electronic structure of bilayer graphene from infrared spectroscopy. *Phys. Rev. B*, 78:235408, Dec 2008.
- [31] Melvin Cutler and N. F. Mott. Observation of Anderson localization in an electron gas. *Phys. Rev.*, 181:1336–1340, May 1969.
- [32] F. Freitag, J. Trbovic, M. Weiss, and C. Schönenberger. Spontaneously gapped ground state in suspended bilayer graphene. *Phys. Rev. Lett.*, 108:076602, Feb 2012.
- [33] Wenzhong Bao, Jairo Velasco, Fan Zhang, Lei Jing, Brian Standley, Dmitry Smirnov, Marc Bockrath, Allan H. MacDonald, and Chun Ning Lau. Evidence for a spontaneous gapped state in ultraclean bilayer graphene. *Proceedings of the National Academy of Sciences*, 109(27):10802–10805, 2012.
- [34] Dominik Suszalski, Grzegorz Rut, and Adam Rycerz. Thermoelectric properties of gapped bilayer graphene. *Journal of Physics: Condensed Matter*, 31(41):415501, Jul 2019.

- [35] Valeri N. Kotov, Bruno Uchoa, Vitor M. Pereira, F. Guinea, and A. H. Castro Neto. Electron-electron interactions in graphene: Current status and perspectives. *Rev. Mod. Phys.*, 84:1067–1125, Jul 2012.
- [36] Dominik Suszalski, Grzegorz Rut, and Adam Rycerz. Conductivity scaling and the effects of symmetry-breaking terms in bilayer graphene hamiltonian. *Phys. Rev. B*, 101:125425, Mar 2020.
- [37] M. I. Katsnelson. Minimal conductivity in bilayer graphene. *The European Physical Journal B - Condensed Matter and Complex Systems*, 52(2):151–153, Jul 2006.
- [38] Youngwoo Nam, Dong-Keun Ki, Mikito Koshino, Edward McCann, and Alberto F Morpurgo. Interaction-induced insulating state in thick multilayer graphene. *2D Materials*, 3(4):045014, oct 2016.
- [39] R. G. Chambers. Shift of an electron interference pattern by enclosed magnetic flux. *Phys. Rev. Lett.*, 5:3–5, Jul 1960.
- [40] Akira Tonomura, Tsuyoshi Matsuda, Ryo Suzuki, Akira Fukuhara, Nobuyuki Osakabe, Hiroshi Umezaki, Junji Endo, Kohsei Shinagawa, Yutaka Sugita, and Hideo Fujiwara. Observation of aharonov-bohm effect by electron holography. *Phys. Rev. Lett.*, 48:1443–1446, May 1982.
- [41] S. M. Roy. Condition for nonexistence of aharonov-bohm effect. *Phys. Rev. Lett.*, 44:111–114, Jan 1980.
- [42] P. Bocchieri and A. Loinger. Charges in multiply connected spaces. *Il Nuovo Cimento A (1965-1970)*, 66(2):164–172, Nov 1981.
- [43] Nobuyuki Osakabe, Tsuyoshi Matsuda, Takeshi Kawasaki, Junji Endo, Akira Tonomura, Shinichiro Yano, and Hiroji Yamada. Experimental confirmation of aharonov-bohm effect using a toroidal magnetic field confined by a superconductor. *Phys. Rev. A*, 34:815–822, Aug 1986.
- [44] Adam Rycerz. Magnetoconductance of the corbino disk in graphene. *Phys. Rev. B*, 81:121404, Mar 2010.
- [45] M. I. Katsnelson. Quantum transport via evanescent waves in undoped graphene. *Journal of Computational and Theoretical Nanoscience*, 8(6):912–918, Jun 2011.
- [46] Adam Rycerz and Dominik Suszalski. Graphene disk in a solenoid magnetic potential: Aharonov-bohm effect without a two-slit-like setup. *Phys. Rev. B*, 101:245429, Jun 2020.
- [47] C. R. Dean, A. F. Young, I. Meric, C. Lee, L. Wang, S. Sorgenfrei, K. Watanabe, T. Taniguchi, P. Kim, K. L. Shepard, and et al. Boron nitride substrates for high-quality graphene electronics. *Nature Nanotechnology*, 5(10):722–726, Aug 2010.

- [48] A. Rycerz, J. Tworzydło, and C. W. J. Beenakker. Valley filter and valley valve in graphene. *Nature Physics*, 3(3):172–175, Mar 2007.
- [49] D W Boukhvalov and M I Katsnelson. Chemical functionalization of graphene. *Journal of Physics: Condensed Matter*, 21(34):344205, jul 2009.
- [50] B. Sachs, T. O. Wehling, M. I. Katsnelson, and A. I. Lichtenstein. Adhesion and electronic structure of graphene on hexagonal boron nitride substrates. *Phys. Rev. B*, 84:195414, Nov 2011.
- [51] Dominik Suszalski, Grzegorz Rut, and Adam Rycerz. Mesoscopic valley filter in graphene corbino disk containing a p–n junction. *Journal of Physics: Materials*, 3(1):015006, nov 2019.
- [52] Dominik Suszalski, Grzegorz Rut, and Adam Rycerz. Mesoscopic valley filter in graphene corbino disk containing a p–n junction. *Journal of Physics: Materials*, 3(1):015006, Nov 2019.
- [53] R. D. Yamaletdinov, V. A. Slipko, and Y. V. Pershin. Kinks and antikinks of buckled graphene: A testing ground for the φ^4 field model. *Phys. Rev. B*, 96:094306, Sep 2017.
- [54] Pablo San-Jose, Elsa Prada, Henning Schomerus, and Sigmund Kohler. Laser-induced quantum pumping in graphene. *Applied Physics Letters*, 101(15):153506, 2012.
- [55] Yongjin Jiang, Tony Low, Kai Chang, Mikhail I. Katsnelson, and Francisco Guinea. Generation of pure bulk valley current in graphene. *Phys. Rev. Lett.*, 110:046601, Jan 2013.
- [56] Evgeny Grichuk and E. Manykin. Adiabatic quantum pumping in graphene with magnetic barriers. *The European Physical Journal B*, 86(5):210, May 2013.
- [57] Babak Abdollahipour and Elham Moomivand. Magnetopumping current in graphene corbino pump. *Physica E: Low-dimensional Systems and Nanostructures*, 86:204 – 209, 2017.
- [58] Manato Fujimoto, Henri Koschke, and Mikito Koshino. Topological charge pumping by a sliding moiré pattern. *Phys. Rev. B*, 101:041112, Jan 2020.
- [59] Dominik Suszalski and Adam Rycerz. Adiabatic quantum pumping in buckled graphene nanoribbon driven by a kink, 2020.
- [60] *Properties of Carbon Nanotubes*. Imperial College Press, 1998.
- [61] Dominik Suszalski and Adam Rycerz. Adiabatic pumping driven by moving kink and quantum standard ampere in buckled graphene nanoribbon, 2020.

Lifshitz transition and thermoelectric properties of bilayer graphene

Dominik Suszalski, Grzegorz Rut, and Adam Rycerz

Marian Smoluchowski Institute of Physics, Jagiellonian University, Łojasiewicza 11, PL-30348 Kraków, Poland



(Received 19 December 2017; published 5 March 2018)

This is a numerical study of thermoelectric properties of ballistic bilayer graphene in the presence of a trigonal warping term in the effective Hamiltonian. We find, in the mesoscopic samples of the length $L > 10 \mu\text{m}$ at sub-Kelvin temperatures, that both the Seebeck coefficient and the Lorentz number show anomalies (the additional maximum and minimum, respectively) when the electrochemical potential is close to the Lifshitz energy, which can be attributed to the presence of the van Hove singularity in a bulk density of states. At higher temperatures the anomalies vanish, but measurable quantities characterizing the remaining maximum of the Seebeck coefficient still unveil the presence of massless Dirac fermions and make it possible to determine the trigonal warping strength. Behavior of the thermoelectric figure of merit (ZT) is also discussed.

DOI: [10.1103/PhysRevB.97.125403](https://doi.org/10.1103/PhysRevB.97.125403)

I. INTRODUCTION

It is known that thermoelectric phenomena provide valuable insight into the details of the electronic structure of graphene and other relativistic condensed-matter systems that cannot be solely determined by conductance measurements [1]. Such a fundamental perspective has inspired numerous studies on Seebeck and Nernst effects in mono- (MLG) and bilayer (BLG) graphenes [2–9] as well as in other two-dimensional systems [10–13]. The exceptionally high thermal conductivity of graphenes has also drawn significant attention [14–19] after a seminal work by Balandin *et al.* [20]. A separate issue concerns thermal and thermoelectric properties of tailor-made graphene systems [1,21–26], including superlattices [21], nanoribbons [22–25], or defected graphenes [25,26], for which peculiar electronic structures may result in high thermoelectric figures of merit $ZT > 2$ at room temperature [24,25].

Unlike in conventional metals or semiconductors, thermoelectric power in graphenes can change a sign upon varying the gate bias [2–4], making it possible to design thermoelectronic devices that have no analogues in other materials [27]. In BLG the additional band-gap tunability [28–30] was utilized to noticeably enhance the thermoelectric power in a dual-gated setup [8].

At sufficiently low temperatures, one can expect thermoelectric properties of BLG to reflect most peculiar features of its electronic structure. These features include the presence (in the gapless case) of three additional Dirac points in the vicinity of each of the primary Dirac points K and K' [31–34]. In turn, when varying chemical potential the system is expected to undergo the Lifshitz transition at $\mu = \pm E_L$ (the Lifshitz energy) [34]. What is more, electronic density of states (DOS) shows van Hove singularities at $\mu = \pm E_L$. Unlike in systems with Mexican-hat band dispersion, for which diverging DOS appears at the bottom of the conduction band and at the top of the valence band [12,13], in BLG each van Hove singularity separates populations of massless Dirac-Weyl quasiparticles ($|\mu| < E_L$) with approximately conical dispersion relation, and massive chiral quasiparticles ($|\mu| > E_L$) characterized

by the effective mass $m_{\text{eff}} \approx 0.033 m_e$, with m_e being the free-electron mass. Although the value of E_L is related to several directly-measurable quantities, such as the minimal conductivity [35–37], available experimental results cover the full range of $E_L \sim 0.1\text{--}1 \text{ meV}$ [34].

The purpose of this paper is to show that thermoelectric measurements in ballistic BLG (see Fig. 1) can provide insights into the nature of quasiparticles near the charge-neutrality point and allow one to estimate the Lifshitz energy. We consider a relatively large, rectangular sample of ballistic BLG (with the length $L = 17.7 \mu\text{m}$ and the width $W = 20 L$) and calculate its basic thermoelectric properties (including the Seebeck coefficient S and the Lorentz number \mathcal{L}) within the Landauer-Büttiker formalism [38,39]. Our main findings are outlined in Fig. 1, where N_{max}^S ($N_{\text{min}}^{\mathcal{L}}$)—the number of maxima (minima) of S (\mathcal{L}) appearing for $\mu > 0$ is indicated in the E_L - T parameter plane. For instance, a handbook value of $E_L/k_B \approx 10 \text{ K}$ [40] leads to the anomalies, including additional extrema at $\mu \approx E_L$, at sub-Kelvin temperatures. We further show that even for $T \gtrsim 1 \text{ K}$ (at which $N_{\text{max}}^S = N_{\text{min}}^{\mathcal{L}} = 1$) the value of E_L determines the carrier concentration corresponding to the remaining maximum of S (or the minimum of \mathcal{L}).

The paper is organized as follows: The model and theory are described in Sec. II, followed by the numerical results and discussions on the conductance, thermopower, validity of the Wiedemann-Franz law, the role of phononic thermal conductivity, and the figure of merit (Sec. III). A comparison with the linear model for transmission-energy dependence (see Appendix) is also included. The conclusions are given in Sec. IV.

II. MODEL AND THEORY

A. The Hamiltonian

We start our analysis from the four-band effective Hamiltonian for low-energy excitations [34], which can be

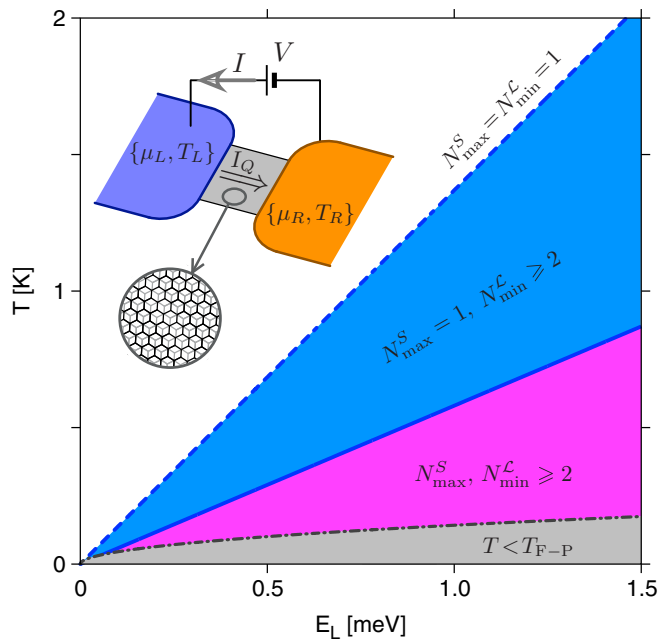


FIG. 1. The system studied numerically in the paper (inset) and the thermoelectric phase diagram (main) for Bernal-stacked bilayer graphene. Thermal and electric currents (I_Q, I) flow between the leads, modeled as infinitely-doped graphene regions with electrochemical potentials $\mu_{L(R)} \rightarrow \infty$ (at a fixed $\mu_R - \mu_L \equiv eV$, with the electron charge $-e$ and the voltage V), and temperatures $T_{L(R)}$, attached to the rectangular sample. Additional gate electrodes (not shown) are used to tune the chemical potential in the sample area μ at zero bias between the layers. The number of distinct maxima of the Seebeck coefficient (N_{\max}^S) and minima of the Lorentz factor (N_{\min}^L), occurring for $0 < \mu < \infty$, are indicated in the Lifshitz energy-temperature parameter plane. The border of the Fabry-Pérot transport regime $T < T_{F-P}$ (in which $N_{\max}^S, N_{\min}^L \gg 1$), corresponding to the system length $L = 10^4 l_{\perp} = 17.7 \mu\text{m}$, is also depicted.

written as

$$H = \xi \begin{pmatrix} 0 & v_F \pi & \xi t_{\perp} & 0 \\ v_F \pi^{\dagger} & 0 & 0 & v_3 \pi \\ \xi t_{\perp} & 0 & 0 & v_F \pi^{\dagger} \\ 0 & v_3 \pi^{\dagger} & v_F \pi & 0 \end{pmatrix}, \quad (1)$$

where the valley index $\xi = 1$ (-1) for K (K') valley, $v_F = \sqrt{3} t_0 a / (2\hbar) \simeq 10^6$ m/s is the asymptotic Fermi velocity defined via the intralayer hopping $t_0 = 3.16$ eV and the lattice parameter $a = 0.246$ nm, $\pi = \hbar e^{-i\theta} (-i\partial_x + \partial_y)$, θ denotes the angle between the main system axis and the armchair direction. (For the numerical calculations, we set $\hbar v_F = 0.673$ eV nm.) The nearest-neighbor interlayer hopping is $t_{\perp} = 0.381$ eV [41] defining $l_{\perp} = \hbar v_F / t_{\perp} = 1.77$ nm, and $v_3 = v_F t' / t_0$ with t' being the next-nearest neighbor (or *skew*) interlayer hopping.

The Hamiltonian (1) leads to the bulk dispersion relation for electrons [31,34]

$$E_{\pm}^{(e)}(\mathbf{k}) = \left[\frac{1}{2} t_{\perp}^2 + (v_F^2 + \frac{1}{2} v_3^2) k^2 \pm \sqrt{\Gamma(\mathbf{k})} \right]^{1/2},$$

$$\Gamma(\mathbf{k}) = \frac{1}{4} (t_{\perp}^2 - \hbar^2 v_3^2 k^2)^2 + \hbar^2 v_F^2 k^2 (t_{\perp}^2 + \hbar^2 v_3^2 k^2) + 2\xi t_{\perp} \hbar^3 v_3 v_F^2 k^3 \cos 3\varphi, \quad (2)$$

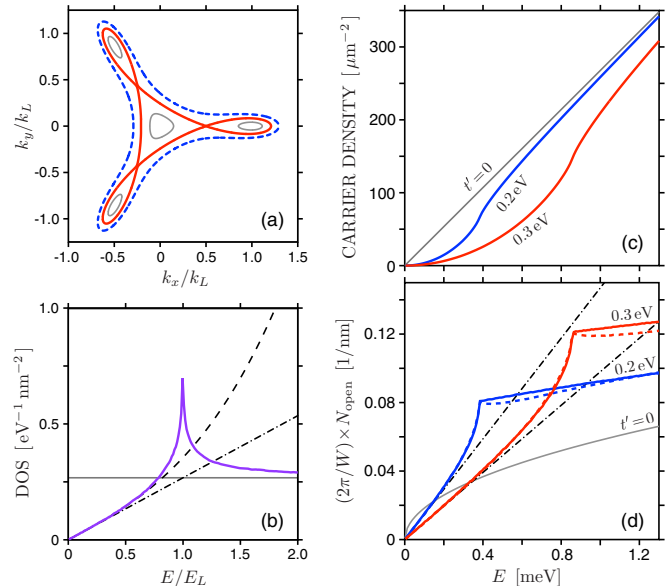


FIG. 2. Physical consequences of the dispersion relation given by Eq. (2). (a) Equienergy surfaces for $E = 0.5 E_L$ (gray solid lines), $E = E_L$ (red solid line), and $E = 1.5 E_L$ (blue dashed line) for the crystallographic orientation $\theta = 0$. (b) Density of states (purple solid line) and the approximating expressions given by Eqs. (7), (8), and (9) (gray solid, black dashed, and black dotted-dashed line, respectively). (c) Carrier density and (d) the number of open channels for different values of t' (specified for each line). Solid and dashed lines in panel (d) corresponds to $\theta = 0$ and $\theta = \pi/6$, dotted-dashed lines represent the approximating Eq. (12).

where $\mathbf{k} \equiv (k_x, k_y)$ is the in-plane wave vector (with $\mathbf{k} = 0$ referring to the K or K' point), $k = |\mathbf{k}|$, and the angle $0 \leq \varphi < 2\pi$ can be defined as the argument $\arg z$ of a complex number

$$z = e^{-i\theta} (k_x + ik_y). \quad (3)$$

For holes, we have $E_{\pm}^{(h)}(\mathbf{k}) = -E_{\pm}^{(e)}(\mathbf{k})$ [42].

B. Low-energy electronic structure

Basic consequences of Eq. (2) are illustrated in Fig. 2. In the energy range $|E| < E_L$, with the Lifshitz energy

$$E_L = \frac{1}{4} t_{\perp} \left(\frac{v_3}{v_F} \right)^2, \quad (4)$$

there are four distinct parts of the Fermi surface [see Fig. 2(a)], centered at $z = z_0, \dots, z_3$, where $z_0 = 0$, $z_j = k_L \exp(2\pi i j / 3)$, $j = 1, 2, 3$, and

$$k_L = \frac{t_{\perp} v_3}{\hbar v_F^2}. \quad (5)$$

For $|E| \geq E_L$ the Fermi surface becomes connected, and the transition at $E = \pm E_L$ is accompanied by the van Hove singularity in the density of states $\rho(E)$ [see Fig. 2(b)], which can be defined (for electrons) via

$$\int_0^E dE' \rho(E') \equiv n(E) = \frac{\mathcal{A}(E)}{\pi^2}, \quad (6)$$

where $n(E)$ is the physical carrier density (taking into account spin and valley degeneracies $g_s = g_v = 2$) depicted in Fig. 2(c), and $\mathcal{A}(E)$ denotes the area bounded by the Fermi surface in the (k_x, k_y) plane [43]. In particular, taking the limit of $t' \rightarrow 0$ we have

$$\rho_{t' \rightarrow 0}(|E| \ll t_\perp) \approx \frac{2m_{\text{eff}}}{\pi \hbar^2} = \frac{t_\perp}{\pi(\hbar v_F)^2} \equiv \rho_0, \quad (7)$$

where we have introduced the effective mass relevant in the absence of trigonal warping ($E_L = 0$). At finite t' ($E_L > 0$) the value of ρ_0 defined in Eq. (7) is approached by the actual $\rho(E)$ for $|E| \gtrsim E_L$ [see Fig. 2(b)]. Also, in the $t' \neq 0$ case, we find that the approximating formula

$$\rho(E) \approx \frac{\rho_0 |E|}{E_L} [1 + 0.33(E/E_L)^2], \quad (8)$$

reproduces the actual $\rho(E)$ with 1% accuracy for $|E| \leq E_L/2$ (being the energy interval most relevant for discussion presented in the remaining parts of this paper). For $|E| \ll E_L$, leaving only the leading term on the right-hand side of Eq. (8) brought us to

$$\rho(|E| \ll E_L) \approx \frac{4|E|}{\pi(\hbar v_3)^2}, \quad (9)$$

which can be interpreted as a double-monolayer DOS with the Fermi velocity replaced by v_3 .

Although the trigonal-warping effects become hardly visible in $\rho(E)$ for $E \gtrsim E_L$, characteristic deformations of the Fermi surface can be noticed also for $E \gg E_L$. We point out that a compact quantity taking this fact into account, which can be determined directly from Eq. (2) without resorting to quantum transport simulations, is the number of propagating modes (*open channels*) $N_{\text{open}}(\theta, E)$ presented in Fig. 2(d). It can be defined as a total number of solutions, with real k_x , of equations

$$E_+^{(p)}(k_x, q \Delta k_y) = E, \quad E_-^{(p)}(k_x, q \Delta k_y) = E, \quad (10)$$

where $p = e$ for electrons ($E > 0$) or $p = h$ for holes ($E < 0$), $q = 0, \pm 1, \pm 2, \dots$, and $\Delta k_y = 2\pi/W$ (we suppose the periodic boundary conditions along the y axis) that correspond to a chosen sign of the group velocity, e.g., $(v_g)_{\pm, q}^{(p)} = \partial E_{\pm}^{(p)}(k_x, q \Delta k_y) / \partial k_y > 0$. Apart from the $t' \rightarrow 0$ limit, for which

$$N_{\text{open}}(t' \rightarrow 0, |E| \ll t_\perp) \approx 2 \sqrt{\frac{|E| t_\perp}{(\hbar v_F)^2}} \frac{1}{\Delta k_y}, \quad (11)$$

the number of open channels is anisotropic and shows the periodicity with a period $\pi/3$. In the low-energy limit

$$N_{\text{open}}(\theta, |E| \ll E_L) \approx 2F(\theta) \frac{|E|}{\hbar v_3} \frac{1}{\Delta k_y}, \quad (12)$$

where

$$F(\theta) = 1 + \sum_{j=1,2,3} \left[1 - \frac{8}{9} \cos^2 \left(\theta + \frac{2\pi}{3} j \right) \right]^{1/2}, \quad (13)$$

$$\approx 3.126 + 0.029 \cos 6\theta.$$

The anisotropy is even more apparent for $|E| \gtrsim E_L$. In particular, $N_{\text{open}}(\theta = 0, E)$ grows monotonically with increasing

E , whereas $N_{\text{open}}(\theta = \pi/6, E)$ has a shallow minimum at $E \approx 1.11 E_L$.

It is also visible in Fig. 2(d) that the effects of increasing t' are essentially opposite at different energy ranges: For $|E| \gtrsim E_L$, N_{open} grows systematically with t' ; for $|E| \ll E_L$ we have $N_{\text{open}} \propto 1/t'$ following from Eq. (12). Such a feature has no analogues in behaviors of other characteristics presented in Fig. 2.

C. Thermoelectric properties

In the linear-response regime, thermoelectric properties of a generic nanosystem in graphene are determined via Landauer-Büttiker expressions for the electrical and thermal currents [44,45]

$$I = -\frac{g_s g_v e}{h} \int dE T(E) [f_L(E) - f_R(E)], \quad (14)$$

$$I_Q = \frac{g_s g_v}{h} \int dE T(E) [f_L(E) - f_R(E)] (E - \mu), \quad (15)$$

where $g_s = g_v = 2$ are spin and valley degeneracies, $T(E) \equiv \text{Tr}(\mathbf{t}\mathbf{t}^\dagger)$ with \mathbf{t} being the transmission matrix [36], $f_{L(R)}$ is the distribution functions for the left (right) lead with electrochemical potential $\mu_{L(R)}$ and temperature $T_{L(R)}$. Assuming that $\mu_L - \mu_R \equiv -eV$ and $T_L - T_R \equiv \Delta T$ are infinitesimally small [hereinafter, we refer to the averages $\mu = (\mu_L + \mu_R)/2$ and $T = (T_L + T_R)/2$], we obtain the conductance G , the Seebeck coefficient S , and the electronic part of the thermal conductance K_{el} , as follows [39]

$$G = \frac{I}{V} \Big|_{\Delta T=0} = e^2 L_0, \quad (16)$$

$$S = -\frac{V}{\Delta T} \Big|_{I=0} = \frac{L_1}{e T L_0}, \quad (17)$$

$$K_{\text{el}} = \frac{I_Q}{\Delta T} \Big|_{I=0} = \frac{L_0 L_2 - L_1^2}{T L_0}, \quad (18)$$

where L_n (with $n = 0, 1, 2$) is given by

$$L_n = \frac{g_s g_v}{h} \int dE T(E) \left(-\frac{\partial f_{\text{FD}}}{\partial E} \right) (E - \mu)^n, \quad (19)$$

with $f_{\text{FD}}(\mu, T, E) = 1 / [\exp((E - \mu)/k_B T) + 1]$ the Fermi-Dirac distribution function.

By definition, the Lorentz number accounts only the electronic part of the thermal conductance,

$$\mathcal{L} = \frac{K_{\text{el}}}{T G} = \frac{L_0 L_2 - L_1^2}{e^2 T^2 L_0^2}. \quad (20)$$

The thermoelectric figure of merit accounts the total thermal conductance ($K_{\text{tot}} = K_{\text{el}} + K_{\text{ph}}$)

$$ZT = \frac{T G S^2}{K_{\text{tot}}} = \left(\frac{K_{\text{el}}}{K_{\text{el}} + K_{\text{ph}}} \right) \frac{L_1^2}{L_0 L_2 - L_1^2}, \quad (21)$$

where the phononic part can be calculated using

$$K_{\text{ph}} = \frac{1}{2\pi} \int d\omega \hbar \omega \frac{\partial f_{\text{BE}}}{\partial T} \mathcal{T}_{\text{ph}}(\omega), \quad (22)$$

with $f_{\text{BE}}(T, \omega) = 1 / [\exp(\hbar \omega / k_B T) - 1]$ the Bose-Einstein distribution function and $\mathcal{T}_{\text{ph}}(\omega)$ the phononic transmission

spectrum. For BLG in a gapless case considered in this work, we typically have $K_{\text{ph}} \sim K_{\text{el}}$ (see Sec. III D) [46]. As $\mathcal{T}_{\text{ph}}(\omega)$ in Eq. (22) is generally much less sensitive to external electrostatic fields than $T(E)$ in Eq. (18) it should be possible—at least in principle—to independently determine K_{ph} and K_{el} in the experiment.

It can be noticed that ultraclean ballistic graphene shows approximately linear transmission to Fermi-energy dependence $T(E) \propto |E|$ (where $E = 0$ corresponds to the charge-neutrality point) [47–50]. Straightforward analysis (see Appendix A) leads to extremal values of the Seebeck coefficient as a function of the chemical potential

$$S_{\text{max}} = -S_{\text{min}} \approx k_B/e = 86 \mu\text{V/K}, \quad (23)$$

providing yet another example of a material characteristic given solely by fundamental constants [47,51]. Similarly, the Lorentz number reaches, at $\mu = 0$, the maximal value given by

$$\mathcal{L}_{\text{max}} = \frac{9\zeta(3)}{2\ln 2} \left(\frac{k_B}{e}\right)^2 = 2.37 \mathcal{L}_{\text{WF}}, \quad (24)$$

with $\mathcal{L}_{\text{WF}} = \frac{1}{3}\pi^2(k_B/e)^2$ being the familiar Wiedemann-Franz constant. Although the disorder and electron-phonon coupling may affect the above-mentioned values, existing experimental works report S_{max} and \mathcal{L}_{max} close to those given by Eqs. (23) and (24) for both MLG and BLG, provided the temperature is not too low [2–7,18].

At low temperatures, the linear model no longer applies, partly due to the contribution from evanescent modes [47,52] and partly due to direct trigonal-warping effects on the electronic structure (see Sec. II B). For this reason, thermoelectric properties calculated numerically from Eqs. (16)–(21) are discussed next.

III. RESULTS AND DISCUSSION

A. Zero-temperature conductivity

For $T \rightarrow 0$ Eq. (16) leads to the conductivity

$$\sigma(T \rightarrow 0) = \frac{G(T \rightarrow 0)L}{W} = \frac{g_0 L}{W} \text{Tr}(\mathbf{t}\mathbf{t}^\dagger), \quad (25)$$

with the conductance quantum $g_0 = 4e^2/h$. As the right-hand side of Eq. (25) is equal to $\text{Tr}(\mathbf{t}\mathbf{t}^\dagger)$ with a constant prefactor, $\sigma(T \rightarrow 0)$ gives a direct insight into the transmission-energy dependence that defines all the thermoelectric properties [see Eqs. (16)–(21)].

In order to determine the transmission matrix \mathbf{t} for a given electrochemical potential μ we employ the computational scheme similar to that presented in Ref. [36]. However, at finite-precision arithmetics, the mode-matching equations become ill defined for sufficiently large L and μ , as they contain both exponentially growing and exponentially decaying coefficients. This difficulty can be overcome by dividing the sample area into N_{div} consecutive, equally-long parts, and matching wave functions for all $N_{\text{div}} + 1$ interfaces [53].

Numerical results are presented in Fig. 3. A striking feature of all datasets is the presence of quasiperiodic oscillations of the Fabry-Pérot type. Although such oscillations can be regarded as artifacts originating from a perfect, rectangular

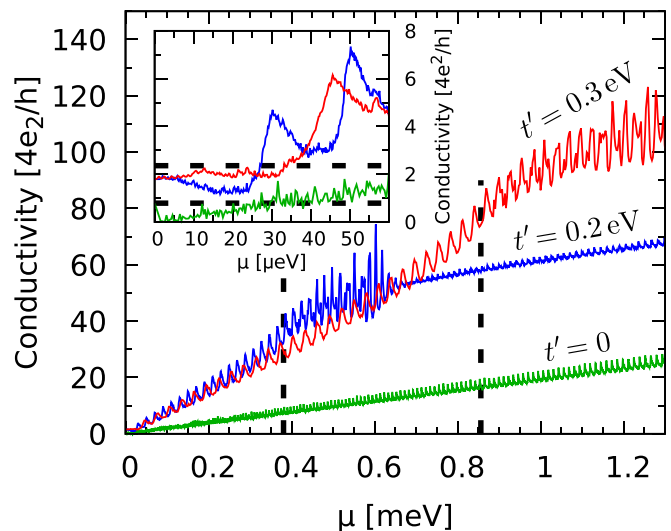


FIG. 3. Zero-temperature conductivity [see Eq. (25) in the main text] for $L = W/20 = 10^4 l_\perp = 17.7 \mu\text{m}$ and $\theta = 0$ [54] plotted as a function of the chemical potential. The value of skew-interlayer hopping t' is specified for each line. Remaining tight-binding parameters are given below Eq. (1) in the main text. Vertical lines mark values of the Lifshitz energy, given by Eq. (4), for $t' = 0.2 \text{ eV}$ and $t' = 0.3 \text{ eV}$. Inset is a zoom in, for low chemical potentials, with horizontal lines depicting $\sigma = 2 \sigma_{\text{MLG}} = (8/\pi) e^2/h$ and $\sigma = 6 \sigma_{\text{MLG}}$.

shape of the sample area (vanishing immediately when, e.g., samples with nonparallel edges are considered, see Ref. [55]) their periodic features are useful to benchmark the numerical procedure applied.

In particular, for $t' = 0$, the conductivity shows abrupt features at energies associated with resonances at normal incidence ($k_y = 0$) [52], namely

$$E_n(t' = 0) \approx \pm \hbar v_F l_\perp \left(\frac{\pi n}{L}\right)^2, \quad n = 1, 2, 3, \dots, \quad (26)$$

where the approximation refers to the parabolic dispersion relation applying for $|E_n| \ll t_\perp$, or equivalently for $n \ll L/(\pi l_\perp) \approx 3180$ in our numerical example. In turn, the separation between consecutive resonances is

$$\begin{aligned} \Delta E_n(t' = 0) &= |E_{n+1} - E_n| \approx \frac{2n+1}{t_\perp} \left(\frac{\pi \hbar v_F}{L}\right)^2 \\ &\approx 2 \frac{\pi \hbar v_F}{L} \sqrt{\frac{|E_n|}{t_\perp}}, \end{aligned} \quad (27)$$

with the last approximation corresponding to $n \gg 1$.

For $t' \neq 0$ the analysis is much more cumbersome even at low energies, as we have resonances associated with four distinct Dirac cones. However, resonances at normal incidence associated with the central cone, occurring at $E_n \approx \pi \hbar v_3 n/L$ ($n = \pm 1, \pm 2, \dots$), allow us to estimate the order of magnitude of the relevant separation as

$$\Delta E_n(t' \neq 0) \sim \frac{\pi \hbar v_3}{L} = 2 \frac{\pi \hbar v_F}{L} \sqrt{\frac{E_L}{t_\perp}} \equiv k_B T_{\text{F-P}}, \quad (28)$$

finding that the period of Fabry-Pérot oscillations is now energy independent and should be comparable with $\Delta E_n(0)$

given by Eq. (27) for $\mu = E_n \approx E_L(t')$. The data displayed in Fig. 3 show that the oscillation period is actually energy independent in the surprisingly-wide interval of $\mu \lesssim 1.5E_L$, with the multiplicative factor $\Delta E_n(t')/\Delta E_n(0)|_{\mu=E_L(t')} \approx 3$. The oscillation amplitude is also enhanced, in comparison to the $t' = 0$ case, for $\mu \lesssim 1.5E_L$. For $\mu \gtrsim 1.5E_L$, both the oscillation period and amplitude are noticeably reduced, resembling the oscillation pattern observed for the $t' = 0$ case. It is also visible in Fig. 3, that the mean conductivity (averaged over the oscillation period) linearly increase with μ for $\mu \lesssim E_L$, with a slope weakly dependent on t' . Such a behavior indicates that $\text{Tr}(\mathbf{tt}^\dagger) < N_{\text{open}}$ [see Fig. 2(d)] which can be interpreted as a backscattering (or transmission reduction) appearing when different classes of quasiparticles are present in the leads and in the sample area. For larger μ , the transmission reduction is still significant, but its dependence on t' is weakened, and the sequence of lines from Fig. 2(d) is reproduced.

A detailed explanation of the above-reported observations, in terms of simplified models relevant for $|\mu| \ll E_L$ and for $|\mu| \gtrsim E_L$, will be presented elsewhere. Here we only notice that the linear model for transmission-energy dependence is justified, for $|\mu| \lesssim E_L$, with the numerical results presented in Fig. 3.

The rightmost equality in Eq. (28) defines the Fabry-Pérot temperature, which can be written as

$$T_{\text{F-P}} = \frac{\pi t_\perp t'_\perp l_\perp}{k_B t_0 L} = 13890 \text{ K} \times \frac{t'_\perp l_\perp}{t_0 L}. \quad (29)$$

For $L = 10^4 l_\perp$, we obtain $T_{\text{F-P}} = 88 \text{ mK}$ if $t' = 0.2 \text{ eV}$, or $T_{\text{F-P}} = 132 \text{ mK}$ if $t' = 0.3 \text{ eV}$. For higher temperatures, Fabry-Pérot oscillations are smeared out due to thermal excitations involving transmission processes from a wider energy window [see Eqs. (16) and (19)].

B. Thermopower and Wiedemann-Franz law

As the finite- T conductivity is simply given by a convolution of $T(E) = \text{Tr}(\mathbf{tt}^\dagger)$ with the derivative of the Fermi-Dirac function, we proceed directly to the numerical analysis of the Seebeck coefficient and the Lorentz number given by Eqs. (17)–(20) [56]. In Fig. 4, these thermoelectric properties are displayed as functions of μ , for a fixed $t' = 0.3 \text{ eV}$ (corresponding to $E_L/k_B \approx 10 \text{ K}$) and varying temperature. Quasiperiodic oscillations are still prominent in datasets for the lowest presented temperature, $T = 80 \text{ mK} \approx 0.6 T_{\text{F-P}}$, although it is rather close to $T_{\text{F-P}}$. This is because all the abrupt features of $T(E)$ are magnified when calculating S , or \mathcal{L} , since they affect the nominator and the denominator in the corresponding Eq. (17), or Eq. (20), in a different manner. For $T = 0.2 \text{ K} \approx 1.5 T_{\text{F-P}}$ the oscillations vanish for S and are strongly suppressed for \mathcal{L} ; instead, we observe the anomalies: the secondary maximum of S and minimum of \mathcal{L} , located near $\mu = E_L$. The secondary maximum of S vanishes for $T = T_\star^S = 0.515 \text{ K}$, but \mathcal{L} still shows the two shallow minima at this temperature. (We find that the minima of \mathcal{L} merge at $T_\star^\mathcal{L} = 1.20 \text{ K} = 2.33 T_\star^S$, the corresponding dataset is omitted for clarity.) For $T = 2 \text{ K}$, each of S and \mathcal{L} shows a single extremum for $\mu > 0$.

The crossover temperatures T_\star^S and $T_\star^\mathcal{L}$ as functions of E_L , varied in the range corresponding to $0.1 \text{ eV} \leq t' \leq 0.35 \text{ eV}$,

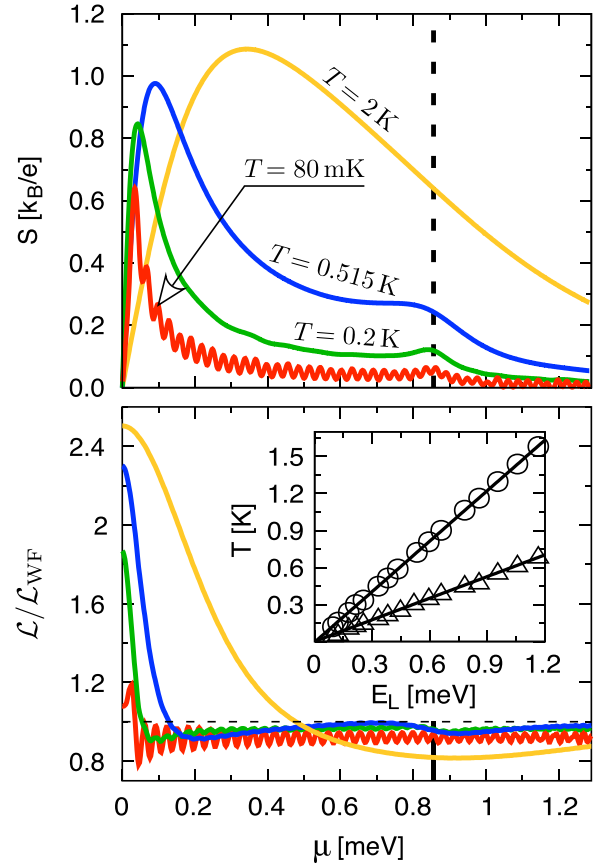


FIG. 4. Seebeck coefficients S and Lorentz number \mathcal{L} for $t' = 0.3 \text{ eV}$, as a function of the chemical potential. The temperature is specified for each line in the top panel and is the same in both panels. Vertical lines mark the Lifshitz energy; horizontal line in bottom panel corresponds to the Wiedemann-Franz value $\mathcal{L} = \mathcal{L}_{\text{WF}} = \frac{1}{3}\pi^2(k_B/e)^2$. Inset shows crossover temperatures, corresponding to vanishing of the secondary maximum of S (triangles) and minimum of \mathcal{L} (circles), plotted as functions of the Lifshitz energy, together with the best-fitted linear functions [see Eqs. (30) and (31)].

are also plotted in Fig. 4 (see the inset). The least-squares fitted lines are given by

$$T_{\star,\text{fit}}^S = 0.0504(5) \times E_L/k_B, \quad (30)$$

$$T_{\star,\text{fit}}^\mathcal{L} = 0.1176(3) \times E_L/k_B, \quad (31)$$

with standard deviations of the last digit specified by numbers in parentheses.

These findings can be rationalized by referring to the onset on low-energy characteristics given in Sec. II B (see Fig. 2). In particular, the abrupt features of $T(E)$ near $E = E_L$, attributed to the van Hove singularity of $\rho(E)$ shown in Fig. 2(b), or to the anisotropy of $N_{\text{open}}(\theta, E)$ in Fig. 2(d), are smeared out when calculating thermoelectric properties for energies of thermal excitations

$$k_B T \gtrsim 0.1 E_L. \quad (32)$$

However, some other features, related to trigonal-warping effects on $N_{\text{open}}(\theta, E)$ or $n(E)$ [see Fig. 2(c)] away from

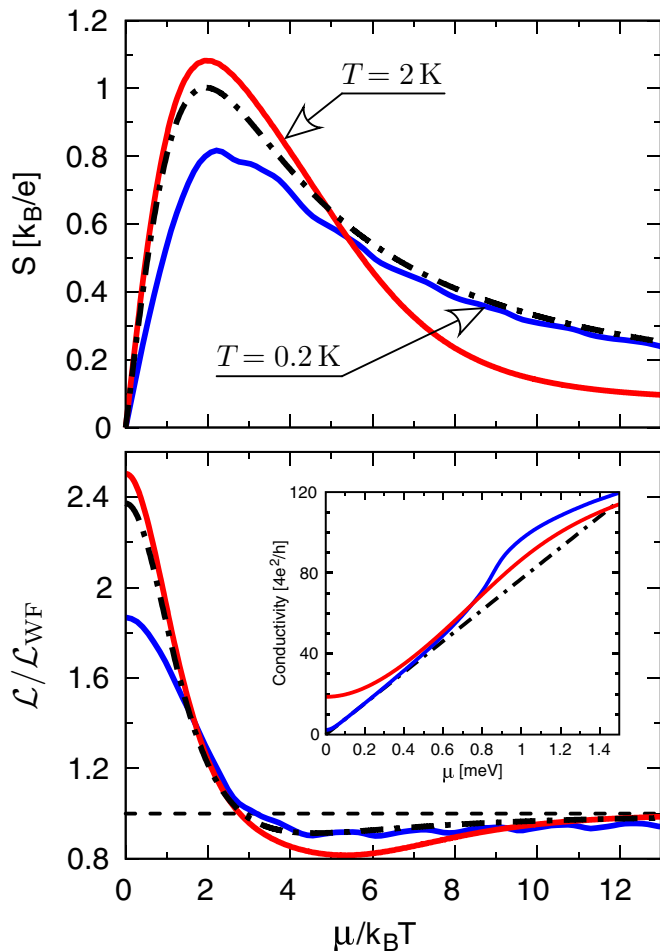


FIG. 5. Same as Fig. 4 but plotted versus the dimensionless variable $\mu/(k_B T)$. Solid lines in both panels represent the datasets for $T = 0.2$ K and $T = 2$ K. Dashed-dotted lines correspond to Eqs. (A4) and (A5) in Appendix, following from the linear model for transmission-energy dependence. Dashed line in bottom panel marks $\mathcal{L} = \mathcal{L}_{WF}$. Inset shows the finite- T conductivity (solid lines) $\sigma = GL/W$ [see Eqs. (16) and (19) in the main text] and the linear fit (dash-dot line) to the corresponding $T = 0$ dataset in Fig. 3.

$E = E_L$, visible in thermoelectric properties, may even be observable at higher temperatures.

C. Comparison with the linear model for transmission-energy dependence

In Fig. 5 we display the selected numerical data from Fig. 4, for $T = 0.2$ K and $T = 2$ K, as functions of $\mu/(k_B T)$ [solid lines] in order to compare them with predictions of the linear model for transmission-energy dependence $T(E) \propto |E|$ [dashed-dotted lines] elaborated in Appendix. For $T = 2$ K, both S and \mathcal{L} show an agreement better than 10% with the linear model for $\mu \lesssim E_L \approx 5 k_B T$. For $T = 0.2$ K, larger deviations appear for low chemical potentials due to the influence of transport via evanescent waves, which are significant for $\mu < \hbar v_F/L \approx 2-3 k_B T$. For larger μ , a few-percent agreement with the linear model is restored and sustained as long as $\mu \lesssim E_L \approx 40 k_B T$.

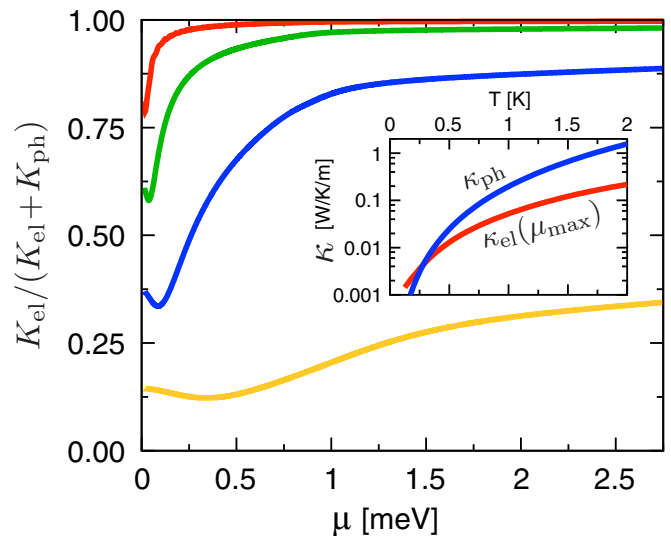


FIG. 6. Relative electronic contribution to the thermal conductance for $t' = 0.3$ eV as a function of the chemical potential. The temperatures are (top to bottom) $T = 80$ mK, 0.2 K, 0.515 K, and 2 K. Inset shows phononic [blue line] and electronic [red line] thermal conductivities ($\kappa = KL/(2dW)$, with $d = 0.335$ nm the separation between layers) as functions of temperature, with the chemical potential fixed at $\mu = \mu_{\max}$ corresponding to the maximal Seebeck coefficient.

Another remarkable feature of the results presented in Fig. 5 becomes apparent when determining the extrema: The maximal thermopower corresponds to $\mu_{\max}^{(S)}/(k_B T) = 2.0$ at $T = 2$ K, or to $\mu_{\max}^{(S)}/(k_B T) = 2.2$ at $T = 0.2$ K; the minimal Lorentz number corresponds to $\mu_{\min}^{(L)}/(k_B T) = 5.4$ at $T = 2$ K, or to $\mu_{\min}^{(L)}/(k_B T) = 4.6$ at $T = 0.2$ K. In other words, an almost perfect agreement with the linear model [see, respectively, the second equality in Eq. (A6), or the second equality in Eq. (A7) in Appendix] is observed provided that

$$\frac{\hbar v_F}{L} \ll k_B T \sim \mu_{\max}^{(S)} \sim \mu_{\min}^{(L)} \ll E_L. \quad (33)$$

In consequence, the effects that we describe may be observable for the sample length $L > 10 \mu\text{m}$.

D. Electronic and phononic parts of the thermal conductance

Before discussing the thermoelectric figure of merit ZT we first display, in Fig. 6, values of the dimensionless prefactor in the last expression of Eq. (21), quantifying relative electronic contribution to the thermal conductance. The phononic transmission spectrum [see Eq. (22)] was calculated numerically by employing, for the sample length $L = 17.7 \mu\text{m}$, the procedure presented by Alofi and Srivastava [57] adapting the Callaway theory [58] for mono- and few-layer graphenes [59]. The results show that in sub-Kelvin temperatures the electronic contribution usually prevails, even if the system is quite close to the charge-neutrality point, as one can expect for a gapless conductor. For $T > 1$ K, however, the phononic contribution overrules the electronic one in the full range of chemical potential considered.

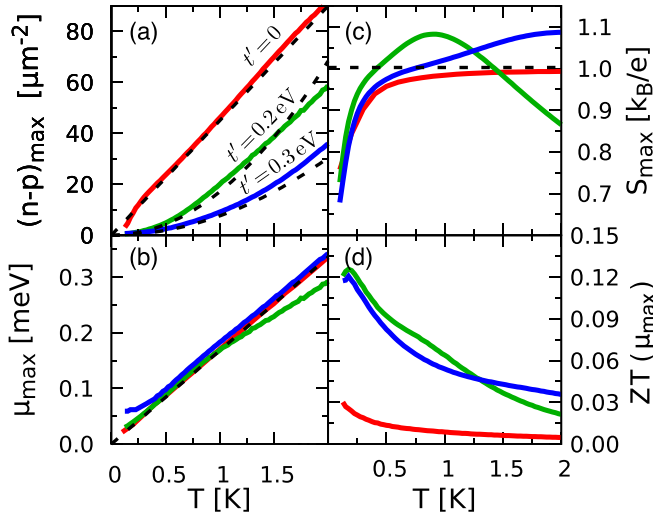


FIG. 7. Effective carrier concentration $(n-p)_{\max}$ (a) and chemical potential μ_{\max} (b) corresponding to the maximal Seebeck coefficient S_{\max} (c) as functions of temperature. The figure of merit $ZT(\mu_{\max})$ (d) is also displayed. Solid lines represent the numerical results for different values of t' [specified in panel (a)]. Dashed lines mark predictions of the linear model for transmission-energy dependence $T(E) \propto |E|$.

A direct comparison of the phononic and the electronic and thermal conductivities calculated in the physical units (see inset in Fig. 6) further shows that, if the chemical potential is adjusted to $\mu_{\max} \equiv \mu_{\max}^{(S)}$ for a given temperature, both properties are of the same order of magnitude up to $T = 2$ K. Also, for $\mu = \mu_{\max}$, we find that $K_{\text{el}} = K_{\text{ph}}$ at the temperature $T_{\text{el-ph}} \approx 0.3$ K, which is almost insensitive to the value of t' .

E. Maximal performance versus temperature

In Fig. 7 we present parameters characterizing the maximal thermoelectric performance for a given temperature ($0 < T \leq 2$ K). As the existing experimental works refer to the carrier concentration rather than to the corresponding chemical potential, we focus now on the functional dependence of the former on T (and t').

Taking into account that the maximal performance is expected for $\mu \sim k_B T$ (see previous subsection), and that a gapless system is under consideration, one cannot simply neglect the influence of minority carriers. For the conduction band ($\mu > 0$), the *effective carrier concentration* can be written as

$$n-p = \int_0^{\infty} dE \rho(E) f(\mu, E) - \int_{-\infty}^0 dE \rho(E) [1 - f(\mu, E)], \quad (34)$$

where we have supposed the particle-hole symmetry $\rho(E) = \rho(-E)$. [For the valence band ($\mu < 0$), the effective concentration $p-n$ is simply given by the formula on the right-hand side of Eq. (34) with an opposite sign.] Next, the approximating

Eqs. (7) and (8) for the density of states lead to

$$n-p \approx \rho_0 k_B T \times \begin{cases} y, & \text{if } t' = 0, \\ \tau_L [\mathcal{I}_1(y) + 0.33 \tau_L^2 \mathcal{I}_3(y)], & \text{if } t' \neq 0, \end{cases} \quad (35)$$

where $y = \mu/k_B T$, $\tau_L = k_B T/E_L$, and we have defined

$$\mathcal{I}_n(y) = \int_{-y}^{\infty} \frac{(x+y)^n}{e^x + 1} dx - \int_y^{\infty} \frac{(x-y)^n}{e^x + 1} dx. \quad (36)$$

(In particular, $\mathcal{I}_0(y) = y$.) Numerical evaluation of the integrals in Eq. (35) for $y = y_{\max}$ given by Eq. (A6) in Appendix brought us to

$$(n-p)_{\max} \approx \rho_0 k_B T \times \begin{cases} 1.949 & \text{if } t' = 0, \\ 3.269 \tau_L (1 + 3.23 \tau_L^2) & \text{if } t' \neq 0. \end{cases} \quad (37)$$

In turn, the carrier concentration corresponding to the maximum of S for a given T is determined by the value of E_L . [A similar expression for the minimum of \mathcal{L} , see Eq. (A7) in Appendix, is omitted here.]

Solid lines in Fig. 7(a) show the values of $(n-p)_{\max}$ calculated from Eq. (34) for the actual density of states and the chemical potential $\mu = \mu_{\max}$ [displayed with solid lines in Fig. 7(b)] adjusted such that the Seebeck coefficient, obtained numerically from Eq. (17), reaches the *conditional* maximum (S_{\max}) [see Fig. 7(c)] at a given temperature T (and one of the selected values of $t' = 0, 0.2$ eV, or 0.3 eV). The numerical results are compared with the linear-model predictions (dashed lines in all panels), given explicitly by Eq. (37) [Fig. 7(a)] or Eq. (A6) in Appendix [Figs. 7(b) and 7(c)]. Again, the linear model shows a relatively good agreement with corresponding data obtained via the mode-matching method; moderate deviations are visible for $t' \neq 0$ when $\mu_{\max} \gtrsim E_L/2$. In such a range, both $\rho(E)$ no longer follows the approximating Eq. (9), and the sudden rise of $T(E)$ near $E \approx E_L$ starts to affect thermoelectric properties.

Figures 7(c) and Fig. 7(d) display, respectively, the maximal Seebeck coefficient (S_{\max}) and figure of merit [$ZT(\mu_{\max})$] as functions of temperature. For $t' \neq 0$, the former shows broad peaks, centered near temperatures corresponding to $\mu_{\max} \approx 0.4 E_L$, for which the prediction of the linear model [see Eq. (A6) in Appendix] is slightly exceeded (by less than 10%), whereas for $t' = 0$ a monotonic temperature dependence, approaching the linear-model value, is observed. The figure of merit (calculated for $\mu = \mu_{\max}$) shows relatively fast temperature decay due to the role of phononic thermal conductivity (see Sec. III D). We find that $ZT(\mu_{\max})$, although being relatively small, is noticeably elevated in the presence of trigonal warping in comparison to the $t' = 0$ case. The behavior of S_{\max} presented in Fig. 7(c) suggests a procedure, allowing one to determine the trigonal-warping strength via directly measurable quantities.

For any $t' \neq 0$, one can determine a unique *global* maximum of $S = S(\mu, T)$, which is reached at $\mu = \mu_{\max}^S$ and $T = T_{\max}^S$. Our numerical findings for $0.1 \text{ eV} \leq t' \leq 0.35 \text{ eV}$ are presented in Fig. 8, where we have plotted (instead of μ_{\max}^S), the optimal effective concentration $(n-p)_{\max}^S$ [see the inset]. The

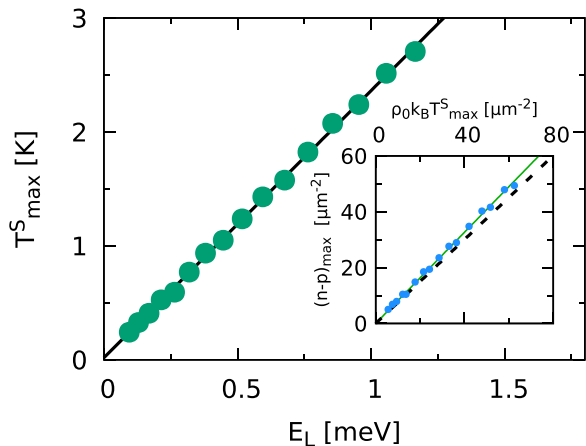


FIG. 8. Temperature corresponding to the maximal thermopower as a function of the Lifshitz energy (data points). Least-squares fitted linear dependence [see Eq. (38)] is also displayed (line). Inset shows the carrier concentration versus $\rho_0 k_B T^S_{\max}$, together with the model prediction (dashed line) and the linear fit (solid line) [see Eqs. (37) and (39)].

best-fitted lines displayed in Fig. 8 are given by

$$T^S_{\max, \text{fit}} = 0.203(2) \times E_L/k_B, \quad (38)$$

$$(n-p)^S_{\max, \text{fit}} = 0.816(5) \times \rho_0 k_B T^S_{\max}, \quad (39)$$

where numbers in parentheses are standard deviations for the last digit. A few-percent deviation of the actual $(n-p)^S_{\max}$ from predictions of the linear model [see dashed line in the inset, obtained from Eq. (37) by setting $\tau_L = k_B T^S_{\max, \text{fit}}/E_L \approx 0.20$] is relatively small taking into account that the existence of a global maximum of $S(\mu, T)$ is directly linked to the breakdown of the linear model occurring for $\mu \sim k_B T \gtrsim E_L$ (and therefore is not observed in the $t' = 0$ case). We further notice that Eqs. (38) and (39) provide direct relations between the two independent driving parameters corresponding to the optimal thermopower, T^S_{\max} and $(n-p)^S_{\max}$, and the trigonal warping strength quantified by E_L .

IV. CONCLUSIONS

We have investigated the thermopower, violation of the Wiedemann-Franz law, and the thermoelectric figure of merit, for large ballistic samples of bilayer graphene in the absence of electrostatic bias between the layers (a gapless case) and close to the charge-neutrality point. Although the thermoelectric performance is not high in such a parameter range, we find that low-temperature behavior of thermoelectric properties is determined by microscopic parameters of the tight-binding Hamiltonian, including the skew-interlayer hopping integral responsible for the trigonal warping, and by the relativistic nature of effective quasiparticles (manifesting itself in linear energy dependence of both the density of states and the electrical conductivity).

In particular, at sub-Kelvin temperatures, clear signatures of the Lifshitz transition, having forms of anomalies in chemical-potential dependences of the Seebeck coefficient and the Lorentz number, occurs in a vicinity of the Lifshitz energy

(defined by the microscopic parameters and quantifying the trigonal-warping strength). The anomalies are blurred out by thermal excitations above the crossover temperatures (different for the two thermoelectric properties) that are directly proportional to the Lifshitz energy.

At higher temperatures (of the order of 1 K) the trigonal-warping strength can be determined from thermoelectric measurements following one of the two different approaches: (i) finding the carrier concentration corresponding to the maximal thermopower as a function of temperature, or (ii) finding the *optimal* temperature, i.e., such that the thermopower reaches its global maximum. The first possibility is linked to the properties of massless quasiparticles, due to which the carrier concentration corresponding to the maximal thermopower depends approximately quadratically on temperature and reciprocally on the Lifshitz energy. On the other hand, existence of unique optimal temperature (equal to 2 K if the handbook value of the Lifshitz energy $E_L/k_B \approx 10$ K is supposed) is related to the gradual conductivity enhancement, and subsequent suppression of the thermopower, with increasing population of thermally-excited massive quasiparticles above the Lifshitz energy.

To conclude, we have shown that thermoelectric measurements may complement the list of techniques allowing one to determine tight-binding parameters of bilayer-graphene Hamiltonian. Unlike the well-established techniques [34] (or the other recently proposed [36,37]), they neither require high-magnetic-field measurements nor refer to conductivity scaling with the system size. Instead, the proposed single-device thermoelectric measurements must be performed on large ballistic samples (with the length exceeding 10 μm), such that quantum-size effects define the energy scale much smaller than the Lifshitz energy.

As we have focused on clean ballistic systems, several factors which may modify thermoelectric properties of graphene-based devices, including the disorder [34], lattice defects [60], or magnetic impurities [61], are beyond the scope of this study. However, recent progress in quantum-transport experiments on ultraclean freestanding monolayer samples exceeding 1 μm size [49,62] allows us to expect that similar measurements would become possible in bilayer graphene soon. Also, as the effects we describe are predicted to appear away from the charge-neutrality point, the role of above-mentioned factors should be less significant than for phenomena appearing precisely at the charge-neutrality point, such as the minimal conductivity [63,64]. Similar reasoning may apply to the role of interaction-induced spontaneous energy gap [65–67] (we notice that experimental values coincide with energy scales defined by quantum-size effects, e.g., $\hbar v_F/L \approx 3$ meV for $L = 250$ nm in Ref. [67]).

Note added. Recently, we become aware of theoretical works on strained monolayer graphene reporting quite similar, double-peak spectra of the Seebeck coefficient for sufficiently high uniaxial strains [68].

ACKNOWLEDGMENTS

We thank Colin Benjamin and Francesco Pellegrino for the correspondence and one of the referees for pointing out the role of the phononic part of the thermal conductance. The work was supported by the National Science Centre of Poland

(NCN) via Grant No. 2014/14/E/ST3/00256. Computations were partly performed using the PL-Grid infrastructure. D.S. acknowledges the financial support from dotation KNOW from Krakowskie Konsorcjum ‘‘Materia-Energia-Przyszłość’’ im. Mariana Smoluchowskiego.

APPENDIX: LINEAR MODEL FOR TRANSMISSION-ENERGY DEPENDENCE

At sufficiently high temperatures, thermoelectric properties given by Eqs. (16)–(21) become insensitive to the detailed functional form of $T(E)$, and simplified models can be considered. Here we assume $T(E) = \mathcal{C}|E|$, with \mathcal{C} being a dimensionless parameter. In turn, Eq. (19) leads to

$$L_0 = \frac{\mathcal{D}}{\beta} \left(y \int_0^y \frac{dx}{\cosh x + 1} + \int_y^\infty \frac{x dx}{\cosh x + 1} \right) = \frac{\mathcal{D}}{\beta} \ln(2 \cosh y + 2), \quad (\text{A1})$$

$$L_1 = \frac{\mathcal{D}}{\beta^2} \left(\int_0^y \frac{x^2 dx}{\cosh x + 1} + y \int_y^\infty \frac{x dx}{\cosh x + 1} \right) = \frac{\mathcal{D}}{\beta^2} \left[\frac{\pi^2}{3} + y^2 - y \ln(2 \cosh y + 2) + 4\text{Li}_2(-e^{-y}) \right], \quad (\text{A2})$$

$$L_2 = \frac{\mathcal{D}}{\beta^3} \left(y \int_0^y \frac{x^2 dx}{\cosh x + 1} + \int_y^\infty \frac{x^3 dx}{\cosh x + 1} \right) = \frac{\mathcal{D}}{\beta^3} \left[\frac{\pi^2}{3} y - y^3 + y^2 \ln(2 \cosh y + 2) - 8y\text{Li}_2(-e^{-y}) - 12\text{Li}_3(-e^{-y}) \right], \quad (\text{A3})$$

where $\mathcal{D} = (g_s g_v / h) \mathcal{C}$, $\beta = 1/k_B T$, $y = \beta \mu$, and $\text{Li}_s(z)$ is the polylogarithm function [69]. Subsequently, the Seebeck coefficient and the Lorentz number [see Eqs. (17) and (20) in the main text] are given by

$$S = \frac{k_B}{e} \left[-y + \frac{\frac{\pi^2}{3} + y^2 + 4\text{Li}_2(-e^{-y})}{\ln(2 \cosh y + 2)} \right], \quad (\text{A4})$$

$$\frac{K_{\text{el}}}{TG} = \left(\frac{k_B}{e} \right)^2 \left\{ \frac{\pi^2 y + y^3 - 12\text{Li}_3(-e^{-y})}{\ln(2 \cosh y + 2)} - \left[\frac{\frac{\pi^2}{3} + y^2 + 4\text{Li}_2(-e^{-y})}{\ln(2 \cosh y + 2)} \right]^2 \right\}. \quad (\text{A5})$$

As the right-hand sides in Eqs. (A4) and (A5) depend only on a single dimensionless variable (y) they are convenient to be compared with thermoelectric properties obtained numerically via the mode-matching method (see Sec. III for details). In particular, the function of Eq. (A4) is odd and has a single maximum for $y > 0$, i.e.,

$$S_{\text{max}} = 1.0023 k_B/e \quad \text{for} \quad y_{\text{max}}^{(S)} = 1.9488, \quad (\text{A6})$$

which is approximated by Eq. (23) in the main text. Analogously, the function of Eq. (A5) is even, and has a maximum at $y = 0$, that brought us to Eq. (24) in the main text. It also reaches a minimum

$$\mathcal{L}_{\text{min}} = 3.0060 (k_B/e)^2 \approx 0.91 \mathcal{L}_{\text{WF}} \quad \text{for} \quad y_{\text{min}}^{(\mathcal{L})} = 4.5895, \quad (\text{A7})$$

with the Wiedemann-Franz constant the $\mathcal{L}_{\text{WF}} = \frac{1}{3}\pi^2(k_B/e)^2$. For $y \rightarrow \infty$ we have $\mathcal{L} \rightarrow \mathcal{L}_{\text{WF}}$.

-
- [1] P. Dollfus, V. H. Nguyen, and J. Saint-Martin, *J. Phys.: Condens. Matter* **27**, 133204 (2015).
- [2] Y. M. Zuev, W. Chang, and P. Kim, *Phys. Rev. Lett.* **102**, 096807 (2009).
- [3] P. Wei, W. Bao, Y. Pu, C. N. Lau, and J. Shi, *Phys. Rev. Lett.* **102**, 166808 (2009).
- [4] J. G. Checkelsky and N. P. Ong, *Phys. Rev. B* **80**, 081413(R) (2009).
- [5] E. H. Hwang, E. Rossi, and S. Das Sarma, *Phys. Rev. B* **80**, 235415 (2009).
- [6] S. G. Nam, D. K. Ki, and H. J. Lee, *Phys. Rev. B* **82**, 245416 (2010).
- [7] C.-R. Wang, W.-S. Lu, and W.-L. Lee, *Phys. Rev. B* **82**, 121406(R) (2010).
- [8] C.-R. Wang, W.-S. Lu, L.-Hao, W.-L. Lee, T.-K. Lee, F. Lin, I.-C. Cheng, and J. Z. Chen, *Phys. Rev. Lett.* **107**, 186602 (2011).
- [9] M. M. Wysokiński and J. Spalek, *J. Appl. Phys.* **113**, 163905 (2013).
- [10] D. M. Newns, C. C. Tsuei, R. P. Huebener, P. J. M. van Bentum, P. C. Pattnaik, and C. C. Chi, *Phys. Rev. Lett.* **73**, 1695 (1994).
- [11] T. Cao, Z. Li, and S. G. Louie, *Phys. Rev. Lett.* **114**, 236602 (2015).
- [12] L. Seixas, A. S. Rodin, A. Carvalho, and A. H. Castro Neto, *Phys. Rev. Lett.* **116**, 206803 (2016).
- [13] H. Sevinçli, *Nano Lett.* **17**, 2589 (2017).
- [14] M. T. Pettes, I. Jo, Z. Yao, and L. Shi, *Nano Lett.* **11**, 1195 (2011).
- [15] A. A. Balandin, *Nat. Mater.* **10**, 569 (2011).
- [16] Y. Xu, Z. Li, and W. Duan, *Small* **10**, 2182 (2014).
- [17] W. Zhao, Y. Wang, Z. Wu, W. Wang, K. Bi, Z. Liang, J. Yang, Y. Chen, Z. Xu, and Z. Ni, *Sci. Rep.* **5**, 11962 (2015).
- [18] J. Crossno, J. K. Shi, K. Wang, X. Liu, A. Harzheim, A. Lucas, S. Sachdev, P. Kim, T. Taniguchi, K. Watanabe, T. A. Ohki, and K. C. Fong, *Science* **351**, 1058 (2016).
- [19] X. Zhang, Y. Gao, Y. Chen, and M. Hu, *Sci. Rep.* **6**, 22011 (2016).
- [20] A. A. Balandin, S. Ghosh, W. Bao, I. Calizo, D. Teweldebrhan, F. Miao, and C. Lau, *Nano Lett.* **8**, 902 (2008).
- [21] Y. Chen, T. Jayasekera, A. Calzolari, K. W. Kim, and M. B. Nardelli, *J. Phys.: Condens. Matter* **22**, 372202 (2010).
- [22] W. Huang, J.-S. Wang, and G. Liang, *Phys. Rev. B* **84**, 045410 (2011).
- [23] L. Liang, E. Cruz-Silva, E. C. Girão, and V. Meunier, *Phys. Rev. B* **86**, 115438 (2012).
- [24] H. Sevinçli, C. Sevik, T. Çağın, and G. Cuniberti, *Sci. Rep.* **3**, 1228 (2013).

- [25] M. S. Hossain, F. Al-Dirini, F. M. Hossain, and E. Skafidas, *Sci. Rep.* **5**, 11297 (2015).
- [26] Y. Anno, Y. Imakita, K. Takei, S. Akita, and T. Arie, *2D Mater.* **4**, 025019 (2017).
- [27] X. Chen, L. Zhang, and H. Guo, *Phys. Rev. B* **92**, 155427 (2015).
- [28] E. McCann, *Phys. Rev. B* **74**, 161403(R) (2006).
- [29] H. K. Min, B. Sahu, S. K. Banerjee, and A. H. MacDonald, *Phys. Rev. B* **75**, 155115 (2007).
- [30] Y. Zhang, T.-T. Tang, C. Girit, Z. Hao, M. C. Martin, A. Zettl, M. F. Crommie, Y. R. Shen, and F. Wang, *Nature (London)* **459**, 820 (2009).
- [31] E. McCann and V. I. Fal'ko, *Phys. Rev. Lett.* **96**, 086805 (2006).
- [32] M. Orlita, P. Neugebauer, C. Faugeras, A.-L. Barra, M. Potemski, F. M. D. Pellegrino, and D. M. Basko, *Phys. Rev. Lett.* **108**, 017602 (2012).
- [33] M. I. Katsnelson, *Graphene: Carbon in Two Dimensions* (Cambridge University Press, Cambridge, 2012).
- [34] E. McCann and M. Koshino, *Rep. Prog. Phys.* **76**, 056503 (2013).
- [35] A. G. Moghaddam and M. Zareyan, *Phys. Rev. B* **79**, 073401 (2009).
- [36] G. Rut and A. Rycerz, *Europhys. Lett.* **107**, 47005 (2014).
- [37] G. Rut and A. Rycerz, *Phys. Rev. B* **93**, 075419 (2016).
- [38] M. Paulsson and S. Datta, *Phys. Rev. B* **67**, 241403(R) (2003).
- [39] K. Esfarjani, M. Zebarjadi, and Y. Kawazoe, *Phys. Rev. B* **73**, 085406 (2006).
- [40] See e.g. M. S. Dresselhaus and G. Dresselhaus, *Adv. Phys.* **30**, 139 (1981); reprinted in **51**, 1 (2002).
- [41] The values of t_0 and t_\perp are taken from: A. B. Kuzmenko, I. Crassee, D. van der Marel, P. Blake, and K. S. Novoselov, *Phys. Rev. B* **80**, 165406 (2009).
- [42] The combined particle-hole-reflection symmetry applies as we have neglected the next-nearest-neighbor intralayer hopping t_2 , which is not determined for BLG [34]. Effects of $t_2 \sim t_\perp$ are insignificant when discussing the band structure for $|E| \sim E_L \ll t_\perp$.
- [43] We notice a generic relation between $\rho(E)$ and the cyclotron mass $m_C(E) = (\pi\hbar^2/2)\rho(E)$.
- [44] R. Landauer, *IBM J. Res. Dev.* **1**, 223 (1957).
- [45] M. Buttiker, Y. Imry, R. Landauer, and S. Pinhas, *Phys. Rev. B* **31**, 6207 (1985); M. Buttiker, *Phys. Rev. Lett.* **57**, 1761 (1986); *IBM J. Res. Dev.* **32**, 317 (1988).
- [46] For BLG, contributions of out-of-plane phonons, governing the thermal properties at low-temperatures, are additionally reduced in comparison to MLG, see: A. I. Cocemasov, D. L. Nika, and A. A. Balandin, *Nanoscale* **7**, 12851 (2015); D. L. Nika and A. A. Balandin, *J. Phys.: Condens. Matter* **24**, 233203 (2012); N. Mingo and D. A. Broido, *Phys. Rev. Lett.* **95**, 096105 (2005).
- [47] J. Tworzydło, B. Trauzettel, M. Titov, A. Rycerz, and C. W. J. Beenakker, *Phys. Rev. Lett.* **96**, 246802 (2006).
- [48] R. Danneau, F. Wu, M. F. Craciun, S. Russo, M. Y. Tomi, J. Salmilehto, A. F. Morpurgo, and P. J. Hakonen, *Phys. Rev. Lett.* **100**, 196802 (2008).
- [49] M. Kumar, A. Laitinen, and P. J. Hakonen, [arXiv:1611.02742](https://arxiv.org/abs/1611.02742).
- [50] In some geometries, the transmission is suppressed by approximately constant factor for $E < 0$ due to contact effects; see supplemental information in Ref. [49].
- [51] R. R. Nair, P. Blake, A. N. Grigorenko, K. S. Novoselov, T. J. Booth, T. Stauber, N. M. R. Peres, and A. K. Geim, *Science* **320**, 1308 (2008).
- [52] I. Snyman and C. W. J. Beenakker, *Phys. Rev. B* **75**, 045322 (2007).
- [53] Typically, using double-precision arithmetic, we put $N_{\text{div}} = 20$ for $L = W/20 = 10^4 l_\perp$ and $|\mu| \leq 2$ meV. Numbers of different transverse momenta $k_y = 2\pi q/W$, where $q = 0, \pm 1, \pm 2, \dots, \pm q_{\text{max}}$, necessary to determine $\text{Tr}(\text{tt}^\dagger)$ in Eq. (25) with a 10-digit accuracy were found to be $1955 \leq 2q_{\text{max}} + 1 \leq 8149$, with the lower (upper) value corresponding to $\mu = 0$ and $t' = 0.1$ eV ($\mu = 2$ meV and $t' = 0.35$ eV).
- [54] For $L = W/20 = 10^4 l_\perp$, effects of the crystallographic orientation are negligible starting from $|\mu| \gtrsim \hbar v_F/L \approx 38 \mu\text{eV}$, as the summation over normal modes in Eq. (25) involves numerous contributions, corresponding to different angles of incident, that are comparable.
- [55] G. Rut and A. Rycerz, *Acta Phys. Polon. A* **126**, A-114 (2014).
- [56] Due to the presence of Fabry-Pérot oscillations, the well-known Mott formula $S = (\pi^2/3)e^{-1}k_B^2 T \times [\ln T(E)/\partial E]_{E=\mu}$ cannot be directly applied.
- [57] A. Alofi and G. P. Srivastava, *Phys. Rev. B* **87**, 115421 (2013); A. Alofi, Theory of Phonon Thermal Transport in Graphene and Graphite, Ph.D. Thesis, University of Exeter, 2014; <http://hdl.handle.net/10871/15687>.
- [58] J. Callaway, *Phys. Rev.* **113**, 1046 (1959).
- [59] The model parameters are chosen such that the experimental results of Ref. [14] are reproduced if $L = 0.25 \mu\text{m}$. Namely, the Callaway model parameters are $B_U = 4.77 \times 10^{-25} \text{s K}^{-3}$ and $B_N = 3.18 \times 10^{-25} \text{s K}^{-3}$, the defect concentration is $c_d = 1.6 \times 10^{-4}$, and the concentration of C^{13} isotope is 10^{-2} . Remaining parameters of the phonon dispersion relations are same as in the first paper of Ref. [57].
- [60] M. S. Dresselhaus, A. Jorio, A. G. Souza Filho, and R. Saito, *Phil. Trans. R. Soc. A* **368**, 5355 (2010).
- [61] B. Uchoa, T. G. Rappoport, and A. H. Castro Neto, *Phys. Rev. Lett.* **106**, 016801 (2011); J. Hong, E. Bekyarova, W. A. de Heer, R. C. Haddon, and S. Khizroev, *ACS Nano* **7**, 10011 (2013).
- [62] P. Rickhaus, P. Makk, M.-H. Liu, E. Tóvári, M. Weiss, R. Maurand, K. Richter, and C. Schönenberger, *Nat. Commun.* **6**, 6470 (2015).
- [63] A. S. Mayorov, D. C. Elias, M. Mucha-Kruczynski, R. V. Gorbachev, T. Tudorovskiy, A. Zhukov, S. V. Morozov, M. I. Katsnelson, V. I. Fal'ko, A. K. Geim, and K. S. Novoselov, *Science* **333**, 860 (2011).
- [64] S. Samaddar, I. Yudhistira, S. Adam, H. Courtois, and C. B. Winkelmann, *Phys. Rev. Lett.* **116**, 126804 (2016).
- [65] G. M. Rutter, S. Jung, N. N. Klimov, D. B. Newell, N. B. Zhitenev, and J. A. Stroscio, *Nat. Phys.* **7**, 649 (2011).
- [66] F. Freitag, J. Trbovic, M. Weiss, and C. Schönenberger, *Phys. Rev. Lett.* **108**, 076602 (2012).
- [67] W. Bao, J. Velasco, Jr., F. Zhang, L. Jing, B. Standley, D. Smirnov, M. Bockrath, A. H. MacDonald, and C. N. Lau, *Proc. Natl. Acad. Sci. USA* **109**, 10802 (2012).
- [68] A. Mani and C. Benjamin, *Phys. Rev. E* **96**, 032118 (2017); [arXiv:1707.07159](https://arxiv.org/abs/1707.07159).
- [69] K. Oldham, J. Myland, and J. Spanier, *An Atlas of Functions* (Springer-Verlag, New York, 2009), Chap. 25.

Thermoelectric properties of gapped bilayer graphene

Dominik Suszalski, Grzegorz Rut and Adam Rycerz 

Marian Smoluchowski Institute of Physics, Jagiellonian University, Łojasiewicza 11, PL–30348 Kraków, Poland

E-mail: rycerz@th.if.uj.edu.pl

Received 15 April 2019, revised 14 June 2019

Accepted for publication 26 June 2019

Published 15 July 2019



Abstract

Unlike in conventional semiconductors, both the chemical potential and the band gap in bilayer graphene (BLG) can be tuned via application of external electric field. Among numerous device implications, this property also designates BLG as a candidate for high-performance thermoelectric material. In this theoretical study we have calculated the Seebeck coefficients for abrupt interface separating weakly- and heavily-doped areas in BLG, and for a more realistic rectangular sample of mesoscopic size, contacted by two electrodes. For a given band gap (Δ) and temperature (T) the maximal Seebeck coefficient is close to the Goldsmid–Sharp value $|S|_{\max}^{\text{GS}} = \Delta/(2eT)$, the deviations can be approximated by the asymptotic expression $|S|_{\max}^{\text{GS}} - |S|_{\max} = (k_B/e) \times [\frac{1}{2} \ln u + \ln 2 - \frac{1}{2} + \mathcal{O}(u^{-1})]$, with the electron charge $-e$, the Boltzmann constant k_B , and $u = \Delta/(2k_B T) \gg 1$. Surprisingly, the effects of trigonal warping term in the BLG low-energy Hamiltonian are clearly visible at few-Kelvin temperatures, for all accessible values of $\Delta \leq 300$ meV. We also show that thermoelectric figure of merit is noticeably enhanced ($ZT > 3$) when a rigid substrate suppresses out-of-plane vibrations, reducing the contribution from ZA phonons to the thermal conductivity.

Keywords: graphene, bilayer graphene, thermoelectrics, Seebeck effect, ballistic transport

 Supplementary material for this article is available [online](#)

(Some figures may appear in colour only in the online journal)

1. Introduction

In recent years, bilayer graphene (BLG) devices made it possible to demonstrate several intriguing physical phenomena, including the emergence of quantum spin Hall phase [1, 2], the fractal energy spectrum known as Hofstadter’s butterfly [3, 4], or unconventional superconductivity [5, 6], just to mention a few. From a bit more practical perspective, a number of plasmonic and photonic instruments were designed and build [7–9] constituting platforms for application considerations. BLG-based thermoelectric devices have also attracted a significant attention [10–13], next to the devices based on other two-dimensional (2D) materials [14–16].

In a search for high-performance thermoelectric material, one’s attention usually focusses on enhancing the dimensionless figure of merit [17, 18]

$$ZT = \frac{GS^2T}{K}, \quad (1)$$

where G , S and K are (respectively): the electrical conductance, the Seebeck coefficient quantifying the thermopower, and the thermal conductance; the last characteristic can be represented as $K = K_{\text{el}} + K_{\text{ph}}$, with K_{el} (K_{ph}) being the electronic (phononic) part. This is because the maximal energy conversion efficiency is related to ZT via [19]

$$\eta_{\max} = \frac{\Delta T}{T_h} \frac{\sqrt{1 + ZT_{\text{av}}} - 1}{\sqrt{1 + ZT_{\text{av}}} + \frac{T_c}{T_h}}, \quad (2)$$

where T_c (T_h) is the hot- (or cool) side temperature, $\Delta T = T_h - T_c$, and $T_{\text{av}} = (T_c + T_h)/2$. In particular, for $ZT_{\text{av}} = 3$ we have $\eta_{\max} > \frac{1}{3} \Delta T/T_h$ (with $\Delta T/T_h$ the Carnot efficiency), and therefore $ZT > 3$ is usually regarded as a

condition for thermoelectric device to be competitive with other power generation systems.

As the Seebeck coefficient is squared in equation (1), a maximum of ZT —considered as a function of the driving parameters specified below—is commonly expected to appear close to a maximum of $|S|$. Here we show this is not always the case in gapped BLG: when discussing in-plane thermoelectric transport in a presence of perpendicular electric field such that the band gap is much greater than the energy of thermal excitations ($\Delta \gg k_B T$), the maximal absolute thermopower $|S|_{\max}$ corresponds to the electrochemical potential relatively close to the center of a gap, namely $\mu_{\max}^{|S|} \approx \pm \frac{1}{2} k_B T \ln(2\Delta/k_B T)$, whereas the maximal figure of merit ZT_{\max} appears near the maximum of the valence band (or the minimum of the conduction band), i.e. $\mu_{\max}^{ZT} \approx \pm \Delta/2$. In contrast to ZT_{\max} , $|S|_{\max}$ is not directly related to the value of the transmission probability near the band boundary, and these two quantities show strikingly different behaviors with increasing Δ for a given T .

Qualitatively, one can expect that thermoelectric performance of BLG is enhanced with increasing Δ , since abrupt switching behavior is predicted for the conductance G when passing $\mu = \pm \Delta/2$ for $\Delta \gg k_B T$ [20, 21]. (Moreover, the gap opening suppresses κ_{ei} , reducing the denominator in equation (1).) Such a common intuition is build on the Mott formula, according to which S is proportional to the logarithmic derivative of G as a function of the Fermi energy E_F . One cannot, however, directly apply the Mott formula for gapped systems at nonzero temperatures, and the link between a rapid increase of $G(E_F)$ for $E_F \approx \Delta/2$ and high $|S|$ is thus not direct in the case of gapped BLG, resulting in $\mu_{\max}^{|S|} \ll \Delta/2$.

The results of earlier numerical work [22] suggest that $|S|_{\max}$, obtained by adjusting μ for a given Δ and T , is close to

$$|S|_{\max}^{\text{GS}} = \frac{\Delta}{2eT}, \quad (3)$$

being the Goldsmid–Sharp value for wide-gap semiconductors [23]. In this paper, we employ the Landauer–Büttiker approach for relatively large ballistic BLG samples, finding that equation (3) provides a reasonable approximation of the actual $|S|_{\max}$ for $\Delta \sim k_B T$ only. For larger Δ , a logarithmic correction becomes significant, and the deviation exceeds k_B/e ($\approx 86 \mu\text{V K}^{-1}$) for $\Delta \gtrsim 10 k_B T$. We further find that—although $|S|_{\max}$ grows monotonically when increasing Δ at fixed T and may reach (in principle) arbitrarily large value— ZT_{\max} shows a conditional maximum at $\Delta_*(T) \sim 10^2 k_B T$ (for $T \leq 10$ K). An explanation of these findings in terms of a simplified model for transmission-energy dependence is provided.

2. Model and methods

The two systems considered are shown schematically in figures 1(a) and (b). The first system (hereinafter called an *abrupt interface*) clearly represents an idealized case, as we have supposed that both the doping and temperature change rapidly on the length-scale much smaller than the Fermi wavelength for an electron. Therefore, a comparison with the second system,

in which chemical potentials and temperatures are attributed to macroscopic reservoirs (the two leads), separated by a sample area of a finite length L , is essential to validate the applicability of our predictions for real experiments.

We take the four-band Hamiltonian for BLG [24]

$$H = \xi \begin{pmatrix} -U/2 & v_F \pi & \xi t_{\perp} & 0 \\ v_F \pi^{\dagger} & -U/2 & 0 & v_3 \pi \\ \xi t_{\perp} & 0 & U/2 & v_F \pi^{\dagger} \\ 0 & v_3 \pi^{\dagger} & v_F \pi & U/2 \end{pmatrix}, \quad (4)$$

where the valley index $\xi = 1$ for K valley or $\xi = -1$ for K' valley, $\pi = p_x + ip_y$, $\pi^{\dagger} = p_x - ip_y$, with $\mathbf{p} = (p_x, p_y)$ the carrier momentum, $v_F = \sqrt{3}at_0/(2\hbar)$ is the Fermi velocity, $v_3 = (t'/t_0)v_F$, U is the electrostatic bias between the layers, and $a = 0.246$ nm is the lattice parameter. Following [25], we set $t_0 = 3.16$ eV—the nearest-neighbor in-plane hopping energy, $t_{\perp} = 0.381$ eV—the direct interlayer hopping energy; the skew interlayer hopping energy is set as $t' = 0$ or $t' = 0.3$ eV in order to discuss the role of trigonal warping¹. The band gap $\Delta \approx |U|$ for $|U| \ll t_{\perp}$ and $t' = 0$ (remaining details are given in *supplementary information, section I* (stacks.iop.org/JPhysCM/31/415501/mmedia)). Solutions of the subsequent Dirac equation, $H\Psi = E\Psi$, with $\Psi = (\Psi_{A1}, \Psi_{B1}, \Psi_{B2}, \Psi_{A2})^T$ the probability amplitudes, are matched for the interfaces separating weakly- and heavily-doped regions allowing us to determine the energy-dependent transmission probability $T(E)$ (see *supplementary information, section II*).

At zero temperature, the relation between physical carrier concentration (the doping) and the Fermi energy E_F can be approximated by a close-form expression for $t' = 0$ and $|E_F| - \Delta/2 \ll t_{\perp}$, namely

$$n(E_F) \approx \frac{t_{\perp}}{\pi(\hbar v_F)^2} \max(0, |E_F| - \Delta/2), \quad (5)$$

following from a piecewise-constant density of states in such a parameter range [24]. The prefactor in equation (5) $(1/\pi)t_{\perp}/(\hbar v_F)^2 \approx 0.268 \text{ nm}^{-2} \text{ eV}^{-1}$. In a general situation, it is necessary to perform the numerical integration of the density of states following from the Hamiltonian H (4) (see *supplementary information, section I*); however, equation (5) gives a correct order of magnitude for $\Delta \gg k_B T$. In the remaining part of the paper, we discuss thermoelectric characteristics as functions of the electrochemical potential μ , keeping in mind that the doping $n = n(|\mu|)$ is a monotonically increasing function of $|\mu|$.

Next, we employ the Landauer–Büttiker expressions for the electrical and thermal currents [26, 27]

$$I = -\frac{g_s g_v e}{h} \int dE T(E) [f_L(E) - f_R(E)], \quad (6)$$

$$I_Q = \frac{g_s g_v}{h} \int dE T(E) [f_L(E) - f_R(E)] (E - \mu), \quad (7)$$

¹ Remaining parameters of the systems studied numerically are, for an abrupt interface of figure 1(a): $W = 10^3 l_{\perp} = 1.77 \mu\text{m}$ (with $l_{\perp} = \hbar v_F/t_{\perp}$); and for a rectangular setup of figure 1(b): $L = W/20 = 10^4 l_{\perp}$.

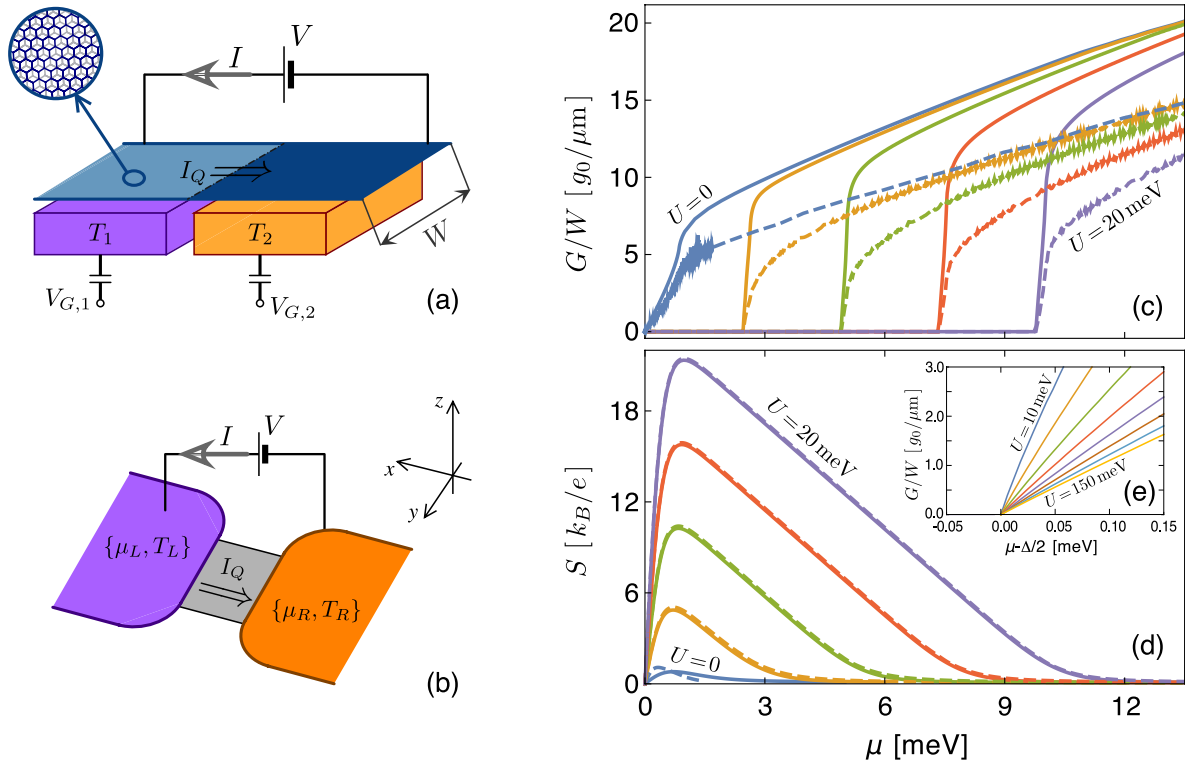


Figure 1. Systems studied numerically in the paper (*left*) and their basic thermoelectric characteristics (*right*). (a) BLG strip of width W with a voltage source driving electric current through the strip. Two gate electrodes, with different temperatures T_1 and T_2 , induce an abrupt interface (dash-dot line) between the weakly-doped (light area) and the heavily-doped (dark area) regions. (b) A finite, weakly-doped section of the strip (of length L) with leads driving both thermal and electric currents. In both cases, additional gate electrodes (not shown) allow to tune the electrostatic bias between the layers (See footnote 1.). The coordinate system is also shown. (c) Zero-temperature conductance, specified in the units of $g_0 = 4e^2/h$, and (d) the Seebeck coefficient at $T = 5$ K as functions of the chemical potential. Solid lines correspond to the system of panel (a), dashed lines correspond to the system of panel (b). (e) Zoom-in of the conductance as a function of the chemical potential measured from the conduction band minimum ($\mu = \Delta/2$) for the system of panel (a). Skew-interlayer hopping is fixed at $t' = 0.3$ eV. The electrostatic bias between the layers is varied from $U = 0$ to $U = 20$ meV in steps of 5 meV (c) and (d) or from $U = 10$ meV to $U = 150$ meV in steps of 20 meV (e). (The extreme values of U are specified for corresponding lines.)

where $g_s = g_v = 2$ are spin and valley degeneracies, f_L and f_R are the distribution functions for the left and right reservoirs, with their electrochemical potentials μ_L and μ_R , and temperatures T_L and T_R . We further suppose that $\mu_L - \mu_R \equiv -eV$ and $T_L - T_R \equiv \Delta T$ are infinitesimally small (the linear-response regime) and define $\mu = (\mu_L + \mu_R)/2$ and $T = (T_L + T_R)/2$. The conductance G , the Seebeck coefficient S , and the electronic part of the thermal conductance K_{el} , are given by [28]

$$G = \left. \frac{I}{V} \right|_{\Delta T=0} = e^2 L_0, \quad (8)$$

$$S = - \left. \frac{V}{\Delta T} \right|_{I=0} = \frac{L_1}{e T L_0}, \quad (9)$$

$$K_{el} = \left. \frac{I_Q}{\Delta T} \right|_{I=0} = \frac{L_0 L_2 - L_1^2}{T L_0}, \quad (10)$$

where

$$L_n = \frac{g_s g_v}{h} \int dE T(E) \left(- \frac{\partial f_{FD}}{\partial E} \right) (E - \mu)^n \quad (n = 0, 1, 2) \quad (11)$$

with $f_{FD}(\mu, T, E) = 1 / [\exp((E - \mu)/k_B T) + 1]$ being the Fermi–Dirac distribution function. In particular, for $T \rightarrow 0$, equation (8) reduces to $G = (g_s g_v e^2/h) T(\mu)$, the well-known zero-temperature Landauer conductance.

The phononic part of the thermal conductance, occurring in equation (1), can be calculated using

$$K_{ph} = \frac{1}{2\pi} \int d\omega \hbar \omega \frac{\partial f_{BE}}{\partial T} \mathcal{T}_{ph}(\omega), \quad (12)$$

with $f_{BE}(T, \omega) = 1 / [\exp(\hbar \omega/k_B T) - 1]$ the Bose–Einstein distribution function and $\mathcal{T}_{ph}(\omega)$ the phononic transmission spectrum. We calculate $\mathcal{T}_{ph}(\omega)$ by adopting the procedure developed by Alofi and Srivastava [29] to the two systems considered in this work (see *supplementary information, section IV*).

3. Numerical results

Before discussing the thermoelectric properties in details, we present zero-temperature conductance spectra, which represent the input data to calculate thermoelectric properties (see section 2). Since the Hamiltonian given by equation (4) is

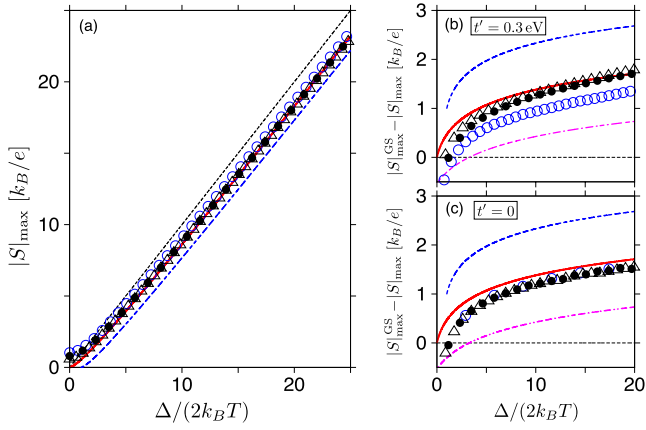


Figure 2. (a) Maximal absolute value of the Seebeck coefficient and (b), (c) its deviation from the Goldsmid–Sharp value $|S|_{\max}^{\text{GS}} = \Delta/(2eT)$ calculated numerically for the system of figure 1(a) (datapoints) as functions of the energy gap for different temperatures $T = 1$ K (open circles), $T = 5$ K (full circles), and $T = 10$ K (triangles). Skew-interlayer hopping integral is $t' = 0.3$ eV (a) and (b) or $t' = 0$ (c). Lines depict $S_{\max} = S_{\max}^{\text{GS}}$ (black dotted line), and predictions of the model for transmission-energy dependence given by equation (14) with $\alpha = 0$ (blue dashed line), $\alpha = 1$ (red solid line), and $\alpha = 2$ (magenta dash-dot line—omitted in panel (a) for clarity).

particle-hole symmetric, it is sufficient to limit the discussion to $\mu \geq 0$.

Typically, the conductance $G(\mu)$ of the finite-strip section, compared with the case of an abrupt interface, is reduced by approximately 50% near the conduction band minimum ($\mu = \Delta/2$) due to backscattering on the second interface, and slowly approaches the abrupt-interface limit for $\mu \gg \Delta/2$; see figure 1(c). Additionally, for a rectangular setup of figure 1(b) oscillations of the Fabry–Pérot type are well-pronounced, see [13]. In contrast, the Seebeck coefficient is almost identical for both systems, see figure 1(d). We further notice that the conductance near $\mu = \Delta/2$, displayed in figure 1(e), is gradually suppressed with increasing U . (Hereinafter, the bandgap Δ is determined numerically for the dispersion relation following from equation (4), see *supplementary information, section I*. In general, $\Delta < |U|$ [24]).

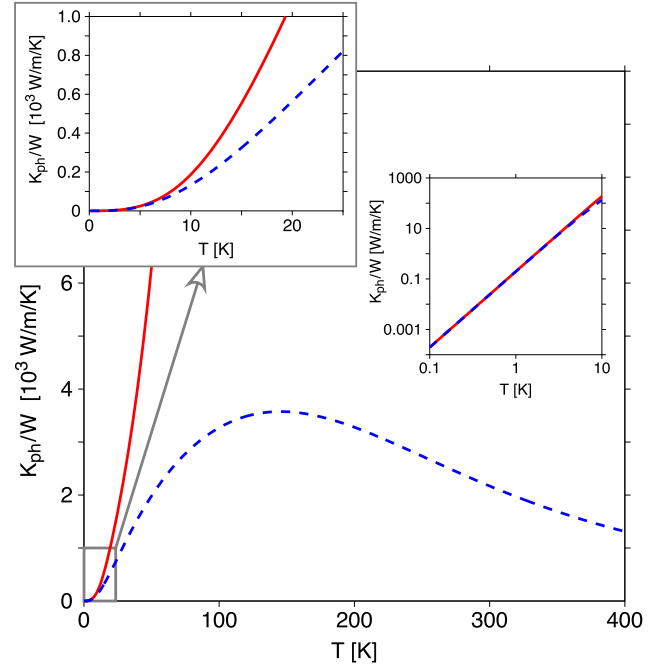


Figure 3. Phononic parts of the thermal conductance for the systems of figures 1(a) (solid line) and (b) (dashed line) as functions of temperature. Insets are zoom in, for low temperatures, in the linear (top left) and the log–log (right) scale.

$$T^{(\alpha)} = \mathcal{C}(\Delta) \times \begin{cases} \delta(E - \frac{1}{2}\Delta) + \delta(E + \frac{1}{2}\Delta) & \text{if } \alpha = 0 \\ \Theta(|E| - \frac{1}{2}\Delta)(|E| - \frac{1}{2}\Delta)^{\alpha-1} & \text{if } \alpha > 0 \end{cases} \quad (13)$$

with the prefactor $\mathcal{C}(\Delta)$ quantifying the transmission probability near the band boundary $|E| \approx \frac{1}{2}\Delta$, $\delta(x)$ being the Dirac delta function, and $\Theta(x)$ being the Heaviside step function. The analytic expressions presented here, and later in section 4, are (unless otherwise specified) valid for any $\alpha \geq 0$, although when comparing model predictions with the numerical data we limit our considerations to integer α .

In particular, equation (13) leads to the maximal absolute value of the Seebeck coefficient

$$\begin{aligned} |S|_{\max}^{(\alpha)} \times (k_B/e)^{-1} &\approx \sqrt{(u+\alpha)(u+\alpha-1)} - \ln\left(\sqrt{u+\alpha} + \sqrt{u+\alpha-1}\right) \\ &= u - \frac{1}{2} \ln(4u) + \alpha - \frac{1}{2} + \frac{3-7\alpha+\alpha^2}{8u} + \mathcal{O}(u^{-2}) \end{aligned} \quad \text{for } \alpha \geq 0, \quad (14)$$

The close overlap of the thermopower spectra presented in figure 1(d) allows us to limit the discussion of $|S|_{\max}$ to the case of an abrupt interface, see figures 2(a)–(c). In order to rationalize the deviations of the numerical data from $|S|_{\max}^{\text{GS}}$ given by equation (3), we propose a family of models for the transmission-energy dependence, namely

where the first asymptotic equality corresponds to $u = \Delta/(2k_B T) \gg 1$ (see *supplementary information*). It is clear from figure 2(a) that $|S|_{\max}^{(\alpha)}$ with $\alpha = 1$ (red solid line) reproduces the actual numerical results (datapoints) noticeably better than $|S|_{\max}^{(\alpha)}$ with $\alpha = 0$ (blue dashed line) or $|S|_{\max}^{\text{GS}}$ (black dotted line). What is more, the deviations $|S|_{\max}^{\text{GS}} - |S|_{\max}$,

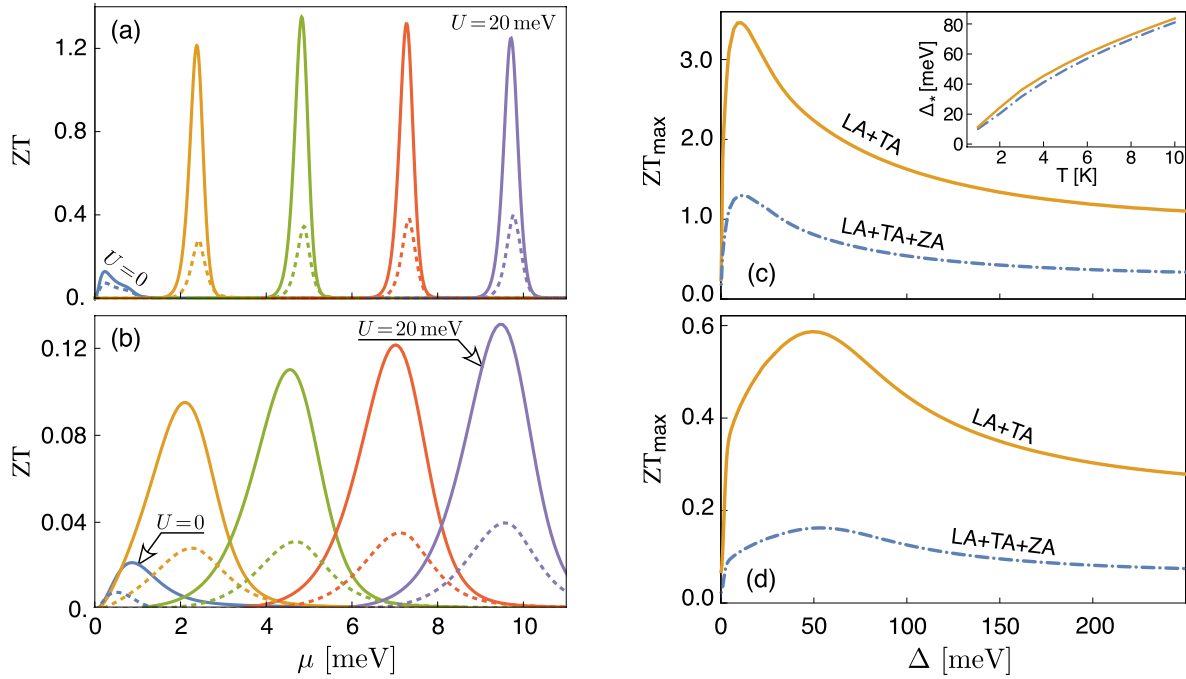


Figure 4. *Left:* thermoelectric figure of merit displayed as a function of the chemical potential for temperatures (a) $T = 1$ K and (b) $T = 5$ K. Solid lines correspond for the system of figure 1(a), dashed lines correspond for the system of figure 1(b). (Remaining parameters are same as in figures 1(c) and (d).) *Right:* maximal value of the figure of merit for the system of figure 1(a), versus the energy gap for temperatures (c) $T = 1$ K and (d) $T = 5$ K. Inset in panel (c) shows the optimal gap Δ_* as a function of temperature. Different lines in panels (c) and (d) correspond to the limit of rigid substrate eliminating ZA phonons (solid lines) or the free-standing sample (dashed-dotted lines).

displayed as functions of Δ , allows one to easily identify the effects of trigonal warping, see figures 2(b) for $t' = 0.3$ eV and 2(c) for $t' = 0$.

Next, we investigate the figure of merit (ZT) given by equation (1). For this purpose, it is necessary to calculate both the electronic part of thermal conductance (K_{el}), that is determined by the energy-dependent transmission $T(E)$ (see section 2), as well as the phononic part (K_{ph}), presented in figure 3. We find that for $T < 10$ K the two systems considered show almost equal $K_{ph} (\propto T^3)$, and different values of ZT (see figures 4(a) and (b)) follow predominantly from the G reduction discussed above. Unlike $|S|_{max}$, a value of which (for a given T) is limited only by the largest experimentally-accessible $\Delta \approx 300$ meV [24, 30], ZT_{max} shows well-defined conditional maximum for the optimal bandgap $\Delta_*/k_B T \approx 100$ –150 (at the temperature range $10 \text{ K} \geq T \geq 1 \text{ K}$) and decreases for $\Delta > \Delta_*$; see figures 4(c) and (d).

Also in figures 4(c) and (d), we compare ZT_{max} for free-standing BLG, in which all polarizations of phonons (LA, TA, and ZA) contribute to the thermal conductance (see *supplementary information, section IV*) with an idealized case of BLG on a *rigid substrate*, eliminating out-of-plane (ZA) phonons. In the latter case, ZT_{max} is amplified, approximately by a factor of 3 (for any Δ), exceeding $ZT = 3$ for $T = 1$ K and $\Delta \approx \Delta_* = 10$ meV.

4. Discussion

Let us now discuss here why we have identified apparently different behaviors of $|S|_{max}$ and ZT_{max} with increasing Δ . To understand these observations, we refer to the model $T^{(\alpha)}(E)$ given by equation (13) with $\alpha \geq 0$, for which $|S|_{max}^{(\alpha)}$, approximated by equation (14), corresponds to

$$\begin{aligned} \frac{|S|_{max}}{k_B T} &\approx \ln \left(\sqrt{u + \alpha} + \sqrt{u + \alpha - 1} \right) \\ &\approx \frac{1}{2} \ln \left(\frac{2\Delta}{k_B T} \right) \quad \text{for } \Delta \gg k_B T. \end{aligned} \quad (15)$$

In contrast, the chemical potential corresponding the the maximal ZT is much higher and can be approximated (in the $\Delta \gg k_B T$ limit) by

$$\mu_{max}^{ZT} \approx \frac{\Delta}{2} - 1.145 k_B T \quad \text{for } \alpha = 1, \quad (16)$$

or

$$\mu_{max}^{ZT} \approx \frac{\Delta}{2} + 0.668 k_B T \quad \text{for } \alpha = 2, \quad (17)$$

where we have further supposed that $K_{ph} \gg K_{el}$, being equivalent to

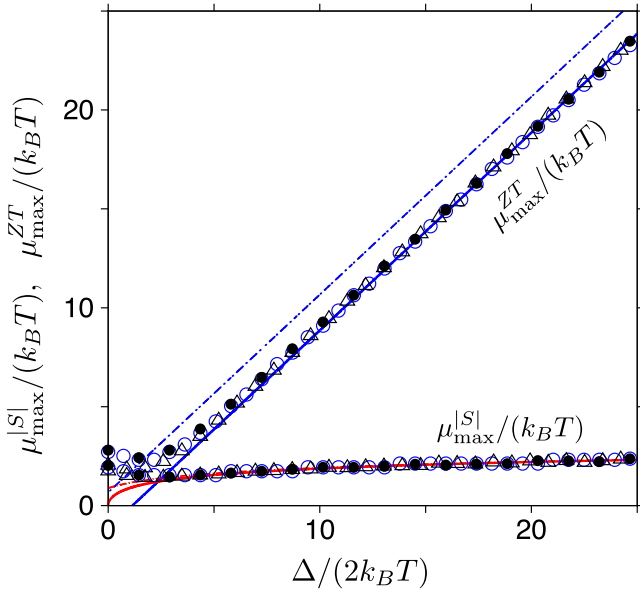


Figure 5. Chemical potential corresponding to the maximal absolute thermopower presented in figure 2 ($\mu_{\max}^{|S|}$) and the maximal figure of merit presented in figure 4 (μ_{\max}^{ZT}) as function of the energy gap. Points correspond to same datasets as in figures 2(a) and (b) (skew-interlayer hopping integral is $t' = 0.3$ eV). Lines depict approximating equation (15) with $\alpha = 1$ (red solid line) and $\alpha = 2$ (red dash-dot line), equations (16) (blue solid line), and (17) (blue dash-dot line).

$$ZT \approx GS^2 \frac{T}{k_{\text{ph}}(T)}. \quad (18)$$

As the last term in equation (18) depends only on T we can focus now on the *power factor* (GS^2), a maximal value of which can be approximated by

$$(GS^2)_{\max} \approx \mathcal{M}_{\max}^{(\alpha)} \frac{g_s g_v k_B^2}{h} (k_B T)^{\alpha-1} \mathcal{C}(\Delta), \quad (19)$$

where the prefactor $\mathcal{M}_{\max}^{(\alpha)}$ depends only on α and is equal to 1.27 for $\alpha = 1$ or to 4.06 for $\alpha = 2$ (see also *supplementary information, section III*).

The positions of maxima visible in figures 4(a) and (b) are numerically close to the approximation given by equation (16). Also, the data visualized in figure 5, together with the lines corresponding to equations (16) and (17), further support our conjecture that the model $T^{(\alpha)}(E)$, given by equation (13) with $\alpha = 1$ (the *step-function model*), is capable of reproducing basic thermoelectric characteristics of gapped BLG with a reasonable accuracy.

Although it might seem surprising at first glance that the step-function model ($\alpha = 1$) reproduces the actual numerical results much better than $T^{(\alpha)}(E)$ with $\alpha = 2$, as the conductance spectra in figure 1(e) exhibit linear, rather than step-line, energy dependence for $\mu \geq \Delta/2$. However, for the temperature range of $1 \text{ K} \leq T \leq 10 \text{ K}$ the $T(E)$ behavior for $E - \Delta/2 \gg 0.1$ eV, visualized with the data in figure 1(c), prevails (notice that the full width at half maximum for $-\partial f_{\text{FD}}/\partial E$ in equation (11) is $\approx 3.53 k_B T$). For this reason, a

simple step-function model grasps the essential features of the actual $T(E)$.

Apart from pointing out that $\mu_{\max}^{|S|} \ll \mu_{\max}^{ZT} \approx \Delta/2$ for $\Delta \gg k_B T$ (some further implications of this fact are discussed below), the analysis starting from $T^{(\alpha)}(E)$ models also leads to the conclusion that—unlike $|S|_{\max}$ that is not directly related to $\mathcal{C}(\Delta)$ —for the figure of merit we have: $ZT_{\max} \propto (GS^2)_{\max} \propto \mathcal{C}(\Delta)$ (see equations (18) and (19)). It becomes clear now that a striking ZT_{\max} suppression for large Δ is directly link to the local G suppression for large U , illustrated in figure 1(e). Power-law fits to the datasets presented in figures 4(c) and (d), of the form $ZT_{\max} \propto \Delta^{-\gamma}$ for $\Delta > \Delta_*$, lead to $\gamma \approx 0.5$. It is worth to stress here that the dispersion relation, and also the number of open channels as a function of energy above the band boundary, $N_{\text{open}}(|E| - \Delta/2)$ (see *supplementary information, section II*), is virtually unaffected by the increasing Δ . Therefore, the average transmission for an open channel near the band boundary decreases with Δ . This observation can be qualitatively understood by pointing out a peculiar (Mexican hat-like) shape of the dispersion relation for $\Delta > 0$ [31]. In the energy range $\Delta/2 < |E| < |U|/2$ there is a continuous crossover from zero transmission (occurring for $|E| < \Delta/2$) to a high-transmission range ($|E| > |U|/2$). As the width of such a crossover energy range, $(|U| - \Delta)/2$, increases monotonically with Δ , the continuity of $T(E)$ implies that the average transmission near $|E| \approx \Delta/2$ decreases with Δ .

For a bit more formal explanation, we need to refer the total transmission probability through an abrupt interface (see *supplementary information, section II*). For the incident wavefunction with the momentum parallel to the barrier (conserved during the scattering) $\hbar k_y$ (where $k_y = 2\pi q/W$ and $q = 0, \pm 1, \pm 2, \dots$ assuming the periodic boundary conditions) we have

$$T_{k_y} = \sum_{m,n} |t_n^m|^2 j_x(\psi_{II}^n) / j_x(\psi_I^m), \quad (20)$$

where $\{t_n^m\}$ is the 2×2 transmission matrix ($m, n = 1, 2$ are the subband indices) to be determined via the mode-matching, and $j_x(\psi_X^n)$ is the x -component of electric current for the wave function propagating in the direction of incidence, with $X = I, II$ indicating the side of a barrier. For $E = \epsilon + \Delta/2$ (with $0 < \epsilon \ll \Delta/2$) there are propagating modes in a weakly-doped area ($X = II$) with $n = 1$ (the lower subband) only; in the simplest case without trigonal warping ($t' = 0$) we find that the relevant current occurring in equation (20) scales as

$$j_x(\psi_{II}^1) \propto \sqrt{\epsilon/\Delta}. \quad (21)$$

The above allows us to expect that the full transmission scales as $T(E) = \sum_{k_y} T_{k_y} \propto \sqrt{\epsilon/\Delta}$ also for $t' \neq 0$, provided that the band gap is sufficiently large ($\Delta \gg E_L$, with $E_L = \frac{1}{4} t_{\perp} (t'/t_0)^2$ the Lifshitz energy). As the number of propagating modes is approximately Δ -independent, scaling roughly as $N_{\text{open}} \propto \sqrt{\epsilon}$, we can further predict that zero- (or low-) temperature conductance should follow the approximate scaling law

$$G(\mu) \propto (\mu - \Delta/2) / \sqrt{\Delta} \quad (\text{for } \mu \geq \Delta/2). \quad (22)$$

This expectation is further supported with the numerical data presented in figure 1(e).

An initial increase of ZT_{\max} with Δ for $0 < \Delta \ll \Delta_*$, also apparent in figures 4(c) and (d), can be understood by pointing out that the electronic and phononic parts of the thermal conductance are of the same order of magnitude ($K_{\text{el}} \sim K_{\text{ph}}$) in such a range. In consequence, an upper bound to ZT can be written as (up to the order of magnitude) $ZT \lesssim TGS^2/K_{\text{el}}$, allowing a rapid increase of ZT with Δ (see *supplementary information, section III*), until K_{el} (decreasing with Δ) is overruled by K_{ph} (Δ -independent).

In the remaining part of this section, we briefly discuss the possible influence of electron–electron interactions, neglected in our numerical analysis.

Several experimental works on free-standing BLG report an *intrinsic* (or spontaneous) band gap of $\Delta_{\text{int}}(T=0) \approx 1.5$ meV vanishing above the critical temperature $T_{\text{crit}} \approx 12$ K [32–34]. To the contrary, no signatures of an intrinsic band gap are reported for BLG in van der Waals heterostructures (VDWHs) [35], in which thermoelectric properties may be significantly enhanced due to the suppression of out-of-plane (ZA) vibrations. Possibly, the above-mentioned difference could be attributed to a modification of the effective dielectric constant due to the materials surrounding a BLG sample in VDWHs. In fact, a basic mean-field description, relating $\Delta_{\text{int}} > 0$ to the alternating spin order, allows one to expect that $\Delta_{\text{int}} \sim t_0 \exp(-\text{const.} \times t_0/U_{\text{eff}})$ (where $\text{const.} \sim 1$ is determined by the bandwidth), and thus a moderate decrease of the effective Hubbard repulsion (U_{eff}) strongly suppresses Δ_{int} ; see [36].

Although temperatures considered in this paper ($0 < T \leq 10$ K) are essentially lower than T_{crit} , we focus on the case with a bias between the layers $|U| \approx \Delta \sim 10$ – 100 meV, and much smaller Δ_{int} should not affect the physical properties under consideration.

Additionally, the maximal ZT appears near the bottom of the conduction band or the top of the valence band ($|\mu_{\text{max}}^{ZT}| \approx \Delta/2$), where one of the layers is close to the charge-neutrality, and thus one can expect the Coulomb-drag effects to be insignificant [37].

5. Concluding remarks

We have numerically investigated thermoelectric properties of large ballistic samples of electrostatically-gapped BLG. A logarithmic deviation of the maximal absolute thermopower from the Goldsmid–Sharp relation is identified and rationalized with the help of the step-function model for the transmission-energy dependence. In addition to the earlier findings that the trigonal warping term modifies the density of states [24] and transport properties [13] also for Fermi energies $\gg 1$ meV, we show here that signatures of trigonal warping may still be visible in thermoelectric characteristics for the band gaps as large as $\Delta \sim 100$ meV.

Next, the analysis is supplemented by determining the total (i.e. electronic and phononic) thermal conductance, making it possible to calculate the dimensionless figure of merit (ZT). The behavior of maximal ZT with the increasing gap can also be interpreted in terms of the step-function model, provided that we supplement the model with the scaling rule for the typical transmission probability for an open channel near the minimum of the conduction band (or the maximum of the valence band), which is $\propto \Delta^{-0.5}$ (for large Δ). This can be attributed to the Mexican-hat like shape of the dispersion relation.

Although some other two-dimensional systems with the Mexican-hat like (or *quartic*) [15] dispersion also show enhanced thermoelectric properties, two unique features of BLG are worth to stress: (i) the possibility of tuning both the chemical potential and the band gap in a wide range, and (ii) the ballistic scaling behavior of transport characteristics with a barrier width. It is also worth to stress that the value of $ZT > 1$ (or $ZT > 3$ in the absence of out-of-plane vibrations) is reached at $T = 1$ K for a moderate bandgap $\Delta \approx 10$ meV, corresponding to the electric field of ≈ 3 mV \AA^{-1} , making it possible to consider an experimental setup in which the spontaneous electric field from a specially-chosen substrate (e.g. ferroelectric) is employed to reduce the energy-consumption in comparison to a standard dual-gated setup [30].

High values of ZT at a 1 K temperature may not have practical device implications *per se*, however, we hope that scaling mechanisms identified in our work will help to find the best thermoelectric among graphene-based (and related) systems. The necessity to reduce the phononic part of the thermal conductance with a simultaneous increase of the maximal accessible band gap (possibly in a setup not involving an extra power supply to sustain the perpendicular electric field), further accompanied by some magnification of the electric-conductance step on the band boundary, strongly suggests to focus future studies on graphene-based van der Waals heterostructures.

Acknowledgments

We thank Romain Danneau and Bartłomiej Wiendlocha for discussions. The work was supported by the National Science Centre of Poland (NCN) via Grant No. 2014/14/E/ST3/00256. Computations were partly performed using the PL-Grid infrastructure.

Author contributions

DS and AR developed the code for a rectangular BLG sample, DS performed the computations for a rectangular BLG sample; G.R. developed the code for the system with abrupt interface and performed the computations; all authors were involved in analyzing the numerical data and writing the manuscript.

Additional information

Supplementary information accompanies this paper.

ORCID iDs

Adam Rycerz  <https://orcid.org/0000-0001-7873-0183>

References

- [1] Qiao Z, Tse W K, Jiang H, Yao Y and Niu Q 2011 Two-dimensional topological insulator state and topological phase transition in bilayer graphene *Phys. Rev. Lett.* **107** 256801
- [2] Maher P *et al* 2013 Evidence for a spin phase transition at charge neutrality in bilayer graphene *Nat. Phys.* **9** 154
- [3] Dean C T *et al* 2013 Hofstadter's butterfly and the fractal quantum Hall effect in Moiré superlattices *Nature* **497** 598
- [4] Ponomarenko L A *et al* 2013 Cloning of Dirac fermions in graphene superlattices *Nature* **497** 594
- [5] Cao Y *et al* 2018 Unconventional superconductivity in magic-angle graphene superlattices *Nature* **556** 43
- [6] Cao Y *et al* 2018 Correlated insulator behaviour at half-filling in magic-angle graphene superlattices *Nature* **556** 80
- [7] Yang L, Deslippe J, Park C H, Cohen M L and Louie S G 2009 Excitonic effects on the optical response of graphene and bilayer graphene *Phys. Rev. Lett.* **103** 186802
- [8] Bonaccorso F, Sun Z, Hasan T and Ferrari A C 2010 Graphene photonics and optoelectronics *Nat. Photon.* **4** 611
- [9] Grigorenko A N, Polini M and Novoselov K S 2012 Graphene plasmonics *Nat. Photon.* **6** 749
- [10] Wang C R *et al* 2011 Enhanced thermoelectric power in dual-gated bilayer graphene *Phys. Rev. Lett.* **107** 186602
- [11] Chien Y Y, Yuan H, Wang C R and Lee W L 2016 Thermoelectric power in bilayer graphene device with ionic liquid gating *Sci. Rep.* **6** 20402
- [12] Mahapatra P S, Sarkar K, Krishnamurthy H R, Mukerjee S and Ghosh A 2017 Seebeck coefficient of a single van der Waals junction in twisted bilayer graphene *Nano Lett.* **17** 6822
- [13] Suszalski D, Rut G and Rycerz A 2018 Lifshitz transition and thermoelectric properties of bilayer graphene *Phys. Rev. B* **97** 125403
- [14] Lee M J *et al* 2016 Thermoelectric materials by using two-dimensional materials with negative correlation between electrical and thermal conductivity *Nat. Commun.* **7** 12011
- [15] Sevinçli H 2017 Quartic dispersion, strong singularity, magnetic instability, and unique thermoelectric properties in two-dimensional hexagonal lattices of group-VA elements *Nano Lett.* **17** 2589
- [16] Qin D, Yan P, Ding G, Ge X, Song H and Gao G 2018 Monolayer PdSe₂: a promising two-dimensional thermoelectric material *Sci. Rep.* **8** 2764
- [17] Mahan G D and Sofo J O 1995 The best thermoelectric *Proc. Natl Acad. Sci. USA* **93** 7436
- [18] Kim H S, Liu W, Chen G, Chu C W and Ren Z 2015 Relationship between thermoelectric figure of merit and energy conversion efficiency *Proc. Natl Acad. Sci. USA* **112** 8205
- [19] Ioffe A F 1957 *Semiconductor Thermoelements and Thermoelectric Cooling* (London: Infosearch)
- [20] Cutler M and Mott N F 1969 Observation of Anderson Localization in an electron gas *Phys. Rev.* **181** 1336
- [21] Rut G and Rycerz A 2014 Minimal conductivity and signatures of quantum criticality in ballistic graphene bilayer *Europhys. Lett.* **107** 47005
- [22] Hao L and Lee T K 2010 Thermopower of gapped bilayer graphene *Phys. Rev. B* **81** 165445
- [23] Goldsmid H J and Sharp J W 1999 Estimation of the thermal band gap of a semiconductor from Seebeck measurements *J. Electron. Mater.* **28** 869
- [24] McCann E and Koshino M 2013 The electronic properties of bilayer graphene *Rep. Prog. Phys.* **76** 056503
- [25] Kuzmenko A B, Crassee I, van der Marel D, Blake P and Novoselov K S 2009 Determination of the gate-tunable band gap and tight-binding parameters in bilayer graphene using infrared spectroscopy *Phys. Rev. B* **80** 165406
- [26] Landauer R 1957 Spatial variation of currents and fields due to localized scatterers in metallic conduction *IBM J. Res. Dev.* **1** 233
- [27] Büttiker M, Imry Y, Landauer R and Pinhas S 1985 Generalized many-channel conductance formula with application to small rings *Phys. Rev. B* **31** 6207
- [28] Esfarjani K and Zebarjadi M 2006 Thermoelectric properties of a nanocontact made of two-capped single-wall carbon nanotubes calculated within the tight-binding approximation *Phys. Rev. B* **73** 085406
- [29] Alofi A and Srivastava G P 2013 Thermal conductivity of graphene and graphite *Phys. Rev. B* **87** 115421
- [30] Zhang Y, Tang T-T, Girit C, Hao Z, Martin M C, Zettl A, Crommie M F, Shen Y R and Wang F 2009 Direct observation of a widely tunable bandgap in bilayer graphene *Nature* **429** 820
- [31] McCann E 2006 Asymmetry gap in the electronic band structure of bilayer graphene *Phys. Rev. B* **74** 161403
- [32] Yankowitz M *et al* 2014 Band structure mapping of bilayer graphene via quasiparticle scattering *APL Mater.* **2** 092503
- [33] Grushina A L, Ki D-K, Koshino M, Nicolet A L A, Faugeras C, McCann E, Potemski M and Morpurgo A F 2015 Insulating state in tetralayers reveals an even-odd interaction effect in multilayer graphene *Nat. Commun.* **6** 6419
- [34] Nam Y, Ki D-K, Koshino M, McCann E and Morpurgo A F 2016 Interaction-induced insulating state in thick multilayer graphene *2D Mater.* **3** 045014
- [35] Kraft R *et al* 2018 Tailoring supercurrent confinement in graphene bilayer weak links *Nat. Commun.* **9** 1722
- [36] Hirsch J E 1985 Two-dimensional Hubbard model: numerical simulation study *Phys. Rev. B* **31** 4403
- [37] Gorbachev R V *et al* 2012 Strong Coulomb drag and broken symmetry in double-layer graphene *Nat. Phys.* **8** 896

Supplementary Information

Thermoelectric properties of gapped bilayer graphene

Dominik Suszalski, Grzegorz Rut, and Adam Rycerz

Marian Smoluchowski Institute of Physics, Jagiellonian University, Łojasiewicza 11, PL-30348 Kraków, Poland

(Dated: June 15, 2019)

I. DISPERSION RELATION, THE ACTUAL BANDGAP, AND DOPING

The Hamiltonian H given by Eq. (4) in the main text leads to the dispersion relation for electrons [1]

$$E_{\pm}^{(e)}(\mathbf{k}) = \left[\frac{1}{2}t_{\perp}^2 + \frac{1}{4}U^2 + \hbar^2 \left(v_F^2 + \frac{1}{2}v_3^2 \right) k^2 \pm \sqrt{\Gamma(\mathbf{k})} \right]^{1/2},$$

$$\text{with } \Gamma(\mathbf{k}) = \frac{1}{4} \left(t_{\perp}^2 - \hbar^2 v_3^2 k^2 \right)^2 + \hbar^2 v_F^2 k^2 \left(t_{\perp}^2 + U^2 + \hbar^2 v_3^2 k^2 \right) + 2\xi t_{\perp} \hbar^3 v_3 v_F^2 k^3 \cos 3\varphi, \quad (\text{S1})$$

where \pm refers to the upper/lower band, $\mathbf{k} \equiv (k_x, k_y)$ is the wavevector, with $\mathbf{k} = 0$ referring to the K or K' point (marked by $\xi = 1$ or $\xi = -1$, respectively), $k \equiv |\mathbf{k}|$, and the angle $0 \leq \varphi < 2\pi$ is the argument $\arg z$ of a complex number $z = k_x + ik_y$. For holes, we simply have $E_{\pm}^{(h)}(\mathbf{k}) = -E_{\pm}^{(e)}(\mathbf{k})$. This is a consequence of the combined particle-hole-reflection symmetry, which is preserved as we have neglected the next-nearest neighbor intralayer hopping (t_2). The precise value of t_2 ($\sim t_{\perp}$) is difficult to determine for BLG [2]; however, its effects are insignificant when discussing the band structure for $|E| \ll t_{\perp}$.

The value of a band gap Δ can be determined numerically via

$$\frac{\Delta}{2} = \min E_{-}^{(e)}(\mathbf{k}) = -\max E_{-}^{(h)}(\mathbf{k}). \quad (\text{S2})$$

For $v_3 \neq 0$ the band gap can be approximated as follows

$$\Delta \approx \Delta_0 \left(1 - \Delta_0 \frac{\sqrt{2}v_3}{t_{\perp}v_F} - \Delta_0^2 \frac{5v_3^2}{4U^2v_F^2} \right), \quad \text{with } \Delta_0 = \frac{|U|t_{\perp}}{\sqrt{U^2 + t_{\perp}^2}} \quad (\text{S3})$$

(Δ_0 is the exact value of a gap in the absence of trigonal warping). Although its accuracy is better than 0.5% for $t' = 0.3$ eV and $|U| \leq 300$ meV, the approximating Eq. (S3) is insufficient to present the numerical data in the energy scale used in Fig. 1(e) in the main text; instead, we have determined Δ for a given U directly by performing the minimization in Eq. (S2) numerically.

In general, $\Delta < |U|$ for $|U| > 0$, leading to a peculiar (the Mexican hat-like) profile of the dispersion relation for $E_{-}^{(e)}(\mathbf{k})$ and $E_{-}^{(h)}(\mathbf{k})$ bands in the presence of a gap (see the second paper in Ref. [1]).

The dispersion relation given by Eq. (S1) also allows us to define the density of states at the Fermi energy (E_F) in a compact form

$$\rho(E_F) \equiv \rho^{(e)}(E_F) + \rho^{(h)}(E_F) = \frac{1}{\pi^2} \sum_{\substack{c=e,h \\ m=\pm}} \left| \frac{\partial}{\partial E} \mathcal{A}_m^{(c)}(E) \right|_{E=E_F}, \quad (\text{S4})$$

where we took into account spin and valley degeneracies ($g_s = g_v = 2$) and $\mathcal{A}_{\pm}^{(e,h)}(E_F)$ denotes the area bounded by the Fermi surface in the (k_x, k_y) plane. (In case $E = E_F$ is beyond the energy range of a given band, we put $\mathcal{A}_m^{(c)}(E) = 0$.) In particular, for $v_3 = 0$ and $\max(0, |E_F| - \Delta/2) \ll t_{\perp}$, we have

$$\rho(E_F) \approx \frac{t_{\perp}}{\pi(\hbar v_F)^2} \Theta(|E_F| - \Delta/2), \quad (\text{S5})$$

with $\Theta(E)$ being the Heaviside step function. The prefactor in Eq. (S5) is often written in a form $2m_{\text{eff}}/(\pi^2\hbar)$, with the effective mass $m_{\text{eff}} \approx 0.033 m_e$ (where m_e is the free-electron mass) coinciding with the standard cyclotronic mass $m_C(E_F) = (\pi\hbar^2/2)\rho(E_F)$. Integrating Eq. (S5) over the energy, we obtain the physical carrier concentration (or *doping*) given by Eq. (5) in the main text.

At finite temperatures ($T > 0$), the *effective carrier concentration* can be defined via its relation to the Hall resistance, namely $R_H = -1/(en_{\text{eff}})$ (with the electron charge $-e$), leading to

$$n_{\text{eff}} = n_e - n_h = \int_0^\infty dE \rho(E) f_{\text{FD}}(\mu, T, E) - \int_{-\infty}^0 dE \rho(E) [1 - f_{\text{FD}}(\mu, T, E)], \quad (\text{S6})$$

where n_e (n_h) is the concentration of electrons (holes) and $f_{\text{FD}}(\mu, T, E) = 1/[\exp((E-\mu)/k_B T) + 1]$ is the Fermi-Dirac distribution function for a given electrochemical potential μ .

II. TRANSMISSION PROBABILITY

A. A semi-infinite system in BLG

In the case of an abrupt potential barrier separating weakly- and heavily doped regions (see Fig. 1(a) in the main text) we start from the substitution in the Hamiltonian (see Eq. (4) in the main text) $\mathbf{p} \rightarrow \mathbf{p} + e\mathbf{A}$, with a vector potential $\mathbf{A} = (A_x, A_y)$ (not further specified, since it is disregarded in the forthcoming calculations). The i -th component of the current (with $i = x$ or y) corresponding to the Hamiltonian H reads, for the K valley,

$$j_i(\psi) = \psi^\dagger \cdot \left. \frac{\partial H}{\partial A_i} \right|_{A_i \rightarrow 0} \cdot \psi \quad \text{with} \quad \left. \frac{\partial H}{\partial A_i} \right|_{A_i \rightarrow 0} = ev_F \begin{pmatrix} 0 & 1 & 0 & 0 \\ 1 & 0 & 0 & \nu \\ 0 & 0 & 0 & 1 \\ 0 & \nu & 1 & 0 \end{pmatrix}, \quad (\text{S7})$$

where we have defined a dimensionless parameter $\nu = v_3/v_F$.

Next, the transmission probability can be found by simple mode-matching of wavefunctions in the heavily- and weakly-doped regions. Although deriving the corresponding functions is not a challenging task, they cannot be presented in a closed form. Below, we briefly present a procedure for finding the solutions corresponding to waves moving in desired directions (i.e., to the left or to the right):

(i) The wavefunctions satisfying the Dirac equation $H\psi(x, y) = E\psi(x, y)$ can be found algebraically in to the momentum representation, $\pi_i = \hbar k_i$. The general solution has a form of a spinor $\psi(x, y) = \exp[i(k_x x + k_y y)](\psi_1, \psi_2, \psi_3, \psi_4)^T$. There are four independent solutions, each corresponding to a different value of k_x (for a system with periodic boundary conditions the transverse wave number $k_y = 2\pi n/W$, with $n = 0, \pm 1, \pm 2, \dots$, and W being the width of the system).

(ii) In order to determine the corresponding direction of propagation for a given solution of the Dirac equation, one needs to follow the subsequent two-step procedure. *First*, one has to check a sign of the current employing Eq. (S7). The positive (*or* negative) sign indicates the transmitted/incoming (*or* reflected) wave. *Second*, when dealing with the wavefunction carrying zero current, it is important to check the sign of the imaginary part of k_x . Positive (*or* negative) $\text{Im}(k_x)$ corresponds to a solution decaying exponentially to the right (*or* to the left). When discussing the transmission through a single barrier separating the heavily- and weakly doped regions we can, however, limit ourselves to the solutions with real $k_x \neq 0$ (which are *normalizable* with respect to the carried current). Out of four solutions of the Dirac equation, there are at most two carrying a positive or negative current.

(iii) Subsequent calculation of the transmission probability becomes similar to the one usually performed for systems containing a sample area between two highly-conducting contacts. In the contact region, here modelled as heavily-doped bilayer graphene (for $x < 0$) the wavefunction takes a form

$$\psi_I(x) = \psi_{R,I}^{1(2)}(x) + r_1^{1(2)}\psi_{L,I}^1(x) + r_2^{1(2)}\psi_{L,I}^2(x), \quad (\text{S8})$$

while the wavefunction in the weakly-doped sample area ($x > 0$) reads

$$\psi_{II}(x) = t_1^{1(2)}\psi_{R,II}^1(x) + t_2^{1(2)}\psi_{R,II}^2(x). \quad (\text{S9})$$

The lower indexes, R and L , refer to the waves moving to the right ($j_x > 0$) and to the left ($j_x < 0$), respectively. The upper indexes, $1(2)$, correspond to the two subbands. The parameters $r_1^{1(2)}$, $r_2^{1(2)}$, $t_1^{1(2)}$, $t_2^{1(2)}$ are closely related to the reflection and transmission probabilities and can be calculated via mode-matching at $x = 0$, namely: $\psi_I(0) = \psi_{II}(0)$. The final transmission probability is given by a sum over the all possible current ratios

$$T_{k_y} = \sum_{m,n} |t_n^m|^2 j_x(\psi_{R,II}^n) / j_x(\psi_{R,I}^m). \quad (\text{S10})$$

The comparison of the Landauer-Büttiker conductance, following from Eq. (S10), with the number of open channels, which is determined solely by the dispersion relation given by Eq. (S1), is presented in Fig. 1.

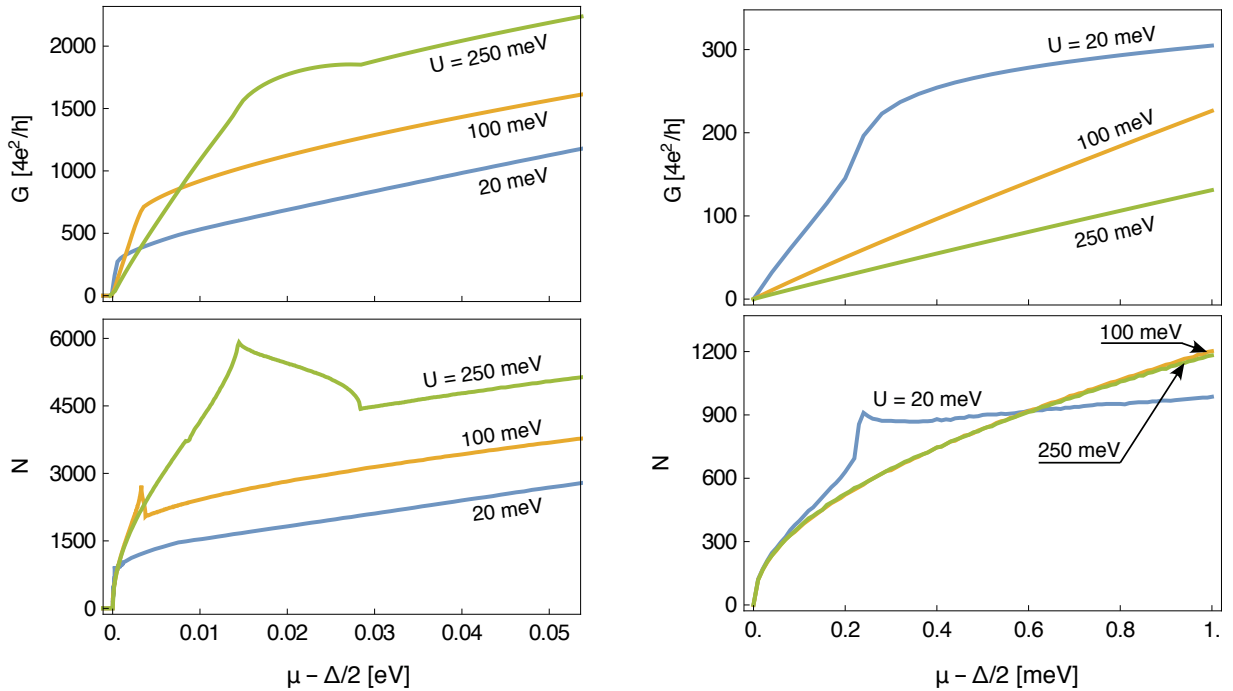


FIG. 1: The conductance (top) and the number of open channels (bottom) for an abrupt potential barrier in BLG, corresponding to the width $W = 10^3 l_{\perp} = 1.77 \mu\text{m}$ and the trigonal-warping strength $t' = 0.3 \text{ eV}$, displayed as functions of the chemical potential. The electrostatic bias between the layers (U) is specified for each line. Right panels are zoom-ins, for low values of $\mu - \Delta/2$, for the data shown in left panels.

B. Mode-matching for a rectangular sample

In order to determine the transmission probability at a given energy: $T(E)$, for a rectangular sample attached to the two heavily-doped regions (the *leads*), we employ the computational scheme similar to the presented in Ref. [3]. However, at finite-precision arithmetics, the mode-matching equations become ill-defined for sufficiently large L and μ , since they contain both exponentially-growing and exponentially-decaying coefficients. This difficulty can be overcome by dividing the sample area ($0 < x < L$) into N_{div} consecutive, equally-long parts, and then matching the wave functions for all $(N_{\text{div}}+1)$ interfaces. Typically, using the double-precision arithmetic, we put $N_{\text{div}} = 20$ for $L = W/20 = 10^4 l_{\perp}$. The necessary number of different transverse momenta $k_y = 2\pi q/W$ (where $q = 0, \pm 1, \pm 2, \dots, \pm q_{\text{max}}$) varies with the energy E , scaling roughly as $2q_{\text{max}}+1 \propto \sqrt{|E| - \Delta/2}$ (for $|E| > \Delta/2$). For instance, to determine $T(E)$ with a 10-digit accuracy for $\Delta = U = 0$ we took: $1955 \leq 2q_{\text{max}}+1 \leq 8149$, with the lower (upper) value corresponding to $E = 0$ and $t' = 0.1 \text{ eV}$ ($E = 2 \text{ meV}$ and $t' = 0.35 \text{ eV}$).

III. SIMPLIFIED MODELS FOR TRANSMISSION-ENERGY DEPENDENCE

A. Basic definitions

For sufficiently large Δ , transmission spectra $T(E)$ for either the single-barrier or the rectangular-sample case show essentially abrupt switching near $E \approx \Delta/2$, with some secondary details becoming irrelevant when calculating thermoelectric properties at nonzero temperature. Therefore, one can consider a family of simplified models for transmission-energy dependence, as given by Eq. (13) in the main text

$$T^{(\alpha)}(E) = \mathcal{C}^{(\alpha)}(\Delta) \times \begin{cases} \delta(E - \frac{1}{2}\Delta) + \delta(E + \frac{1}{2}\Delta) & \text{for } \alpha = 0 \\ \Theta(|E| - \frac{1}{2}\Delta) (|E| - \frac{1}{2}\Delta)^{\alpha-1} & \text{for } \alpha > 0 \end{cases}, \quad (\text{S11})$$

with $\delta(x)$ being the Dirac delta function, and $\Theta(x)$ being the Heaviside step function. A compact form of Eq. (S11) implies that the prefactor $\mathcal{C}^{(\alpha)}(\Delta)$ is dimensionless for $\alpha = 1$ only; in general, we have $[\mathcal{C}^{(\alpha)}(\Delta)] = \text{eV}^{-\alpha+1}$ (for $\alpha \geq 0$).

The cumulants L_n , determining the thermoelectric properties via Eqs. (8)–(10) in the main text, are well-defined for the transmission-energy dependence of the form $T^{(\alpha)}(E)$ (S11) with arbitrary $\alpha \geq 0$. Substituting the derivative of the Fermi-Dirac distribution function

$$-\frac{\partial f_{\text{FD}}}{\partial E} = \frac{1}{4 \cosh^2[(E - \mu)/2k_B T]} \cdot \frac{1}{k_B T}, \quad (\text{S12})$$

and introducing the dimensionless variables

$$t = \frac{E}{k_B T}, \quad v = \frac{\mu}{k_B T}, \quad u = \frac{\Delta}{2k_B T}, \quad (\text{S13})$$

we can write

$$L_n^{(\alpha)} = \frac{g_s g_v}{h} \frac{(k_B T)^n}{4} \int dt (t-v)^n T^{(\alpha)}(t \cdot k_B T) \cosh^{-2}\left(\frac{t-v}{2}\right) \equiv \frac{g_s g_v}{h} (k_B T)^{n+\alpha-1} \mathcal{C}^{(\alpha)}(\Delta) \mathcal{L}_n^{(\alpha)}, \quad (\text{S14})$$

where the last factor ($\mathcal{L}_n^{(\alpha)}$) is dimensionless and \mathcal{C} -independent. Explicitly, we obtain

$$\mathcal{L}_n^{(0)} = \frac{1}{4}(u-v)^n \cosh^{-2}\left(\frac{u-v}{2}\right) + \frac{1}{4}(-u-v)^n \cosh^{-2}\left(\frac{-u-v}{2}\right), \quad (\text{S15})$$

$$\mathcal{L}_n^{(\alpha)} = \frac{1}{4} \int_y^\infty dt (t-v)^n (t-u)^{\alpha-1} \cosh^{-2}\left(\frac{t-v}{2}\right) + \frac{1}{4} \int_{-\infty}^{-y} dt (t-v)^n (-t-u)^{\alpha-1} \cosh^{-2}\left(\frac{t-v}{2}\right) \quad (\alpha > 0). \quad (\text{S16})$$

B. Maximal absolute thermopower

Subsequent approximations, performed when calculating $\mathcal{L}_n^{(\alpha)}$ for $y \gg 1$, depend on mutual relation between x and y . In particular, for the Seebeck coefficient, we first rewrite Eq. (9) from the main text as follows

$$S = \frac{k_B}{e} \mathcal{L}_1^{(\alpha)} / \mathcal{L}_0^{(\alpha)}. \quad (\text{S17})$$

Since the maximal $|S|$ is expected for $|v| \ll u$, we can employ the approximation

$$\frac{1}{4} \cosh^{-2}\left(\frac{t-v}{2}\right) \approx \begin{cases} e^{-t+v} & \text{for } u < t < \infty, \\ e^{t-v} & \text{for } -\infty < t < -u, \end{cases} \quad (\text{S18})$$

(valid for $u \pm v \gg 1$), in order to get closed-form approximating expressions for the first three cumulants

$$\mathcal{L}_0^{(\alpha)} \approx e^{v-u} + e^{-v-u}, \quad (\text{S19})$$

$$\mathcal{L}_1^{(\alpha)} \approx e^{v-u}(-v+u+\alpha) - e^{-v-u}(v+u+\alpha), \quad (\text{S20})$$

$$\mathcal{L}_2^{(\alpha)} \approx e^{v-u}[(v-u)(v-u-2\alpha) + \alpha(\alpha+1)] + e^{-v-u}[(v+u)(v+u+2\alpha) + \alpha(\alpha+1)]. \quad (\text{S21})$$

The right-hand side of Eq. (S17) can now be approximated by

$$S \approx \frac{k_B}{e} [(u+\alpha) \tanh v - v], \quad (\text{S22})$$

with the maximal absolute value

$$|S|_{\text{max}} (k_B/e)^{-1} \approx \sqrt{(u+\alpha)(u+\alpha-1)} - \ln(\sqrt{u+\alpha} + \sqrt{u+\alpha-1}), \quad (\text{S23})$$

appearing for

$$v|_{\text{max}}^{|S|} \approx \pm \ln(\sqrt{u+\alpha-1} + \sqrt{u+\alpha}). \quad (\text{S24})$$

These are Eqs. (14) and (15) in the main text.

C. Thermoelectric figure of merit (ZT) for $T \rightarrow 0$

Similarly, neglecting the phononic part of the thermal conductivity (or, equivalently, taking the $T \rightarrow 0$ limit) we can express the thermoelectric figure of merit as follows

$$ZT(T \rightarrow 0) = ZT_{\text{el}} \equiv \frac{GS^2T}{K_{\text{el}}} = \frac{\left(\mathcal{L}_1^{(\alpha)}\right)^2}{\mathcal{L}_0^{(\alpha)}\mathcal{L}_2^{(\alpha)} - \left(\mathcal{L}_1^{(\alpha)}\right)^2}. \quad (\text{S25})$$

This time, the approximation of Eqs. (S19)–(S21) does not lead to closed-form expressions for $ZT_{\text{el,max}}^{(\alpha)}$; least-square fitting of power-law formulas for $10 \leq u \leq 30$ brought us to

$$ZT_{\text{el,max}}^{(\alpha=1)} \approx 0.192(2) \cdot u^{2.374(3)}, \quad ZT_{\text{el,max}}^{(\alpha=2)} \approx 0.1809(4) \cdot u^{2.217(1)}, \quad (\text{S26})$$

with standard deviations for the last digit specified by numbers in parentheses. For $T > 0$, we generally have $ZT < ZT_{\text{el,max}}$, and the unlimited increase of ZT with u is not observed; however, we have $ZT \sim ZT_{\text{el,max}}^{(\alpha=1)}$ (up to the order of magnitude) for $T = 1$ K and $u \sim 1$.

D. ZT at finite temperatures and the power factor

In contrast with the $T \rightarrow 0$ limit discussed above, for any $T > 0$ there exists a value of Δ , above which the electronic part of the thermal conductance is suppressed ($K_{\text{ph}} > K_{\text{el}}$). In turn, for $u \gg 1$ (being equivalent to $\Delta \gg k_B T > 0$), one can expect that the figure of merit

$$ZT(\Delta \gg k_B T > 0) \approx ZT_{\text{ph}} \equiv \frac{GS^2T}{K_{\text{ph}}} = \frac{T}{K_{\text{ph}}(T)} \frac{L_1^2}{T^2 L_0}, \quad (\text{S27})$$

where we have emphasised that the phononic part of thermal conductance depends only on temperature, $K_{\text{ph}} = K_{\text{ph}}(T)$. Subsequently, when looking for the maximal ZT as a function of the chemical potential μ at a fixed T , one need to focus on the maximal power factor which is, for the transmission-energy dependence of the form $T^{(\alpha)}(E)$ (S11), given by

$$(GS^2)_{\text{max}}^{(\alpha)} = \frac{g_s g_v}{h} k_B^2 (k_B T)^{\alpha-1} \mathcal{C}^{(\alpha)}(\Delta) \left[\left(\mathcal{L}_1^{(\alpha)}\right)^2 / \mathcal{L}_0^{(\alpha)} \right]_{\text{max}}. \quad (\text{S28})$$

Defining $\mathcal{M}_{\text{max}}^{(\alpha)} = \left[\left(\mathcal{L}_1^{(\alpha)}\right)^2 / \mathcal{L}_0^{(\alpha)} \right]_{\text{max}}$, we restore the structure of Eq. (19) in the main text.

As the maximal ZT corresponds to $v_{\text{max}}^{ZT} \sim u$, the approximating Eq. (S18) cannot be applied in this case. Instead, for $u \gg 1$ we have

$$\mathcal{L}_n^{(\alpha)} \equiv \mathcal{L}_{n,+}^{(\alpha)} + \mathcal{L}_{n,-}^{(\alpha)} \approx \mathcal{L}_{n,+}^{(\alpha)}, \quad (\text{S29})$$

where the parts $\mathcal{L}_{n,+}^{(\alpha)}$ and $\mathcal{L}_{n,-}^{(\alpha)}$ are the integrals over $t > 0$ and $t < 0$ (respectively) in Eq. (S16). The results are

$$\mathcal{M}_{\text{max}}^{(\alpha=1)} \approx 1.265, \quad \mathcal{M}_{\text{max}}^{(\alpha=2)} \approx 4.060, \quad (\text{S30})$$

corresponding to

$$v_{\text{max}}^{ZT} \approx u - 1.145 \text{ for } \alpha = 1, \quad \text{or} \quad v_{\text{max}}^{ZT} \approx u + 0.668 \text{ for } \alpha = 2. \quad (\text{S31})$$

The above Eqs. (S30) and (S31) are equivalent to Eqs. (16) and (17) in the main text.

IV. PHONONIC PART OF THE THERMAL CONDUCTIVITY

A. Brief overview

Here we overview the Callaway method [4], further modified by Alofi and Srivastava [5, 6] in order to determine the phononic part of the thermal conductance K_{ph} ; see Eq. (12) in the main text. For the sake of consistency with

TABLE I: Parameters used in our numerical calculations. Most of the values are taken from Refs. [8, 9].

Symbol	Numerical value	Units
L	1.77×10^{-5}	m
d	3.3544×10^{-10}	m
V_m	5.3×10^{-6}	m ³ /mol
v_l	2.16×10^4	m/s
v_t	1.4×10^4	m/s
b	3.13×10^{-7}	m ² /s
ζ	946091^a or 0^b	m ² /s ²
B_N	3.18×10^{-25}	s K ⁻³
B_U	4.77×10^{-25}	s K ⁻³
α	3	–
A_d	0.00169	–
ω_{LA}^D	472.6	THz
ω_{TA}^D	306.4	THz
ω_{ZA}^D	149.9	THz
$\bar{\Theta}$	2365.4	K

^aBLG; ^bMLG.

the notation of Refs. [5, 6], let us define the *thermal conductivity* for a rectangular BLG sample

$$\kappa_{\text{el,ph}} = \frac{L}{2d} \frac{K_{\text{el,ph}}}{W}, \quad (\text{S32})$$

with el (ph) denoting the electronic (phononic) part, L and W the sample length and width (respectively), and $d = 0.335$ nm the separation between graphene layers. (For the remaining model parameters, see Table I.)

The phononic part of the thermal conductivity — in the remaining of this section simply denoted as $\kappa \equiv \kappa_{\text{ph}}$ — can be calculated in the two steps, earlier presented in Ref. [6]:

In the first step, sufficient for the case of low temperatures, one can simply use the Debye approximation, in which a relevant element of the conductivity tensor reads

$$\kappa_{x,x}^D = \frac{\hbar^2 d}{2V_m k_B T^2} \sum_p \int_0^{\omega_{D,p}} d\omega \omega^2 v_p^2 \tau_p D_p(\omega) n(\omega) [n(\omega) + 1], \quad (\text{S33})$$

where V_m ($= 5.3 \times 10^{-6}$ m³/mol) is the molar volume, $n(\omega)$ is the Bose-Einstein distribution function, $\omega_{D,p}$ is the Debye frequency (with the index p labeling phonon polarization, $p = LA, TA, \text{ or } ZA$; the corresponding phonon frequencies are listed in Table I). The relaxation time τ_p , group velocity v_p and density of states $D_p(\omega)$ are defined in next three subsections.

The second step, necessary at higher temperatures, requires one also to calculate a correction originating from the momentum conservation in the three-phonon processes of the type N . Such a correction reads

$$\kappa_{x,x}^{\text{corr}} = \frac{\hbar^2 d}{2V_m k_B T^2} \sum_p \frac{\left\{ \int_0^{\omega_{D,p}} d\omega \omega^2 v_p^2 \tau_p \tau_N^{-1} D_p(\omega) n(\omega) [n(\omega) + 1] \right\}^2}{\int_0^{\omega_{D,p}} d\omega \omega^2 v_p^2 \tau_p \tau_N^{-1} (1 - \tau_p \tau_N^{-1}) D_p(\omega) n(\omega) [n(\omega) + 1]}, \quad (\text{S34})$$

where $\tau_N = B_N \omega^2 T^3$ (here $B_N = 3.18 \times 10^{-25}$ s K⁻³ is a parameter fitted to the experimental data) denotes the relaxation time for three-phonon processes of the type N . The prefactor $1/2$, in both $\kappa_{x,x}^D$ and $\kappa_{x,x}^{\text{corr}}$, originates from averaging the group velocity over possible directions (we focus here on the in-plane heat transfer, see Ref. [7]).

B. Relaxation times

We take into account the three main sources of the phonon scattering: boundaries (index bs), point defects and isotopes (pd), and three-phonon scattering processes (anh). Assuming that these mechanisms are mutually independent,

we employ the Matthiessen rule to write down the formula for the total relaxation time τ_p :

$$\tau_p^{-1} = \tau_{p,bs}^{-1} + \tau_{p,pd}^{-1} + \tau_{p,anh}^{-1}. \quad (\text{S35})$$

The elements on the right-hand side of Eq. (S35) are given by:

$$\tau_{p,bs}^{-1} = v_p/L,$$

where L is the length of the system [8], v_p is the group velocity for phonons of the polarization p ,

$$\tau_{p,pd}^{-1} = \frac{2\pi}{\omega_{D,p}^2} \omega^3 A_d,$$

where $\omega_{D,p}$ is the Debye frequency for the polarization p , A_d is a parameter quantifying the concentration of impurities (i.e., point defects or C^{13} atoms), and

$$\tau_{p,anh}^{-1} = \{B_N + B_U \exp[-\bar{\Theta}/(\alpha T)]\} \omega^2 T^3,$$

with the parameters $B_U = 4.77 \times 10^{-25} \text{ s K}^{-3}$ and $B_N = 3.18 \times 10^{-25} \text{ s K}^{-3}$ (adjusted to match the results of Ref. [5]), $\alpha = 3$, and $\bar{\Theta} = 2365.4 \text{ K}$ being the Debye temperature averaged over the polarizations $p = LA, TA, ZA$.

C. Group velocities

The group velocity v_p is defined as a derivative of the frequency ω_p over the wave vector q ,

$$v_p = \frac{\partial \omega_p}{\partial q}. \quad (\text{S36})$$

In the case of monolayer graphene, group velocities for acoustic phonons are given by

$$v_{LA}^{MLG} = v_l, \quad (\text{S37})$$

$$v_{TA}^{MLG} = v_t, \quad (\text{S38})$$

$$v_{ZA}^{MLG} = 2\sqrt{b\omega_{ZA}}, \quad (\text{S39})$$

where $v_l = 2.16 \times 10^4 \text{ m/s}$, $v_t = 1.4 \times 10^4 \text{ m/s}$, and $b = 3.13 \times 10^{-7} \text{ m}^2/\text{s}$. In the case of bilayer graphene, it becomes necessary to take the coupling between the layers into account. This alters only the expression for v_{ZA} , leading to

$$v_{LA}^{BLG} = v_l, \quad (\text{S40})$$

$$v_{TA}^{BLG} = v_t, \quad (\text{S41})$$

$$v_{ZA}^{BLG} = \gamma \sqrt{\gamma - \zeta} \left(\sqrt{2} \omega_{ZA} b \right)^{-1}, \quad (\text{S42})$$

where $\gamma = \sqrt{\zeta^2 + (2b\omega)^2}$, and $\zeta = 946091 \text{ m}^2/\text{s}$ is a parameter quantifying the coupling between the layers. Taking the $\zeta \rightarrow 0$ limit, we obtain the expression for decoupled layers. In such a case, group velocities for monolayer (MLG) and bilayer graphene (BLG) are the same.

D. Phononic density of states

In the case of LA or TA polarization, the density of states (DOS) reads

$$D_p(\omega) = \begin{cases} \arcsin(\omega/\omega_z) (V_m/d) \omega / (\pi v_p)^2, & \text{if } \omega \leq \omega_z, \\ (V_m/d) \omega / (2\pi v_p^2), & \text{if } \omega > \omega_z, \end{cases} \quad (\text{S43})$$

where $\omega_z = 5.8 \text{ THz}$ for BLG (or $\omega_z = 0$ for MLG). In the case of ZA polarization, we have

$$D_{ZA}(\omega) = \begin{cases} (V_m/d) \omega / (2\pi^2 b \omega'_z) \int_0^{\arcsin(2b\omega/\gamma)} \left\{ 1 - [\gamma \sin(\phi) / (2b\omega'_z)]^2 \right\}^{-1/2} d\phi, & \text{if } \omega \leq \omega'_z, \\ (V_m/d) \omega / (\pi^2 \gamma) \int_0^{\pi/2} \left\{ 1 - [2b\omega'_z \sin(\phi) / \gamma]^2 \right\}^{-1/2} d\phi, & \text{if } \omega > \omega'_z, \end{cases} \quad (\text{S44})$$

where $\omega'_z = 14.48 \text{ THz}$ for BLG (or $\omega'_z = 0$ for MLG).

E. An abrupt interface

In the limit of $L \rightarrow 0$, our model of thermal conductivity is noticeably simplified: The three-phonon scattering processes, as well as the contributions from impurities and boundaries, become irrelevant (namely, we can put $\tau_p^{-1} \rightarrow \tau_{p,bs}^{-1}$, $\tau_{p,pd}^{-1} \rightarrow 0$, and $\tau_{p,anh}^{-1} \rightarrow 0$ in Eq. (S35)). In turn, Eq. (S33) simplifies to

$$\kappa_{x,x}^0 = \frac{\hbar^2 L d}{2V_m k_B T^2} \sum_p \int_0^{\omega_p^D} d\omega \omega^2 v_p D_p(\omega) n(\omega) [n(\omega) + 1], \quad (\text{S45})$$

showing an explicit linear dependence of the thermal conductivity on the length L , and leading to a finite thermal conductance per unit width, $K_{\text{ph}}/W = (2d/L)\kappa_{x,x}^0$ [see also Eq. (S32)].

-
- [1] E. McCann and V.I. Fal'ko, Phys. Rev. Lett. **96**, 086805 (2006); E. McCann, Phys. Rev. B **74**, 161403(R) (2006).
 - [2] E. McCann and M. Koshino, Rep. Prog. Phys. **76**, 056503 (2013).
 - [3] G. Rut and A. Rycerz, Europhys. Lett. **107**, 47005 (2014).
 - [4] J. Callaway, Phys. Rev. **113**, 1046 (1959).
 - [5] A. Alofi and G.P. Srivastava, Phys. Rev. B **87**, 115421 (2013); A. Alofi and G.P. Srivastava, Appl. Phys. Lett. **104**, 031903 (2014).
 - [6] A. Alofi, *Theory of Phonon Thermal Transport in Graphene and Graphite*, Ph.D. Thesis, University of Exeter, 2014; <http://hdl.handle.net/10871/15687>.
 - [7] P.G. Klemens, Thermal Conductivity **22**, 365–365 (1993).
 - [8] J. Callaway, *Quantum theory of the solid state*, Academic Press, San Diego, 2013.
 - [9] T. Nihira and T. Iwata, Phys. Rev. B **68**, 134305 (2005).



PAPER

OPEN ACCESS

RECEIVED

4 September 2019

REVISED

1 October 2019

ACCEPTED FOR PUBLICATION

23 October 2019

PUBLISHED

21 November 2019

Original content from this work may be used under the terms of the [Creative Commons Attribution 3.0 licence](#).

Any further distribution of this work must maintain attribution to the author(s) and the title of the work, journal citation and DOI.



Mesoscopic valley filter in graphene Corbino disk containing a p–n junction

Dominik Suszalski, Grzegorz Rut and Adam Rycerz¹

Marian Smoluchowski Institute of Physics, Jagiellonian University, Łojasiewicza 11, PL–30348 Krakow, Poland

¹ Author to whom any correspondence should be addressed.E-mail: rycerz@th.if.uj.edu.pl**Keywords:** valleytronics, graphene, quantum transport, quantum Hall effect

Abstract

The Corbino geometry allows one to investigate the propagation of electric current along a p–n interface in ballistic graphene in the absence of edge states appearing for the familiar Hall-bar geometry. Using the transfer matrix in the angular-momentum space we find that for sufficiently strong magnetic fields the current propagates only in one direction, determined by the magnetic field direction and the interface orientation, and the two valleys, K and K' , are equally occupied. Spatially-anisotropic effective mass may suppress one of the valley currents, selected by the external electric field, transforming the system into a mesoscopic version of the valley filter. The filtering mechanism can be fully understood within the effective Dirac theory, without referring to atomic-scale effects which are significant in proposals operating on localized edge states.

1. Introduction

One-dimensional conduction channels associated with edge states are often considered as background for solid-state quantum information processing not only in systems showing the quantum Hall effect [1–8], but also in graphene [9, 10] or transition metal dichalcogenide nanoribbons [11]. The aforementioned nanostructures are formed of two-dimensional materials that host an additional electronic valley degree of freedom, allowing dynamic control and the development of valleytronic devices [12], such as the valley filter [13, 14].

The operation of early proposed valley filters in graphene, employing the constriction with zigzag edges [13] or the line defect [15], was strongly affected by atomic-scale defects [16] and local magnetic order [17]. To overcome these difficulties, alternative proposals utilizing strain-induced pseudomagnetic fields [18–23], disorder and curvature effects in carbon nanotubes [24], or various types of domain walls in graphene, bilayer graphene [25], or topological systems [26, 27], were put forward. Despite such theoretical and computational efforts the experimental breakthrough is still missing, although some recent progress can be noticed [28–30]. Therefore, conceptually novel mechanisms of valley filtering are very desired.

In this paper, we explore the possibility of valley filtering for peculiar edge states mixing Landau levels from both sides of the p–n interface in the quantum Hall regime [4–6]. Such unconventional edge states can be regarded as degenerate versions of snake states, recently observed in ultraclean graphene devices [31, 32] (see figure 1). As the charge density is centered far from physical edges of the system, and transport is essentially of a *mesoscopic*, rather than *nanoscopic*, nature (i.e. the wavefunction varies on a length scale given by the magnetic length $l_B = \sqrt{\hbar/eB} \gg a$, with $a = 0.246$ nm being the lattice parameter; see [33]), some of the above-mentioned obstacles in sustaining the valley polarization of current may be overcome. Additionally, the Corbino geometry [34–37] allows one to eliminate conventional edge states, making it possible to fully control the spatial distribution of electric current via external electric and magnetic fields.

Possible classical carrier trajectories for weak-to-moderate magnetic fields are depicted schematically in the top and middle panels of figure 1. Snake states (bottom panel) cannot be understood fully classically, as they involve relativistic Klein tunneling through the region of an opposite polarity. In the quantum Hall regime the current flows along one section of the p–n interface only (see figure 2). The physical meaning of a ‘weak’,

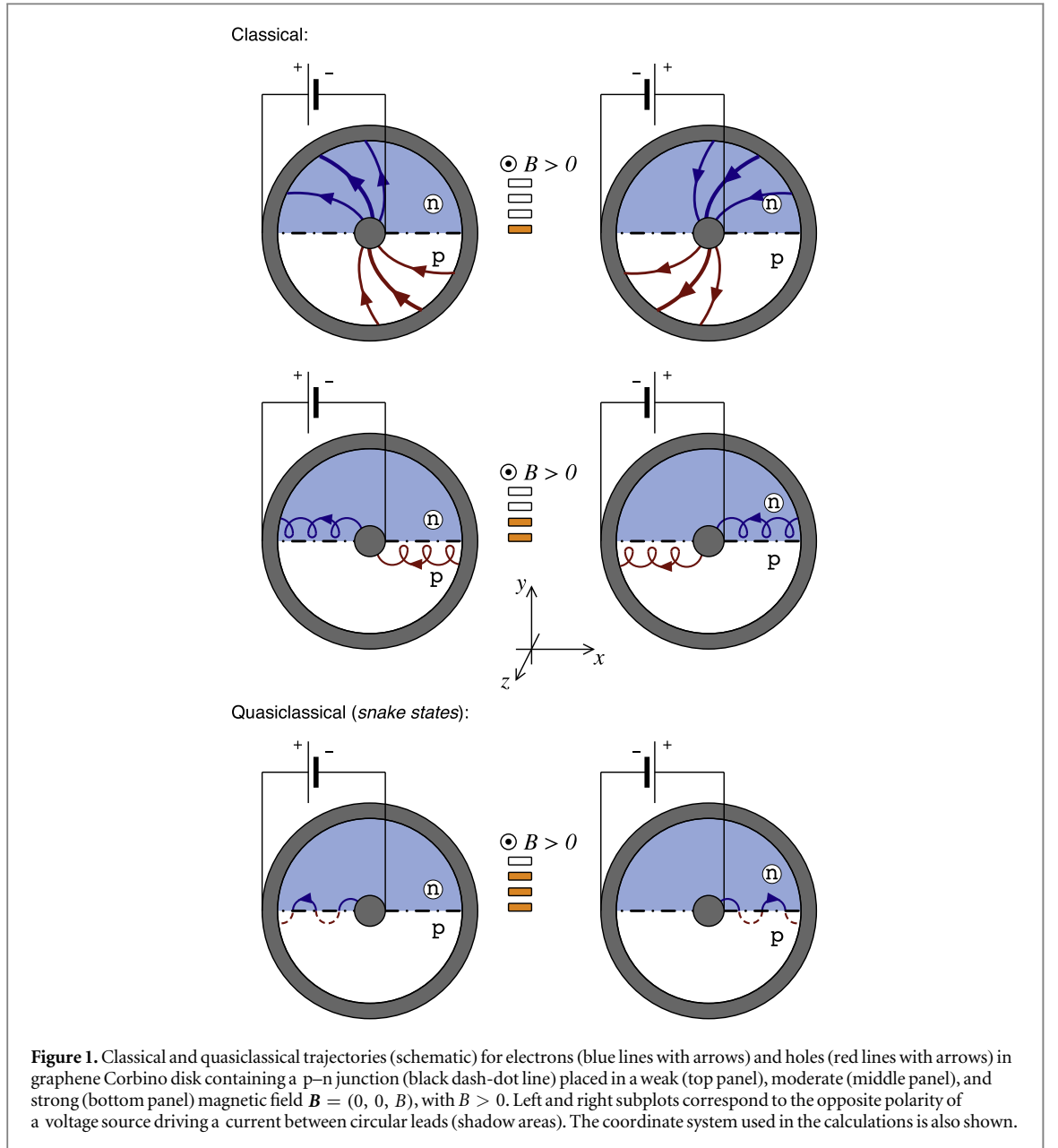


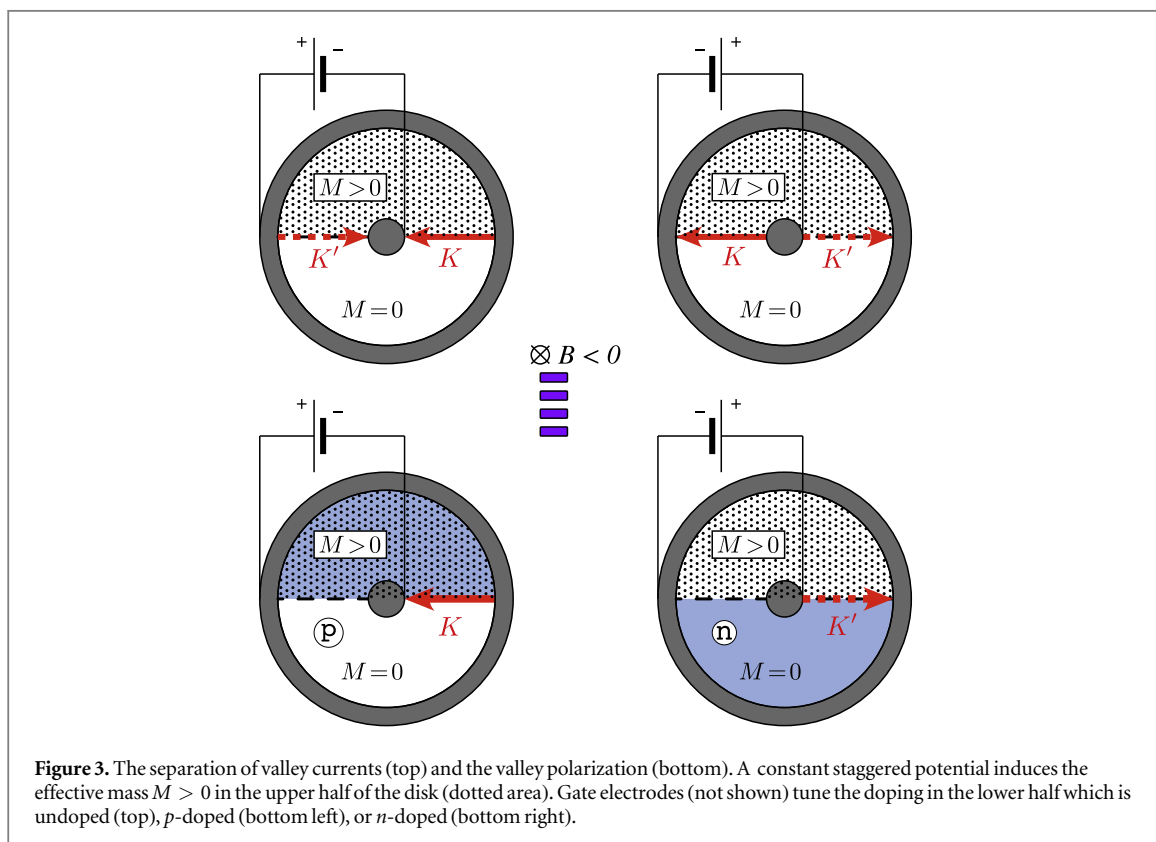
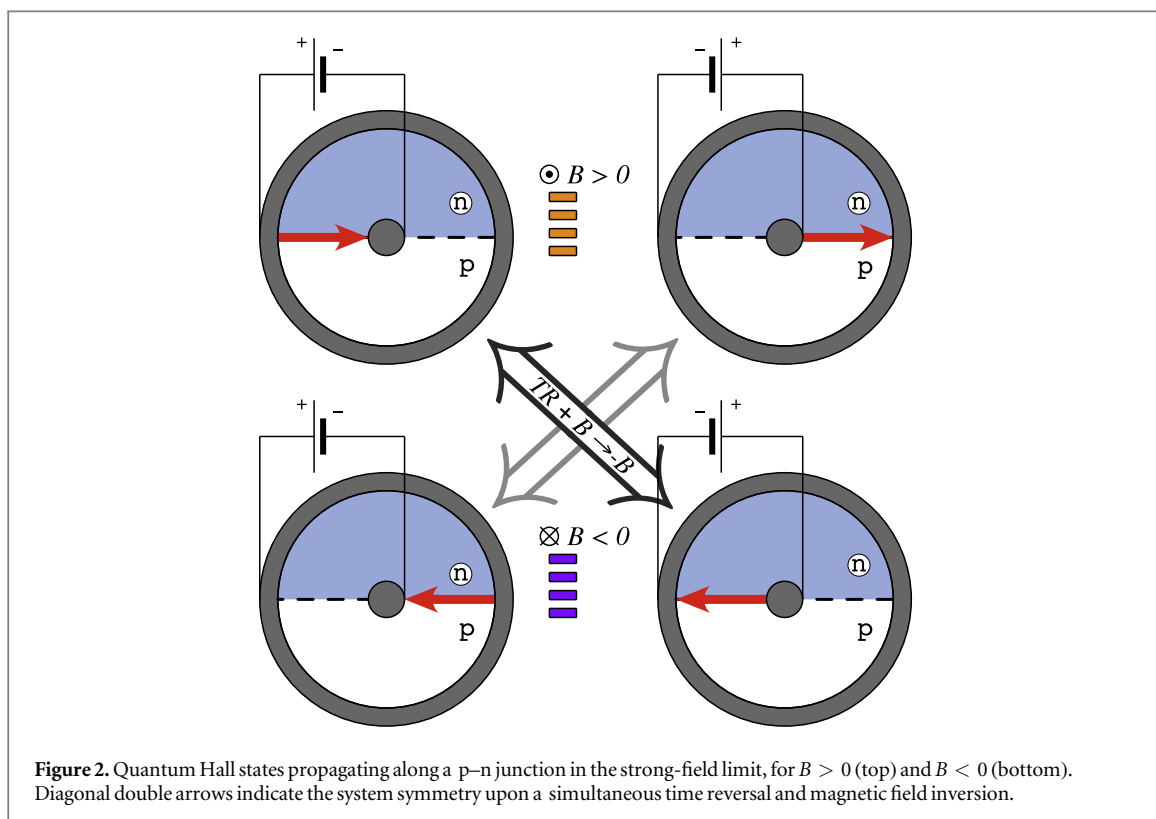
Figure 1. Classical and quasiclassical trajectories (schematic) for electrons (blue lines with arrows) and holes (red lines with arrows) in graphene Corbino disk containing a p–n junction (black dash-dot line) placed in a weak (top panel), moderate (middle panel), and strong (bottom panel) magnetic field $\mathbf{B} = (0, 0, B)$, with $B > 0$. Left and right subplots correspond to the opposite polarity of a voltage source driving a current between circular leads (shadow areas). The coordinate system used in the calculations is also shown.

‘moderate’, or ‘strong’, field is determined by mutual relations between the characteristic sample length $L \equiv R_o - R_i$ (with the outer disk radius R_o and the inner radius R_i), the magnetic length $l_B (\propto B^{-1/2})$, and the cyclotron radius $r_c (\propto B^{-1})^2$. In turn, the larger the disk size the lower field is required to eliminate currents distant from the p–n interface, providing the sake of scalability missing in previously proposed nanoscopic valley filters³.

We show, using the numerical transfer-matrix technique, that the presence of a non-uniform staggered potential, introducing the position-dependent mass term in the effective Dirac equation for low-energy excitations [38], leads to a spatial separation of valley currents and that the valley polarization may be controlled by changing the gate potentials (see figure 3). Although to set a staggered potential one needs to initially modify the sample on a microscopic level, e.g. by chemical functionalization [39–41] or the adsorption of hexagonal boron nitride (h-BN) [42, 43], the operation of such a *mesoscopic valley filter* is then fully-electrostatically controlled. We further find, that the constant magnetic field of 1 T is sufficient to obtain a nearly perfect polarization in the disk of a 400 nm diameter. What is more, the filter operation can be directly attributed to a peculiar combination of symmetry breakings for the Dirac Hamiltonian: The mass term breaks the effective

² Related to the *local* carrier concentration via $r_c = \hbar k / eB = \sqrt{\pi|n|} l_B^2$, with $k = \sqrt{\pi|n|}$ being the wave vector.

³ For $r_c \lesssim l_B$, quantum effects dominate and may fully eliminate the moderate-field range (see middle panel in figure 1) for smaller disks. As r_c is related to the carrier concentration, particular scenario of the classical-to-quantum transition also depends on the electrostatic potential profile.



time-reversal symmetry in a single valley (*symplectic symmetry*), whereas the magnetic field breaks the *true* time-reversal symmetry (involving the valley exchange). Together, these two symmetry-breaking factors lead to the inequivalence of valleys, providing an opportunity to produce nonequilibrium valley polarization of current.

Referring to the above scenario may also partly explain the valley polarization occurrence in nanobubbles [20, 21], since geometric deformations usually led to a nonzero mass term [44]. However, in such systems,

valley-dependent gauge fields play a dominant role, so an interpretation in terms of basic symmetry breakings is not as clear as in the real magnetic field case considered here.

The paper is organised as follows: in section 2, we briefly present the effective Dirac theory and the transfer matrix approach to the scattering problem in the angular-momentum space (adjusted to the Corbino-disk symmetry). In section 3, we discuss our numerical results concerning the current distribution and valley filtering in the presence of external electromagnetic field and the staggered potential. The conclusions are given in section 4.

2. Model and methods

2.1. The effective Dirac equation

Let us start by considering a ring-shaped sample, characterized by the inner radius R_i and the outer radius R_o , surrounded by metallic contacts modelled by heavily-doped graphene areas (we set $R_o = 4R_i = 200$ nm for all systems considered in the paper). Since we focus on *smooth* (or long-range) disorder, the intervalley scattering can be neglected and one can consider the single-valley Dirac equation

$$(\xi\pi_x\sigma_x + \pi_y\sigma_y)\psi(r, \phi) = [E - \mathcal{V}(r, \phi) - \mathcal{M}(r, \phi)\sigma_z]\psi(r, \phi), \quad (1)$$

where $\xi = 1$ (-1) is the valley index for K (K') valley, σ_α (with $\alpha = x, y, z$) is the Pauli matrix, $\pi_\alpha/v_F = (-i\hbar\partial_\alpha + eA_\alpha)$ is the gauge-invariant momentum operator with $v_F \approx 10^6$ m s⁻¹ the Fermi velocity, E denotes the Fermi energy, and $\mathcal{V}(r, \phi)$ and $\mathcal{M}(r, \phi)$ are position-dependent electrostatic potential energy and mass (respectively) in polar coordinates (r, ϕ) . We choose the symmetric gauge $\mathbf{A} = \frac{B}{2}(-y, x)$ with a uniform magnetic field B . Furthermore, $B \neq 0$ for the disk area ($R_i < r < R_o$) only; inside the leads ($r < R_i$ or $r > R_o$) we simply set $B = 0$, as the value of B becomes irrelevant in the high-doping limit (see e.g. [34]).

In the case of a system with cylindrical symmetry (namely, \mathcal{V} and \mathcal{M} being ϕ -independent), the Hamiltonian in equation (1) commutes with the angular-momentum operator, $L_z = -i\hbar\partial_\phi + \xi\hbar\sigma_z/2$, and the wavefunction can be expressed as a product of radial and angular parts

$$\psi_l(r, \phi) = \varphi_l(\phi)\theta_l(r) \equiv e^{i(l-\xi\sigma_z/2)\phi} \begin{bmatrix} \theta_{A,l}(r) \\ \theta_{B,l}(r) \end{bmatrix}, \quad (2)$$

where l is an half-odd integer, and A (B) labels the upper (lower) spinor element.

2.2. Mode-matching in the angular-momentum space

To solve the scattering problem numerically we simplify here, for the case of a monolayer, the method earlier developed for the Corbino disk in bilayer graphene [45].

If \mathcal{V} or \mathcal{M} in equation (1) is ϕ -dependent the cylindrical symmetry is broken, however, one still can employ the angular-momentum eigenfunctions to represent a general solution as a superposition

$$\psi(r, \phi) = \sum_k \psi_k(r, \phi), \quad (3)$$

with $\psi_k(r, \phi)$ given by equation (2) (see also appendix A).

Substituting the above into equation (1) we obtain

$$\sum_k \hbar v_F [\partial_r - f^k(r)] \psi_k(r, \phi) = \sum_k \xi \{ i\sigma_x [E - \mathcal{V}(r, \phi)] - \sigma_y \mathcal{M}(r, \phi) \} \psi_k(r, \phi), \quad (4)$$

where $f^k(r) = [\xi(k/r + l_B^{-2}r/2)\sigma_z - 1/(2r)\mathbb{I}_{2 \times 2}]$, the magnetic length $l_B = \sqrt{\hbar/(eB)}$, and $\mathbb{I}_{n \times n}$ is the $n \times n$ identity matrix. Multiplication over the conjugate angular wavefunction $\varphi_l^*(\phi)$ and subsequent integration over the polar angle ϕ leads to

$$\left[\partial_r - f^l(r) - i\sigma_x \frac{\xi E}{\hbar v_F} \right] \theta_l(r) = \sum_k \xi [-i\sigma_x \mathbb{V}_{lk}(r) - \sigma_y \mathbb{M}_{lk}(r)] \theta_k(r), \quad (5)$$

with

$$\mathbb{V}_{lk}(r) = \frac{1}{2\pi} \int_0^{2\pi} d\phi [\mathcal{V}(r, \phi) / (\hbar v_F)] e^{i(k-l)\phi}, \quad (6)$$

and

$$\mathbb{M}_{lk}(r) = \frac{1}{2\pi} \int_0^{2\pi} d\phi [\mathcal{M}(r, \phi) / (\hbar v_F)] e^{i(k-l)\phi}. \quad (7)$$

(Notice that the angular dependence of \mathcal{V} or \mathcal{M} introduces the mode-mixing in our scattering problem.)

The general solution of equation (5) can be written as a vector

$\theta(r) = [\theta_{l_{\min}}^A(r), \dots, \theta_{l_{\max}}^A(r), \theta_{l_{\min}}^B(r), \dots, \theta_{l_{\max}}^B(r)]^T$, with cutoff angular-momentum quantum numbers

l_{\min} and l_{\max} . (Hereinafter, $L = l_{\max} - l_{\min} + 1$ is the total number of transmission modes.) Subsequently, one can write

$$\{[\partial_r + 1/(2r)]\mathbb{I}_{2L \times 2L} - \xi\sigma_z \otimes \mathbb{I}_L\}\boldsymbol{\theta}(r) = \xi \left[i \frac{E}{\hbar v_F} \sigma_x \otimes \mathbb{I}_{L \times L} - i\sigma_x \otimes \mathbb{V} - \sigma_y \otimes \mathbb{M} \right] \boldsymbol{\theta}(r), \quad (8)$$

where $\mathbb{A} \otimes \mathbb{B}$ is the Kronecker product of matrices \mathbb{A} and \mathbb{B} , and the diagonal matrix

$$\mathbb{L} = \text{diag} \left(\frac{l_{\min}}{r} + \frac{r}{2l_B^2}, \frac{l_{\min} + 1}{r} + \frac{r}{2l_B^2}, \dots, \frac{l_{\max}}{r} + \frac{r}{2l_B^2} \right). \quad (9)$$

Once the scattering matrix is determined (see appendix A for details), transport properties of the system can be calculated within the Landauer–Büttiker formalism in the linear-response regime [46, 47]. In particular, the electrical conductance and valley polarization are given by

$$G = G_0 \sum_{\xi=\pm 1} \text{Tr} \mathbf{T}_\xi, \quad \mathcal{P} = \frac{\text{Tr} \mathbf{T}_{\xi=1} - \text{Tr} \mathbf{T}_{\xi=-1}}{\text{Tr} \mathbf{T}_{\xi=1} + \text{Tr} \mathbf{T}_{\xi=-1}}, \quad (10)$$

where $G_0 = 2e^2/h$, the prefactor 2 marks the spin degeneracy (we neglect the Zeeman effect⁴), and $\mathbf{T}_\xi = \mathbf{t}_\xi^\dagger \mathbf{t}_\xi$ with \mathbf{t}_ξ being the transmission matrix for one valley. We further neglect the electron–electron interaction and electron–phonon coupling, which is a common approach to nanosystems in monolayer graphene close to the Dirac point, as the scattering processes associated with these many-body effects are usually slower than the ballistic-transport processes [48, 49].

The matrix \mathbf{t} is also employed when calculating the radial current density, which is given by

$$j_r(r, \phi) = ev_F \sum_l \psi_l^\dagger(r, \phi) J_r(\phi) \psi_l(r, \phi), \quad (11)$$

with the radial current density operator

$$J_r(\phi) = \xi\sigma_x \cos \phi + \sigma_y \sin \phi, \quad (12)$$

and $\psi_l(r, \phi) = \sum_k (\mathbf{t}_\xi)_{l,k} e^{i(k - \xi\sigma_z/2)\phi} (1, \xi)^T / \sqrt{r}$ being the transmitted wavefunction in the outer contact ($r > R_o$). The matrix element $(\mathbf{t}_\xi)_{l,k}$ denotes the transmission probability amplitude from channel k to l . Similarly, the Cartesian components of the current density $\mathbf{j}(r, \phi) = (j_x, j_y)$ are calculated by replacing the operator J_r in equation (11) by

$$J_x = \xi\sigma_x \quad \text{or} \quad J_y = \sigma_y \quad (\text{respectively}). \quad (13)$$

3. Quantum transport in crossed electric and magnetic fields

3.1. Definitions

In order to study a role of the p–n junction in quantum transport through graphene-based Corbino disk, we choose the electrostatic potential energy as follows

$$\mathcal{V}(r, \phi) = -e\mathcal{E}r \sin(\phi - \phi_V), \quad (14)$$

where \mathcal{E} is the electric field (we further define $V \equiv e\mathcal{E}R_o$) and the angle ϕ_V defines the crystallographic orientation of the p–n interface [50, 51]. Furthermore, we investigate how the transport is affected by the mass term

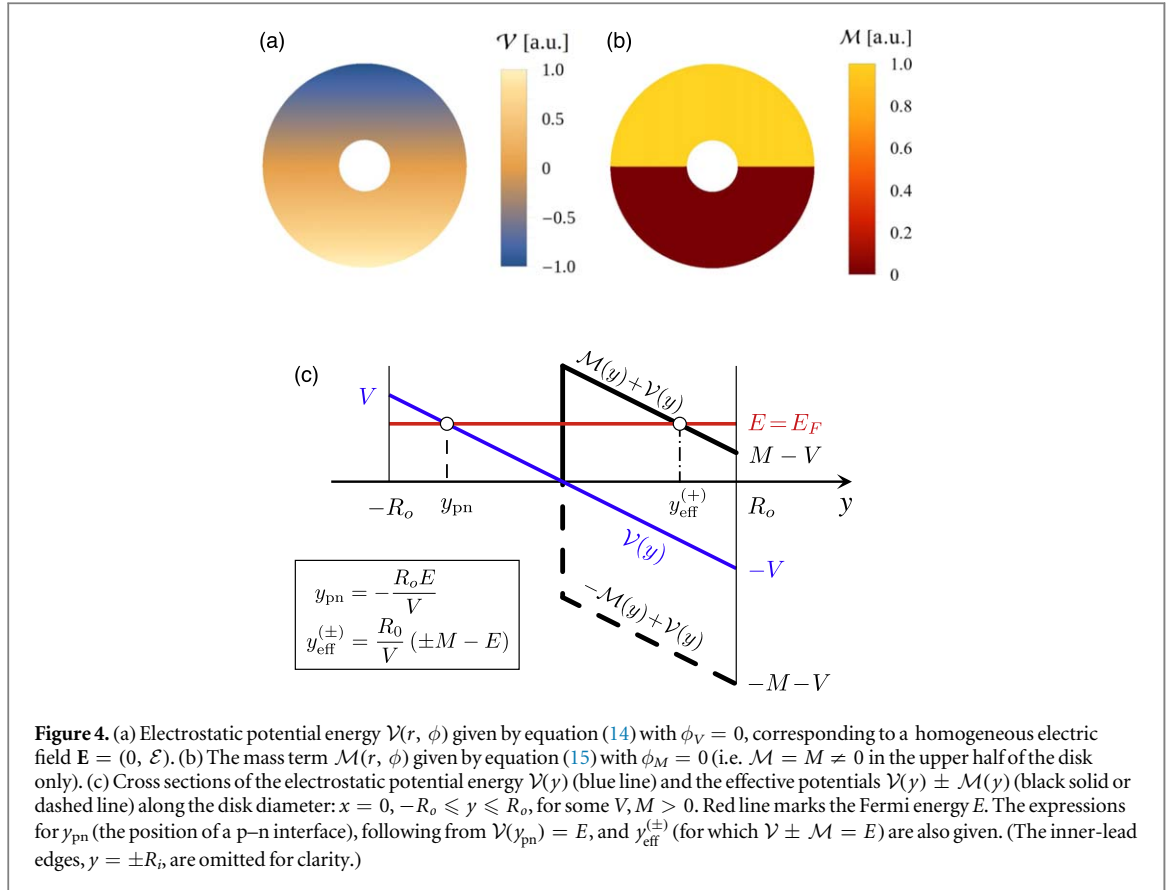
$$\mathcal{M}(r, \phi) = M\Theta(\phi - \phi_M)\Theta(\pi + \phi_M - \phi), \quad (15)$$

with the angle ϕ_M specifying the mass arrangement, and $\Theta(x)$ being the Heaviside step function. The mass term given by equation (15) is restricted to a half of the disk, $\phi \in [\phi_M, \pi + \phi_M]$, see figure 4. In the heavily-doped contact regions, $\mathcal{V}(r, \phi) = \mathcal{M}(r, \phi) = 0$.

It is worth to mention that we have also considered other functional forms of the mass term, including $\mathcal{M}(r, \phi)$ smoothly varying with the distance from a p–n junction, always finding a parameter range in which the valley-filtering mechanism that we describe was highly efficient. Even for a simple model given by equation (15), changing the Fermi energy (E) allows one to shift a p–n interface ($E - \mathcal{V}(r, \phi) = 0$) with respect to the mass boundary, leading to a rich phase diagram discussed later in this section.

The specific forms of the potential energy $\mathcal{V}(r, \phi)$ and the mass term $\mathcal{M}(r, \phi)$, given by equations (14) and (15), lead to the matrix elements

⁴ For $B = 1$ T the Zeeman splitting is $\Delta E_Z = g\mu_B B \approx 0.1$ meV [with $g \approx 2$ and $\mu_B = e\hbar/(2m_e)$ the Bohr magneton] and cannot affect the filter operation appearing at the potential and mass-term amplitudes of $V \sim M \gtrsim 10$ meV.



$$\mathbb{V}_{lk} = -\delta_{|l-k|,1} \frac{Vr\pi}{\hbar v_F R_o} i^{k-l} \exp[i(k-l)\phi_V], \quad (16)$$

and

$$\mathbb{M}_{lk} = \frac{Mr}{\hbar v_F R_o} \begin{cases} \pi & \text{if } |l-k| = 1, \\ i^{1-(-1)^{k-l}} e^{i(k-l)\phi_M} & \text{if } |l-k| \neq 1. \end{cases} \quad (17)$$

3.2. Quantum Hall regime in the massless case

We consider now the case of $M = 0$ in equation (15). The Fermi energy is set as $E = 0$ and thus the p–n interface overlaps with the disk diameter ($y_{pn} = 0$) for any $V \neq 0$.

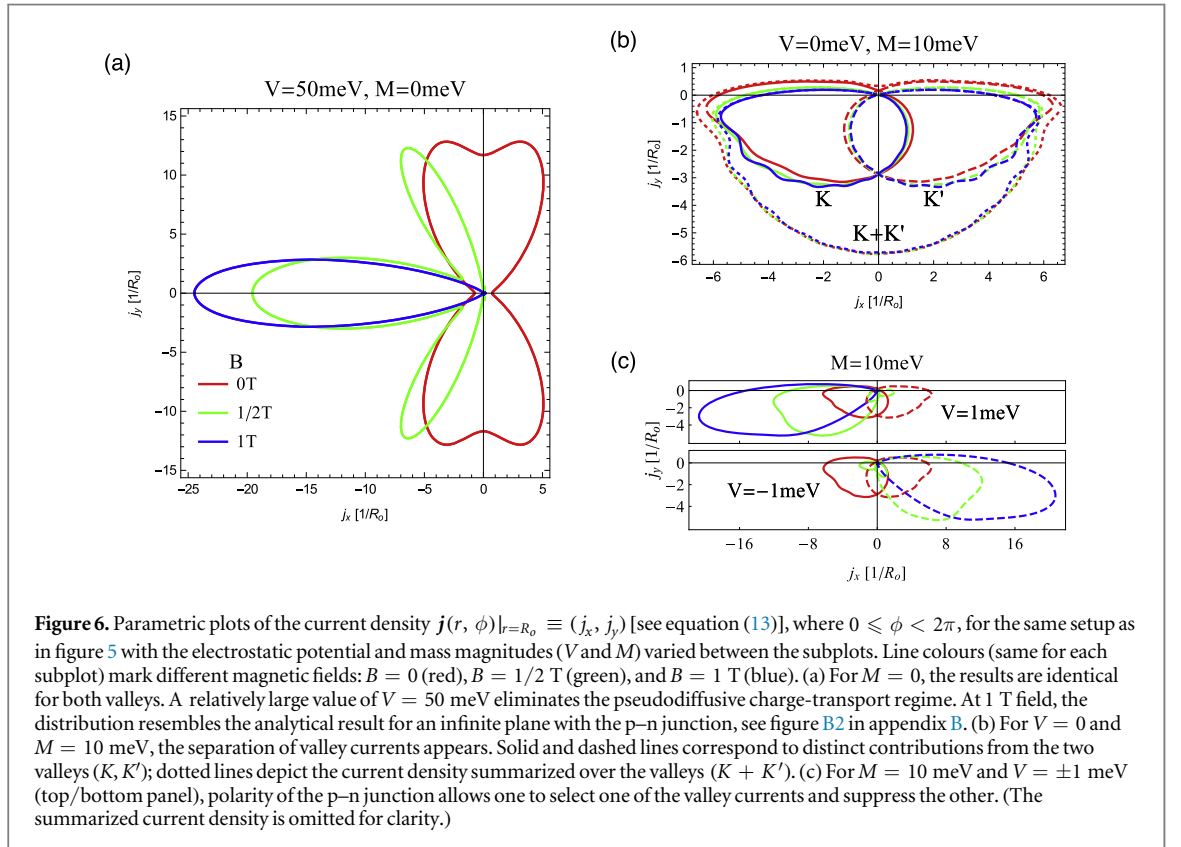
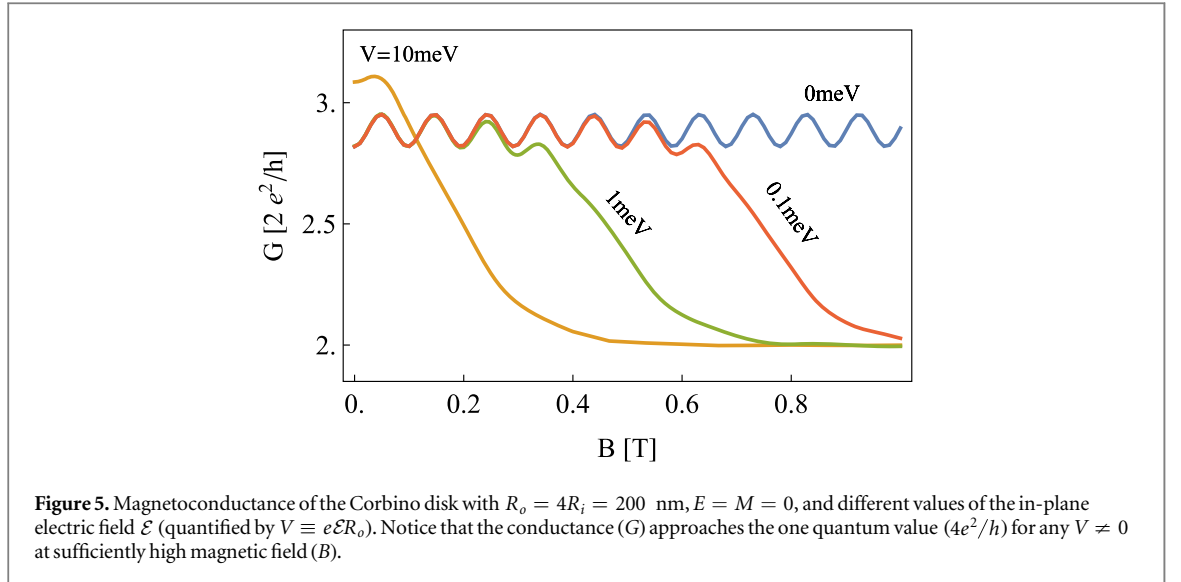
For moderate values of the electric field ($|V| < 10$ meV) and weak magnetic fields the magnetoconductance behavior is the same as in a case without the p–n junction [34], see figure 5. The increase of G at weak magnetic fields, visible for $|V| = 10$ meV, indicates the system is close to the ballistic transport regime. This occurs when the (position-dependent) cyclotron diameter $2r_c(0, y) \gtrsim R_o - R_i$, enhancing vertical currents along the classical trajectories (see the top panel in figure 1). For our choice of the parameters, the cyclotron radius,

$$r_c(x, y) = \frac{|E - \mathcal{V}(x, y)|}{eBv_F}, \quad (18)$$

is bounded by $r_c(0, y) \geq (R_i/R_o)|V|/(eBv_F)$ along the vertical diameter ($x = 0$) and for $R_i \leq |y| \leq R_o$.

Another apparent feature of the data presented in figure 5 is a rapid conductance drop, occurring for any $V \neq 0$ at sufficiently high field. Unlike in a uniformly-doped disk out of the charge-neutrality point, where G vanishes in the high-field limit [34], here G approaches the value of $4e^2/h$ (i.e. the *conductance quantum* with spin and valley degeneracies) signalling the crossover from pseudodiffusive to quantum-hall transport regime. The limiting value of G reproduces the experimental result of [36], and can be easily explained by analysing symmetries of the Dirac theory [52].

A bit more detailed view of the effect is provided with the evolution of angle-dependent current density at the outer disk edge ($r = R_o$) with increasing field, presented in figure 6(a). We choose a high electric field ($V = 50$ meV) to ensure the system undergoes a crossover directly from ballistic to quantum-Hall transport regime, as the contribution from evanescent waves is negligible. For $B = 0$ (red line) the current flows in directions along which the doping is extremal, namely, $\phi = \pm\pi/2$. For higher fields the transport is dominated



by a single direction, for which $\mathcal{V}(r, \phi) = 0$ (i.e. $\phi = \pi$), with some secondary currents at $|\phi| \lesssim \pi/2$ visible for $B = 1/2$ T (green line), and vanishing for $B = 1$ T (blue line). This picture is in agreement with the results of previous theoretical studies (see [52] and appendix B for details).

As the magnetic length at 1 Tesla field $l_B(B = 1 \text{ T}) \approx 26$ nm is still comparable with the system size (in particular, the inner radii $R_i = 50$ nm), the transport cannot be understood classically or quasiclassically. Therefore, several features depicted schematically in figure 1 (such as the orbits in the middle panel) have no correspondants in numerical results presented in figure 6(a). However, an apparent asymmetry of the current distribution for $B \neq 0$ is directly linked to the left-right mirror symmetry breaking, also present in the classical level: both the trajectories and quantum-hall edge states are symmetric upon a simultaneous left-right reflection and the field inversion (see figure 2); the same applies to the voltage-source polarity (or time) reversal combined with the magnetic field inversion.

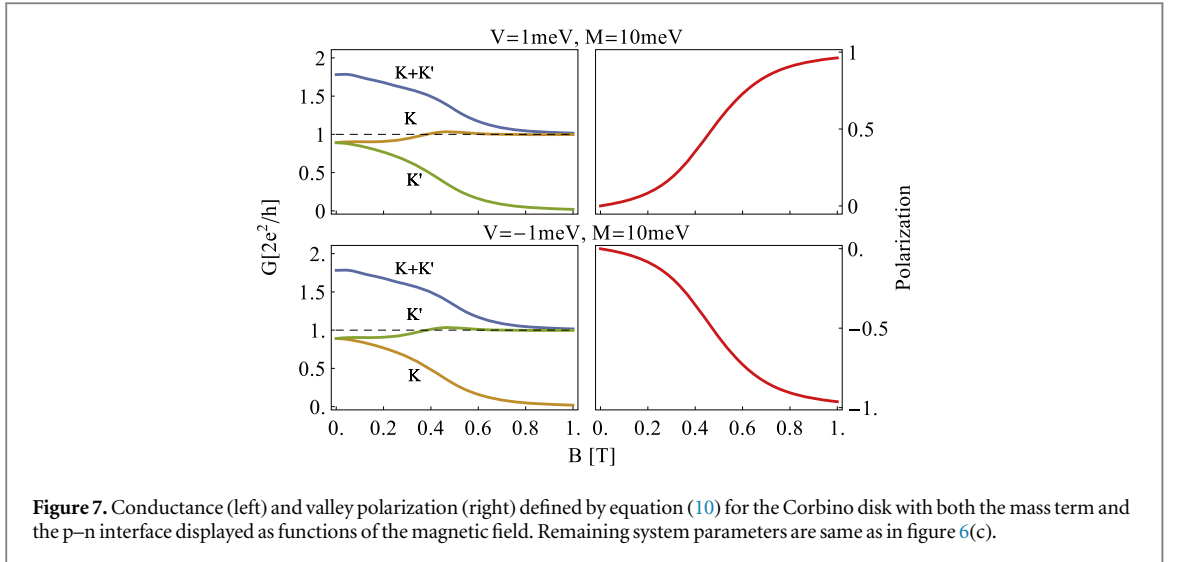


Figure 7. Conductance (left) and valley polarization (right) defined by equation (10) for the Corbino disk with both the mass term and the p–n interface displayed as functions of the magnetic field. Remaining system parameters are same as in figure 6(c).

3.3. Mass term and the valley filter operation

So far, we have put $M = 0$ in equation (15) and the transport characteristics were identical for both valleys (K and K'). A different picture emerges in the system with nonzero and spatially-varying mass term (the $M \neq 0$ case). Our simplified model, in which the mass is present only in the upper half of the system (see figure 4), already allows to demonstrate the mesoscopic valley-filtering mechanism. In this subsection, we present the central results of the paper, providing a quantitative description of the effects depicted schematically in figure 3.

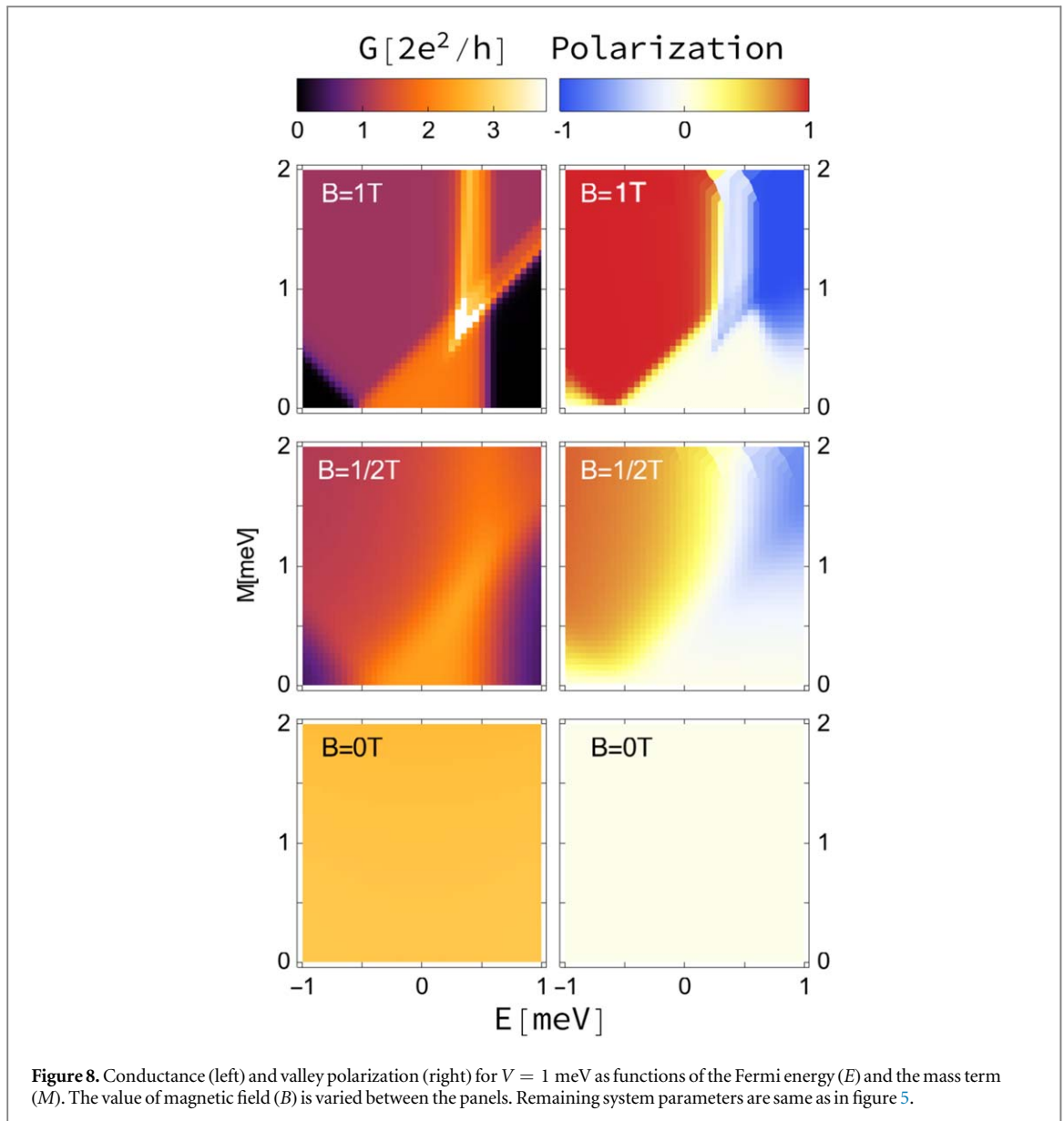
Quite surprisingly, even at zero electric and magnetic fields the currents corresponding to different valleys are well separated (see figure 6(b)). This can be interpreted as a zero-doping version of the edge-state formation (the Fermi energy is fixed at $E = 0$). As the mass opens a band gap in the upper half of the disk ($0 < \phi < \pi$), there are no extended states available, and the current is pushed away towards the lower half ($-\pi < \phi < 0$). In turn, the border between areas with $\mathcal{M} = 0$ and $\mathcal{M} \neq 0$ plays a role of an artificial edge of the system (notice that the p–n junction is absent for $V = 0$). The *total* current distribution (dotted lines in figure 6(b)) is approximately uniform in the lower half of the disk (as this part is in the pseudodiffusive charge-transport regime), with some local maxima for $\phi \approx 0$ and $\phi \approx -\pi$, signaling contributions from the zero-energy edge states. The emergence of such states is well-described in graphene literature, see e.g. [53]; their analogs in bilayer graphene in a position-dependent perpendicular electric field were also discussed [25]. A basic reasoning why electrons in different valleys prefer opposite directions of propagation is given in appendix C.

A direct link between the valley polarization of current and the direction of propagation for zero-energy edge states leads to the spatial separation of valley currents, which is apparent even in our relatively small system, for which the role of evanescent waves is still significant (and manifests itself by a nonzero current density for any $-\pi < \phi < 0$).

Next, the valley-filtering mechanism is demonstrated by creating the p–n interface in a presence of the mass term ($V \neq 0$, $M \neq 0$). Figure 6(c) shows a strong suppression of one of the valley currents in relatively weak electric and magnetic fields (and the valley is selected by a *sign* of V), provided that the mass term is sufficiently strong. The valley polarization \mathcal{P} gradually increases with the magnetic field, becoming almost perfect for $B = 1 \text{ T}$ (see figure 7).

The operation of our valley filter is characterized in details by the numerical results presented in figure 8, where we have fixed $V = 1 \text{ meV}$, and visualized the transport characteristics in the Fermi energy–mass (E – M) parameter plane, for three selected values of the magnetic field ($B = 0, 1/2, \text{ and } 1 \text{ T}$). Notice that varying E corresponds to a vertical shift of the p–n interface; in particular, for $E = VR_i/R_o = 0.25 \text{ meV}$ we have $y_{\text{pn}} = -R_i$ (see figure 4) and the p–n interface is a tangent line to the inner disk edge at the lower (i.e. mass-free) half. At zero magnetic field, the density maps shown in bottom panels are perfectly uniform, and no valley polarization is visible. For higher fields, distinct regions of the ‘phase diagram’ are formed, including the unpolarized highly-conducting region ($G \approx 2G_0$, $\mathcal{P} \approx 0$) at the central-bottom part of each subplot, the two polarized highly-conducting regions ($G \approx G_0$, $\mathcal{P} \approx \pm 1$) near the upper corners, and the two tunneling regions ($G \approx 0$, $\mathcal{P} \approx 0$) near the lower corners. At 1 T field (top panels), the boundaries between above-mentioned regions are already well-developed.

Some further insights into relations connecting the diagram structure and characteristic features of the effective potential profile, $\mathcal{V}(r, \phi) \pm \mathcal{M}(r, \phi) \equiv \mathcal{V}(y) \pm \mathcal{M}(y)$ in equation (1), are given in figure 9. In brief, the boundaries between regions on the E – M diagram can be attributed to the situations when the p–n line is



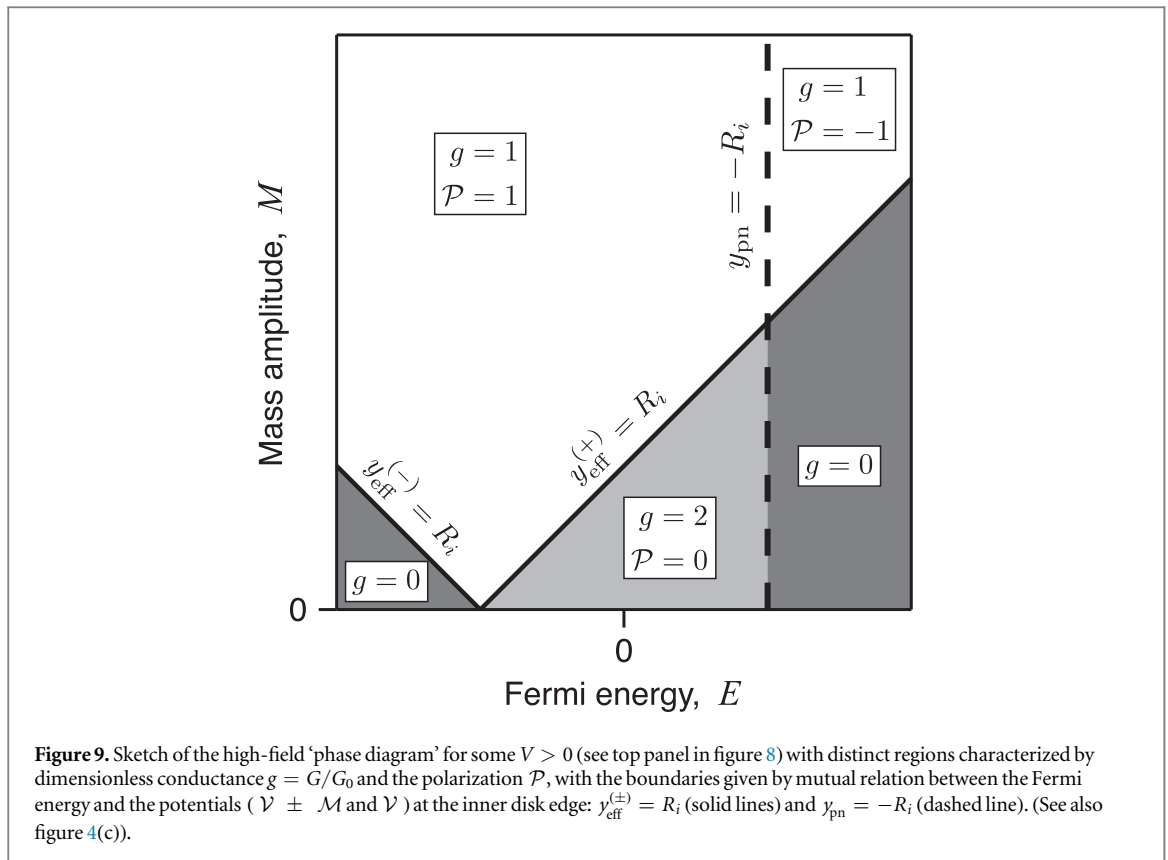
a tangent to the inner disk edge at the mass-free part, $y_{pn} = -R_i$ (vertical dashed line), or when the Fermi energy is equal to the effective potential along a tangent line to the inner disk edge at the nonzero mass part, $y_{\text{eff}}^{(\pm)} = R_i$ (diagonal solid lines). The sketch of figure 9 corresponds to the high-field limit, in which $l_B \ll R_i$ and varying E may lead to an abrupt switching between the regions. In a finite-field situation (see figure 8), finite widths of quantum Hall states result in blurs (and shifts) of the boundaries, with a general trend to expand the unpolarized highly-conducting region with decreasing B .

Numerous experimental realizations of a non-uniform mass in monolayer graphene [39–43] suggest to focus on a constant and relatively large $M \gg 1$ meV. In such a case, the magnetic field of $B = 1$ T allows one to control the valley polarization of current independently by tuning the Fermi energy (E) or by reversing the p–n junction polarity ($V \rightarrow -V$).

It is also worth stressing, that high valley polarization remains unaffected when the p–n interface is moved by a distance of $\Delta y \approx R_i = 50$ nm away from the mass boundary, allowing us to coin the term of mesoscopic valley filter.

4. Conclusions

We have demonstrated, as a proof of principle, that the Corbino disk in monolayer graphene modified such that the mass term in effective Dirac equation is present in a half of the disk (leading to the energy gap of $\gtrsim 1$ meV) may act as a highly efficient valley filter, when placed in crossed electric and magnetic fields inducing a p–n interface close to the mass-region boundary. Although introducing the mass term involves a microscopic



modification of a sample, the output (valley) polarization of current may be controlled electrostatically in constant magnetic field, alternatively by: (i) inverting the p–n junction polarity, or (ii) shifting the p–n line with respect to the mass boundary by tuning a global doping of a sample. The magnetic field of 1 T is sufficient to obtain the polarization better than 99% for the device size (namely: the outer disk diameter) of 400 nm.

An additional interesting feature of the system is that the currents belonging to different valleys are spatially separated, flowing in opposite directions along the p–n interface. In the absence of a p–n interface, there are two equal currents propagating along the mass boundary; in-plane electric field amplifies one of these currents and suppresses the other. The filtering mechanism is directly linked to global symmetry breakings of the Dirac Hamiltonian, and therefore we expect it to be robust against typical perturbations in real experiments.

For instance, the operation of mesoscopic valley filter which we have described should not be noticeably affected by the long-range (or smooth) impurities, as they generally do not introduce the intervalley scattering [54, 55]. (In contrast, short-range impurities mix the valleys and may restore the equilibrium valley occupation.) Recent experimental works on ultraclean graphene p–n junctions [31, 32] allow us to believe that such systems, accordingly modified to induce a position-dependent quasiparticle mass, may also act as highly-efficient mesoscopic valley filters. Since the valley filtering takes place in a proximity of the p–n interface, which can be shifted (or bent) during an experiment by using external gates, we anticipate that more complex multiterminal geometry will make it possible to setup a few filters in series in order to independently produce and detect valley-pseudospin polarization by means of nonlocal measurements. Numerical simulations for the multiterminal geometry are, however, beyond the scope of this paper.

Acknowledgments

Discussions with Piotr Witkowski are appreciated. The work was supported by the National Science Centre of Poland (NCN) via Grant No. 2014/14/E/ST3/00256. Computations were partly performed using the PL-Grid infrastructure.

Appendix A. Transfer matrix approach

A general wavefunction corresponding to the l th transmission channel is given by a linear combination of two linearly-independent spinor functions

$$\theta^l(r) = a_1^l \theta_1^l(r) + a_2^l \theta_2^l(r), \quad (\text{A1})$$

where a_α^l ($\alpha = 1, 2$) are arbitrary complex amplitudes and $\theta_\alpha^l(r) = [\theta_{\alpha,A}^l, \theta_{\alpha,B}^l]^T(r)$ is a normalized spinor function with A and B being the sublattice indices. The normalization has to be carried out in such a way that the total current remains constant (i.e. l, α -independent). To satisfy this condition, we write down the current density for the l th transmission channel

$$\vec{j}_l = ev_F [\theta^l(r)]^\dagger \cdot [\xi \sigma_x \cos(\varphi) + \sigma_y \sin(\varphi)] \cdot \theta^l(r). \quad (\text{A2})$$

In principle, it is sufficient to normalize only the wavefunctions in the leads since the relation between them (namely: between the incoming, the transmitted, and the reflected wavefunction) ultimately defines matrices \mathbf{r} and \mathbf{t} . Current conservation guarantees that amplitudes r_{mn} and t_{mn} preserve the probabilistic interpretation. Therefore, a direct normalization for the wavefunctions in the sample area is not essential for the successful mode matching.

Next, it is convenient to present a complete set of wavefunctions as a vector with each element corresponding to a different transmission channel. Since only a limited number of channels contributes significantly to the quantum transport, one can look for a truncated solution by introducing the cutoff-transmission channels l_{\min} and l_{\max} such that $l \in [l_{\min}, l_{\max}]$. The total number of transmission channels, $M = (l_{\max} - l_{\min} + 1)$, is chosen to be large enough to reach the convergence. In such a notation, we can write

$$\boldsymbol{\theta}(r) = \mathbb{M}(r) \begin{pmatrix} \mathbf{a}_1 \\ \mathbf{a}_2 \end{pmatrix}, \quad (\text{A3})$$

where $\mathbb{M}(r)$ is a $2M \times 2M$ matrix, $\mathbf{a}_\alpha = [a_\alpha^{l_{\min}}, \dots, a_\alpha^{l_{\max}}]^T$. The explicit form of matrix $\mathbb{M}(r)$ will be presented later. The notation of equation (A3) is convenient when dealing with a system with mode mixing introduced by a position-dependent potential.

We are primarily interested in a relation between the two sets of amplitudes defining wavefunctions at different radii, say: r and R_i . Such a relation can be written introducing a propagator $\mathbb{U}(r, R_i)$,

$$\boldsymbol{\theta}(r) = \mathbb{U}(r, R_i) \boldsymbol{\theta}(R_i). \quad (\text{A4})$$

The propagator $\mathbb{U}(r, R_i)$ can be found by substituting equations (A4) into (8) from the main text (the Dirac equation). The resulting equation takes the following form

$$\partial_r \mathbb{U}(r, R_i) = \mathbb{A}(r) \mathbb{U}(r, R_i), \quad (\text{A5})$$

with an initial condition $\mathbb{U}(R_i, R_i) = \mathbb{I}_{2M \times 2M}$. The matrix $\mathbb{A}(r)$ in equation (A5) carries the complete information about the potential and the mass term in the system.

Formally, equation (A5) defines $2M$ independent systems of $2M$ ordinary differential equations, each of which describing a column in the matrix $\mathbb{U}(r, R_i)$. We have employed a fixed-step explicit Runge Kutta method of the 4th order [56]. Both the step-size as well as the number of transmission channels M are adjusted to reach the numerical convergence; in practice, these parameters depend on the system size, as well as on the magnetic field, in an approximately linear manner similarly as in the case of bilayer graphene (see [45]).

Once the propagator for the sample area $\mathbb{U}(R_o, R_i)$ is determined, we can translate it onto a transfer matrix, connecting the wavefunctions in the leads with wavefunctions in the sample area, via the mode-matching

$$\begin{aligned} \phi^L(R_o) &= \phi^S(R_o) \\ &= \mathbb{U}(R_o, R_i) \phi^S(R_i) \\ &= \mathbb{U}(R_o, R_i) \phi^L(R_i), \end{aligned} \quad (\text{A6})$$

where $\phi^L(R_o) = \mathbb{M}_L(r) \mathbf{a}$. As the doping in the leads is set to infinity, the matrix $\mathbb{M}_L(r)$ can be presented as a Kronecker product $\mathbb{M}_L(r) = \mathbb{B}(r) \otimes \mathbb{I}_{M \times M}$ (we have omitted the phase constants as they are insignificant when calculating the transport properties), where

$$\mathbb{B}(r) = \frac{1}{\sqrt{r}} \begin{bmatrix} 1 & 1 \\ \xi & -\xi \end{bmatrix}. \quad (\text{A7})$$

Columns in the matrix $\mathbb{B}(r)$ represents independent wavefunctions, corresponding to different directions of propagation (incoming and outgoing waves). The transfer matrix is thus given by

$$\mathbb{T} = \mathbb{M}_L^{-1}(R_o) \mathbb{U}(R_o, R_i) \mathbb{M}_L(R_i). \quad (\text{A8})$$

Finally, the transmission properties of the system can be obtained by retrieving the scattering-matrix elements from \mathbb{T} . The transfer matrix can be expressed by blocks of the scattering matrix as follows

$$\mathbb{T} = \begin{bmatrix} (\mathbf{t}')^{-1} & \mathbf{r}' \cdot (\mathbf{t}')^{-1} \\ -(\mathbf{t}')^{-1} \cdot \mathbf{r}' & (\mathbf{t}')^{-1} \end{bmatrix}, \quad (\text{A9})$$

where \mathbf{t} and \mathbf{r} are the transmission and reflection matrix (respectively) for a wavefunction incoming from the inner lead; similarly, \mathbf{t}' and \mathbf{r}' are the transmission and reflection matrix for a wavefunction incoming from the outer lead.

Appendix B. Solutions for an infinite graphene plane

The clear asymmetry of a current propagating along the p–n junction in the quantum Hall regime (see figure 6(a) in the main text) illustrate an intrinsic feature that is not related to the Corbino geometry. In this appendix we derive analytically the eigenfunctions for the low-energy Hamiltonian of graphene in crossed electric and magnetic fields

$$H = \begin{pmatrix} -e\mathcal{E}x & \xi\pi_x - i\pi_y \\ \xi\pi_x + i\pi_y & -e\mathcal{E}x \end{pmatrix}, \quad (\text{B1})$$

where $\pi_\alpha = -i\hbar\partial_\alpha + eA_\alpha$ with the Landau gauge $\mathbf{A} = (0, Bx)$, and the mass term is neglected for simplicity. (Notice that the electrostatic potential energy term in equation (B1) corresponds to $\phi_V = \pi/2$ in equation (14)). It is clear now that the Hamiltonian (B1) is invariant under the time reversal combined with the magnetic field inversion, namely

$$H(-\xi, -B) = \mathcal{T}_\xi H(\xi, B) \mathcal{T}_\xi^{-1}, \quad (\text{B2})$$

where $\mathcal{T}_\xi = \sigma_0 \mathcal{C}$ is a single-valley time reversal operator with \mathcal{C} denoting complex conjugation. (In the four-component notation, the full time reversal is $\mathcal{T} = \tau_x \otimes \mathcal{T}_\xi$, where τ_x is the Pauli matrix acting on valley degrees of freedom.)

Due to the translation symmetry in the y -direction, H (B1) also commutes with $-i\hbar\partial_y$, and thus we can choose the wavefunction as $\Psi(x, y) = \Phi(x) \exp(ik_y y)$, with the wavenumber k_y , reducing the scattering problem to a single-dimensional one. The corresponding Dirac equation reads

$$\begin{bmatrix} \frac{e\mathcal{E}}{i\hbar v_F} x & \xi\partial_x + k_y + \frac{eB}{\hbar} x \\ \xi\partial_x - k_y + \frac{eB}{\hbar} x & \frac{e\mathcal{E}}{i\hbar v_F} x \end{bmatrix} \Phi(x) = \frac{iE}{\hbar v_F} \Phi(x). \quad (\text{B3})$$

One can further simplify the above equation introducing the dimensionless variable $\chi = l_B^{-1}x + l_B k_y$, where $l_B = \sqrt{\hbar/e|B|}$ is the magnetic length. Without loss of generality, we can suppose that $B > 0$. Equation (B3) can now be written as

$$\begin{bmatrix} -\gamma\chi & -i(\xi\partial_\chi + \chi) \\ -i(\xi\partial_\chi - \chi) & -\gamma\chi \end{bmatrix} \Phi(x) = \varepsilon\Phi(x), \quad (\text{B4})$$

where we have defined $\gamma = el_B^2 \mathcal{E}/(\hbar v_F)$ and $\varepsilon = l_B[E/(\hbar v_F) - \gamma k_y]$. When considering an infinite graphene plane we can choose (without loosing the generality) the zero Fermi energy ($E_F = 0$), what leads to

$$\varepsilon = -l_B \gamma k_y. \quad (\text{B5})$$

Following [57, 58], we find the solutions of equation (B4) by solving an auxiliary eigensystem

$$\mathcal{H}\varphi(x) = \varepsilon^2\varphi(x) \quad (\text{B6})$$

for the operator

$$\mathcal{H} = \varepsilon(H + \tilde{H}) - H\tilde{H}, \quad (\text{B7})$$

where $\tilde{H} = \sigma_z H \sigma_z$, which is chosen such that each eigenfunction of \mathcal{H} satisfies equation (B4) as well. Equation (B6) can be rewritten as follows

$$\begin{pmatrix} -O_- & i\xi\gamma \\ i\xi\gamma & -O_+ \end{pmatrix} \begin{pmatrix} u \\ v \end{pmatrix} = \varepsilon^2 \begin{pmatrix} u \\ v \end{pmatrix}, \quad (\text{B8})$$

where $O = 2\varepsilon\gamma\chi + \varepsilon^2 - (1 - \gamma^2)\chi^2 + \partial_\chi^2 \pm \xi$, and u, v are spinor elements of the wavefunction $\varphi(x)$.

We can now write down the fourth-order differential equation for u , namely

$$\gamma^2 u + O_+ O_- u = 0, \quad (\text{B9})$$

being equivalent to the set of two second-order equations

$$\sqrt{1 - \gamma^2} u_\pm = \pm[2\gamma\varepsilon\chi + \varepsilon^2 - (1 - \gamma^2)\chi^2 + \partial_\chi^2] u_\pm. \quad (\text{B10})$$

The solutions are

$$u_{\pm} = a^{\pm} D_{-(1\pm 1)/2+w}(\rho) + b^{\pm} D_{-(1\mp 1)/2-w}(i\rho), \quad (\text{B11})$$

where $D_{\nu}(x)$ is the parabolic cylinder function [59], $\rho = \sqrt{2}(\chi - \gamma^2\chi - \gamma\varepsilon)(1 - \gamma^2)^{-3/4}$, $w = \varepsilon^2(1 - \gamma^2)^{-3/2}/2$, and a^{\pm}, b^{\pm} are arbitrary constants. Since we are interested in square-integrable wavefunctions, we set $b^{\pm} = 0$. Using equation (B8), we obtain the full form of the spinor function

$$\begin{pmatrix} u_{\pm} \\ v_{\pm} \end{pmatrix} = a^{\pm} D_{-(1\pm 1)/2+w}(\rho) \times \begin{bmatrix} 1 \\ i(1 \pm \xi\sqrt{1 - \gamma^2})/\gamma \end{bmatrix}. \quad (\text{B12})$$

Both the solutions $(u_+, v_+)^T$ and $(u_-, v_-)^T$, as well as their arbitrary linear combination, satisfy equation (B8). Therefore, we construct an eigenfunction of equation (B6), corresponding to an eigenvalue $\varepsilon^2 > 0$, by taking [60]

$$\varphi_{\varepsilon^2>0}(x) \equiv \begin{pmatrix} u \\ v \end{pmatrix} = A \left[c \begin{pmatrix} u_+ \\ v_+ \end{pmatrix} + \begin{pmatrix} u_- \\ v_- \end{pmatrix} \right], \quad (\text{B13})$$

where $c = \varepsilon[1 + \xi\sqrt{1 - \gamma^2}]/[\sqrt{2}\gamma(1 - \gamma^2)^{3/4}]$, and A is the normalization constant

$$A = \sqrt{\frac{(1 - \gamma^2)^{1/4}\gamma^2(4\sqrt{\pi}l_B)^{-1}}{\Gamma[1 + w](1 + \xi\sqrt{1 - \gamma^2})}}. \quad (\text{B14})$$

The case of $\varepsilon^2 = 0$ (the *zero mode*) is slightly different, and it is instructive to consider it separately. The corresponding solution of equation (B6) reads

$$\varphi_{\varepsilon^2=0}(x) = Ce^{-\sqrt{1-\gamma^2}x^2/2} \begin{pmatrix} i\xi\sqrt{1-\gamma^2-1} \\ \gamma \\ 1 \end{pmatrix}, \quad (\text{B15})$$

with

$$C = \sqrt{\frac{\gamma^2(1 - \gamma^2)^{1/4}}{2\sqrt{\pi}(1 + \xi\sqrt{1 - \gamma^2})l_B}}. \quad (\text{B16})$$

In a general case, the normalization of $\varphi(x)$ leads also to a discrete spectrum of eigenvalues

$$\varepsilon_n^2 = 2(1 - \gamma^2)^{3/2} n, \quad (\text{B17})$$

with $n = 0, 1, 2, \dots$; see [50, 57, 58]. The above, together with equation (B5), implies the wavenumber quantization

$$k_y^{(n)} = \pm \frac{\sqrt{2(1 - \gamma^2)^{3/2}n}}{\gamma l_B}. \quad (\text{B18})$$

We further notice that the zero mode ($n = 0$) lacks the additional twofold degeneracy of higher modes ($n > 0$).

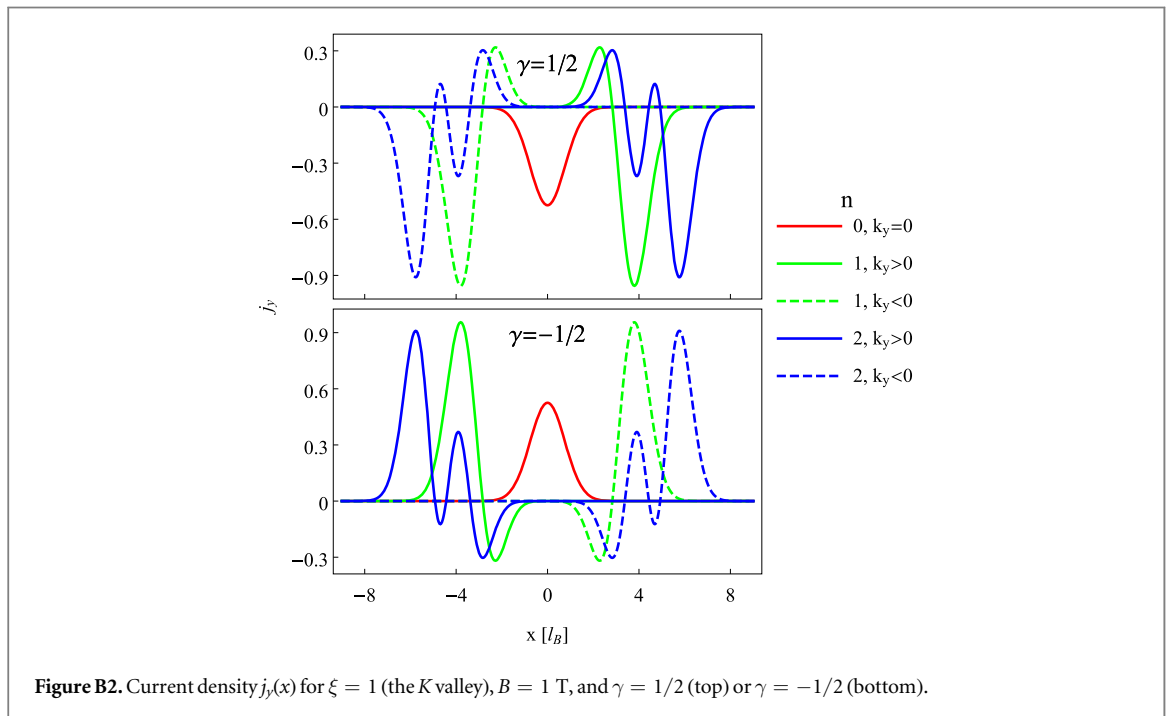
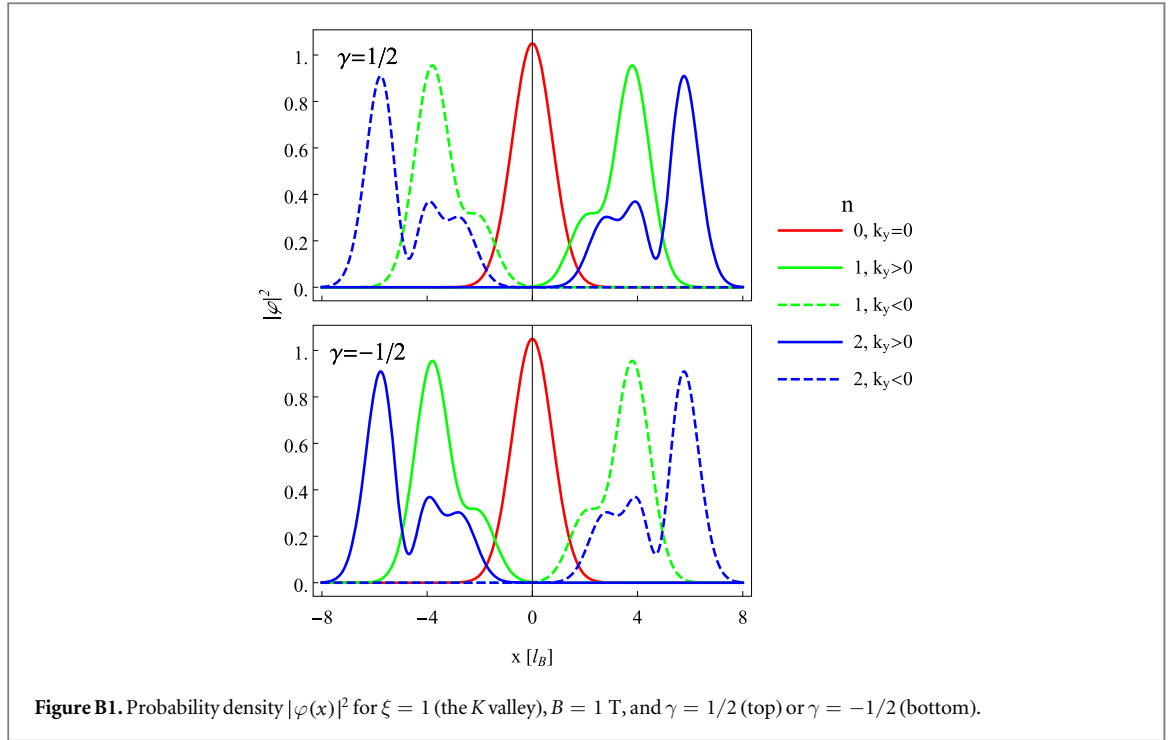
Explicit forms of wavefunctions, given above by equations (B13) and (B15), allows one to calculate the probability density $|\varphi(x)|^2$ (see figure B1) as well as the local current density $j_y = \varphi^\dagger(x) \cdot \sigma_y \cdot \varphi(x)$ (see figure B2).

As we have neglected the mass term throughout this Appendix, the physical quantities displayed in figures B1 and B2 are same for both valleys, K and K' , indicated by $\xi = 1$ or $\xi = -1$ (respectively) in equation (B1). Also, the probability density $|\varphi(x)|^2$ is affected by the direction of electric field, indicated by $\text{sgn } \mathcal{E} \equiv \text{sgn } \gamma$, only in a way that the two solutions for $n > 0$, characterized by opposite wavenumbers (k_y and $-k_y$) are exchanged upon $\gamma \rightarrow -\gamma$, see figure B1. In contrast, the current density $j_y(x)$ also changes sign upon $\gamma \rightarrow -\gamma$, see figure B2. Revisiting the derivation for $B < 0$, one quickly can find that $|\varphi(x)|^2$ and $j_y(x)$ are affected by the magnetic field inversion ($B \rightarrow -B$) at fixed γ in the same way as by the electric field inversion ($\gamma \rightarrow -\gamma$) at fixed B .

Another striking feature of the results presented in figure B2 is that for either the $n = 0$ or $n > 0$ modes, the total current (integrated over x) flows in one direction only, determined by the signs of \mathcal{E} and B . For $n > 0$, this can be attributed to the fact that solutions with $k_y > 0$ and $k_y < 0$ are localized at the opposite sides of a p–n interface, resulting in the *same* sign of the group velocity. For $n = 0$, the solution given by equation (B15) can be regarded as a linear combination of edge states from both sides of the interface, for which the current density is centered precisely at the interface line (as depicted schematically in figure 2 in the main text).

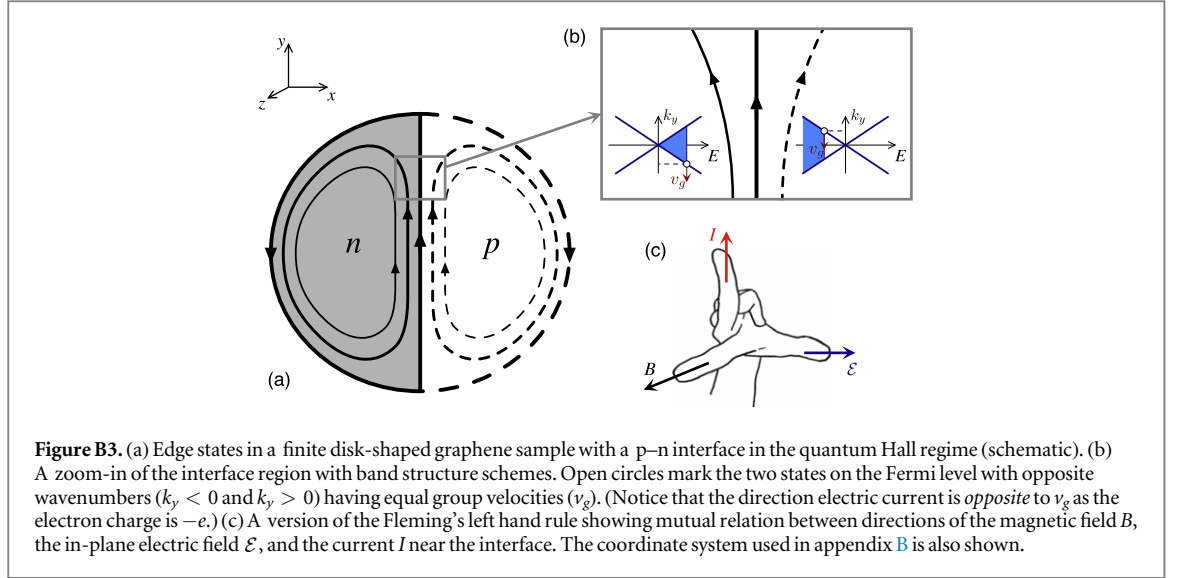
We now comment on the relation between solutions for an infinite plane with trajectories depicted in figure 1.

The snake states (bottom panel in figure 1) can be represent as linear combinations of the solutions with $n = 0$ and $n > 0$, having a property that the full combination propagates in the same direction as each of its components. On the other hand, classical trajectories propagating in the direction (approximately)



perpendicular to the interface (top panel in figure 1) represent finite-size effects having no analogs in an infinite plane. Most intriguing are the trajectories depicted in the middle panel of figure 1, propagating in *both* directions along the interface. Formally, this is possible since the total current, considered as a quadratic form, is neither positively nor negatively defined, and thus a generic quantum state composed of eigenstates with different n -s may also carry the current in opposite direction than each of the components.

In real sample of a finite size, edge states associated with a p-n junction derived in this appendix are always accompanied by edge states close to a physical system boundary transporting the charge in opposite direction, see figure B3(a). When a disk-shaped sample is clamped with circular electrodes, forming the Corbino setup, edge currents are eliminated by the outer lead and the schematic current distribution for the lowest modes, visualized in figure B3(b), may be closely reproduced by the physical current density (see figure 6(a) in the main text). Remarkably, the familiar Fleming's left hand rule, relating the directions of the current, the magnetic field,



and the charge displacement (or the in-plane electric field) has also a version for graphene p–n junction in the quantum Hall regime, see figure B3(c).

Appendix C. Mass confinement and the valley separation

We argue here that the mechanism behind spatial separation of currents in different valleys, appearing for a nonzero mass term (see figure 6(b) in the main text), can essentially be understood by analyzing the zero-energy wavefunction in the presence of infinite mass confinement proposed in the seminal work by Berry and Mondragon [61].

In the absence of electric field ($\mathcal{E} = 0$), a general zero-energy solution of equation (B3) for $\xi = 1$ (the K valley) can be written as [62]

$$\Phi_{0,k_y,\xi=1}^{[\mathcal{E}=0]}(x) = C_1 \begin{bmatrix} 0 \\ e^{-\chi^2/2} \end{bmatrix} + C_2 \begin{bmatrix} e^{\chi^2/2} \\ 0 \end{bmatrix}, \quad (\text{C1})$$

with C_1 and C_2 being arbitrary complex numbers, and $\chi = l_B^{-1}x + l_B k_y$ again. For $\xi = -1$ (the K' valley), the two basis solutions on the right-hand side of equation (C1) have interchanged spinor components.

Neglecting the intervalley scattering, one can show that confinement of the carriers in a bounded domain implies zero outward current at any point of the boundary at each valley ($\xi = \pm 1$), namely

$$j_{\mathbf{n}(\alpha)} = \langle \xi \sigma_x \cos \alpha + \sigma_y \sin \alpha \rangle_{\Phi_\xi} = 0, \quad (\text{C2})$$

where $\mathbf{n}(\alpha) = (\cos \alpha, \sin \alpha)$ is the unit vector normal to the boundary, and the spinor wavefunction $\Phi_\xi = (\Phi_{\xi,A}, \Phi_{\xi,B})^T$. Equation (C2) can be rewritten as

$$\xi \cos \alpha \operatorname{Re}(\Phi_{\xi,A}^* \Phi_{\xi,B}) + \sin \alpha \operatorname{Im}(\Phi_{\xi,A}^* \Phi_{\xi,B}) = 0, \quad (\text{C3})$$

which is equivalent to

$$\left(\frac{\Phi_{\xi,B}}{\Phi_{\xi,A}} \right)^\xi = i\mathcal{B} \exp(i\alpha), \quad (\text{C4})$$

where \mathcal{B} is real and depends on the physical nature of the confinement [61].

Infinite mass confinement at $x = 0$, restricting the wavefunction to the right hemiplane ($x > 0$), corresponds to $\mathcal{B} = 1$ and $\alpha = \pi$ in equation (C4) and leads to the boundary condition

$$\Phi_{\xi,A}|_{x=0} = i\xi \Phi_{\xi,B}|_{x=0}. \quad (\text{C5})$$

Subsequently, the coefficients in equation (C1) follow

$$C_{\xi,2} = i\xi C_{\xi,1} \exp(-k_y^2 l_B^2). \quad (\text{C6})$$

The vertical current density for the zero-energy solution is

$$j_y = \langle \sigma_y \rangle_{\Phi_{0,k_y,\xi}^{[\mathcal{E}=0]}} = -2\xi |C_{\xi,1}|^2 \exp(-k_y^2 l_B^2), \quad (\text{C7})$$

where the last equality follows from equation (C6).

Clearly, the uniform current in equation (C7) changes sign upon the valley exchange ($\xi \rightarrow -\xi$), providing a qualitative understanding of the valley separation, as the effect associated with zero-energy mode should overrule the effects originating from higher modes for a generic system close to the charge-neutrality point (allowing for $|k_y l_B| \ll 1$).

ORCID iDs

Adam Rycerz  <https://orcid.org/0000-0001-7873-0183>

References

- [1] Banerjee M, Heiblum M, Umansky V, Feldman D E, Oreg Y and Stern A 2018 Observation of half-integer thermal Hall conductance *Nature* **559** 205
- [2] Mross D F, Oreg Y, Stern A, Margalit G and Heiblum M 2018 Theory of disorder-induced half-integer thermal hall conductance *Phys. Rev. Lett.* **121** 026801
- [3] Beenakker C W J, Emary C, Kindermann M and van Velsen J L 2003 Proposal for production and detection of entangled electron-hole pairs in a degenerate electron gas *Phys. Rev. Lett.* **91** 147901
- [4] Williams J R, Dicarolo L and Marcus C M 2007 Quantum hall effect in a gate-controlled p–n junction of graphene *Science* **317** 638
- [5] Abanin D A and Levitov L S 2007 Quantized transport in graphene p–n junctions in a magnetic field *Science* **317** 641
- [6] Carmier P, Lewenkopf C and Ullmo D 2011 Semiclassical magnetotransport in graphene n–p junctions *Phys. Rev. B* **84** 195428
- [7] Zimmermann K, Jordan A, Gay F, Watanabe K, Taniguchi T, Han Z, Bouchiat V, Sellier H and Sacépé B 2017 Tunable transmission of quantum Hall edge channels with full degeneracy lifting in split-gated graphene devices *Nat. Commun.* **8** 14983
- [8] Qi C, Ouyang L and Hu J 2018 Realizing robust large-gap quantum spin Hall state in 2D HgTe monolayer on insulating substrate *2D Mater* **5** 045012
- [9] Fujita M, Wakabayashi K, Nakada K and Kusakabe K 1996 Peculiar localized state at zigzag graphite edge *J. Phys. Soc. Japan* **65** 1920
- [10] Nakada K, Fujita M, Dresselhaus G and Dresselhaus M S 1996 Edge state in graphene ribbons: nanometer size effect and edge shape dependence *Phys. Rev. B* **54** 1795
- [11] Colomé E and Franz M 2018 Antichiral edge states in a modified Haldane nanoribbon *Phys. Rev. Lett.* **120** 086603
- [12] Schaibley J R, Yu H, Clark G, Rivera P, Ross J S, Seyler K L, Yao W and Xu X 2016 Valleytronics in 2D materials *Nat. Rev. Mater.* **1** 16055
- [13] Rycerz A, Tworzydło J and Beenakker C W J 2007 Valley filter and valley valve in graphene *Nat. Phys.* **3** 172
- [14] Rycerz A 2008 Nonequilibrium valley polarization in graphene nanoconstrictions *Phys. Status Solidi a* **205** 1281
- [15] Gunlycke D and White C T 2011 Graphene valley filter using a line defect *Phys. Rev. Lett.* **106** 136806
- [16] Akhmerov A R, Bardarson J H, Rycerz A and Beenakker C W J 2008 Theory of the valley-valve effect in graphene nanoribbons *Phys. Rev. B* **77** 205416
- [17] Wimmer M, Adagideli I, Berber S, Tománek D and Richter K 2008 Spin currents in rough graphene nanoribbons: universal fluctuations and spin injection *Phys. Rev. Lett.* **100** 177207
- [18] Zhai F, Ma Y and Zhang Y-T 2011 A valley-filtering switch based on strained graphene *J. Phys.: Condens. Matter.* **23** 385302
- [19] Jiang Y, Low T, Chang K, Katsnelson M I and Guinea F 2013 Generation of pure bulk valley current in graphene *Phys. Rev. Lett.* **110** 046601
- [20] Settnes M, Power S R, Brandbyge M and Jauho A-P 2016 Graphene nanobubbles as valley filters and beam splitters *Phys. Rev. Lett.* **117** 276801
- [21] Milovanović S P and Peeters F M 2016 Strain controlled valley filtering in multi-terminal graphene structures *Appl. Phys. Lett.* **109** 203108
- [22] Zhang X-P, Huang C and Cazalilla M A 2017 Valley Hall effect and nonlocal transport in strained graphene *2D Mater.* **4** 024007
- [23] Zhang Y, Guo B, Zhai F and Jiang W 2018 Valley-polarized edge pseudomagnetoplasmons in graphene: a two-component hydrodynamic model *Phys. Rev. B* **97** 115455
- [24] Pályi A and Burkard G 2011 Disorder-mediated electron valley resonance in carbon nanotube quantum dots *Phys. Rev. Lett.* **106** 086801
- [25] Schroer A, Silvestrov P G and Recher P 2015 Valley-based Cooper pair splitting via topologically confined channels in bilayer graphene *Phys. Rev. B* **92** 241404(R)
- [26] Cheng S-G, Liu H, Jiang H, Sun Q-F and Xie X C 2018 Manipulation and characterization of the valley-polarized topological kink states in graphene-based interferometers *Phys. Rev. Lett.* **121** 156801
- [27] Pan H, Li X, Zhang F and Yang S A 2015 Perfect valley filter in a topological domain wall *Phys. Rev. B* **92** 041404(R)
- [28] Gorbachev R et al 2014 Detecting topological currents in graphene superlattices *Science* **346** 448
- [29] Mak K F, McGill K L, Park J and McEuen P L 2014 The valley Hall effect in MoS₂ transistors *Science* **344** 1489
- [30] Shimazaki Y, Yamamoto M, Borzenets I V, Watanabe K, Taniguchi T and Tarucha S 2015 Generation and detection of pure valley current by electrically induced Berry curvature in bilayer graphene *Nat. Phys.* **11** 1032
- [31] Rickhaus P, Makk P, Liu M-H, Tóvári E, Weiss M, Maurand R, Richter K and Schönenberger C 2015 Snake trajectories in ultraclean graphene p–n junctions *Nat. Commun.* **6** 6470
- [32] Makk P, Handschin C, Tovari E, Watanabe K, Taniguchi T, Richter K, Liu M-H and Schönenberger C 2018 Coexistence of classical snake states and Aharonov–Bohm oscillations along graphene p–n junctions *Phys. Rev. B* **98** 035413
- [33] Liu Y, Tiwari R P, Brada M, Bruder C, Kuznetsov F V and Mele E J 2015 Snake states and their symmetries in graphene *Phys. Rev. B* **92** 235438
- [34] Rycerz A 2010 Magneto conductance of the Corbino disk in graphene *Phys. Rev. B* **81** 121404(R)
- [35] Katsnelson M I 2010 Aharonov–Bohm effect in undoped graphene: magnetotransport via evanescent waves *Europhys. Lett.* **89** 17001
- [36] Peters E C, Giesbers A J M, Burghard M and Kern K 2014 Scaling in the quantum Hall regime of graphene Corbino devices *Appl. Phys. Lett.* **104** 203109
- [37] Kumar M, Laitinen A and Hakonen P 2018 Unconventional fractional quantum Hall states and Wigner crystallization in suspended Corbino graphene *Nature Commun.* **9** 2776
- [38] Katsnelson M I 2012 *Graphene: Carbon in Two Dimensions* (Cambridge: Cambridge University Press) ch 1

- [39] Boukhvalov D W and Katsnelson M I 2009 Chemical functionalization of graphene *J. Phys.: Condens. Matter* **21** 344205
- [40] Haberer D et al 2010 Tunable band gap in hydrogenated quasi-free-standing graphene *Nano Lett.* **10** 3360
- [41] Hong J, Bekyarova E, de Heer W A, Haddon R C and Khizroev S 2013 Chemically engineered graphene-based 2D organic molecular magnet *ACS Nano* **7** 10011
- [42] Sachs B, Wehling T O, Katsnelson M I and Lichtenstein A I 2011 Adhesion and electronic structure of graphene on hexagonal boron nitride substrates *Phys. Rev. B* **84** 195444
- [43] Yankowitz M, Xue J and LeRoy B J 2014 Graphene on hexagonal boron nitride *J. Phys.: Condens. Matter* **26** 303201
- [44] Rycerz A 2013 Strain-induced transitions to quantum chaos and effective time-reversal symmetry breaking in triangular graphene nanoflakes *Phys. Rev. B* **87** 195431
- [45] Rut G and Rycerz A 2016 Trigonal warping, pseudodiffusive transport, and finite-system version of the Lifshitz transition in magnetoconductance of bilayer graphene Corbino disks *Phys. Rev. B* **93** 075419
- [46] Landauer R 1970 Electrical resistance of disordered one-dimensional lattices *Phil. Mag.* **21** 863
- [47] Büttiker M 1992 Scattering theory of current and intensity noise correlations in conductors and wave guides *Phys. Rev. B* **46** 12485
- [48] Müller M, Schmalian J and Fritz L 2009 Graphene: a nearly perfect fluid *Phys. Rev. Lett.* **103** 025301
- [49] Lucas A and Fong K C 2018 Hydrodynamics of electrons in graphene *J. Phys.: Condens. Matter* **30** 053001
- [50] Lukose V, Shankar R and Baskaran G 2007 Novel electric field effects on Landau levels in graphene *Phys. Rev. Lett.* **98** 116802
- [51] Shytov A, Rudner M, Gu N, Katsnelson M and Levitov L 2009 Atomic collapse, Lorentz boosts, Klein scattering, and other quantum-relativistic phenomena in graphene *Sol. State Commun.* **149** 1087
- [52] Beenakker C W J 2008 Andreev reflection and Klein tunneling in graphene *Rev. Mod. Phys.* **80** 1337
- [53] Wimmer M 2009 Quantum transport in nanostructures: from computational concepts to spintronics in graphene and magnetic tunnel junctions *PhD Thesis* Regensburg University, Germany ch 6
- [54] Bardarson J H, Tworzydło J, Brouwer P W and Beenakker C W J 2007 Demonstration of one-parameter scaling at the Dirac point in graphene *Phys. Rev. Lett.* **99** 106801
- [55] Rycerz A 2012 Random matrices and quantum chaos in weakly-disordered graphene nanoflakes *Phys. Rev. B* **85** 245424
- [56] Burden R L and Faires J D 2011 *Numerical Analysis* (Boston: Brooks/Cole) ch 5
- [57] Peres N M R and Castro E V 2007 Algebraic solution of a graphene layer in transverse electric and perpendicular magnetic fields *J. Phys.: Condens. Matter* **19** 406231
- [58] Nath D and Roy P 2014 Dirac oscillator in perpendicular magnetic and transverse electric fields *Ann. Phys.* **351** 13
- [59] Abramowitz M and Stegun I A (ed) 1965 *Handbook of Mathematical Functions* (New York: Dover Publications) ch 19
- [60] MacDonald A H 1983 Quantized Hall conductance in a relativistic two-dimensional electron gas *Phys. Rev. B* **28** 2235
- [61] Berry M V and Mondragon R I 1987 Neutrino billiards: time-reversal symmetry-breaking without magnetic fields *Proc. R. Soc. A* **41** 53
- [62] Prada E, San-Jose P, Wunsch B and Guinea F 2007 Pseudo-diffusive magnetotransport in graphene *Phys. Rev. B* **75** 113407

Conductivity scaling and the effects of symmetry-breaking terms in bilayer graphene Hamiltonian

Dominik Suszalski,¹ Grzegorz Rut,^{1,2} and Adam Rycerz¹

¹Marian Smoluchowski Institute of Physics, Jagiellonian University, Łojasiewicza 11, PL-30348 Kraków, Poland

²CRIF sp. z o.o., Lublańska 38, PL-31476 Kraków, Poland



(Received 9 December 2019; accepted 11 March 2020; published 30 March 2020)

We study the ballistic conductivity of bilayer graphene in the presence of symmetry-breaking terms in an effective Hamiltonian for low-energy excitations, such as the trigonal-warping term (γ_3), the electron-hole symmetry-breaking interlayer hopping (γ_4), and the staggered potential (δ_{AB}). Earlier, it was shown that for $\gamma_3 \neq 0$, in the absence of remaining symmetry-breaking terms (i.e., $\gamma_4 = \delta_{AB} = 0$), the conductivity (σ) approaches the value of $3\sigma_0$ for the system size $L \rightarrow \infty$ [with $\sigma_0 = 8e^2/(\pi h)$ being the result in the absence of trigonal warping, $\gamma_3 = 0$]. We demonstrate that $\gamma_4 \neq 0$ leads to the divergent conductivity ($\sigma \rightarrow \infty$) if $\gamma_3 \neq 0$, or to the vanishing conductivity ($\sigma \rightarrow 0$) if $\gamma_3 = 0$. For realistic values of the tight-binding model parameters, $\gamma_3 = 0.3$ eV, $\gamma_4 = 0.15$ eV (and $\delta_{AB} = 0$), the conductivity values are in the range $\sigma/\sigma_0 \approx 4 - 5$ for $100 \text{ nm} < L < 1 \mu\text{m}$, in agreement with existing experimental results. The staggered potential ($\delta_{AB} \neq 0$) suppresses zero-temperature transport, leading to $\sigma \rightarrow 0$ for $L \rightarrow \infty$. Although $\sigma = \sigma(L)$ is no longer universal, the Fano factor approaches the pseudodiffusive value ($F \rightarrow 1/3$ for $L \rightarrow \infty$) in any case with nonvanishing σ (otherwise, $F \rightarrow 1$), signaling the transport is ruled by evanescent waves. Temperature effects are briefly discussed in terms of a phenomenological model for staggered potential $\delta_{AB} = \delta_{AB}(T)$ showing that, for $0 < T \leq T_c \approx 12$ K and $\delta_{AB}(0) = 1.5$ meV, $\sigma(L)$ is noticeably affected by T for $L \gtrsim 100$ nm.

DOI: [10.1103/PhysRevB.101.125425](https://doi.org/10.1103/PhysRevB.101.125425)

I. INTRODUCTION

The universal conductivity of monolayer graphene (MLG), $\sigma_{\text{MLG}} = 4e^2/(\pi h)$ (with the elementary charge e and the Planck constant h), accompanied by the pseudodiffusive shot noise (quantified by the Fano factor $F = 1/3$), is one of the most recognizable landmarks of the Dirac nature of electrons that dwell in this material [1–5]. These unique characteristics are linked to the dominant role of transport via evanescent waves in graphene near the charge-neutrality point [6]. What is more, the effective Hamiltonian for low-energy excitations,

$$H_{\text{MLG}} = v_F(p_x\sigma_x + p_y\sigma_y), \quad (1)$$

where $v_F = \sqrt{3}t_0a/(2\hbar) \approx 10^6$ m/s is the energy-independent Fermi velocity (with $t_0 \approx 3$ eV the nearest-neighbor hopping integral and $a = 0.246$ nm the lattice spacing), $p_j = -i\hbar\partial_j$ are in-plane momentum operators, and σ_j are the Pauli matrices acting on the sublattice degree of freedom (with $j = x, y$), possesses several symmetries which are crucial for the simplicity of transport properties. (We further note that the absence of valley-coupling factors is supposed throughout the paper, and the discussion is limited to the K valley.) These include the rotational invariance (RI), the electron-hole symmetry (EHS), and the sublattice equivalence (SE), which is embedded in the so-called

symplectic symmetry (or time-reversal symmetry in a single valley) [7,8].

In bilayer graphene (BLG) the situation is more complex due to the couplings between the layers [9–13]. Historically, the effective Hamiltonians for BLG were constructed by taking only the leading tight-binding parameters of the Slonczewski-Weiss-McClure model [14,15], which are indicated in Fig. 1(a).

Even in the simplest possible approach [9,10], including the nearest-neighbor interlayer hopping γ_0 (being numerically different than t_0) and the direct interlayer hopping γ_1 , SE is already eliminated due to the inequivalence of sites connected by γ_1 (dimer sites) and the remaining ones (nondimer sites), giving an opportunity to open the band gap by perpendicular electric field introducing the layer inequivalence [16]. (The second-nearest-neighbor interlayer hopping, formally breaking EHS, is usually omitted as—in the low-energy limit—it only shifts the charge-neutrality point by a constant value; see Ref. [17].) Quite surprisingly, the approach of Refs. [9,10] leads to the conductivity $\sigma_0 = 2\sigma_{\text{MLG}} = 8e^2/(\pi h)$ and $F = 1/3$ (in the absence of a gap), as one could expect for two *decoupled* layers. The results are also size independent, provided that $W \gg L \gg l_\perp$, with the sample width W , the length L marked in Fig. 1(b), and $l_\perp = \sqrt{3}a\gamma_0/(2\gamma_1) \approx 1.77$ nm being a new length scale due the coupling between the layers.

Next, skew-interlayer hopping (or the trigonal-warping term) γ_3 [18] breaks RI, leading to the appearance of three additional Dirac cones at each valley [16]. The effect of γ_3 on quantum transport is also significant [11–13]; namely, the conductivity $\sigma(L)$ is no longer universal but length dependent, approaching the value of $3\sigma_0$ for large L [19]. In contrast,

Published by the American Physical Society under the terms of the [Creative Commons Attribution 4.0 International](https://creativecommons.org/licenses/by/4.0/) license. Further distribution of this work must maintain attribution to the author(s) and the published article's title, journal citation, and DOI.

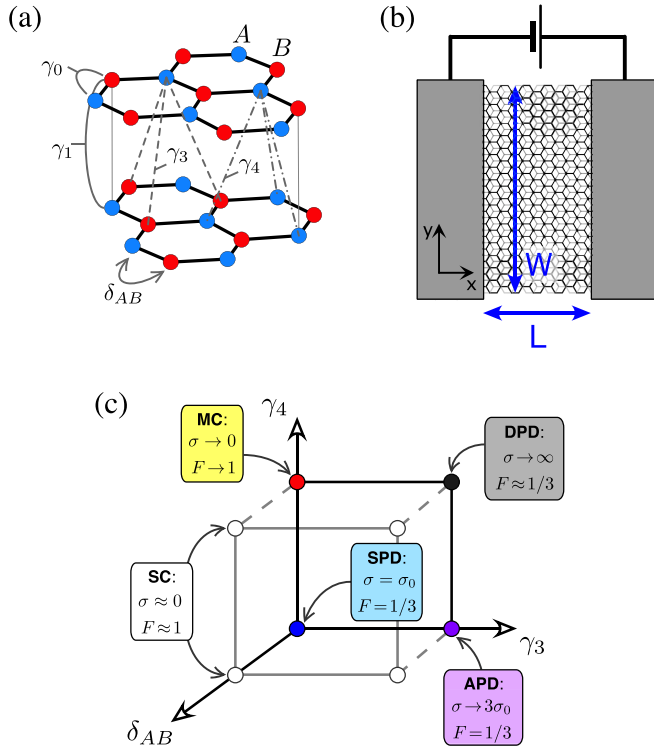


FIG. 1. (a) Tight-binding parameters for Bernal-stacked bilayer graphene, (b) schematics of the system studied in the paper, and (c) outline of our results for the conductivity σ and the Fano factor F . The limits of σ and F in (c) correspond to $L \rightarrow \infty$ at a fixed $W/L \gg 1$, indicating the following transport regimes: the standard pseudodiffusive (SPD), the asymptotic pseudodiffusive (APD), the divergent pseudodiffusive (DPD), the marginally conducting (MC), and the semiconducting (SC). Approximate equalities are used in the cases when the limiting values are closely approached in the mesoscopic range $100 \text{ nm} \leq L \leq 1 \mu\text{m}$.

the Fano factor is unaffected (i.e., $F = 1/3$), showing that the pseudodiffusive nature of charge transport in BLG cannot be attributed any particular value of σ .

In this paper, we complement the previous studies of ballistic charge transport in BLG by examining numerically the effect of EHS-breaking interlayer hopping γ_4 on the σ (and F) dependence on L . The results show that for $\gamma_4 \neq 0$, $\sigma(L)$ may be either divergent (for $\gamma_3 \neq 0$) or vanishing (for $\gamma_3 = 0$) with $L \rightarrow \infty$ (with $F \approx 1/3$ in the first case or $F \rightarrow 1$ in the second case), as marked schematically in Fig. 1(c). These findings extend the collection of possible behaviors associated with transport via evanescent waves in graphene-based systems. The role of an intrinsic (i.e., not related to the external electric field but rather interaction induced) band gap reported by some experimental works [20–23] (and parametrized here by the staggered potential δ_{AB}) is also discussed.

The remaining part of the paper is organized as follows. In Sec. II we present the model Hamiltonian and discuss how each of the symmetry-breaking terms (γ_3 , γ_4 , or δ_{AB}) affects the low-energy dispersion relation. Then, in Sec. III we demonstrate, by means of numerical mode matching for the Dirac equation, the behavior of σ and F with growing L separately in the presence and in the absence of each

symmetry breaking. The concluding remarks are given in Sec. IV.

The numerical results presented in the main text are supplemented with the explicit mode-matching analysis for the special cases of $\gamma_3 \neq 0$, $\gamma_4 = \delta_{AB} = 0$ (Appendix A) and $\gamma_3 = \delta_{AB} = 0$, $\gamma_4 \neq 0$ (Appendix B).

II. THE MODEL

We start from the minimal version of the four-band Hamiltonian [16], in which all the symmetry breakings mentioned in Sec. I are quantified by independent parameters:

$$H_{\text{BLG}} = \begin{pmatrix} \delta_{AB}/2 & v_0\pi & \gamma_1 & -v_4\pi^\dagger \\ v_0\pi^\dagger & -\delta_{AB}/2 & -v_4\pi^\dagger & v_3\pi \\ \gamma_1 & -v_4\pi & -\delta_{AB}/2 & v_0\pi^\dagger \\ -v_4\pi & v_3\pi^\dagger & v_0\pi & \delta_{AB}/2 \end{pmatrix}, \quad (2)$$

where $\pi = e^{-i\theta}(p_x + ip_y)$, $\pi^\dagger = e^{i\theta}(p_x - ip_y)$, with the angle θ (between an armchair direction and the x axis) defining the crystallographic orientation of the sample, $v_0 = \sqrt{3}a\gamma_0/(2\hbar)$, $v_3 = v_0\gamma_3/\gamma_0$, and $v_4 = v_0\gamma_4/\gamma_0$. In the forthcoming numerical discussion, we set $\theta = \pi/4$, $\gamma_0 = 3.16 \text{ eV}$, and $\gamma_1 = 0.381 \text{ eV}$ [24]; for each of the remaining parameters the cases of zero and nonzero value are studied independently to demonstrate the impact of a particular symmetry breaking on ballistic transport. Namely, we took $\gamma_3 = 0$ or 0.3 eV , $\gamma_4 = 0$ or 0.15 eV , and $\delta_{AB} = 0$ or 1.5 meV .

Our specific choice of the staggered potential δ_{AB} in the Hamiltonian H_{BLG} (2) follows from the demand that it opens a band gap without breaking EHS, which is solely controlled by γ_4 . (In the parametrization of Ref. [16] the energy difference between dimer and nondimer sites V also breaks EHS; here we set $V = 0$). Physically, δ_{AB} represents the irreducible part of a gap (i.e., one that cannot be closed by external electric fields) and can be attributed to charge or spin order which may appear in the BLG ground state when electron-electron repulsive interactions are taken into account [25,26].

In Fig. 2 we present the low-energy band structure following from the Hamiltonian H_{BLG} (2) by displaying the cross sections, for $p_y = \hbar k_y = 0$, of dispersion relations for eight different combinations of symmetry-breaking parameters γ_3 , γ_4 , and δ_{AB} . An apparent feature visible in Fig. 2(a) is the energy shift of a secondary Dirac cone (same for all three secondary cones) due to EHS breaking for $\gamma_4 \neq 0$ [see Fig. 2(c) for a comparison], making it impossible (for $\gamma_3 \neq 0$ and $\delta_{AB} = 0$) to achieve the exact zero-doping case, in which the transport is fully carried by evanescent waves. In contrast, for $\gamma_3 = 0$ [see Figs. 2(e) and 2(f)], the effects of γ_4 are marginal (apart from clear electron-hole asymmetries visible for $\gamma_4 \neq 0$), and the zero-doping case can be achieved for both $\gamma_4 = 0$ or $\gamma_4 \neq 0$. For $\delta_{AB} \neq 0$, we have an indirect band gap for $\gamma_4 \neq 0$ and $\gamma_4 \neq 0$ [see Fig. 2(b)], or direct band gaps in the remaining cases, allowing one to obtain the zero doping by adjusting the Fermi level to the gap.

The consequences of these features for BLG transport properties are discussed next.

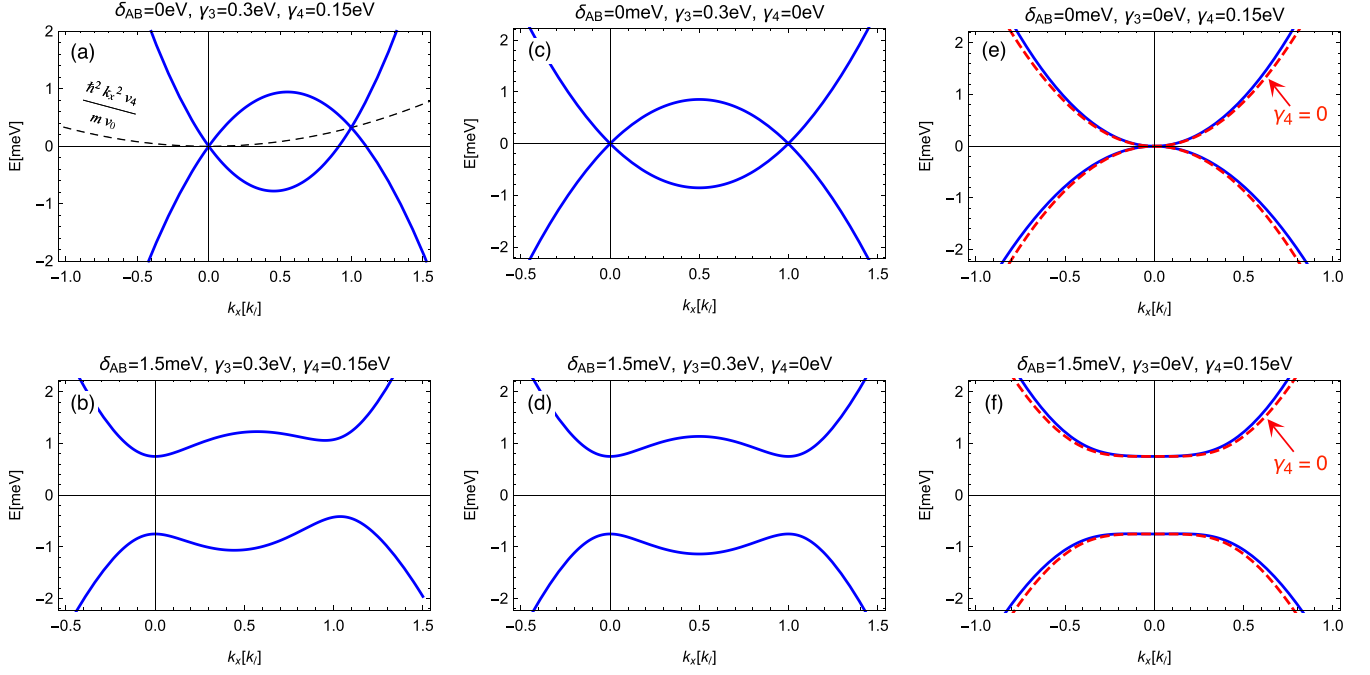


FIG. 2. (a)–(f) Band energies for the Hamiltonian H_{BLG} given by Eq. (2) with $\theta = 0$. Solid lines correspond to the parameters $(\delta_{AB}, \gamma_3, \gamma_4)$ specified in each panel. The dashed black line in (a) marks the parabolic correction due to the electron-hole symmetry breaking interlayer hopping γ_4 (see the explicit formula with $m = \gamma_1/2v_0^2$). The dashed red lines in (e) and (f) depict the reference band structure for $\gamma_3 = \gamma_4 = 0$. The wavenumber $k_x = p_x/\hbar$ is specified in units of $k_l = \frac{2}{3}\sqrt{3}\gamma_1\gamma_3/(av_0^2) \approx 0.05 \text{ nm}^{-1}$, being the k_x position of a secondary Dirac cone calculated for the parameters as listed in (c). Each panel displays the cross section taken at $k_y = 0$.

III. RESULTS AND DISCUSSION

A. Zero-temperature charge transport

We employ the Landauer-Büttiker expressions for zero-temperature conductivity and the Fano factor in the linear-response regime [27], namely,

$$\sigma(T \rightarrow 0) = \frac{g_0 L}{W} \text{Tr}(\mathbf{t}\mathbf{t}^\dagger), \quad (3)$$

$$F = \frac{\text{Tr}[\mathbf{t}\mathbf{t}^\dagger(\mathbf{1} - \mathbf{t}\mathbf{t}^\dagger)]}{\text{Tr}(\mathbf{t}\mathbf{t}^\dagger)}, \quad (4)$$

with the conductance quantum $g_0 = 4e^2/h$ accounting for spin and valley degeneracies. In order to determine the transmission matrix at a given Fermi energy, $\mathbf{t} = \mathbf{t}(E)$, for a rectangular sample attached to the two heavily doped regions, we employ the computational scheme similar to that presented in Ref. [13], with a numerical stabilization introduced in Ref. [28]. In brief, at finite-precision arithmetics, the mode-matching equations may become ill defined for sufficiently large L , as they contain both exponentially growing and exponentially decaying coefficients. This difficulty is overcome by dividing the sample area into N_{div} consecutive, equally long parts and matching the wave functions for all (i.e., $N_{\text{div}} + 1$) interfaces. Typically, using the double-precision arithmetic, we put $N_{\text{div}} = \lfloor L/(40l_\perp) \rfloor + 1$, with $\lfloor x \rfloor$ denoting the floor of x .

Our numerical results for $E = 0$ are presented in Figs. 3 and 4. As the debate on the ground-state nature of BLG is currently ongoing [26] and the existing experimental results are far from being consistent [20–23, 29, 30], we examine eight

possible scenarios by setting different values of the parameters $(\delta_{AB}, \gamma_3, \gamma_4)$ in the low-energy Hamiltonian H_{BLG} (2), corresponding to the dispersion relations presented in Sec. II.

The behavior of transport properties is relatively simple for $\delta_{AB} = 1.5 \text{ meV}$ (coinciding with the gap reported in Refs. [22, 23]); we observe a fast decay of $\sigma(L)$ with growing L , accompanied by $F \rightarrow 1$ (see the blue lines in Figs. 3 and 4), indicating the insulating (or semiconducting) behavior. The remaining parameters (γ_3 and γ_4) are essentially meaningless in such a case; a slightly elevated conductivity (namely, $\sigma > \sigma_0$) is visible for $\gamma_3 = 0.3 \text{ eV}$ and $L < 100l_\perp$, due to the finite-size effects.

In a gapless case ($\delta_{AB} = 0$) we identify four apparently different behaviors of $\sigma(L)$, depending on whether the remaining parameters (γ_3 and γ_4) take zero- or nonzero values.

For $\delta_{AB} = 0$ and $\gamma_3 = 0.3 \text{ eV}$, the values of $\sigma(L)$ are generically elevated (above σ_0) for any L [black lines in Figs. 3(a) and 3(b)], with the Fano factor $F \approx 1/3$ [black lines in Figs. 4(a) and 4(b)]. Starting from $L \approx 2000l_\perp$, one can further distinguish the behaviors for $\gamma_4 = 0.15 \text{ eV}$ [solid black line in Fig. 3(a)], for which $\sigma(L)$ grows approximately linearly with L , and for $\gamma_4 = 0$ [dashed black line], for which $\sigma(L)$ approaches the value of $3\sigma_0$.

For $\gamma_4 = 0.15 \text{ eV}$, the energy shift of three secondary Dirac cones [see Fig. 2(a)] is equal to

$$\Delta E_l = \frac{\hbar^2 k_l^2 v_4}{m v_0} = 2 \frac{\gamma_1 \gamma_3^2 \gamma_4}{\gamma_0^3} \approx 0.33 \text{ meV}, \quad (5)$$

where $m = \gamma_1/2v_0^2$ and $k_l = \gamma_1 v_3/\hbar v_0^2$, leading to a nonzero number of propagating modes (open channels) at zero energy,

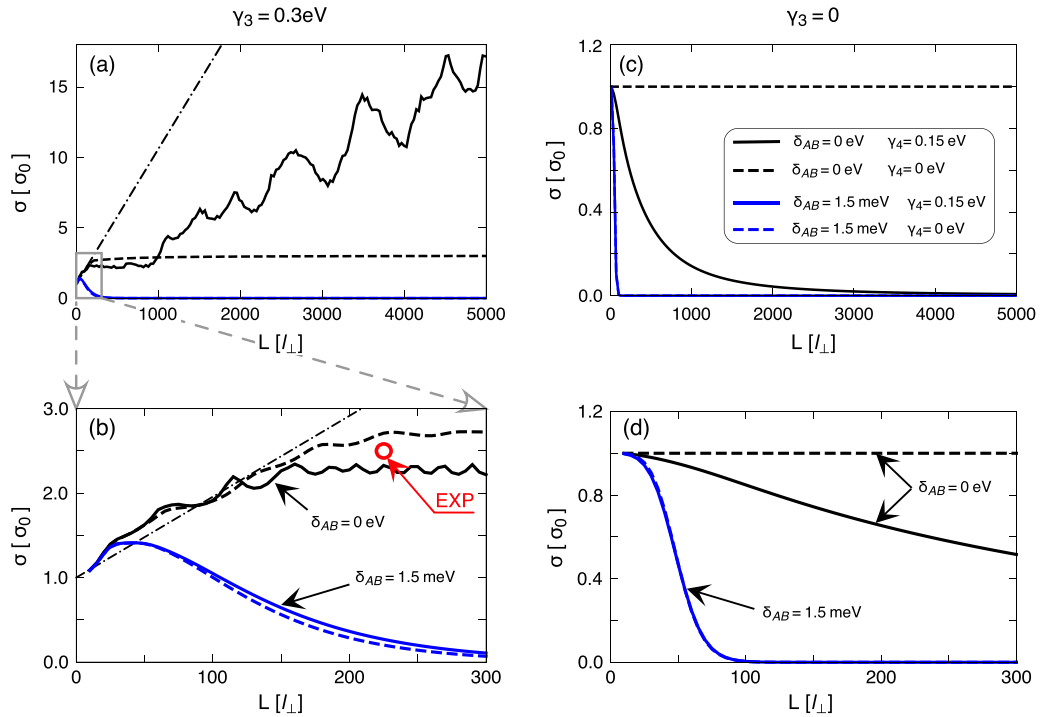


FIG. 3. Conductivity [in units of $\sigma_0 = 8e^2/(\pi h)$] as a function of length L (in units of $l_\perp = \hbar v_0/\gamma_1 = 1.77$ nm) at a fixed $W/L = 20$. The trigonal warping strength is (a, b) $\gamma_3 = 0.3$ eV or (c, d) $\gamma_3 = 0$. Bottom panels are zoom-ins, for small L , of the data presented in top panels. Solid (or dashed) lines in all panels are for $\gamma_4 = 0.15$ eV (or $\gamma_4 = 0$); the staggered potential is $\delta_{AB} = 0$ (black lines) or $\delta_{AB} = 1.5$ meV (blue lines), as indicated with arrows in (b) and (d). The red circle in (b) marks the experimental results of Ref. [29]. Dash-dotted lines in (a) and (b) depict the approximate upper bound given by Eq. (7) in the main text. The line-color encoding shown in (c) is same for all panels.

which can be approximated as [28]

$$N_{\text{open}}(E=0) \approx 0.68 \frac{\Delta E_l W}{\hbar v_3}. \quad (6)$$

Subsequently, the excess conductivity from secondary Dirac cones can roughly be bounded as

$$\sigma(L) - \sigma_0 \lesssim \frac{g_0 N_{\text{open}} L}{W} = 9.6 \times 10^{-3} \sigma_0 \frac{L}{l_\perp}, \quad (7)$$

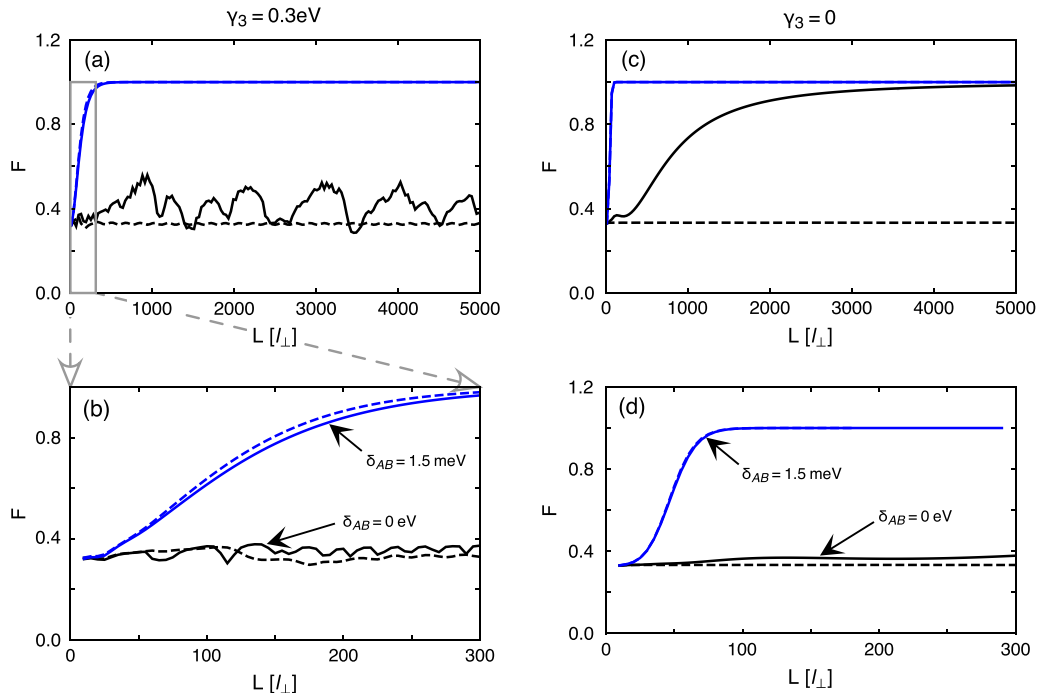


FIG. 4. (a)–(d) The Fano factor F as a function of L . The system parameters and the line-color encoding are the same as in Fig. 3.

with the rightmost equality corresponding to $W/L = 20$ and σ_0 on the left-hand side representing a contribution from evanescent waves in the primary Dirac cone [see the dash-dotted lines in Figs. 3(a) and 3(b)]. The transmission reduction for propagating modes, approximately by a factor of 2, can be attributed to the additional backscattering appearing in the double-barrier geometry, which is usually much weaker for a single barrier [31]. A secondary feature of $\sigma(L)$ is a quasiperiodic oscillation due to the Fabry-Pérot resonances appearing for $L = n\Delta L$, where $n = 1, 2, \dots$, and (up to the order of magnitude) $\Delta L \sim \pi \hbar v_3 / \Delta E_l \approx 340 l_\perp$ [28].

None of these effects is present for $\gamma_4 = 0$, for which the conductivity follows the scenario earlier described in Refs. [12,13]. (In Appendix A, we present the analytical derivation explaining why $\sigma(L) \rightarrow 3\sigma_0$ for $L \rightarrow \infty$ and arbitrarily small $\gamma_3 \neq 0$.) We further notice that the available experimental value in Ref. [29], reporting $\sigma \approx 2.5\sigma_0$ for $L \approx 400 \text{ nm} = 226 l_\perp$ [red circle in Fig. 3(b)], is equally close to both the results for $\gamma_4 = 0$ and 0.15 eV, and the determination of γ_4 via conductivity measurements requires a sample length exceeding $L \gtrsim 2 \mu\text{m}$.

For $\delta_{AB} = \gamma_3 = 0$, the conductivity behavior with growing L is a bit more peculiar.

If $\gamma_4 = 0$, we simply have $\sigma(L) = \sigma_0$ and $F = 1/3$ for any $L \gg l_\perp$ [see dashed black lines in Figs. 3(c), 3(d), 4(c), and 4(d)], reproducing the analytical results of Refs. [9,10].

In contrast, if $\gamma_4 = 0.15 \text{ eV}$ (solid black lines) we observe a slow power-law decay of $\sigma(L)$ with growing L , which can be approximated as $\sigma(L) \propto L^{-2.0}$ for $L \gtrsim 1000 l_\perp$, accompanied by $F \rightarrow 1$. Notice that the Fano factor is $F \approx 1/3$ in the range of $L \leq 300 l_\perp$ shown in Fig. 4(d); the convergence to 1 becomes visible for $L \gtrsim 1000 l_\perp$ [see Fig. 4(c)]. Unlike for nonrelativistic electrons [32], we still obtain a finite $\sigma(L)$ in the limit of infinite doping in the leads at fixed W and L , signaling the relativistic nature of charge carriers. The vanishing conductivity for $L \rightarrow \infty$ at a fixed W/L , in the absence of a gap, clearly represents a remarkable feature of the results, providing an opportunity to verify the $\gamma_3 = 0$ model as put forward in Ref. [21] within ballistic transport experiments. A further reasoning that such a behavior appears generically for $\gamma_3 = 0$ and $\gamma_4 \neq 0$ is given in Appendix B.

B. Finite-temperature effects

For $T > 0$ and in the linear-response regime the electronic noise is dominated by the Nyquist-Johnson term of $S(0) \approx 4k_B T \sigma W/L$ [27], and the Fano factor becomes irrelevant. Therefore, we limit our discussion to the temperature-dependent conductivity, which is given by

$$\sigma(T > 0) = \frac{g_0 L}{W} \int dE \text{Tr}(\mathbf{t}\mathbf{t}^\dagger) \left(-\frac{\partial f_{\text{FD}}}{\partial E} \right), \quad (8)$$

where $f_{\text{FD}}(\mu, T, E) = [\exp((E - \mu)/k_B T) + 1]^{-1}$ is the Fermi-Dirac distribution function for a given chemical potential μ , and the remaining symbols are the same as in Eq. (3).

Numerical integration in Eq. (8) is performed, for $\mu = 0$, by taking the energy range of $-E_M \leq E \leq E_M$, with a cut-off energy $E_M = 0.05 \text{ eV}$ (i.e., $E_M > 48 k_B T$ for $T \leq 12 \text{ K}$) being sufficiently high to reach a convergence up to the machine roundoff errors. Additionally, when calculating the

transmission matrix $\mathbf{t}(E)$, we parametrize the staggered potential in the effective Hamiltonian H_{BLG} (2) as follows:

$$\delta_{AB}(T) = \delta_{AB}(0) \begin{cases} \tanh\left(1.74 \sqrt{\frac{T_C}{T} - 1}\right) & \text{if } T \leq T_C \\ 0 & \text{if } T > T_C, \end{cases} \quad (9)$$

with $T_C = 12 \text{ K}$ and $\delta_{AB}(0) = 1.5 \text{ meV}$ reproducing the temperature dependence of a gap reported in Refs. [22,23]. (The gapless case $\delta_{AB}(0) = 0$ is considered separately.)

Our numerical results, for $T = 0$ and the selected temperatures $0 < T \leq T_C$, are presented in Fig. 5. Similarly as in the previous section, the data sets for $\gamma_3 = 0.3 \text{ eV}$ [see Figs. 5(a) and 5(b)] and for $\gamma_3 = 0$ [see Figs. 5(c) and 5(d)] are displayed separately. This time, we limit the presentation to the $\gamma_4 = 0.15 \text{ eV}$ case for clarity (solid lines in all panels), as the curves for $\gamma_4 = 0$ closely follow their $\gamma_4 = 0.15 \text{ eV}$ counterparts, with the exception of $\gamma_3 = \delta_{AB}(0) = 0$ and $T = 0$ [see dashed line in Fig. 5(c)], when the conductivity suppression in the presence of EHS symmetry breaking ($\gamma_4 \neq 0$) is clearly visible.

An apparent feature of the results presented in Fig. 5(a) is that the curves for different temperatures closely follow each other up to $L \lesssim 120 l_\perp$, above which $\sigma(L)$ grows noticeably faster with L for higher T . [Notice that the $T = 0$ curve also shows approximately linear growths with L , which manifests itself for $L \gtrsim 10^3 l_\perp$; see Fig. 3(a).] The position of a coalescence point, $L \approx 120 l_\perp$, can be attributed to fact that above such a length the quantum-size effects are less significant, allowing the finite-temperature effects to dominate transport properties. This can be rationalized taking into account the time-energy uncertainty relation limiting the energy resolution,

$$\delta E \geq \frac{\hbar}{2\tau_{\text{flight}}} = \frac{\hbar v_3}{2L}, \quad (10)$$

with $\tau_{\text{flight}} \approx L/v_3$ being the ballistic time of flight [28], together with the fact that the energy of thermal excitations is $k_B T \gtrsim \Delta E_l$ for $T \gtrsim 4 \text{ K}$, with ΔE_l given by Eq. (5). Subsequently, one can expect that the propagating modes in secondary Dirac cones are employed (by thermal excitations) provided that $\delta E \ll \Delta E_l \lesssim k_B T$, leading to

$$\frac{L}{l_\perp} \gg \frac{\gamma_0^2}{4\gamma_3\gamma_4} \approx 55. \quad (11)$$

For $\gamma_3 = 0$ the above reasoning no longer applies; however, a relatively flat σ dependence on L for $T > 0$ [see Fig. 5(c)] coincides with the divergent lower bound for L in Eq. (11). In such a case, one should rather estimate the time of flight (up to the order of magnitude) as $\tau_{\text{flight}} \sim L/v_0$. In turn, the condition $k_B T \gg \delta E$ allowing the conductivity enhancement by thermal excitations is equivalent to

$$\frac{L}{l_\perp} \gg \frac{\gamma_1}{2k_B T} \approx \frac{2200 \text{ K}}{T}, \quad (12)$$

giving, for instance, $L \gg 440 l_\perp$ for $T = 5 \text{ K}$. The lower bound for L in Eq. (12) allows one to understand why temperature effects on $\sigma(L)$ are noticeably weakened for $\gamma_3 = 0$, comparing to the $\gamma \neq 0$ case.

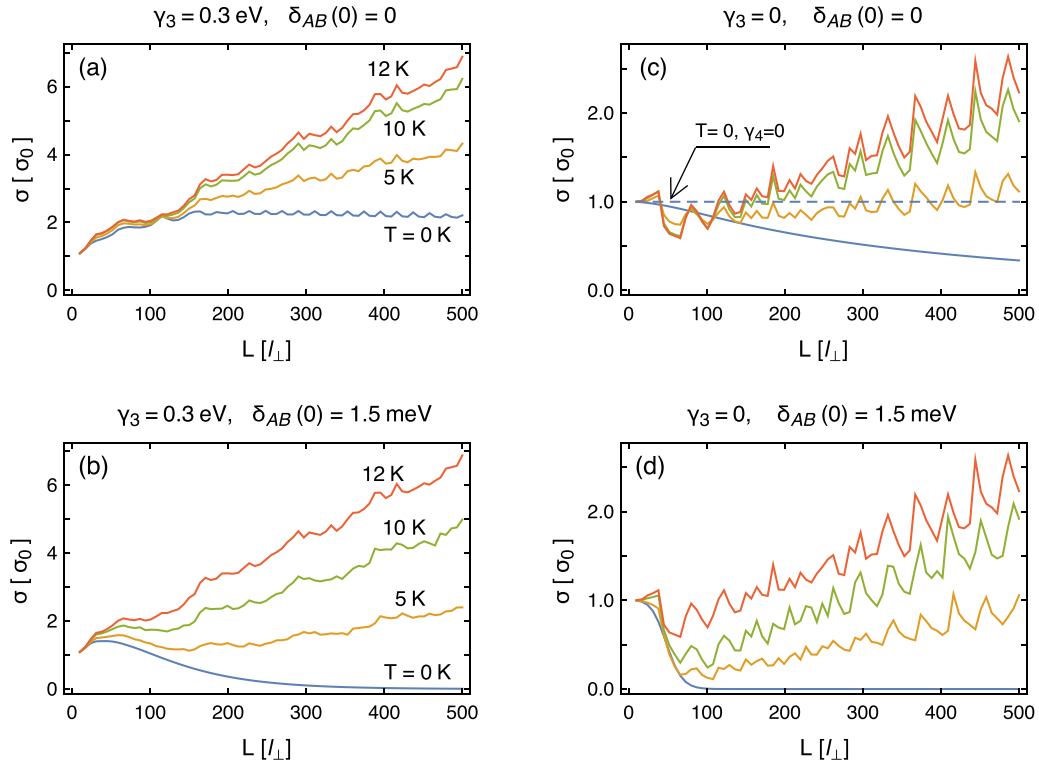


FIG. 5. (a)–(d) Conductivity as a function of L for temperatures $T = 0$ K, $T = 5$ K, $T = 10$ K, and $T = T_C = 12$ K [see Eq. (9) in the main text] indicated by labels in (a) and (b) for all panels. The parameters γ_3 and $\delta_{AB}(0)$ are specified for each panel; the parameter $\gamma_4 = 0.15$ eV for all lines, with the exception of a dashed line for $T = 0$ in (c), for which $\gamma_4 = 0$ (as marked with an arrow).

In the presence of a staggered potential, $\delta_{AB}(0) = 1.5$ meV, the primary temperature effects on $\sigma(L)$ visible in Figs. 5(b) and 5(d) can be attributed to the gap closing for T approaching T_C [see Eq. (9)]. The characteristic system length, above which the value of δ_{AB} becomes significant, derived from the condition for the energy uncertainty $\delta E \ll \delta_{AB}(0)$, reads

$$\frac{L}{l_{\perp}} \gg \begin{cases} \frac{1}{2}\gamma_1\gamma_3/\gamma_0\delta_{AB}(0) \approx 12.1 & \text{if } \gamma_3 \neq 0 \\ \frac{1}{2}\gamma_1/\delta_{AB}(0) \approx 127 & \text{if } \gamma_3 = 0, \end{cases} \quad (13)$$

where we have estimated $\tau_{\text{flight}} \approx L/v_3$ (if $\gamma_3 \neq 0$) or $\tau_{\text{flight}} \sim L/v_0$ (if $\gamma_3 = 0$). This time, our numerical results show that the temperature effects are visible for significantly shorter systems in the $\gamma_3 = 0.3$ eV case, comparing to the $\gamma_3 = 0$ case, in a qualitative agreement with the estimation given in Eq. (13).

IV. CONCLUDING REMARKS

We have investigated, by calculating ballistic transport characteristics within the Landauer-Büttiker formalism, the role of symmetry-breaking terms in the effective Hamiltonian for bilayer graphene. Three such terms, the trigonal warping (γ_3), the electron-hole symmetry-breaking interlayer hopping (γ_4), and the staggered potential (δ_{AB}) quantifying a spontaneous band gap, are independently switched on and off, resulting in different behaviors of the conductivity (σ) and the Fano factor (F) with the increasing system length (L) at a fixed width-to-length ratio (W/L).

In the absence of a gap ($\delta_{AB} = 0$), one can identify three different quantum-transport regimes characterized by the pseudodiffusive shot-noise power, $F = 1/3$: (i) the standard pseudodiffusive regime, characterized by $\sigma(L) = \sigma_0$ [with $\sigma_0 = 8e^2/(\pi h)$ being a double conductivity of a monolayer] and occurring for $\gamma_3 = \gamma_4 = 0$, (ii) the asymptotic pseudodiffusive regime, with $\sigma(L) \rightarrow 3\sigma_0$ for $L \rightarrow \infty$, occurring for $\gamma_3 \neq 0$ and $\gamma_4 = 0$, and (iii) the divergent pseudodiffusive regime, with $\sigma(L) \rightarrow \infty$ for $L \rightarrow \infty$, occurring for $\gamma_3 \neq 0$ and $\gamma_4 \neq 0$. Additionally, for $\gamma_3 = 0$ and $\gamma_4 \neq 0$, the system can be regarded as a marginal conductor, with $\sigma(L) \rightarrow 0$ (showing a power-law decay) and $F \rightarrow 1$ for $L \rightarrow \infty$.

In the presence of a staggered potential at $T = 0$ ($\delta_{AB}(0) > 0$), a semiconducting behavior is observed regardless of the remaining parameters (γ_3 and γ_4); i.e., $\sigma(L) \rightarrow 0$ (showing the exponential decay) and $F \rightarrow 1$ for $L \rightarrow \infty$. For $T > 0$, a zero-gap behavior is gradually restored (for any combination of γ_3 and γ_4) when the energy of thermal excitations $k_B T \gtrsim \delta_{AB}(0)$.

We hope that our numerical results will help verify the bilayer graphene models proposed in the literature, as soon as ballistic samples of the length $L \gtrsim 1 \mu\text{m}$ become available. So far, conductivity measurements for shorter samples [29] suggest that the models neglecting the trigonal warping ($\gamma_3 = 0$) cannot correctly reproduce transport properties in the mesoscopic range, but conclusive information concerning the value of γ_4 is missing.

Apart from the material-science aspects outlined above, the asymptotic conductivity behavior suggests that bilayer graphene represents a model case when discussing the

generality of spontaneous symmetry breaking in quantum systems [33,34]. When σ is considered as an order parameter, our findings can be summarized by putting forward the noncommuting order of limits, as $L \rightarrow \infty$ and the relevant symmetry breakings vanish, namely,

$$\lim_{L \rightarrow \infty} \lim_{d \rightarrow \infty} \lim_{\delta_{AB} \rightarrow 0} \sigma = \lim_{L \rightarrow \infty} \lim_{\delta_{AB} \rightarrow 0} \lim_{d \rightarrow \infty} \sigma = \sigma_0, \quad (14)$$

$$\lim_{d \rightarrow \infty} \lim_{L \rightarrow \infty} \lim_{\delta_{AB} \rightarrow 0} \sigma = \infty, \quad (15)$$

$$\lim_{d \rightarrow \infty} \lim_{\delta_{AB} \rightarrow 0} \lim_{L \rightarrow \infty} \sigma = \lim_{\delta_{AB} \rightarrow 0} [\dots] \sigma = 0, \quad (16)$$

where we have introduced the distance between the layers d (with $d \rightarrow \infty$ corresponding to simultaneous limits of $\gamma_3 \rightarrow 0$ and $\gamma_4 \rightarrow 0$ [35]), and the dots $[\dots]$ in Eq. (16) mark that the order of the two remaining limits is arbitrary in such a case. From this perspective, it becomes clear that both the sublattice and the combined rotational-electron-hole symmetry breakings may appear spontaneously, as consequences of the layer stacking in graphene ($d = \text{const} < \infty$).

The peculiar cases of $\gamma_3 \neq 0$ or $\gamma_4 \neq 0$ in the absence of other symmetry breakings (i.e., $\delta_{AB} = \gamma_4 = 0$ or $\delta_{AB} = \gamma_3 = 0$) do not seem to have as clear a physical interpretation. However, in heterostructures containing graphene, a variety of spontaneous symmetry breakings may appear due to the couplings to surrounding layers, encouraging one to consider also anomalous parameter configurations.

Our considerations are limited to Bernal-stacked bilayer graphene, since other stacking usually opens the band gap leading to the vanishing conductivity. One notable exception is the magic-angle twisted bilayer graphene [36–40] showing a gapless band structure. However, the role of electron-electron interaction in such a system is more significant; in particular, the ground state near the charge-neutrality point is a correlated insulator [38–40]. Therefore, we expect the vanishing zero-energy conductivity to appear generically in bilayer graphene for non-Bernal stackings.

ACKNOWLEDGMENTS

The work was supported by the National Science Centre of Poland (NCN) via Grant No. 2014/14/E/ST3/00256. Computations were partly performed using the PL-Grid infrastructure.

APPENDIX A: TRANSMISSION THROUGH BILAYER GRAPHENE IN THE PRESENCE OF TRIGONAL WARPING ($\gamma_3 \neq 0, \gamma_4 = 0$)

Here, we present the analytical derivation of the total transmission (i.e., transmission probability summed over normal modes), coinciding with the Landauer-Büttiker conductivity [see Eq. (3) in the main text] $\sigma(L) \rightarrow 3\sigma_0$ in the limit of $L, W \rightarrow \infty$, at $W/L = \text{const} \gg 1$. Some partial results were earlier reported in Ref. [12], but the full derivation, to our best knowledge, is missing in the literature.

The dispersion relation for the Hamiltonian given by Eq. (2) in the main text, with $\delta_{AB} = \gamma_4 = 0$, takes the form

$$E^2 = \frac{\gamma_1^2}{2} + \left(v_0^2 + \frac{v_3^2}{2} \right) p^2 \pm \sqrt{\Gamma}, \quad (A1)$$

$$\Gamma = \frac{1}{4} (\gamma_1^2 - v_3^2 p^2)^2 + v_0^2 p^2 (\gamma_1^2 + v_3^2 p^2) + 2\gamma_1 v_3 v_0^2 p^3 \cos(3\varphi), \quad (A2)$$

where $p = \sqrt{p_x^2 + p_y^2}$ and we have set $\theta = 0$ for simplicity (later, we show that the physical results are independent of the lattice orientation in the $L \rightarrow \infty$ limit).

In the vicinity of zero energy ($|E| \rightarrow 0$), there are four solutions of the above equation corresponding to four Dirac cones: the central cone, located at $\mathbf{p} = (p_x, p_y) = (0, 0)$, and three satellite cones, located (in polar coordinates) at $p = \gamma_1 v_3 / v_0^2$, $\varphi = 0, 2\pi/3, 4\pi/3$. Below, we calculate the transmission of the system assuming that the states corresponding to different Dirac cones do not interfere among themselves. Physically, such a supposition corresponds to the conditions for the energy and system sizes

$$|E|, \frac{\hbar v_3}{L}, \frac{\hbar v_3}{W} \ll E_L, \quad (A3)$$

where the Lifshitz energy $E_L = \frac{1}{4} \gamma_1 (v_3 / v_0)^2$. For $\gamma_0 = 3.16$ eV, $\gamma_1 = 0.381$ eV, and $\gamma_3 = 0.3$ eV [24], we have $E_L \approx 1$ meV, and the last two conditions in Eq. (A3) are equivalent to $L, W \gg 4l_{\perp} \gamma_3 / \gamma_0 = 75$ nm.

Expanding the dispersion relation given by Eqs. (A3) and (A4) up to second order around $\mathbf{p} = (0, 0)$, we obtain

$$E^2 = v_3^2 (p_x^2 + p_y^2). \quad (A4)$$

Thus, the central Dirac cone has an isotropic dispersion relation, closely resembling the dispersion relation following from the monolayer graphene Hamiltonian [see Eq. (1) in the main text]; in fact, the only difference is the proportionality coefficient v_3 instead of v_F .

Now, we write the effective single-cone Hamiltonian, corresponding to the dispersion relation given by Eq. (A4):

$$H_{\text{central}} = \begin{pmatrix} 0 & v_3 \pi \\ v_3 \pi^\dagger & 0 \end{pmatrix}. \quad (A5)$$

Solving the scattering problem for a rectangular sample described by the above Hamiltonian with heavily (infinitely) doped leads one gets the formula for the transmission coefficient as a function of the transverse momentum ($k_y = p_y / \hbar$):

$$T(k_y) = \frac{1}{\cosh^2(k_y L)}. \quad (A6)$$

For the periodic boundary conditions, the transverse momentum gets quantized values, $k_y^{(j)} = 2\pi j / W$, with $j = 0, \pm 1, \pm 2, \dots$. For $W \gg L$, one can approximate the sum over $k_y^{(j)}$ by an integral, obtaining the total transmission

$$\sum_j T(k_y^{(j)}) \approx \frac{W}{2\pi} \int_{-\infty}^{+\infty} T(k_y) dk_y = \frac{1}{\pi} \frac{W}{L}. \quad (A7)$$

Next, we expand (up to second order) the dispersion relation around $\mathbf{p} = (\gamma_1 v_3 / v_0^2, 0)$ (i.e., the satellite Dirac cone at

$\varphi = 0$), arriving at

$$E^2 = \frac{v_3^2}{(1 + (v_3/v_0)^2)^2} (p_x^2 + 9p_y^2). \quad (\text{A8})$$

The corresponding single-cone Hamiltonian reads

$$H_{\text{satellite}}^{(\varphi=0)} = \begin{pmatrix} 0 & v_3(p_x + i3p_y) \\ v_3(p_x - i3p_y) & 0 \end{pmatrix}. \quad (\text{A9})$$

This time, solving the scattering problem for a rectangular sample we get the transmission coefficient

$$T(k_y) = \frac{1}{\cosh^2(3k_y L)}, \quad (\text{A10})$$

and the integration over k_y leads to

$$\frac{W}{2\pi} \int_{-\infty}^{+\infty} T(k_y) dk = \frac{1}{3\pi} \frac{W}{L}. \quad (\text{A11})$$

The calculations for remaining Dirac cones at $\varphi \neq 0$ are more involved, yet straightforward. Generalizing the above reasoning for $\mathbf{p} = \gamma_1(v_3/v_0^2)(\cos \varphi, \sin \varphi)$, we get

$$E^2 = \frac{v_3^2}{(1 + (v_3/v_0)^2)^2} [p_x^2 + p_y^2 + 8(p_x \sin \varphi + p_y \cos \varphi)^2], \quad (\text{A12})$$

and

$$H_{\text{satellite}}^{(\varphi)} = (\alpha \sigma_x + \beta \sigma_y), \quad (\text{A13})$$

where

$$\alpha = p_x \cos \varphi - p_y \sin \varphi, \quad (\text{A14})$$

$$\beta = -3p_x \sin \varphi - 3p_y \cos \varphi. \quad (\text{A15})$$

Finally, we have

$$T(k_y) = \frac{1}{\cosh^2[3k_y L / (5 - 4 \cos(2\varphi))]} \quad (\text{A16})$$

and

$$\frac{W}{2\pi} \int_{-\infty}^{+\infty} T(k_y) dk = \frac{5 - 4 \cos(2\varphi)}{3\pi} \frac{W}{L}. \quad (\text{A17})$$

Summing up the contributions from all four Dirac cones, we obtain the total transmission

$$T_{\text{total}} = \frac{6W}{\pi L}. \quad (\text{A18})$$

Substituting the above into Eq. (3) in the main text, we obtain $\sigma = 3\sigma_0$ in physical units. Remarkably, the result is independent of the lattice orientation, as we have $\cos(\varphi) + \cos(\varphi + 4\pi/3) + \cos(\varphi - 4\pi/3) = 0$ for any real value of φ . (Notice that the summation of independent contributions from four Dirac cones, performed above, instantly reproduces the limit of $L, W \rightarrow \infty$.)

Similarly, for the Fano factor we have

$$F = 1 - \frac{\sum_{\text{cones}} \int dk_y [T(k_y)]^2}{\sum_{\text{cones}} \int dk_y T(k_y)} = \frac{1}{3}. \quad (\text{A19})$$

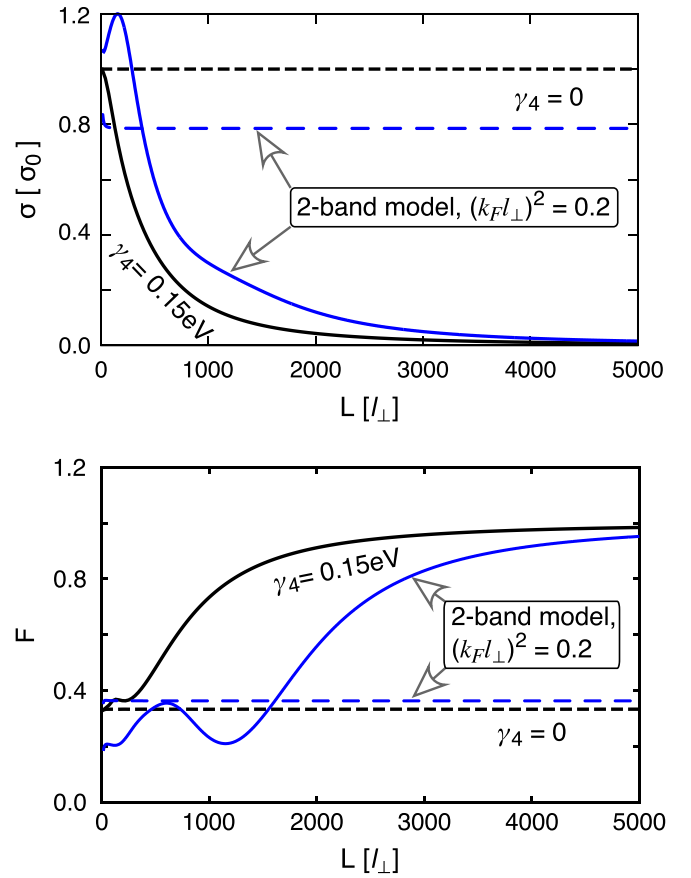


FIG. 6. Conductivity (top) and the Fano factor (bottom) obtained from Eq. (B3) for $(k_F l_\perp)^2 = 0.2$ and $\gamma_4 = 0.15$ eV (solid blue lines), or $\gamma_4 = 0$ (dashed blue lines). The corresponding results for the four-band model are reproduced from Figs. 3(c) and 4(c) for a comparison (solid and dashed black lines).

APPENDIX B: THE EFFECT OF $\gamma_4 \neq 0$ TUNNELING IN THE ABSENCE OF TRIGONAL WARPING ($\gamma_3 = 0$)

In this section, we consider the case complementary to the analyzed in Appendix A. The Hamiltonian given by Eq. (2) in the main text, for $\delta_{AB} = \gamma_3 = 0$, reduces to

$$H_{\text{BLG}} = \begin{pmatrix} 0 & v_0 \pi & \gamma_1 & -v_4 \pi^\dagger \\ v_0 \pi^\dagger & 0 & -v_4 \pi^\dagger & 0 \\ \gamma_1 & -v_4 \pi & 0 & v_0 \pi^\dagger \\ -v_4 \pi & 0 & v_0 \pi & 0 \end{pmatrix}, \quad (\text{B1})$$

leading to the two low-energy bands (with $E = 0$ for $p = 0$) and the two high-energy bands (with $E = \pm \gamma_1$ for $p = 0$) in the dispersion relation. For low energies, one can write the effective two-band Hamiltonian (see Ref. [16])

$$H_{2\text{band}} = \frac{1}{2m} \begin{pmatrix} \mu_4 \pi \pi^\dagger & -(\pi)^\dagger \\ -(\pi^\dagger)^2 & \mu_4 \pi^\dagger \pi \end{pmatrix}, \quad (\text{B2})$$

where $m = \gamma_1/2v_0^2$ and $\mu_4 = 4mv_0 v_4/\gamma_1 = 2v_4/v_0$.

Now, we follow the approach proposed by Katsnelson in Ref. [9], performing the mode matching for two interfaces between heavily and weakly doped areas (the leads and the sample), separated by a distance L . For a fixed but finite

doping in the leads (quantified by the Fermi wavenumber k_F), elementary analysis leads to the following formula for the

transmission coefficient for a given transverse wavenumber k_y (conserved at both the interfaces):

$$T(k_y) = \frac{16\zeta^2\{(-1 - \mu_4)k_FL\zeta \cosh(\zeta) - \mu_4[(-1 - \mu_4)k_FL + 2\zeta^2] \sinh(\zeta)\}^2}{4\zeta^2[\zeta \cosh(2\zeta) - \mu_4k_FL \sinh(2\zeta)]^2 + (k_FL)^2\{-2k_FL\zeta^2 + \mu_4^2k_FL[\cosh(2\zeta) - 1] - 2\mu_4\zeta \sinh(2\zeta)\}^2}, \quad (\text{B3})$$

where we have defined $\zeta = k_yL$.

Changing the variables according to $T(k_y) \equiv T(\zeta, L)$ we find that the Landauer-Büttiker conductivity, for a fixed $W/L \gg 1$, is bounded by

$$\sigma(L) = \frac{1}{2\pi} \int d\zeta T(\zeta, L) \lesssim \frac{\text{const}}{L^2} \quad (\text{for } \mu_4 \neq 0), \quad (\text{B4})$$

vanishing in the $L \rightarrow \infty$ limit. For $\mu_4 = 0$, the conductivity $\sigma(L) \approx (\pi/4)\sigma_0$, and the Fano factor $F \approx 1 - 2/\pi$ for $L \gg$

l_\perp , being numerically close to the results by Snyman and Beenakker [10].

The approximate upper bound for $\mu_4 \neq 0$, given in Eq. (B4), is further supported with the numerical results presented in Fig. 6, where we have set the doping in the leads such that $(k_FL_\perp)^2 = 0.2$ (after Ref. [10]), and $W/L = 20$. Numerical calculations for the full four-band model given the Hamiltonian H_{BLG} (B1) leads to a noticeably faster but also a power-law decay of the conductivity, which can be approximated as $\sigma(L) \propto L^{-2.0}$ for $L \gtrsim 1000 l_\perp$.

- [1] M. I. Katsnelson, *Eur. Phys. J. B* **51**, 157 (2006).
- [2] J. Tworzydło, B. Trauzettel, M. Titov, A. Rycerz, and C. W. J. Beenakker, *Phys. Rev. Lett.* **96**, 246802 (2006).
- [3] F. Miao, S. Wijeratne, Y. Zhang, U. C. Coskun, W. Bao, and C. N. Lau, *Science* **317**, 1530 (2007).
- [4] L. DiCarlo, J. R. Williams, Y. Zhang, D. T. McClure, and C. M. Marcus, *Phys. Rev. Lett.* **100**, 156801 (2008).
- [5] R. Danneau, F. Wu, M. F. Craciun, S. Russo, M. Y. Tomi, J. Salmilehto, A. F. Morpurgo, and P. J. Hakonen, *Phys. Rev. Lett.* **100**, 196802 (2008).
- [6] M. I. Katsnelson, *Graphene: Carbon in Two Dimensions* (Cambridge University Press, Cambridge, UK, 2012), Chap. 3.
- [7] C. W. J. Beenakker, *Rev. Mod. Phys.* **80**, 1337 (2008).
- [8] J. Wurm, A. Rycerz, I. Adagideli, M. Wimmer, K. Richter, and H. U. Baranger, *Phys. Rev. Lett.* **102**, 056806 (2009).
- [9] M. I. Katsnelson, *Eur. Phys. J. B* **52**, 151 (2006).
- [10] I. Snyman and C. W. J. Beenakker, *Phys. Rev. B* **75**, 045322 (2007).
- [11] J. Cserti, *Phys. Rev. B* **75**, 033405 (2007).
- [12] A. G. Moghaddam and M. Zareyan, *Phys. Rev. B* **79**, 073401 (2009).
- [13] G. Rut and A. Rycerz, *Europhys. Lett.* **107**, 47005 (2014).
- [14] J. W. McClure, *Phys. Rev.* **108**, 612 (1957).
- [15] J. C. Slonczewski and P. R. Weiss, *Phys. Rev.* **109**, 272 (1958).
- [16] E. McCann and M. Koshino, *Rep. Prog. Phys.* **76**, 056503 (2013).
- [17] S. Das Sarma, Sh. Adam, E. H. Hwang, and E. Rossi, *Rev. Mod. Phys.* **83**, 407 (2011).
- [18] The next-nearest layer parameter γ_2 is not present in bilayer graphene (see Refs. [14, 15]).
- [19] The limit of $\sigma(L) \rightarrow 3\sigma_0$ for $L \rightarrow \infty$ appears for a generic crystallographic orientation of a sample. In a particular case when the current is passed precisely along a zigzag direction, the limit of $(7/3)\sigma_0$ is predicted (see Ref. [12]).
- [20] W. Bao, J. Velasco, F. Zhang, L. Jing, B. Standley, D. Smirnov, M. Bockrath, A. H. MacDonald, and C. N. Lau, *Proc. Natl. Acad. Sci. USA* **109**, 10802 (2012).
- [21] M. Yankowitz, J. I. Wang, S. Li, A. G. Birdwell, Y.-A. Chen, K. Watanabe, T. Taniguchi, S. Y. Quek, P. Jarillo-Herrero, and B. J. LeRoy, *APL Mater.* **2**, 092503 (2014).
- [22] A. L. Grushina, D.-K. Ki, M. Koshino, A. A. L. Nicolet, C. Faugeras, E. McCann, M. Potemski, and A. F. Morpurgo, *Nat. Commun.* **6**, 6419 (2015).
- [23] Y. Nam, D.-K. Ki, M. Koshino, E. McCann, and A. F. Morpurgo, *2D Mater.* **3**, 045014 (2016).
- [24] The values of γ_0 and γ_1 are taken from A. B. Kuzmenko, I. Crassee, D. van der Marel, P. Blake, and K. S. Novoselov, *Phys. Rev. B* **80**, 165406 (2009).
- [25] Unlike in monolayer graphene, when the vanishing density of states preserves the semimetallic phase, the Mott-insulating phase may generically appear in the BLG ground state for weak interactions; see J. E. Hirsch, *Phys. Rev. B* **31**, 4403 (1985); L. M. Martelo, M. Dzierzawa, L. Siffert, and D. Baeriswyl, *Z. Phys. B* **103**, 335 (1997).
- [26] For the theoretical discussion of a BLG ground-state phase diagram in the presence of interactions, see R. E. Throckmorton and S. Das Sarma, *Phys. Rev. B* **90**, 205407 (2014); J. N. Leaw, H.-K. Tang, P. Sengupta, F. F. Assaad, I. F. Herbut, and S. Adam, *ibid.* **100**, 125116 (2019).
- [27] Yu. V. Nazarov and Ya. M. Blanter, *Quantum Transport: Introduction to Nanoscience* (Cambridge University Press, Cambridge, UK, 2009), Chap. 1.
- [28] D. Suszalski, G. Rut, and A. Rycerz, *Phys. Rev. B* **97**, 125403 (2018).
- [29] A. S. Mayorov, D. C. Elias, M. Mucha-Kruczyński, R. V. Gorbachev, T. Tudorovskiy, A. Zhukov, S. V. Morozov, M. I. Katsnelson, V. I. Falko, A. K. Geim, and K. S. Novoselov, *Science* **333**, 860 (2011).
- [30] R. Kraft, J. Mohrmann, R. Du, P. B. Selvasundaram, M. Irfan, U. N. Kanilmaz, F. Wu, D. Beckmann, H. von Löhneysen, R. Krupke, A. Akhmerov, I. Gornyi, and R. Danneau, *Nat. Commun.* **9**, 1722 (2018).
- [31] D. Suszalski, G. Rut, and A. Rycerz, *J. Phys.: Condens. Matter* **31**, 415501 (2019).

- [32] For Schrödinger electrons, incident on a rectangular barrier at zero energy (with respect to the top of the barrier), the transmission probability reads $T_n = [\cosh^2 Lq_n + (k_\infty^2/2q_n^2 - 1)(k_\infty^2/q_n^2 - 1)^{-1} \sinh^2 Lq_n]^{-1}$, with $q_n = 2\pi n/W$ ($n = 0, 1, 2, \dots$) being the quantized transverse wavenumber for the periodic boundary conditions, and k_∞ denoting the wavenumber in heavily doped leads. For $k_\infty \rightarrow \infty$, we have $T_n \propto (q_n/k_\infty)^2$, vanishing for any n .
- [33] J. van Wezel and J. van den Brink, *Am. J. Phys.* **75**, 635 (2007).
- [34] J. van Wezel, J. Zaanen, and J. van den Brink, *Phys. Rev. B* **74**, 094430 (2006).
- [35] The effect of increasing distance between the layers d on the tight-binding parameters depicted in Fig. 1(a) can roughly be estimated as $\gamma_j \propto \exp(-\beta d_j/d_j^{(0)})$, where the electron-phonon coupling $\beta \approx 2 - 3$, and d_j ($d_j^{(0)}$) is the actual (equilibrium) distance between the atoms connected by γ_j ; see, e.g., M. A. H. Vozmediano, M. I. Katsnelson, and F. Guinea, *Phys. Rep.* **496**, 109 (2010).
- [36] R. Bistritzer and A. H. MacDonald, *Proc. Natl. Acad. Sci. USA* **108**, 12233 (2011).
- [37] Y. Cao, V. Fatemi, S. Fang, K. Watanabe, T. Taniguchi, E. Kaxiras, and P. Jarillo-Herrero, *Nature (London)* **556**, 43 (2018).
- [38] Y. Cao, V. Fatemi, A. Demir, S. Fang, S. L. Tomarken, J. Y. Luo, J. D. Sanchez-Yamagishi, K. Watanabe, T. Taniguchi, E. Kaxiras, Ray C. Ashoori, and P. Jarillo-Herrero, *Nature (London)* **556**, 80 (2018).
- [39] C. Xu and L. Balents, *Phys. Rev. Lett.* **121**, 087001 (2018).
- [40] M. Fidrysiak, M. Zegrodnik, and J. Spałek, *Phys. Rev. B* **98**, 085436 (2018).

Graphene disk in a solenoid magnetic potential: Aharonov-Bohm effect without a two-slit-like setup

Adam Rycerz  and Dominik Suszalski

Institute for Theoretical Physics, Jagiellonian University, Łojasiewicza 11, PL-30348 Kraków, Poland



(Received 8 April 2020; revised manuscript received 29 May 2020; accepted 2 June 2020; published 22 June 2020)

The Aharonov-Bohm effect allows one to demonstrate the physical meaningfulness of magnetic vector potential by passing the current in zero magnetic field regions. In the standard (a *two-slit-like*) setup, a conducting ring is pierced by magnetic flux and the quantum interference for an electron passing simultaneously through the two ring arms is observed. Here we show, by analyzing transport via evanescent waves, that the ballistic Corbino disk in graphene subjected to a solenoid magnetic potential may exhibit conductance oscillations of the Aharonov-Bohm kind although the current flows through a single conducting element only.

DOI: [10.1103/PhysRevB.101.245429](https://doi.org/10.1103/PhysRevB.101.245429)

I. INTRODUCTION

Quantum transport through the Corbino disk in graphene has been addressed both theoretically [1–7] and experimentally [8–12] by numerous authors, as the edge-free geometry allows one to probe the mesoscopic aspects of graphene, such as transport via evanescent waves [13], even in nanometer-scale devices. At zero magnetic field, conductance of ultra-clean ballistic disks as a function of the carrier concentration [10] shows good agreement with the basic mode-matching analysis of Ref. [1]. At nonzero field, periodic (approximately sinusoidal) magnetoconductance oscillations were predicted [2,3] but experimental confirmation of such a remarkable quantum-interference phenomenon is missing.

Theoretical analysis of Ref. [2] employs the rotational symmetry of the problem, resulting in the total angular momentum conservation ($J_z = \hbar j$, with $j = \pm 1/2, \pm 3/2, \dots$, the angular-momentum quantum number). In the case of an undoped disk of the inner radius R_1 and the outer radius R_2 , the Landauer-Büttiker transmission probabilities [14,15] read

$$T_j = \frac{1}{\cosh^2[\ln(R_2/R_1)(j + \Phi_d/\Phi_0)]}, \quad (1)$$

where $\Phi_d = \pi(R_2^2 - R_1^2)B$ is the flux piercing the disk with a uniform magnetic field B , and $\Phi_0 = 2(h/e)\ln(R_2/R_1)$ defines the conductance-oscillation period. Further analysis shows that the formula equivalent to Eq. (1) can also be derived if the carrier concentration (hereinafter quantified by the Fermi energy E_F , with $E_F = 0$ corresponding to the charge-neutrality point) is adjusted to any Landau level, $E_n = \text{sgn}(n)v_F\sqrt{2|n|eB}$, with $n = 0, \pm 1, \pm 2, \dots$, and $v_F \approx 10^6$ m/s being the energy-independent Fermi velocity in graphene.

Away from Landau levels the transmission is strongly suppressed [2,7]. For instance, in the vicinity of the charge-neutrality point ($n = 0$) magnetoconductance oscillations may be observed in the magnetic field range limited by

$$|\Phi_d| \lesssim \frac{2h}{e} \ln\left(\frac{1}{k_F R_1}\right) = \frac{h}{e} \ln\left(\frac{1}{\pi|n_C|R_1^2}\right), \quad (2)$$

where we have further defined $k_F = |E_F|/(\hbar v_F)$ and the outermost right equality follows from the relation between the Fermi wave number and the carrier concentration (n_C), namely, $k_F = \sqrt{\pi|n_C|}$, including the fourfold (spin and valley) degeneracy of each quasiparticle level. On the other hand, the current flow through the system leads to carrier density fluctuations of the order of $\delta n_C \sim 1/(\pi R_2^2)$, even in the absence of the charge inhomogeneity usually appearing due to the electron-hole puddle formation at low densities [16]. Taking the above as the lower bound to $|n_C|$ in Eq. (2), one immediately obtains $|\Phi_d| \lesssim \Phi_0$, suggesting it may be difficult (or even impossible) to observe the magnetoconductance oscillations in the linear-response regime. A proposal to overcome this difficulty by going beyond the linear-response regime was put forward [17].

A separate issue concerns the role of electron-electron interactions, which is usually marginal when discussing ballistic systems in monolayer graphene [18,19], in agreement with fundamental considerations [20,21], but may lead to Wigner crystallization or the appearance of fractional quantum Hall phases, in case the bulk density of states is strongly modified due to the Landau quantization [10,22,23].

Generally speaking, uniform magnetic fields, although being most feasible to generate at micrometer scale, do not seem to provide a realistic opportunity to observe magnetoconductance oscillations in graphene-based Corbino disks. Therefore it is worth to consider other field arrangements, in which phase effects may overrule orbital effects (such as Landau level formation). In this paper, we focus on the case of a disk whose inner area is pierced by a long solenoid (see Fig. 1), generating the flux Φ_i . Earlier, it was shown by Katsnelson [3,24] that for zero doping ($E_F = 0$) the transmission probabilities are given

Published by the American Physical Society under the terms of the [Creative Commons Attribution 4.0 International](https://creativecommons.org/licenses/by/4.0/) license. Further distribution of this work must maintain attribution to the author(s) and the published article's title, journal citation, and DOI.

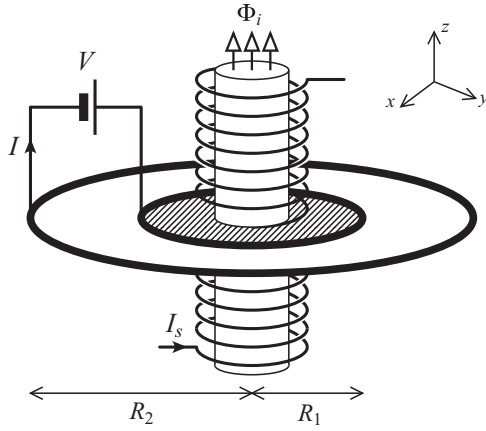


FIG. 1. Schematic of the Corbino disk in graphene of the inner radius R_1 and the outer radius R_2 , contacted by two electrodes (thick black circles). A voltage source (V) drives the current (I) through the disk. A separate gate electrode (not shown) allows the carrier concentration in the disk to be tuned around the neutrality point. A long solenoid, carrying the current I_s , generates the flux Φ_i piercing the inner disk area. The coordinate system is also shown.

by Eq. (1) after substituting

$$\Phi_d \equiv \Phi_i \quad \text{and} \quad \Phi_0 \equiv \Phi_{AB}, \quad (3)$$

with $\Phi_{AB} = h/e$ being the familiar Aharonov-Bohm flux quantum [25]. However, the analysis of such a system away from the charge-neutrality point ($E_F \neq 0$) is missing.

The remaining part of the paper is organized as follows. In Sec. II, we present the results of the mode-matching analysis for the system of Fig. 1 at arbitrary doping and flux. Next, in Sec. III, the numerical discussion of the conductance oscillations is provided. The effect of electrostatic field breaking cylindrical symmetry of the problem is considered in Sec. IV. The conclusions are given in Sec. V.

II. SOLUTION FOR ARBITRARY DOPING AND FLUX

Our analysis starts from the Dirac Hamiltonian in a single valley (K), which is given by

$$H = v_F(\mathbf{p} + e\mathbf{A}) \cdot \boldsymbol{\sigma} + U(r), \quad (4)$$

where $\mathbf{p} = -i\hbar(\partial_x, \partial_y)$ is the in-plane momentum operator, the electron charge is $-e$, the magnetic vector potential of a solenoid is written in the symmetric gauge [26]

$$\mathbf{A} = (A_x, A_y) = \frac{\Phi_i}{2\pi} \left(-\frac{y}{r^2}, \frac{x}{r^2} \right), \quad (5)$$

and $\boldsymbol{\sigma} = (\sigma_x, \sigma_y)$ with σ_x and σ_y being the Pauli matrices. We further suppose that the electrostatic potential energy $U(r)$ depends only on $r = \sqrt{x^2 + y^2}$; namely, we put $U(r) = 0$ in the disk area ($R_1 < r < R_2$), or $U(r) = U_\infty$ otherwise. Since Hamiltonian (4) commutes with the total angular momentum operator, $J_z = -i\hbar\partial_\varphi + \hbar\sigma_z/2$, the energy eigenfunctions can be chosen as eigenstates of J_z

$$\psi_j(r, \varphi) = e^{i(j-1/2)\varphi} \begin{pmatrix} \chi_{j,A}(r) \\ \chi_{j,B}(r)e^{i\varphi} \end{pmatrix}, \quad (6)$$

where j is a half-odd integer, two spinor components (A, B) correspond to the sublattice degree of freedom, and we have introduced the polar coordinates (r, φ) . The Dirac equation now can be written as $H_j(r)\chi_j(r) = E\chi_j(r)$, where $\chi_j(r) = [\chi_{j,A}(r), \chi_{j,B}(r)]^T$, and

$$H_j(r) = -i\hbar v_F \sigma_x \partial_r + U(r) + \hbar v_F \sigma_y \begin{pmatrix} \frac{j-1/2}{r} + \frac{e\Phi_i}{\hbar r} & 0 \\ 0 & \frac{j+1/2}{r} + \frac{e\Phi_i}{\hbar r} \end{pmatrix}. \quad (7)$$

For a piecewise-constant potential energy $U(r)$ and the electron-doping case, $E > U(r)$, the eigenfunctions of $H_j(r)$ (7) for the incoming (i.e., propagating from $r = 0$) and outgoing (propagating from $r = \infty$) waves are given, up to the normalization, by

$$\chi_j^{\text{in}} = \begin{pmatrix} H_{\nu(j)-1/2}^{(2)}(kr) \\ iH_{\nu(j)+1/2}^{(2)}(kr) \end{pmatrix}, \quad \chi_j^{\text{out}} = \begin{pmatrix} H_{\nu(j)-1/2}^{(1)}(kr) \\ iH_{\nu(j)+1/2}^{(1)}(kr) \end{pmatrix}, \quad (8)$$

where

$$\nu(j) = j + \Phi_i/\Phi_{AB}, \quad (9)$$

$H_\nu^{(1,2)}(\rho)$ is the Hankel function of the (first, second) kind, and $k = |E - U(r)|/(\hbar v_F)$. The solution for the disk area can be represented as

$$\chi_j^{(d)} = A_j \chi_j^{\text{in}}(k_F r) + B_j \chi_j^{\text{out}}(k_F r), \quad R_1 < r < R_2, \quad (10)$$

with A_j and B_j being arbitrary constants, and the Fermi wave number $k_F = |E|/(\hbar v_F)$. For the hole doping case, $E < U(r)$, the wave functions are replaced by $\tilde{\chi}_j^{\text{in(out)}} = [\chi_j^{\text{in(out)}}]^*$, where we use the relation $H_\nu^{(2)} = [H_\nu^{(1)}]^*$.

The heavily doped graphene leads are modeled here by taking the limit of $U(r) = U_\infty \rightarrow \pm \infty$ for $r < R_1$ or $r > R_2$. The corresponding wave functions can be simplified to

$$\chi_j^{(1)} = \frac{e^{\pm ik_\infty}}{\sqrt{r}} \begin{pmatrix} 1 \\ 1 \end{pmatrix} + r_j \frac{e^{\mp ik_\infty}}{\sqrt{r}} \begin{pmatrix} 1 \\ -1 \end{pmatrix}, \quad r < R_1, \quad (11)$$

$$\chi_j^{(2)} = t_j \frac{e^{\pm ik_\infty}}{\sqrt{r}} \begin{pmatrix} 1 \\ 1 \end{pmatrix}, \quad r > R_2, \quad (12)$$

where we have introduced the reflection (transmission) amplitudes r_j (t_j) and $k_\infty = |E - U_\infty|/(\hbar v_F) \rightarrow \infty$.

Solving the mode-matching conditions, $\chi_j^{(d)}(R_1) = \chi_j^{(d)}(R_1)$ and $\chi_j^{(d)}(R_2) = \chi_j^{(2)}(R_2)$, we find the transmission probability for j th mode

$$T_j = |t_j|^2 = \frac{16}{\pi^2 k^2 R_1 R_2} \frac{1}{[\mathfrak{D}_{\nu(j)}^{(+)}]^2 + [\mathfrak{D}_{\nu(j)}^{(-)}]^2}, \quad (13)$$

where $\nu(j)$ is given by Eq. (9) and

$$\mathfrak{D}_\nu^{(\pm)} = \text{Im} \left[H_{\nu-1/2}^{(1)}(kR_1) H_{\nu\pm 1/2}^{(2)}(kR_2) \pm H_{\nu+1/2}^{(1)}(kR_1) H_{\nu\pm 1/2}^{(2)}(kR_2) \right]. \quad (14)$$

III. RESULTS AND DISCUSSION

The linear-response conductance is calculated according to the Landauer-Büttiker formula [14,15]

$$G = \frac{I}{V} = g_0 \sum_{j=\pm 1/2, \pm 3/2, \dots} T_j, \quad (15)$$

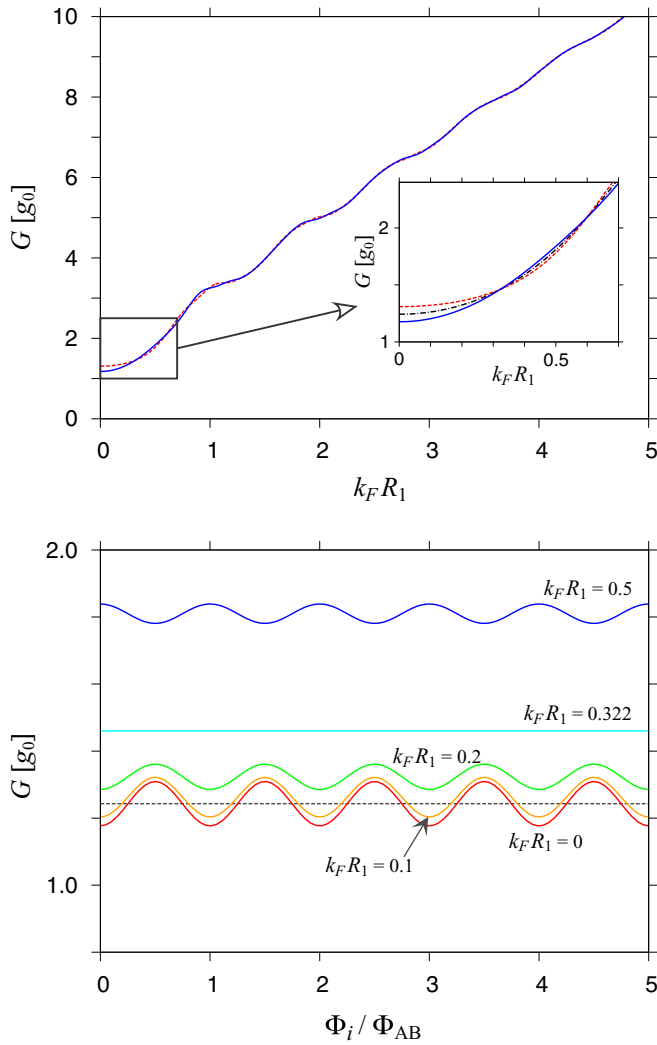


FIG. 2. Conductance as a function of the doping (top) and the flux piercing the inner disk area (bottom) for the radii ratio $R_2/R_1 = 5$. (Top) Different lines correspond to $\Phi_i = 0$ (blue solid line) and $\Phi_i = \Phi_{AB}/2$ (red dashed line). Inset presents a zoom-in, for low dopings, with an additional black dash-dot line depicting the conductance averaged over Φ_i . (Bottom) The doping is varied from $k_F R_1 = 0$ to $k_F R_1 = 0.5$ and specified for each solid line on the plot. Dashed line marks the pseudodiffusive conductance $G_{diff} = 2g_0 / \ln(R_2/R_1)$, with $g_0 = 4e^2/h$.

where the conductance quantum $g_0 = 4e^2/h$, with the factor 4 accounting for spin and valley degeneracy, and the summation over modes is performed numerically up to the machine round-off errors [27]. Our numerical results are presented in Figs. 2 and 3.

The asymptotic properties of the Hankel functions [28] in Eq. (13) lead to $T_j \approx 1$ for $k_F R_1 - \nu(j) \gg 1$, with $\nu(j)$ given by Eq. (9), or to $T_j \approx 0$ for $\nu(j) - k_F R_1 \gg 1$. In turn, the conductivity can be approximated as $G \approx 2g_0 k_F R_1$ for $k_F R_1 \gg 1$ and $R_2 \gg R_1$ (see top panel in Fig. 2), with an excess value of $\sim g_0 R_1/R_2$ (up to the order of magnitude) representing the contribution from evanescent waves.

Furthermore, the structure of Eqs. (9), (13), (14), and (15) results in perfectly periodic functional dependence of $G(\Phi)$,

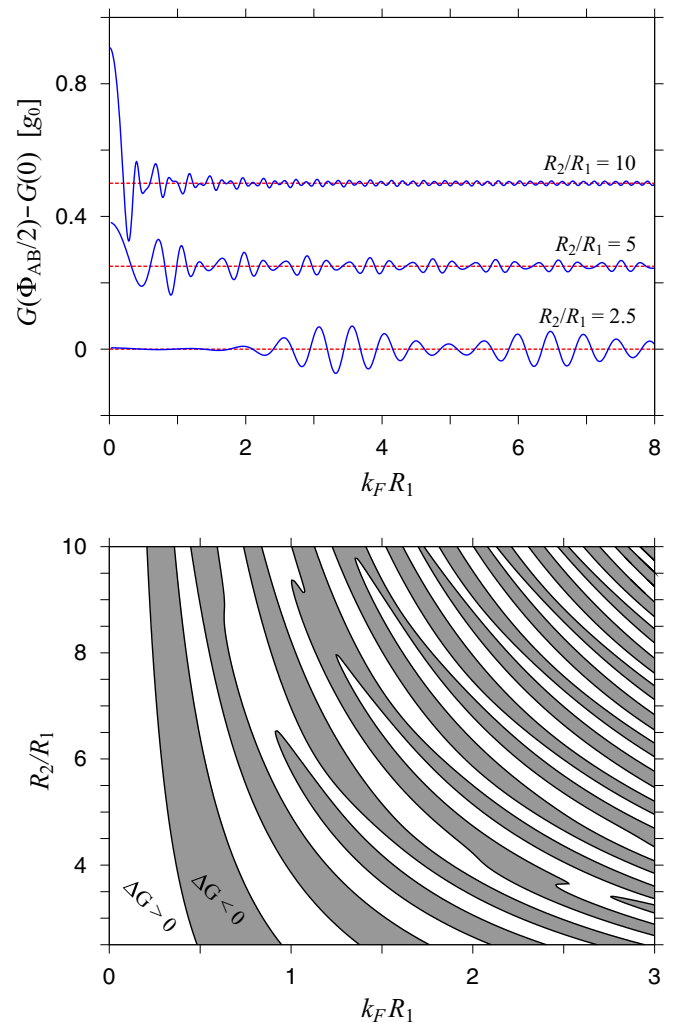


FIG. 3. (Top) Magnitude of the conductance oscillations, $\Delta G = G(\Phi_{AB}/2) - G(0)$, displayed as a function of the doping for selected values of the radii ratio (specified for each line). Notice that the data sets for $R_2/R_1 = 5$ and 10 (blue solid lines) are subjected to vertical shifts of 0.25 and $0.5g_0$ (respectively). Red dashed line shows the actual $\Delta G = 0$ for each case. (Bottom) Nodal lines (black solid) of ΔG as a function of the doping and the radii ratio, separating the areas with $\Delta G > 0$ (white) and $\Delta G < 0$ (shadow).

with a period Φ_{AB} , at arbitrary doping (see Fig. 2). Quite surprisingly, the magnitude of the conductance oscillations

$$\Delta G = G(\Phi_{AB}/2) - G(0), \quad (16)$$

takes relatively large absolute values (namely, $|\Delta G| > 0.1 g_0$) not only in small vicinity of the charge neutrality-point, but also at higher dopings (see Fig. 3), signaling the importance of transport via evanescent waves again. [Notice that the difference between $G(\Phi_{AB}/2)$ and $G(0)$, defining ΔG via Eq. (16), is governed by only a few modes for which $k_F R_1 \approx \nu(j)$ and thus T_j 's are neither ≈ 0 nor ≈ 1 .] A systematic growth of ΔG with R_2/R_1 is visible for $k_F \rightarrow 0$ (with $\Delta G \approx g_0$ for $R_2 \gg R_1$), in consistency with earlier predictions of Refs. [2,3] for the uniform magnetic field case.

For each radii ratio, one can find a unique series of discrete doping values for which $\Delta G = 0$, resulting in $G(\Phi_i) = \text{const}$.

For instance, if $R_2/R_1 = 5$, the first five nodes of ΔG correspond to

$$(k_F R_1)_{\Delta G=0} = 0.322, 0.598, 0.814, 0.987, 1.137. \quad (17)$$

Below the first nodal value (i.e., $|k_F R_1| < 0.322$), we have $\Delta G > 0$ [or, equivalently, $G(\Phi_{AB}) > G(0)$, see Eq. (16)]; then, the sign of ΔG alternates with growing $k_F R_1$, as indicated in the bottom panel in Fig. 3.

It is also visible in Fig. 3 that the pattern of nodal lines is rather irregular, as one could expect since ΔG can be regarded as the rational expression containing Bessel function. Typical separation between the first nodes of ΔG in Eq. (17) can (roughly) be approximated as $\Delta k_F R_1 \approx 0.3$, which corresponds, for the physical size of $R_1 = 50$ nm, to the energy interval of $\Delta E_F/k_B \approx 40$ K (with the Boltzmann constant k_B). In turn, the conductance oscillations should be observable in comparable or higher temperatures than the standard Aharonov-Bohm effect in graphene rings [29,30].

IV. CONDUCTANCE OSCILLATIONS IN THE ABSENCE OF CYLINDRICAL SYMMETRY

So far, the discussion was limited to the case of a perfect cylindrical symmetry, allowing us to calculate the transmission probabilities T_j [see Eq. (13)] analytically by solving the scattering problem separately for each (j th) angular-momentum mode. In real system, several factors may break the cylindrical symmetry, resulting in the mode mixing. In particular, both the spatial corrugations of a graphene sheet and charge-donating impurities placed in the substrate lead to the charge density fluctuations (i.e., *p-n puddles*) [16,31–33]. For best existing devices, carrier density fluctuations are $\delta n < 10^{11}$ cm² near the neutrality point, corresponding to the electrostatic potential fluctuation of the order of $\delta U \sim 10$ meV.

Here we test numerically, how robust the effects described in Sec. III are against the cylindrical symmetry breaking. For this purpose, the electrostatic potential energy in the Hamiltonian (4) is replaced by [7]

$$U(r, \varphi) = -\frac{U_0 r}{R_2} \sin \varphi, \quad R_1 < r < R_2. \quad (18)$$

In the leads, $r < R_1$ or $r > R_2$, we set $U(r, \varphi) = U_\infty$ again. The potential amplitude (without loss of generality, we suppose $U_0 \geq 0$) defines the Fermi energy range, $-U_0 < E_F < U_0$, for which a p-n interface is present in the disk area (see Fig. 4). A special case of $U_0 = 0$ restores the uniform-doping case considered in Sec. III.

Regardless of the value of U_0 , angular-momentum eigenfunctions of the form given by Eqs. (6), (11), and (12), still represent the correct solutions in the leads. Therefore the numerical mode matching can be performed in the angular-momentum space, employing the transfer matrix approach presented with details in Ref. [7]. Since the Fermi wave number $k_F = |E_F - U(r, \varphi)|/(\hbar v_F)$ is now position-dependent, the numerical results presented in Fig. 4 are parametrized by E_F and U_0 . In order to specify these quantities in the physical units, we fixed the disk dimensions at $R_1 = 50$ nm and $R_2 = 5R_1 = 250$ nm [34]. However, it is worth to stress

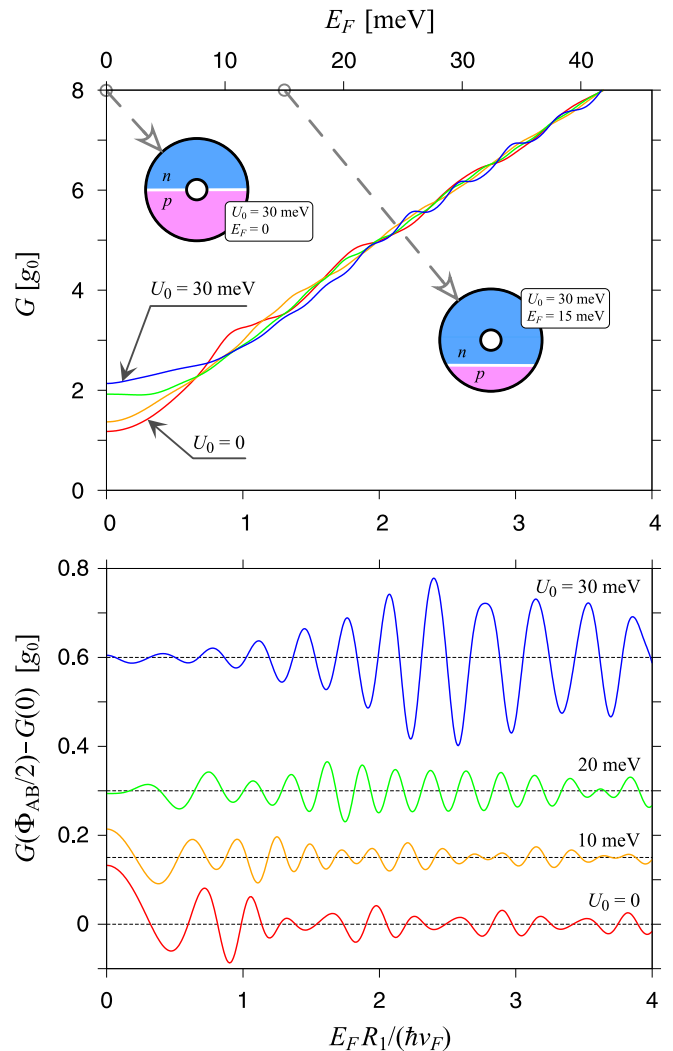


FIG. 4. Conductance for $\Phi_i = 0$ (top) and the oscillation magnitude (bottom) displayed as functions of the Fermi energy for the disk radii $R_1 = R_2/5 = 50$ nm and the electrostatic potential amplitude [see Eq. (18)] varied from $U_0 = 0$ to 30 meV with the steps of 10 meV. Top: Two insets show the positions of a p-n interface in the disk area for $U_0 = 20$ meV and the two different values of E_F . (Bottom) The data sets for $U_0 > 0$ (solid lines) are subjected to vertical shifts; black dashed lines show the actual $\Delta G = 0$.

that the transport characteristics are determined by the dimensionless parameters, $E_F R_1/(\hbar v_F)$ (also displayed in Fig. 4), $U_0 R_1/(\hbar v_F)$, and the radii ratio R_2/R_1 , and therefore remain invariant upon the scaling $R_{1(2)} \rightarrow \lambda R_{1(2)}$, $E_F \rightarrow E_F/\lambda$, and $U_0 \rightarrow U_0/\lambda$, with a real $\lambda > 0$.

If the system is close to the charge-neutrality point, namely for $|E_F| < U_0 R_1/R_2$, the conductance is noticeably enhanced with growing U_0 (see top panel in Fig. 4), as the propagation through heavily p-doped and n-doped areas supplements the transport via evanescent waves. (We further notice that the largest considered $U_0 = 30$ meV corresponds to $U_0 R_1/(\hbar v_F) \approx 2.6 \lesssim R_2/R_1$, and thus the system, at zero field, can be regarded as being in the crossover range between the pseudodiffusive and the ballistic charge transport regimes [35].) For higher $|E_F|$, the effect of U_0 becomes negligible,

and $G \approx 2g_0(k_F)R_1$ with $\langle k_F \rangle = |E_F|/(\hbar v_F)$ being the average Fermi wavenumber on the inner disk edge ($r = R_1$).

The magnetoconductance oscillations magnitude (see bottom panel in Fig. 4) are diminished for $|E_F| < U_0 R_1/R_2$ with growing U_0 . This observation can be rationalized by taking into account that at zero magnetic field main currents flow along the $\varphi \approx \pm\pi/2$ directions (i.e., towards the regions of extreme doping), for which the magnetic phases associated with the vector potential given by Eq. (5) vanish. In contrast, for the unipolar doping ($|E_F| > U_0$) the oscillations are only weakly affected by growing U_0 , and the magnitudes of $\Delta G > 0.1 g_0$ appear for wide range of the doping.

V. CONCLUSIONS

We have demonstrated, performing the numerical analysis of the exact formula for transmission probability for electron with a given angular momentum tunneling through the Corbino disk in graphene, that the conductance (as a function of magnetic flux piercing the disk) shows periodic oscillations of the Aharonov-Bohm kind. Unlike for a uniform magnetic field considered in Refs. [2,3], when similar oscillations appear at discrete Landau levels only, the disk in a solenoid magnetic potential shows the oscillations for any

Fermi energy except from a discrete energy set, defined by the disk radii (R_1 and R_2), the Fermi velocity in graphene (v_F) and the Planck constant (\hbar), for which the conductance is flux-independent.

Most remarkably, away from the charge-neutrality point the conductance oscillations may show a significant magnitude ($\Delta G > 0.1 g_0$, with $g_0 = 4e^2/h$) starting from moderate radii ratios $R_2/R_1 \gtrsim 2$, being comparable to the actual experimental values, see Refs. [9,10]. At the charge neutrality point, the oscillation magnitude grows with the radii ratio, approaching $\Delta G \approx g_0$ for $R_2 \gg R_1$.

Also, we find out that the conductance oscillations are well-pronounced in the presence of a position-dependent electrostatic potential that breaks the cylindrical symmetry and introduces the mode mixing. Some suppression of the effect is predicted for ambipolar dopings (i.e., with a p - n junction in the disk area), but the oscillations are restored away from the charge neutrality point (for unipolar dopings).

ACKNOWLEDGMENTS

We thank Piotr Witkowski for discussions. The work was supported by the National Science Centre of Poland (NCN) via Grant No. 2014/14/E/ST3/00256.

-
- [1] A. Rycerz, P. Recher, and M. Wimmer, *Phys. Rev. B* **80**, 125417 (2009).
- [2] A. Rycerz, *Phys. Rev. B* **81**, 121404(R) (2010).
- [3] M. I. Katsnelson, *Europhys. Lett.* **89**, 17001 (2010).
- [4] Z. Khatibi, H. Rostami, and R. Asgari, *Phys. Rev. B* **88**, 195426 (2013).
- [5] B. Abdollahipour and E. Moomivand, *Physica E* **86**, 204 (2017).
- [6] G. W. Jones, D. A. Bahamon, A. H. Castro Neto, and V. M. Pereira, *Nano Lett.* **17**, 5304 (2017).
- [7] D. Suszalski, G. Rut, and A. Rycerz, *J. Phys. Mater.* **3**, 015006 (2020).
- [8] J. Yan and M. S. Fuhrer, *Nano Lett.* **10**, 4521 (2010).
- [9] E. C. Peters, A. J. M. Giesbers, M. Burghard, and K. Kern, *Appl. Phys. Lett.* **104**, 203109 (2014).
- [10] M. Kumar, A. Laitinen, and P. Hakonen, *Nat. Commun.* **9**, 2776 (2018).
- [11] Y. Zeng, J. I. A. Li, S. A. Dietrich, O. M. Ghosh, K. Watanabe, T. Taniguchi, J. Hone, and C. R. Dean, *Phys. Rev. Lett.* **122**, 137701 (2019).
- [12] C.-I. Liu, D. S. Scaletta, D. K. Patel, M. Kruskopf, A. Levy, H. M. Hill, and A. F. Rigosi, *J. Phys. D: Appl. Phys.* **53**, 275301 (2020).
- [13] M. I. Katsnelson, *Graphene: Carbon in Two Dimensions* (Cambridge University Press, Cambridge, 2012), Chap. 3.
- [14] R. Landauer, *IBM J. Res. Dev.* **1**, 223 (1957).
- [15] M. Büttiker, Y. Imry, R. Landauer, and S. Pinhas, *Phys. Rev. B* **31**, 6207 (1985).
- [16] C. R. Dean, A. F. Young, I. Meric, C. Lee, L. Wang, S. Sorgenfrei, K. Watanabe, T. Taniguchi, P. Kim, K. L. Shepard *et al.*, *Nat. Nanotechnol.* **5**, 722 (2010).
- [17] G. Rut and A. Rycerz, *Philos. Mag.* **95**, 599 (2015).
- [18] D. A. Siegel, C.-H. Park, C. Hwang, J. Deslippe, A. V. Fedorov, S. G. Louie, and A. Lanzara, *Proc. Natl. Acad. Sci. USA* **108**, 11365 (2011).
- [19] C. Hwang, D. A. Siegel, S.-K. Mo, W. Regan, A. Ismach, Y. Zhang, A. Zettl, and A. Lanzara, *Sci. Rep.* **2**, 590 (2012).
- [20] L. M. Martelo, M. Dzierzawa, L. Siffert, and D. Baeriswyl, *Z. Phys. B* **103**, 335 (1997).
- [21] J. D. Stokes, H. P. Dahal, A. V. Balatsky, and K. S. Bedell, *Philos. Mag. Lett.* **93**, 672 (2013).
- [22] D. A. Abanin, I. Skachko, X. Du, E. Y. Andrei, and L. S. Levitov, *Phys. Rev. B* **81**, 115410 (2010).
- [23] D. S. Lee, V. Skákalová, R. T. Weitz, K. von Klitzing, and J. H. Smet, *Phys. Rev. Lett.* **109**, 056602 (2012).
- [24] More generally, for a centrosymmetric field $\mathbf{B} = B(r)\hat{e}_z$, the fraction $\phi = \Phi_d/\Phi_0$ in Eq. (1) is replaced by
- $$\phi \equiv \frac{\Phi_i}{\Phi_{AB}} + \frac{4\pi}{\Phi_0} \int_{R_1}^{R_2} \frac{dr}{r} \int_{R_1}^r dr' r' B(r),$$
- where Φ_i is flux through the inner ring ($r < R_1$). In particular, if $B(r) = 0$ for $r > R_1$, the Aharonov-Bohm-like oscillations occur when varying Φ_i .
- [25] Yu.V. Nazarov and Ya. M. Blanter, *Quantum Transport: Introduction to Nanoscience* (Cambridge University Press, Cambridge, UK, 2009), Chap.1.
- [26] R. P. Feynman, R. B. Leighton, and M. L. Sands, *The Feynman Lectures on Physics* (Addison-Wesley, Reading, MA, 1963), Vol. II, Chap. 14.

- [27] We calculated the Hankel functions, $H_\nu(x)^{(1,2)} = J_\nu(x) \pm iY_\nu(x)$ with $\nu \geq 0$, employing the double-precision regular [irregular] Bessel function of the fractional order $J_\nu(x)$ [$Y_\nu(x)$] as implemented in Gnu Scientific Library (GSL), see <https://www.gnu.org/software/gsl/doc/html/specfunc.html> `bessel-functions`. For $\nu < 0$, we use $H_{-\nu}^{(1)}(x) = e^{i\pi\nu}H_\nu^{(1)}(x)$ or $H_{-\nu}^{(2)}(x) = e^{-i\pi\nu}H_\nu^{(2)}(x)$.
- [28] G. Nemes, *Acta Appl. Math.* **150**, 141 (2017).
- [29] S. Russo, J. B. Oostinga, D. Wehenkel, H. B. Heersche, S. S. Sobhani, L. M. K. Vandersypen, and A. F. Morpurgo, *Phys. Rev. B* **77**, 085413 (2008).
- [30] C. Stampfer, E. Schurtenberger, F. Molitor, J. Guettinger, T. Ihn, and K. Ensslin, *Int. J. Mod. Phys.* **23**, 2647 (2009).
- [31] Y. Zhang, V. W. Brar, C. Girit, A. Zettl, and M. F. Crommie, *Nat. Phys.* **5**, 722 (2009).
- [32] S. Samaddar, I. Yudhistira, S. Adam, H. Courtois, and C. B. Winkelmann, *Phys. Rev. Lett.* **116**, 126804 (2016).
- [33] A. Jayaraman, K. Hsieh, B. Ghawri, P. S. Mahapatra, and A. Ghosh, [arXiv:2003.02880](https://arxiv.org/abs/2003.02880).
- [34] We took the nearest-neighbor hopping integral in graphene $t = 2.7$ eV and the lattice parameter $a = 0.246$ nm, leading to $\hbar v_F = \sqrt{3}ta/2 = 0.575$ eV nm.
- [35] For $E_F = 0$, the parameter $u_0 = U_0R_1^2/(R_2\hbar v_F)$ allows one to distinguish between the pseudodiffusive ($u_0 \ll 1$) and the ballistic ($u_0 \gg 1$) charge transport regimes, with crossover occurring for $u_0 \sim 1$; see also Ref. [7].

From: acta.phys.pol.b@uj.edu.pl

Subject: [APPB-SP] - 5899 - Korekta autorska (Zjazd Fizyków)

Date: 3 March 2020 at 13:04:57 CET

To: adam.rycerz@mac.com

Reply-To: acta.phys.pol.b@uj.edu.pl

Szanowny Panie,

Posyłam link do pliku PDF artykułu zaakceptowanego do druku w Acta Physica Polonica B do korekty autorskiej

https://www.actaphys.uj.edu.pl/sp/appb_sd/20RCk2sbC1ppX79zVSzJZdhP/v1/proof_5899@2020-03-03-1200.pdf

Listę ewentualnych poprawek proszę przysłać w najbliższym dogodnym terminie przez e-mail.

Prosimy o odpowiedź również w przypadku braku poprawek.

Proszę zwrócić uwagę, że jedynie elektroniczne wersje artykułów będą w kolorze, wersje drukowane są czarno-białe.

Numer DOI jest jeszcze niekompletny, właściwy numer zostanie nadany po spaginowaniu zeszytu.

Z poważaniem,

Elzbieta Zachorowska-Such

APP-B Editorial Board

<https://www.actaphys.uj.edu.pl/sp>

Adiabatic quantum pumping in buckled graphene nanoribbon driven by a kink *

DOMINIK SUSZALSKI AND ADAM RYCERZ

Institute of Theoretical Physics, Jagiellonian University, ul. S. Łojasiewicza 11,
PL-30348 Kraków, Poland

(Received February 18, 2020)

We propose a new type of quantum pump in buckled graphene nanoribbon, adiabatically driven by a kink moving along the ribbon. From a practical point of view, pumps with moving scatterers present advantages as compared to gate-driven pumps, like enhanced charge transfer per cycle per channel. The kink geometry is simplified by truncating the spatial arrangement of carbon atoms with the classical ϕ^4 model solution, including a width renormalization following from the Su-Schrieffer-Heeger model for carbon nanostructures. We demonstrate numerically, as a proof of concept, that for moderate deformations a stationary kink at the ribbon center may block the current driven by the external voltage bias. In the absence of a bias, a moving kink leads to highly-effective pump effect, with a charge per unit cycle dependent on the gate voltage.

1. Introduction

The idea of quantum pumping, i.e., transferring the charge between electronic reservoirs by periodic modulation of the device connecting these reservoirs [1], has been widely discussed in the context of graphene nanostructures [2, 3, 4, 5, 6, 7, 8]. Since early works, elaborating the gate-driven pumping mechanism in graphene [2] and bilayer graphene [3], it becomes clear that the transport via evanescent modes may significantly enhance the effectiveness of graphene-based pumps compared to other quantum pumps. Other pumping mechanisms considered involves laser irradiation [4], strain fields [5], tunable magnetic barriers [6], Landau quantization [7], or even sliding the Moiré pattern in twisted bilayer graphene [8].

It is known that quantum pump with a shifting scatterer may show enhanced charge transfer per cycle in comparison to a standard gate-driven

* Presented at 45. Zjazd Fizyków Polskich, Kraków 13–18 września 2019.

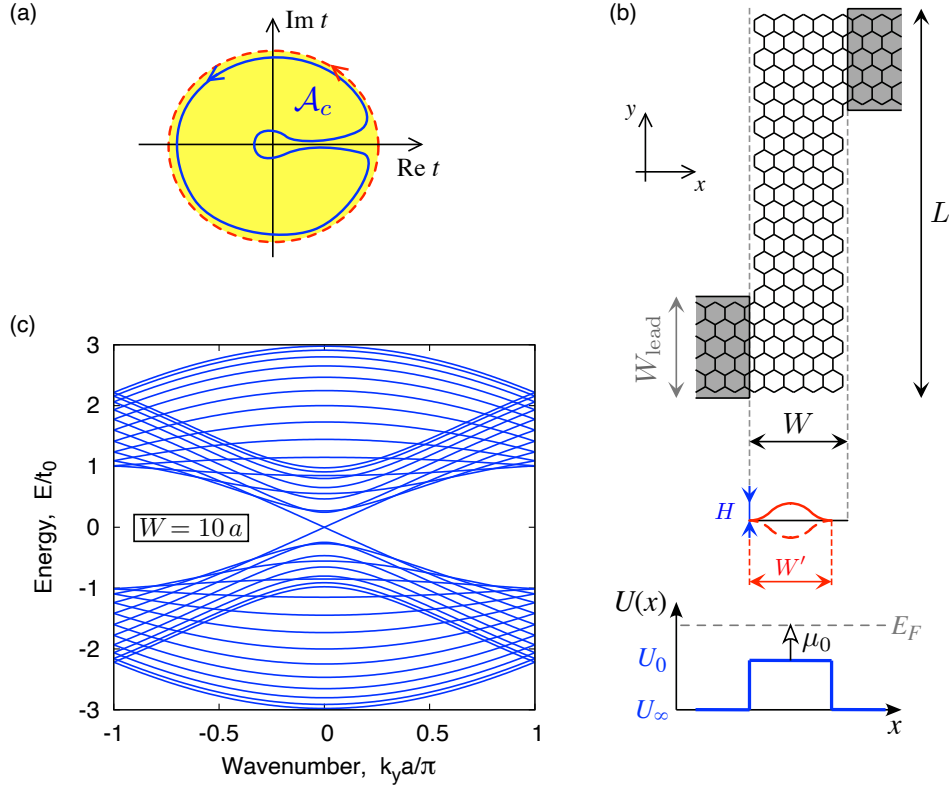


Fig. 1. Buckled graphene nanoribbon as a quantum pump. (a) Typical pumping cycles (schematic) for a single channel characterized by the complex transmission amplitude, $t = \text{Re } t + i \text{Im } t$. Blue solid line enclosing the area \mathcal{A}_c shows one-parameter cycle allowed for a standard gate-driven pump, red dashed line corresponds to the cycle involving a shift of a scatterer. (b) Flat ribbon with armchair edges attached to heavily-doped graphene leads (shaded areas). The ribbon width $W = 5a$ (with $a = 0.246 \text{ nm}$ the lattice spacing) and length $L = 11.5\sqrt{3}a$ are chosen for illustrative purposes only. A cross section of buckled ribbon, characterized by the reduced width $W' < W$ and the buckle height $H > 0$, and the electrostatic potential energy profile $U(x)$, are also shown. (c) Band structure of the infinite metallic-armchair nanoribbon of $W = 10a$ width, same as used in the computations.

pump [1], see also Fig. 1(a)¹. Motivated by this conjecture we consider

¹ In the simplest case of a one-parameter driven, one-channel pump, the charge per cycle is given by $Q = (e/\pi)\mathcal{A}_c$, with \mathcal{A}_c being the \pm area enclosed by the contour in the $(\text{Re } t, \text{Im } t)$ plane (where t is a parameter-dependent transmission amplitude).

a buckled nanoribbon, see Fig. 1(b), similar to the one studied numerically by Yamaletdinov et. al. [9, 10] as a physical realization of the classical ϕ^4 model and its topological solutions (*kinks*) connecting two distinct ground states. Our setup is supplemented with two heavily-doped graphene leads, attached to the clamped edges of a ribbon, allowing to pass electric current along the system.

2. Model and methods

The analysis starts from the Su-Schrieffer-Heeger (SSH) model for the ribbon, including the hopping-matrix elements corresponding to the nearest-neighbor bonds on a honeycomb lattice [11, 12, 13, 14]

$$\mathcal{H}_{\text{ribbon}} = -t_0 \sum_{\langle ij \rangle, s} \exp\left(-\beta \frac{\delta d_{ij}}{d_0}\right) (c_{i,s}^\dagger c_{j,s} + c_{j,s}^\dagger c_{i,s}) + \frac{1}{2} K \sum_{\langle ij \rangle} (\delta d_{ij})^2, \quad (1)$$

with a constrain $\sum_{\langle ij \rangle} \delta d_{ij} = 0$, where δd_{ij} is the change in bond length, and $d_0 = a/\sqrt{3}$ is the equilibrium bond length defined via the lattice spacing $a = 0.246$ nm. The equilibrium hopping integral $t_0 = 2.7$ eV, $\beta = 3$ is the dimensionless electron-phonon coupling, and $K \approx 5000$ eV/nm² is the spring constant for a C-C bond. The operator $c_{i,s}^\dagger$ (or $c_{i,s}$) creates (or annihilates) a π electron at the i -th lattice site with spin s .

In order to determine the spatial arrangement of carbon atoms in a buckled nanoribbon, $\{\mathbf{R}_j = (x_j, y_j, z_j)\}$, we first took the $\{x_j\}$ and $\{y_j\}$ coordinates same as for a flat honeycomb lattice in the equilibrium and set $\{z_j\}$ according to

$$z = H \tanh\left(\frac{y - y_0}{\lambda}\right) \sin^2\left(\frac{\pi x}{W}\right), \quad (2)$$

representing a topologically non-trivial solution of the ϕ^4 model, with H the buckle height, W the ribbon width, y_0 and λ the kink position and size (respectively). Next, x -coordinates are rescaled according to $x_j \rightarrow x_j W'/W$, with W' adjusted to satisfy $\sum_{\langle ij \rangle} \delta d_{ij} = 0$ in the $y_0 \rightarrow \pm\infty$ (“no kink”) limit. In particular, $H = 2a$ and $W = 10a$ corresponds to $W'/W = 0.893$. We further fixed the kink size at $\lambda = 3a$ (closely resembling the kink profile obtained from the molecular dynamics in Ref. [9]); this results in relative bond distortions not exceeding $|\delta d_{ij}|/d_0 \leq 0.08$. Full optimization of the bond lengths in the SSH Hamiltonian (1), which may lead to the alternating bond pattern [14], is to be discussed elsewhere.

Heavily-doped graphene leads, $x < 0$ or $x > W'$ in Fig. 1(b), are modeled as flat regions ($d_{ij} = d_0$) with the electrostatic potential energy $U_\infty = -0.5t_0$ (compared to $U_0 = 0$ in the ribbon), corresponding to 13 propagating

modes for $W_\infty = 20\sqrt{3}a$ and the chemical potential $\mu_0 = E_F - U_0 = 0$. The scattering problem is solved numerically, for each value of the chemical potential μ_0 and the kink position y_0 , using the KWANT package [15] allowing to determine the scattering matrix

$$S(\mu_0, y_0) = \begin{pmatrix} r & t' \\ t & r' \end{pmatrix}, \quad (3)$$

which contains the transmission t (t') and reflection r (r') amplitudes for charge carriers incident from the left (right) lead, respectively.

The linear-response conductance can be determined from the S -matrix via the Landauer-Büttiker formula [1], namely

$$G = G_0 \text{Tr} tt^\dagger = \frac{2e^2}{h} \sum_n T_n, \quad (4)$$

where $G_0 = 2e^2/h$ is the conductance quantum and T_n is the transmission probability for the n -th normal mode. Similarly, in the absence of a voltage bias, the charge transferred between the leads upon varying solely the parameter y_0 is given by

$$\Delta Q = -\frac{ie}{2\pi} \sum_j \int dy_0 \left(\frac{\partial S}{\partial y_0} S^\dagger \right)_{jj}, \quad (5)$$

where the summation runs over the modes in a selected lead. Additionally, the integration in Eq. (5) is performed for a truncated range of $-\Lambda \leq y_0 \leq L + \Lambda$, with $\Lambda = 250a \gg \lambda$ for $L = 75.5\sqrt{3}a$.

3. Results and discussion

In Fig. 1(c) we depict the band structure for an infinite (and flat) metallic-armchair ribbon of $W = 10a$ width. It is remarkable that the second and third lowest-lying subband above the charge-neutrality point (as well as the corresponding highest subbands below this point) show an almost perfect degeneracy near their minima corresponding to $E_{\min}^{(2,3)} \approx 0.25 t_0$, which can be attributed to the presence of two valleys in graphene. For higher subbands, the degeneracy splitting due to the trigonal warping is better pronounced.

The approximate subband degeneracy has a consequence for the conductance spectra of a finite ribbon, presented in Fig. 2: For both the flat ribbon ($H = 0$) and a buckled ribbon with no kink ($H = 2a$, $y_0 \rightarrow -\infty$) the conductance $G \approx G_0$ for $|\mu_0| < E_{\min}^{(2,3)}$ and quickly rises to $G/G_0 \approx 2.5-3$ for $\mu > E_{\min}^{(2,3)}$. For $\mu < 0$ the quantization is not so apparent, partly

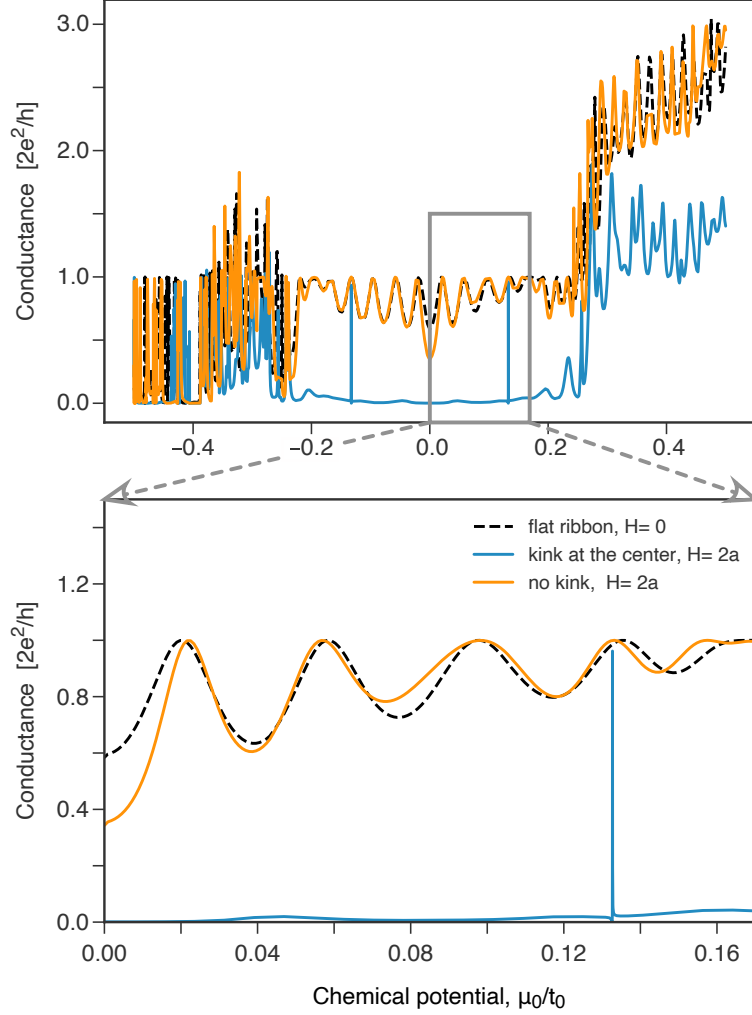


Fig. 2. Conductance of the ribbon with $W = 10a$ as a function of the chemical potential. The remaining parameters are $L = 75.5\sqrt{3}a$ and $W_{\text{lead}} = 20\sqrt{3}a$. Different lines (same in two panels) correspond to the flat ribbon geometry, $H = 0$, $W' = W$ (black dashed), the buckled ribbon with $H = 2a$ and $y_0 = L/2$ (blue solid) or $y_0 \rightarrow -\infty$ (orange solid); see Eq. (2). Bottom panel is a zoom-in of the data shown in top panel.

due the presence of two p-n interfaces (at $x = 0$ and $x = W'$) leading to stronger-pronounced oscillations (of the Fabry-Perrot type), and partly due to a limited number of propagating modes in the leads. For a kink positioned at the center of the ribbon ($H = 2a$, $y_0 = L/2$) the conductance

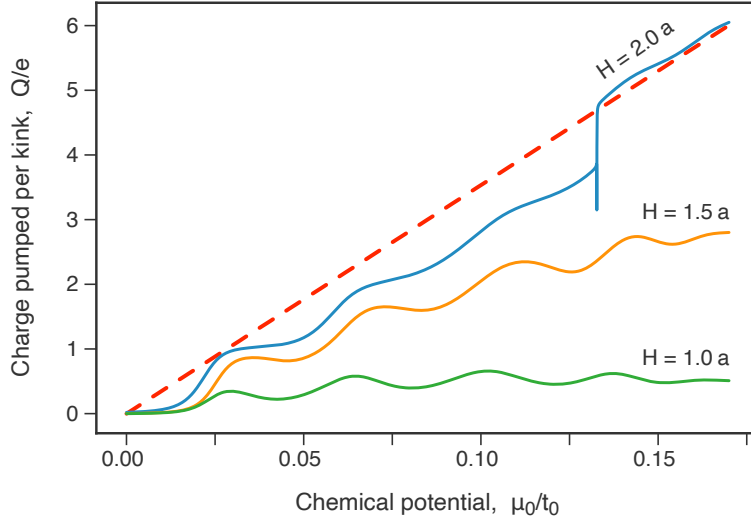


Fig. 3. Charge transferred upon adiabatic kink transition calculated from Eq. (5), for varying buckling amplitude $H/a = 1, 2$ (specified for each line in the plot), displayed as a function of the chemical potential. Dashed line shows the approximation given by Eq. (6). Remaining parameters are same as in Fig. 2.

is strongly suppressed, $G \ll G_0$, in the full $|\mu_0| < E_{\min}^{(2,3)}$ range (with the exception from two narrow resonances at $\mu_0 = \pm 0.1327 t_0$, which vanishes for $y_0 \neq L/2$) defining a feasible energy window for the pump operation.

In Fig. 3 we display the charge transferred between the leads at zero bias, see Eq. (5), when slowly moving a kink along the ribbon (*adiabatic kink transition*). In the energy window considered, the ribbon dispersion relation consists of two subbands with opposite group velocities, $E_{\pm}^{(1)} = \pm \hbar v_F k_y$, see Fig. 1(c). Therefore, the total charge available for transfer at the ribbon section of $L_{\text{eff}} = L - W_{\text{infty}}$ length can be estimated (up to a sign) as

$$\frac{Q_{\text{tot}}}{e} \approx \frac{|\mu_0|}{\hbar v_F} \frac{L_{\text{eff}}}{\pi} = 35.3 \frac{|\mu_0|}{t_0}, \quad (6)$$

where $v_F = \sqrt{3} t_0 a / (2\hbar) \approx 10^6$ m/s is the Fermi velocity in graphene and we put $L - W_{\text{infty}} = 55.5 \sqrt{3} a$. For the strongest deformation ($H = 2a$) the kink almost perfectly blocks the current flow, and the charge transferred is close to the approximation given by Eq. (6); see Fig. 3.

4. Conclusion

We have investigated, by means of computer simulations of electron transport, the operation of adiabatic quantum pump build within a topo-

logical defect moving in buckled graphene nanoribbon. We find that the pump effectiveness is close to the maximal (corresponding to a kink perfectly blocking the current flow) for moderate bucklings, with relative bond distortions not exceeding 8%. As topological defects generally move with negligible energy dissipation, we hope our discussion will be a starting point to design new graphene-based energy conversion devices.

Acknowledgments

We thank Tomasz Romańczukiewicz for discussions. The work was supported by the National Science Centre of Poland (NCN) via Grant No. 2014/14/E/ST3/00256.

REFERENCES

- [1] Yu. V. Nazarov and Ya. M. Blanter, *Quantum Transport: Introduction to Nanoscience*, (Cambridge University Press, Cambridge, 2009), Chapter 1.
- [2] E. Prada, P. San-Jose, and H. Schomerus, *Solid State Comm.* **151**, 1065 (2011).
- [3] M. Wakker and M. Blaauboer, *Phys. Rev. B* **82**, 205432 (2010).
- [4] P. San-Jose, E. Prada, H. Schomerus, and S. Kohler, *Appl. Phys. Lett.* **101**, 153506 (2012).
- [5] Y. Jiang, T. Low, K. Chang, M. I. Katsnelson, and F. Guinea, *Phys. Rev. Lett.* **110**, 046601 (2013).
- [6] E. Grichuk and E. Manykin, *Eur. Phys. J. B* **86**, 210 (2013).
- [7] B. Abdollahipour and E. Moomivand, *Physica E* **86** 204 (2017).
- [8] M. Fujimoto, H. Koschke, and M. Koshino, *Phys. Rev. B* **101**, 041112 (2020).
- [9] R. D. Yamaletdinov, V. A. Slipko, and Y. V. Pershin, *Phys. Rev. B* **96**, 094306 (2017).
- [10] R. D. Yamaletdinov, T. Romańczukiewicz, and Y. V. Pershin, *Carbon* **141**, 253 (2019).
- [11] K. Harigaya, *Prog. Theor. Phys. Suppl.* **113**, 229 (1993).
- [12] J. Ma, S. Guan, and C.-H. Lai, *Phys. Rev. B* **74**, 205401 (2006).
- [13] G. Dresselhaus, M. S. Dresselhaus, and R. Saito, *Physical Properties Of Carbon Nanotubes*, (World Scientific, Singapore, 1998), Chapter 11.
- [14] O. Gröning, S. Wang, X. Yao, et al., *Nature* **560**, 209 (2018).
- [15] C. W. Groth, M. Wimmer, A. R. Akhmerov, and X. Waintal, *New J. Phys.* **16**, 063065 (2014); see also: <https://kwant-project.org>.

Adiabatic pumping driven by moving kink and quantum standard ampere in buckled graphene nanoribbon

Dominik Suszalski and Adam Rycerz

Institute for Theoretical Physics, Jagiellonian University, Łojasiewicza 11, PL–30348 Kraków, Poland

(Dated: July 21, 2020)

A quantum pump in buckled graphene ribbon with armchair edges is discussed numerically. By solving the Su-Schrieffer-Heeger model and performing the computer simulation of quantum transport we find that a kink adiabatically moving along the metallic ribbon results in highly-efficient pumping, with a charge per kink transition close to the maximal value determined by the Fermi velocity in graphene. Remarkably, insulating nanoribbon show the quantized value of a charge per kink ($2e$) in relatively wide range of the system parameters, providing a promising candidate for the quantum standard ampere. We attribute it to the presence of a localized electronic state, moving together with a kink, whose energy lies within the ribbon energy gap.

I. INTRODUCTION

Nanoscale electromechanical devices based on novel two-dimensional materials, such as graphene, constitute a specific class of systems being interesting both due to their fundamental and technological aspects [1, 2]. In attempt to improve electromechanical characteristics of such devices, one need to address fundamental issues concerning the structure of effective Hamiltonian at nanoscale, including tight-binding parameters [3], elastic coefficients [4, 5], and electron phonon-coupling [6]. Numerous works have addressed the idea of quantum pumping in graphene nanostructures [7–15], employing various physical mechanisms. These include gate-driven pumping [7, 8], laser light [9], strain-induced fields [10], tunable magnetoresistance [11], quantum Hall states [12], but also electromechanical effects accompanying sliding Moiré patterns in twisted bilayer [13, 14], or (most recently) moving kink in buckled graphene nanoribbon [15].

As generic quantum pump transfers electric charge between two reservoirs at zero external bias, solely due to periodic modulation of the device connecting the reservoirs [16], new fundamental and practical aspects of any particular pumping mechanism may be unveiled with the charge quantization at nanoscale. Various single-electron pumps were considered as candidates for quantum standard ampere [17–19]: In case the charge pumped per cycle is perfectly quantized (i.e., equal to $Q = ne$, with n integer) in a considerably wide range of driving parameters, the output current delivered by the device is $I_P = nef_P$, with f_P being the external frequency, and the SI unit of current can be re-defined by fixing the elementary charge e at $1.602176634 \times 10^{-19}$ A·s, with the second defined via the ground-state hyperfine transition frequency of the cesium 133 atom, $\Delta\nu_{Cs} = 9\,192\,631\,770$ Hz [20, 21].

So far, single-electron pumps with potential to operate as standard ampere are predominantly based on gate-driven quantum dot systems [19]. We argue here, presenting the results of computer simulation of quantum transport, that electromechanical pump based on buckled graphene ribbon, which has recently attracted some attention as a physical realization of the classical ϕ^4 model and its topological solutions (*kinks*) connecting two distinct ground states [22, 23], may also be considered as a promising counterpart to the above-mentioned single-electron pumps.

Earlier [15], we have shown that the system similar to the presented in Fig. 1 consisting of *metallic* graphene nanoribbon with armchair edges coupled to heavily-doped graphene leads may operate as efficient quantum pump, but the charge per cycle is not quantized. Here, the discussion is supplemented by (i) taking the case of *insulating* nanoribbon into account, and (ii) by optimizing atomic bond lengths in a framework of the Su-Schrieffer-Heeger (SSH) model [24] including electron-phonon coupling of the Peierls type [25]. As a result, we find that for an insulating ribbon a single electronic state localized at the kink is well-separated from extended states, and the charge pumped is quantized. Topological aspects of the system are crucial to understand the charge pump operation, since the electron-phonon coupling leads to the peculiar arrangement of shorten (lengthen) bonds being perpendicular (parallel) to the main ribbon axis in the kink area, resulting in the electron localization.

We also show in this paper that, although the kink shape is well-described within the standard molecular dynamics potentials for graphite-based systems (as implemented in the LAMMPS package [26]), for accurate modeling of quantum transport phenomena one needs to include small corrections to the bond length (up to a few percents the kink area), following from electron-phonon coupling. A minimal quantum-mechanical Hamiltonian, of the SSH type, allowing one to model both the kink shape and the transport, is proposed.

Remaining part of the paper is organized as follows. In Sec. II, we present the model Hamiltonian and our method of approach. In Sec. III, we discuss quantum states of a finite section of buckled ribbon (i.e., *closed* system) with a kink. The conductance, and the adiabatic pumping in the ribbon coupled to the leads (*open* system) is analyzed numerically in Sec. IV. The conclusions are given in Sec. V.

II. MODEL AND METHODS

A. The Hamiltonian

Our analysis starts from the Su-Schrieffer-Heeger (SSH) Hamiltonian for graphene nanostructures [24, 28, 29], with potential energy describing the covalent bonds [4]

$$\mathcal{H}_{\text{SSH}} = T + V_{\text{bonds}} + V_{\text{angles}}, \quad (1)$$

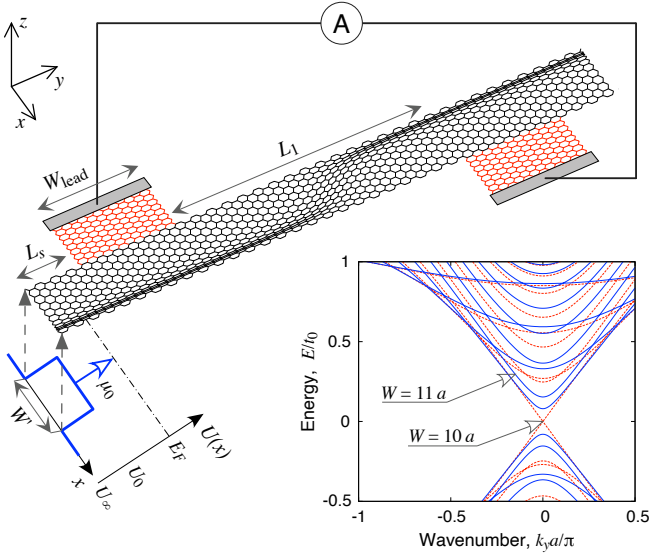


Figure 1: Buckled graphene ribbon as a quantum pump. Top: Nanoribbon buckled by changing the distance between fixed armchair edges from the equilibrium width of $W = 11a$ (with $a = 0.246$ nm the lattice spacing) to $W' = 0.9W$, attached to heavily-doped graphene leads (red), each of width W_∞ , separated by distance L_1 . The total ribbon length is $L = L_1 + 2W_\infty + 2L_s$, where L_s denotes distance between the free ribbon edge and the lead edge. The kink is formed near the ribbon center. The ammeter detects the current driven by a moving kink. The gate electrode (not shown) is placed underneath to tune the chemical potential μ_0 in the ribbon area. The schematic potential profile $U(x)$ (bottom left) and the coordinate system (top left) are also shown. Inset: Band structure of the infinite flat ribbon with armchair edges for $W = 11a$ (solid blue lines) and $W = 10a$ (dashed red lines).

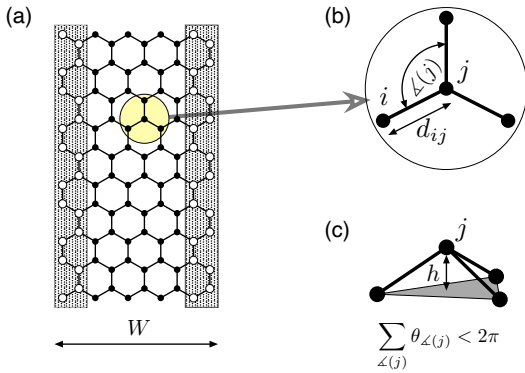


Figure 2: (a) Short section of a nanoribbon of $W = 5a$ width. Two rows of carbon atoms near each armchair edge (open symbols on dotted areas) are fixed implementing the clamped boundary conditions. Remaining atoms (full symbols) are adjusted to minimize the ground-state energy. (b) Bond lengths (d_{ij}) and angles ($\theta_{\angle(j)}$) used in the system Hamiltonian [see Eqs. (1), (2), (3), (4)]. (c) The out-of-plane deformation parametrized by the sum of three angles with a common vertex j , related to a tetrahedron height $h^2 \propto 2\pi - \sum_{\angle(j)} \theta_{\angle(j)}$.

where

$$T = -t_0 \sum_{\langle ij \rangle, s} e^{-\beta \delta d_{ij}/d_0} \left(c_{i,s}^\dagger c_{j,s} + c_{j,s}^\dagger c_{i,s} \right), \quad (2)$$

$$V_{\text{bonds}} = \frac{1}{2} K_d \sum_{\langle ij \rangle} (d_{ij} - d_0)^2, \quad (3)$$

$$V_{\text{angles}} = \frac{1}{2} K_\theta \sum_j \sum_{\angle(j)} (\theta_{\angle(j)} - \theta_0)^2 + V_\delta \sum_j \left(2\pi - \sum_{\angle(j)} \theta_{\angle(j)} \right), \quad (4)$$

with a constrain

$$\sum_{\langle ij \rangle} d_{ij} \equiv \mathcal{C} (= \text{const.}). \quad (5)$$

The kinetic-energy operator for π electrons T (2) includes the hopping-elements (t_{ij}) corresponding to the nearest-neighbors on a honeycomb lattice (denoted by using brackets $\langle ij \rangle$), with the equilibrium hopping integral $t_0 = 2.7$ eV. The change in bond length, $\delta d_{ij} = d_{ij} - d_0$, is calculated with respect to the equilibrium bond length $d_0 = a/\sqrt{3}$, with $a = 2.46$ Å being the lattice spacing. The operator $c_{i,s}^\dagger$ (or $c_{i,s}$) creates (or annihilates) a π electron at the i -th lattice site with spin s . The electron-phonon coupling, quantified by the dimensionless parameter $\beta = -\partial \ln t_{ij} / \partial \ln d_{ij}|_{d_{ij}=d_0}$ (to be specified later), is represented by the exponential factor in Eq. (2) replacing standard Peierls form $(1 - \beta \delta d_{ij}/d_0)$ in order to prevent t_{ij} from changing the sign upon strong lattice deformation.

The next two terms in Eq. (1), V_{bond} (3) and V_{angles} (4), approximates the potential energies for the bond stretching and bond angle bending (respectively); see Fig. 2. The parameters $K_d = 40.67$ eV/Å², $K_\theta = 5.46$ eV/rad², and $\theta_0 = \pi/3$, are taken from Ref. [4] and restore the actual in-plane elastic coefficients of bulk graphene in the case of $\beta = 0$. Otherwise (for $\beta \neq 0$), a correction to the potential energy per bond can be estimated as

$$(N_b)^{-1} \left. \frac{\partial^2 \langle T \rangle}{\partial d_{ij}^2} \right|_{\{d_{ij}=d_0\}} = \frac{\beta t_0}{d_0^2} \sum_s \langle c_{i,s}^\dagger c_{j,s} + c_{j,s}^\dagger c_{i,s} \rangle \approx \beta \times 1.405 \text{ eV/Å}^2 \ll K_d \quad (\text{for } \beta \sim 1), \quad (6)$$

with the number of C-C bonds N_b . The second approximate equality in the above is obtained by substituting $\sum_s \langle c_{i,s}^\dagger c_{j,s} + c_{j,s}^\dagger c_{i,s} \rangle \approx 1.050$ (with i and j the nearest neighbors), being the value for a perfect, bulk graphene sheet at the half electronic filling [30].

The expression for V_{angles} (4) consists of two terms, each involving summation over the three angles $\angle(j)$ having a common vertex at a given lattice site j (see Fig. 2). First term, $\propto K_\theta$, represents the harmonic approximation for in-plane bond angle bending. For out-of plane deformations, quantified by the height h_j of a tetrahedron formed by j -th site

and its three nearest neighbors, this term represents a fourth-order correction to the potential energy. A realistic description of out-of-plane deformations requires a correction of the $\sim h_j^2$ order (for $h_j \ll d_0$). Here we propose a term proportional to the excess angle,

$$\delta_j = 2\pi - \sum_{\angle(j)} \theta_{\angle(j)} \approx 3\sqrt{3} \left(\frac{h_j}{d_0} \right)^2, \quad (7)$$

with the coefficient $V_\delta \approx t_0 = 2.7 \text{ eV}$ roughly approximating the bending rigidity of graphene [5, 6]. The main advantage of such an approach is that it requires no computationally expensive operations since the four-body term ($\propto V_\delta$) depends only on angles ($\theta_{\angle(j)}$) earlier determined for the three-body term ($\propto K_\theta$). The validity of our approach, in comparison with standard molecular dynamics treatments [22, 23], is discussed later in this paper.

B. The optimization procedure

Throughout the paper, we compare the results obtained in the absence of electron phonon coupling, $\beta = 0$, and for the dimensionless parameter $\beta = 3$. In the former case, electronic and lattice degrees of freedom are decoupled, and one simply need to solve a purely classical minimization problem for the potential energy part of the Hamiltonian \mathcal{H}_{SSH} (1), given by $V_{\text{bonds}} + V_{\text{angles}}$ [see Eqs. (3) and (4)]. For the latter case, the average kinetic energy can be calculated as

$$\begin{aligned} \langle T \rangle &= -t_0 \sum_{\langle ij \rangle, s} \exp\left(-\beta \frac{\delta d_{ij}}{d_0}\right) \langle c_{i,s}^\dagger c_{j,s} + c_{j,s}^\dagger c_{i,s} \rangle \\ &= 2 \sum_{ij} t_{ij} \sum_{1 \leq k \leq N_{\text{el}}/2} [\psi_k^{(i)}]^* \psi_k^{(j)} \\ &= 2 \sum_{1 \leq k \leq N_{\text{el}}/2} E_k, \end{aligned} \quad (8)$$

where the factor 2 in the last two expressions follows from a spin degeneracy, $t_{ij} = -t_0 \exp(-\beta \delta d_{ij}/d_0)$ if i and j are the nearest neighbors (otherwise, $t_{ij} = 0$), and $\psi_k^{(j)}$ denotes the probability amplitude for the k -th eigenstate of the kinetic energy operator T (2) at j -th lattice site. We further suppose that the eigenstates are ordered such that the energies $E_1 \leq E_2 \leq \dots \leq E_{N_{\text{el}}}$, with the number of atoms N_{at} , and that the number of electrons N_{el} is even for simplicity.

In both cases ($\beta = 0$ and $\beta = 3$), the numerical minimization of the ground-state energy

$$E_G = E_G(\{\mathbf{R}_j\}) = \langle \mathcal{H}_{\text{SSH}} \rangle, \quad (9)$$

with respect to atomic positions $\{\mathbf{R}_j\}$, is performed employing the modified periodic boundary conditions in y -direction (see Fig. 1). Namely, the system is invariant upon $y \mapsto y + L$ and $z \mapsto -z$, forcing the kink formation in a buckled ribbon. The outermost two rows of atoms near each armchair edge are fixed during the minimization (see Fig. 2), and buckling of the ribbon is realized by changing the distance between the fixed edges [see Fig. 2(a)] from W to $W' < W$.

Furthermore, the number of electrons is fixed at $N_{\text{el}} = N_{\text{at}}$, with $N_{\text{at}} = 3600$ for metallic armchair ribbon ($W = 10a$, $L = 90\sqrt{3}a$) or $N_{\text{at}} = 3960$ for insulating armchair ribbon ($W = 11a$, $L = 90\sqrt{3}a$). Although in open system, coupled to the leads, the average N_{el} varies with the chemical potential, such fluctuations (typically, limited to $\Delta\mu < 0.1 \text{ eV}$ or, equivalently, $\Delta N_{\text{el}}/N_{\text{at}} \approx 0.18 (\Delta\mu/t_0)^2 < 2 \times 10^{-4}$; see Ref. [31]) are insignificant when determining the optimal bond lengths. Alternatively, one can interpret the $\beta = 0$ case as a hypothetical $N_{\text{el}} = 0$ situation, leading to bond length modifications not exceeding a few percents (see below).

For a fixed W'/W ratio and the kink position $y = y_0$, the computations proceed as follows.

The initial arrangement of carbon atoms is given by

$$\mathbf{R}_j^{(0)} = \left(x_j^{(0)}, y_j^{(0)}, z_j^{(0)} \right), \quad j = 1, 2, \dots, N_{\text{at}}, \quad (10)$$

where

$$\begin{aligned} x_j^{(0)} &= X_{W,W'}(\tilde{x}_j), \\ y_j^{(0)} &= \tilde{y}_j, \\ z_j^{(0)} &= H \tanh\left(\frac{\tilde{y}_j - y_0}{\Lambda}\right) \sin^2\left(\frac{\pi \tilde{x}_j}{W}\right), \end{aligned} \quad (11)$$

with $(\tilde{x}_j, \tilde{y}_j)$ being the coordinates of j -th atom on a flat honeycomb lattice, and the scaling function

$$X_{W,W'}(x) = \begin{cases} x, & \text{for } x < 0, \\ (W'/W)x, & \text{for } 0 \leq x < W, \\ x - W + W', & \text{for } x \geq W. \end{cases} \quad (12)$$

The buckle height H in Eq. (11) is adjusted such that $\mathcal{C} = N_b d_0$ in Eq. (5). The kink size is fixed at $\Lambda = 5a$, roughly approximating the kink profiles reported in Refs. [22, 23].

At first step, we minimize the potential energy term $V_{\text{bonds}} + V_{\text{angles}}$, ignoring a constrain given by Eq. (5). This gives us the solution for $\beta = 0$ in the Hamiltonian \mathcal{H}_{SSH} (1).

Next step, performed only if $\beta > 0$, involves a further adjustment of atomic positions $\{\mathbf{R}_j\}$ such that full ground-state energy E_G (9) reaches a minimum. In practice, we determine hopping parameters $\{t_{ij}\}$, wavefunctions $\{\psi_k^{(j)}\}$, and correlation functions $\{\langle c_{i,s}^\dagger c_{j,s} \rangle\}$ [see Eq. (8)] for given $\{\mathbf{R}_j\}$ -s, and then find (within the gradient descent method) a conditional minimum of E_G with respect to $\{\mathbf{R}_j\}$ at fixed values of $\{\langle c_{i,s}^\dagger c_{j,s} \rangle\}$ -s, satisfying a constrain given by Eq. (5). The procedure is iterated until the numerical convergence is reached. Typically, after 3–4 iterations the atomic positions $\{\mathbf{R}_j\}$ -s are determined with the accuracy better than $10^{-5} a$.

C. Comparison with LAMMPS results

A brief comparison of the kink shape following from the numerical procedure described above with the corresponding output produced by the LAMMPS Molecular Dynamics Simulator [26, 27] is presented in Fig. 3.

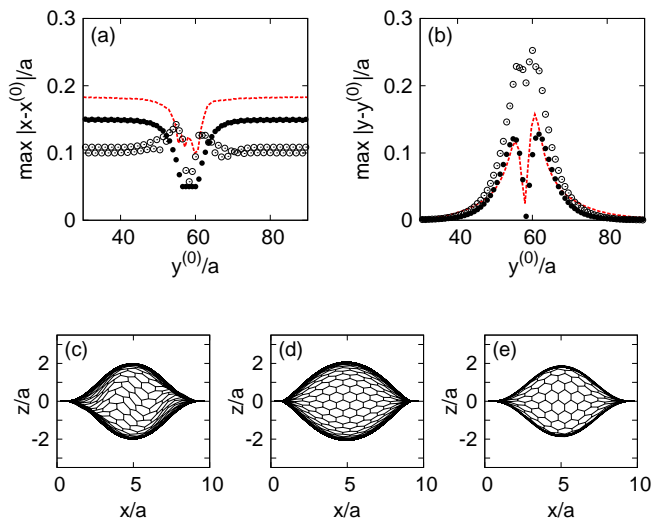


Figure 3: Spatial arrangement of carbon atoms after the optimization procedure presented in Sec. II B compared with the LAMMPS output. (a,b) Maximal displacement of an atom along (a) x -axis or (b) y -axis in the coordinate system of Fig. 1, after the optimization starting from initial coordinates $x = x^{(0)}$, $y = y^{(0)}$ [see Eqs. (10), (11)]. Open (or closed) symbols correspond to $\beta = 0$ (or $\beta = 3$). Red dashed lines show the LAMMPS results for comparison [26, 27]. (c)–(e) C-C bonds after the optimization projected onto the x - z plane for (c) $\beta = 0$, (d) $\beta = 3$, and (e) the LAMMPS results. [Notice that difference in scales for x and z axes visually amplifies the buckling.] The system parameters are $L = 90\sqrt{3}a$, $W = 11a$, $W'/W = 0.9$, and the kink position is $y_0 = (3/8)L \approx 58.5a$ for all cases.

In order to quantify the difference in atomic arrangements obtained within different approaches, we choose the maximal absolute displacement of atom along the x (and y) axis, $\max |x - x^{(0)}|$ (and $\max |y - y^{(0)}|$), where the maximum is taken for a subset of atoms with equal initial $y^{(0)}$ coordinates; see Figs. 3(a) and 3(b). It is sufficient to display the data corresponding to a vicinity of the kink, $30 \leq y^{(0)}/a \leq 90$, since far away from the kink position (being fixed at $y_0 \approx 58.5a$) both the quantities considered become $y^{(0)}$ -independent. (As free boundary conditions are applied in case the LAMMPS package is utilized, some $y^{(0)}$ -dependences reappear near the free zigzag edges, but they are much smaller in magnitude than dependencies in the kink area.)

It is clear from Figs. 3(a) and 3(b) that the LAMMPS results (see red-dashed lines) are closer to the obtained with our optimization procedure in the presence of electron-phonon coupling, $\beta = 3$ (solid symbols), then for $\beta = 0$ (open symbols). Also, x - z views of the system, presented in Figs. 3(c), 3(d), and 3(e), show that approximate mirror symmetry of the kink appears for $\beta = 3$ [see Fig. 3(d)] and for the LAMMPS results [Fig. 3(e)], but is absent for $\beta = 0$ [Fig. 3(c)].

The above observations can be rationalized taking into account that four-body (dihedral) and long-range Lennard-Jones potential energy terms are included in the LAMMPS package but absent in our model Hamiltonian \mathcal{H}_{SSH} (1). In the presence of electron-phonon coupling ($\beta > 0$), however, the average kinetic energy $\langle T \rangle$ (8) can be interpreted as an effective

long-range (and “infinite-body”) attractive interaction between atoms, restoring some features related to the Lennard-Jones forces in molecular dynamics (including an approximate mirror symmetry of the kink).

III. QUANTUM STATES IN CLOSED SYSTEM WITH PERIODIC BOUNDARY CONDITIONS

A. Bond-length modulation

Before discussing the electronic structure of the system, we briefly describe small corrections to the bond lengths appearing in the kink area due to electron-phonon coupling (see Fig. 4), which are essential to understand the results presented in the remaining parts of the paper.

In Figs. 4(a) and 4(b) we visualize the spatial arrangements of shorten and lengthen bonds; namely, $d_{ij} < \langle d_{ij} \rangle_{i,j=1\dots N_{\text{at}}}$ (thick black lines) and $d_{ij} > \langle d_{ij} \rangle$ (thin red lines), where the average bond length $\langle d_{ij} \rangle = 0.998 d_0$ for $\beta = 0$ and $W'/W = 0.9$, or $\langle d_{ij} \rangle \equiv d_0$ for $\beta = 3$ due to a constrain imposed [see Eq. (5)]. Apparently, in the presence of electron-phonon coupling ($\beta = 3$) a large rectangular block is formed in the kink area [i.e., for $|y - y_0| \lesssim 7a$; see Fig. 4(b)], in which almost all bonds oriented in the zigzag direction are shorten (resulting in the hopping element $|t_{ij}| > t_0$) and almost all remaining bonds are lengthen ($|t_{ij}| < t_0$). In the absence of electron-phonon coupling ($\beta = 0$) the situation is less clear [Fig. 4(a)], with a few smaller blocks of shorten or lengthen bonds forming more complex patterns, some of which are isotropic, and some show various crystallographic orientations.

The qualitative finding presented above is further supported with statistical distributions of the relative bond length (d_{ij}/d_0), determined using all $N_b = 5749$ bonds in the system (for $L = 90\sqrt{3}a$ and $W = 11a$) and displayed in Figs. 4(c) and 4(d). In particular, the distribution for $\beta = 3$ [Fig. 4(d)] is significantly wider than for $\beta = 0$ [Fig. 4(c)]. Also, bimodal structure of the distribution is visible in the presence of electron-phonon coupling, suggesting that two distinct populations of shorten and lengthen bonds are formed in this case.

The position dependence of the bond-length modulation is illustrated in Figs. 4(e) and 4(f), where we display the mean $\langle d_{ij} \rangle$ the variance $\text{Var}(d_{ij})$ calculated for bonds connecting atoms in a single zigzag line (parallel to the x direction) as functions of a mean y -position of carbon atoms in the line. It is clear that significant bond-length modulations (however, not exceeding a few percents of d_0) appear only in a small vicinity of the kink position, $|y - y_0| \lesssim 7a$, and that the modulations and noticeably stronger for $\beta = 3$ (solid symbols) than for $\beta = 0$ (open symbols). Remarkably, the LAMMPS results (red-dashed lines) now indicate much weaker bond-length modulations than our numerical results (regardless $\beta = 0$ or $\beta = 3$) but are significantly closer to the $\beta = 0$ results than to the $\beta = 3$ results. This shows that the quantum-mechanical nature of the Hamiltonian \mathcal{H}_{SSH} (1), relevant for spacial arrangement of carbon atoms only if $\beta \neq 0$, is crucial for an accurate description of bond-lengths corrections.

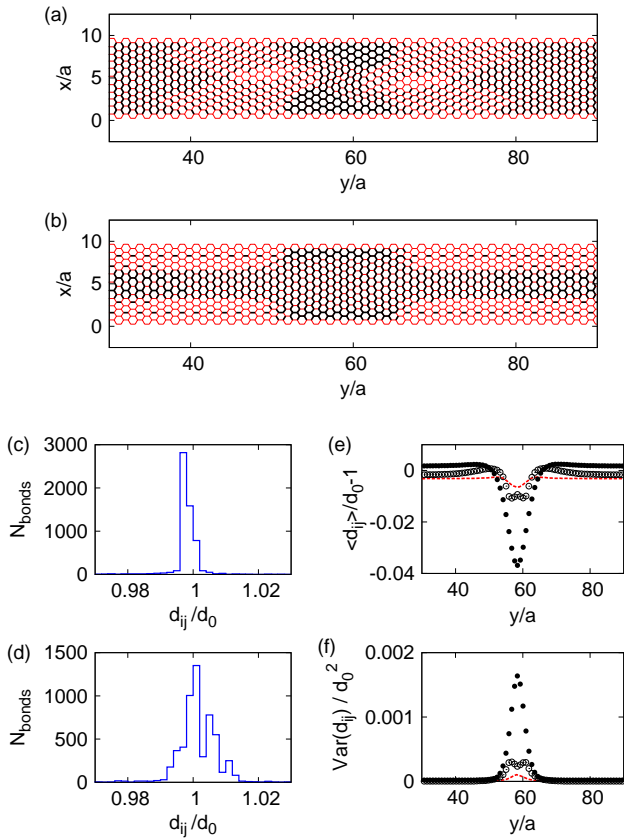


Figure 4: Bond-length modulation for the same system parameters as in Fig. 3. (a) Shorten (thick black) and lengthen (thin red) bonds projected on the (x, y) plane for in the absence of electron-phonon coupling [i.e., $\beta = 0$ in Eq. (1)]. (b) Same as (a) but for $\beta = 3$. (c) and (d) Statistical distributions of the relative bond length for $\beta = 0$ and $\beta = 3$. (e) Average bond length distortion displayed as a function of y coordinate for $\beta = 0$ (open circles) and $\beta = 3$ (full circles). Red dashed line shows the LAMMPS results. (f) Bond length variation vs. y presented with the same symbols (lines) as in (e).

B. The current blocking

In order to understand how the bond-length modulation may affect the transport properties, we focus now on the Dirac points (K and K') and changes in their positions in the first Brillouin zone due to strain-induced fields (see Fig. 5).

Revisiting the derivation of an effective Dirac equation for graphene one finds that weak deformations introduce peculiar gauge fields, with the vector potential for K valley [6]

$$\mathbf{A}_K \equiv \begin{pmatrix} A_{K,x} \\ A_{K,y} \end{pmatrix} = \frac{c\beta}{d_0} \begin{pmatrix} u_{xx} - u_{yy} \\ -2u_{xy} \end{pmatrix}, \quad (13)$$

where c is a dimensionless coefficient of the order of unity, $u_{ij} = \frac{1}{2}(\partial_i u_j + \partial_j u_i)$ (with $i, j = x, y$) is the symmetrized strain tensor for in-plane deformations [32] and the coordinate system is chosen as in Fig. 1 (i.e., such that the x axis corresponds to a zigzag direction of a honeycomb lattice). For the K' valley, the strain-induced field has an opposite sign (namely, $\mathbf{A}_{K'} = -\mathbf{A}_K$).

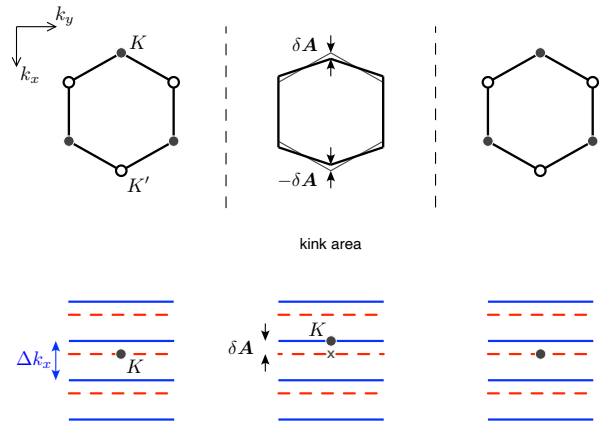


Figure 5: Schematic illustration of the mechanism of current blocking (or electron localization) in metallic (or insulating) graphene nanoribbon with a kink. Top: Relative modification of the bond lengths in the kink area shifts each Dirac point (K and K') in the momentum space by $\pm\delta\mathbf{A}$. Bottom: Transverse momentum quantization near the K point (blue solid or red dashed lines, separated by Δk_x) combined with the K -point shift may locally turn metallic nanoribbon into insulating one or vice versa.

For an approximately uniform compression along the x direction occurring in the kink area, we have $u_x \approx (W'/W)x$, $u_y = y$, and the K point is shift by $\delta\mathbf{A} \propto -(1 - W'/W)\hat{k}_x$ with \hat{k}_x being a unit vector in the k_x direction, while the K' point is shift by $-\delta\mathbf{A}$, as visualized in top panels of Fig. 5. Away from the kink area, buckling without changing bond lengths does not create strain-induced fields ($\delta\mathbf{A} \approx 0$) [33].

Additionally, a finite size along the x direction introduces the well-known geometric quantization, with the discrete values of quasimomentum k_x , separated by $\Delta k_x \sim \pi/W$ (see bottom panels in Fig. 5). In principle, for a particular combination of $\delta\mathbf{A}$ and Δk_x , a nanoribbon may locally change its character from metallic to insulating (or vice versa). In more general situation, if $\delta\mathbf{A}$ and Δk_x are not precisely adjusted to alter the system properties at $E = 0$, one can find some finite energies ($E > 0$ for electrons or $E < 0$ for holes), for which quantum states are available only away from the kink area (or only in the kink area). A direct illustration is provided with the density of states discussed next.

C. Density of states

We consider here two nanoribbons with armchair edges, one of the width $W = 10a$ (the *metallic* case) and the other of $W = 11a$ (the *insulating* case). The system length is $L = 90\sqrt{3}a$ in both cases, with modified periodic boundary conditions (see Sec. II B) applied for both lattice and electronic degrees of freedom. The two values of $\beta = 0$ and $\beta = 3$ in the Hamiltonian \mathcal{H}_{SSH} (1) are considered; the buckling magnitude is fixed at $W'/W = 0.9$. The above parameters allow us to define the two energy scales: The subband

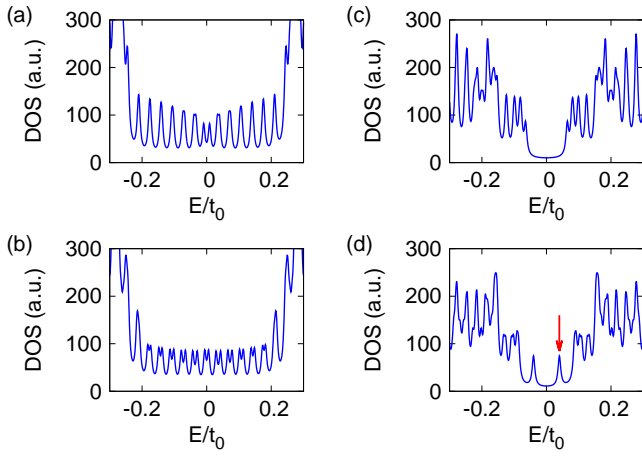


Figure 6: Electronic density of states as a function of energy for a finite section ($L = 90\sqrt{3}a$) of (a,b) metallic [$W = 10a$] and (c,d) insulating [$W = 11a$] ribbons with armchair edges, $W'/W = 0.9$, and a single kink. The bond lengths are optimized for (a,c) $\beta = 0$ or (b,d) $\beta = 3$. Arrow in (d) indicates one of the localized states, at $E = 0.04t_0$, appearing in the gap area. The level broadening parameter [see Eq. (17)] is $\epsilon = 5 \cdot 10^{-3}t_0$.

splitting

$$\Delta E_W = \hbar v_F \Delta k_x \approx 0.3 t_0, \quad (14)$$

and the longitudinal quantization

$$\Delta E_L = 2\pi\hbar v_F / L \approx 0.03 t_0. \quad (15)$$

In Fig. 6, we display the electronic density of states

$$\rho(E) = \sum_n \delta(E - E_n), \quad (16)$$

with E_n denoting the n -th eigenvalue of the kinetic-energy operator T given by Eq. (2), for all four combinations of β and W . For plotting purposes, the δ function is smeared by a finite ϵ ; namely, we put

$$\delta(x) \rightarrow \frac{1}{\pi} \frac{\epsilon}{x^2 + \epsilon^2}, \quad (17)$$

where $\epsilon = 5 \cdot 10^{-3}t_0$.

Since $\Delta E_W \gg \Delta E_L$, metallic [see Figs. 6(a) and 6(b)] or insulating [see Figs. 6(c) and 6(d)] character of the ribbon can still be recognized from the $\rho(E)$ spectrum of its finite section: in the former case, $\rho(E)$ is elevated for any E , whereas in the later case, we have $\rho(E) \approx 0$ in a vicinity of $E = 0$.

The effects of electron-phonon coupling can be summarized as follows. In the metallic case, bond length modulation results in small splittings of the electronic levels [see Fig. 6(b) for $\beta = 3$], originally showing approximate degeneracy [see Fig. 6(a) for $\beta = 0$], due to amplified scattering between the k_y and $-k_y$ states occurring in the kink area. In the insulating case, we have two energy levels, appearing for $\beta = 3$ [see Fig. 6(d)] but absent for $\beta = 0$ [see Fig. 6(c)], one for electrons (marked with red arrow) and one for holes, which occur

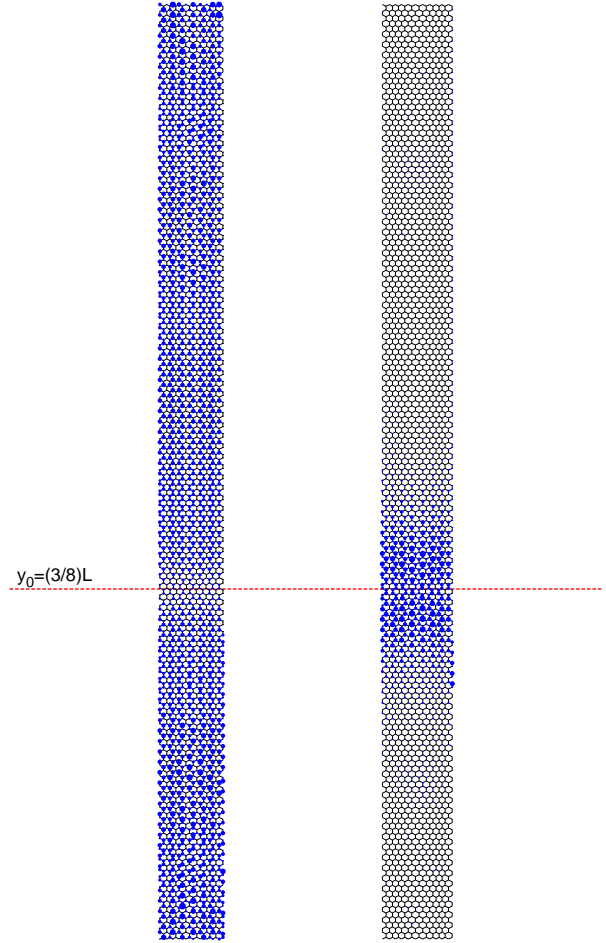


Figure 7: Local density of states for $E = 0.04t_0$ for $W = 10a$ (left) and $W = 11a$ (right). Red horizontal line indicates the kink position. The bond lengths are optimized for $\beta = 3$. Remaining system parameters are same as in Fig. 6.

in the gap range and are well-separated from other levels, suggesting that they are associated with localized states.

The above expectation is further supported with local density of states (presented Fig. 7)

$$\rho_{loc}(\mathbf{R}_j, E) = \sum_n \left| \psi_n^{(j)} \right|^2 \delta(E - E_n), \quad (18)$$

where the δ function is represented via Eq. (17) and the remaining symbols are same as in Eq. (8). Adjusting the energy to the isolated electronic level appearing in the insulating case ($W = 11a$) at $E = 0.04t_0$, we immediately find that the corresponding quantum state is strongly localized in the kink area (see *right* panel in Fig. 7). In the metallic case ($W = 10a$), the value of $E = 0.04t_0$ belongs to a continuum of extended states in the lowest subband, but the corresponding $\rho_{loc}(\mathbf{R}_j, E)$ profile shows a clear suppression in the kink area (see *left* panel in Fig. 7), allowing one to expect that the current propagation in y -direction may be blocked, in the pres-

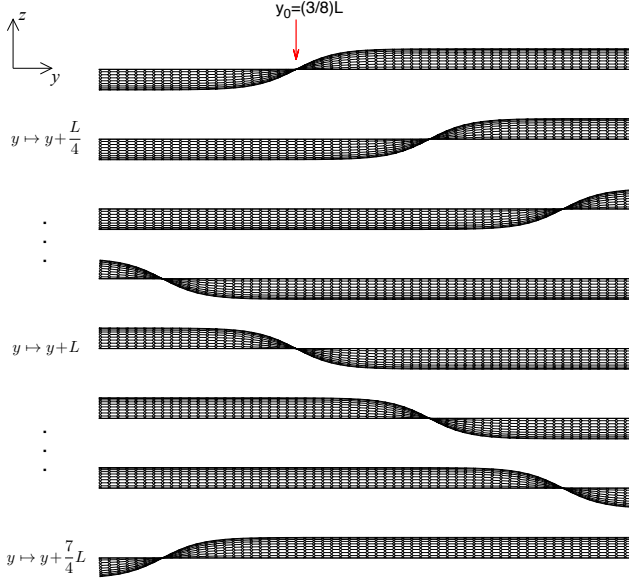


Figure 8: (Top to bottom) Buckled graphene ribbon with a kink, originally placed at $y_0 = \frac{3}{8}L$, subjected to seven consecutive shifts $y \mapsto y + L/4$, visualizing the full pumping cycle (*kink* and *antikink* transition upon $y \mapsto y + 2L$) as seen in the (y, z) plane. A modified periodic boundary conditions (i.e., $y \mapsto y + L, z \mapsto -z$) are applied. The system parameters are $W = 11a$, $W'/W = 0.9$, and $L = 30\sqrt{3}a$. (Notice that a short ribbon is chosen here for illustration only; in the forthcoming calculations we set $L = 90\sqrt{3}a$). The bond lengths are optimized for $\beta = 3$.

ence of a kink, for a whole energy window corresponding to the lowest (or highest) subband for electron (or holes).

IV. CONDUCTANCE AND ADIABATIC PUMPING IN OPEN SYSTEM

In this section we present central results of the paper concerning transport properties of the *open* system (finite section of a nanoribbon attached to the leads) presented in Fig. 1.

A. Simulation details

So far, we have discussed several characteristics of the *closed* system with modified periodic boundary conditions in the y -direction (see Sec. III), making the kink position (y_0) irrelevant for global characteristics, such as the density of states. Now, we use the atomic positions $\{\mathbf{R}_j\} = \{(x_j, y_j, z_j)\}$ obtained with the optimization procedure described in Sec. II B (again, we consider the cases without and with the electron-phonon coupling, $\beta = 0$ and $\beta = 3$) for $y_0 = \frac{3}{8}L$. Next, the kink is placed at the desired position (say, $y_0 + \Delta y$) by applying a shift to all y coordinates, $y \mapsto y + \Delta y$. A series of consecutive shifts, such as visualized in Fig. 8, emulates the kink motion (including full *kink* and *antikink* transitions) in a real system. In case the shift is commensurate

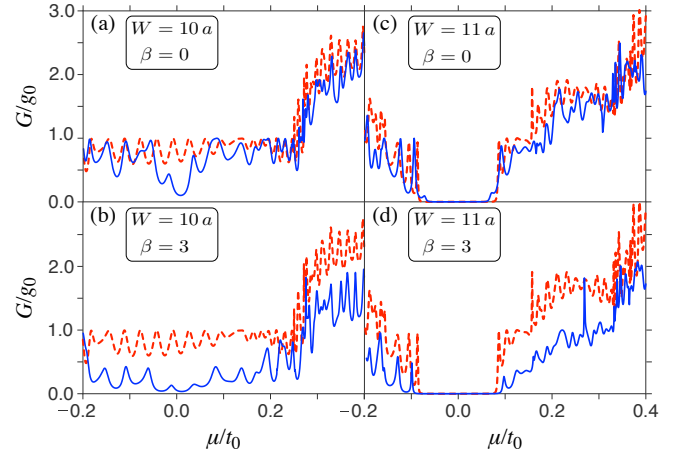


Figure 9: Conductance of graphene ribbon attached to the leads (see Fig. 1) with $L = 90\sqrt{3}a$, $W_\infty = 17.5\sqrt{3}a$, $L_s = 7.5\sqrt{3}a$, and $L_1 = 40\sqrt{3}a$, displayed as a function of the chemical potential. The ribbon with is (a,b) $W = 10a$ or (c,d) $W = 11a$. Blue solid lines in all plots are for $W'/W = 0.9$, the kink position $y_0 = (3/8)L$, and the bond lengths optimized for (a,c) $\beta = 0$, or (b,d) $\beta = 3$; red dashed lines correspond to a flat ribbon case ($W' = W$).

with the longitudinal ribbon periodicity, $\Delta y = \sqrt{3}na$ with n -integer, we simply apply modified periodic boundary conditions for all atoms, for which $y_j + \Delta y < 0$ or $y_j + \Delta y \geq 0$. Otherwise (i.e., if $\Delta y \neq na$), atomic positions after a shift $\{\mathbf{R}_j\}_{\Delta y}$ are determined via third-order spline interpolation using $\{\mathbf{R}_j\}_{\sqrt{3}(n_0-1)a}, \{\mathbf{R}_j\}_{\sqrt{3}n_0a}, \dots, \{\mathbf{R}_j\}_{\sqrt{3}(n_0+2)a}$, with $n_0 = \lfloor \Delta y / (\sqrt{3}a) \rfloor$, and $\lfloor x \rfloor$ the floor function of x .

The hopping-matrix elements (t_{ij}) in Eq. (8) are then determined using atomic positions after a shift, $\{\mathbf{R}_j\}_{\Delta y}$, but we set $t_{ij} = 0$ in case i and j are terminal atoms from the opposite zigzag edges (i.e., periodic boundary conditions are no longer applied for electronic degrees of freedom).

The leads, positioned at the areas of $x < 0$ and $x > W'$ in Fig. 1, are modeled as perfectly flat (i.e., $t_{ij} = -t_0$ for the nearest neighbors i and j) and heavily doped graphene areas, with the electrostatic potential energy $U_\infty = -0.5t_0$ (compared to $U_0 = 0$ in the ribbon area, $0 < x < W'$), each of the width $W_\infty = 17.5\sqrt{3}a$ (corresponding to 11 propagating modes for $E = 0$). What is more, both leads are offset from the free ribbon edges by a distance of $L_s = 7.5\sqrt{3}a$, suppressing the boundary effects. The scattering problem is solved numerically, for each value of the chemical potential $\mu = E - U_0$ and the kink position y_0 , using the KWANT package [34] in order to determine the scattering matrix

$$S(\mu, y_0) = \begin{pmatrix} r & t' \\ t & r' \end{pmatrix}, \quad (19)$$

which contains the transmission t (t') and reflection r (r') amplitudes for charge carriers incident from left (right) lead.

B. Landauer-Büttiker conductance

The linear-response conductance is determined from the S -matrix via the Landauer-Büttiker formula [35, 36], namely

$$G = G_0 \text{Tr} t t^\dagger = \frac{2e^2}{h} \sum_n T_n, \quad (20)$$

where $G_0 = 2e^2/h$ is the conductance quantum and T_n is the transmission probability for the n -th normal mode.

In Fig. 9, we compare the conductance spectra for the same four combinations of parameters W and β as earlier used when discussing the density of states (see Fig. 6). This time, results for a buckled ribbon, with $W'/W = 0.9$ and a kink placed at $y_0 = \frac{3}{8}L$, are compared with the corresponding results for a flat ribbon (solid blue and dashed red lines in Fig. 9, respectively). In the metallic case, electron-phonon coupling strongly suppresses the transport in the presence of a kink [Fig. 9(b)]; the effect of a kink is much weaker in the absence of electron-phonon coupling [Fig. 9(a)]. Similar effects can be noticed in the insulating case, provided that the chemical potential is adjusted to the first conductance step above (or below) the gap range [Figs. 9(c) and 9(d)].

C. The pumping spectra

In the absence of a voltage bias between the leads, the charge transferred solely due to adiabatic kink motion (i.e., by varying the parameter y_0) can be written as [16]

$$\Delta Q = -\frac{ie}{2\pi} \sum_j \int dy_0 \left(\frac{\partial S}{\partial y_0} S^\dagger \right)_{jj}, \quad (21)$$

where the summation runs over the modes in a selected (*output*) lead.

Numerical results for $\Delta Q(\mu)$, obtained by shifting the kink from $y_0 = 0$ to $y_0 = L$, are presented in Fig. 10. Although the current blocking in the metallic case is far from being perfect [see Fig. 9(b)], the related pumping mechanism for $W = 10a$ appears to be rather effective (see top panel in Fig. 10), with $\Delta Q(\mu)$ approaching the total charge available for transfer in a section of the length L_{eff} , a value of which can be approximated by [37]

$$\frac{Q_{\text{kink}}}{e} \approx g_s \frac{L_{\text{eff}} |\mu_0|}{\pi \hbar v_F} = \frac{4}{\pi} \frac{L_{\text{eff}} |\mu_0|}{\sqrt{3} t_0 a}, \quad (22)$$

where $v_F = \sqrt{3} t_0 a / (2\hbar) \approx 10^6$ m/s is the Fermi velocity in graphene and we put $L_1 \leq L_{\text{eff}} \leq L_1 + W_\infty$, estimating the effective length of a ribbon section between the leads (see shaded area in Fig. 10).

Significant changes to the $\Delta Q(\mu)$ spectra are observed in the insulating case of $W = 11a$ (see bottom panel in Fig. 10). Namely, there is an abrupt switching between $\Delta Q \approx 0$ near the center of a gap (at $\mu = 0$) and $\Delta Q \approx 2e$ appearing for μ exceeding the energy level localized in the kink area [see Fig. 6(d)]. The value of $\Delta Q \approx 2e$ remains unaffected until μ approaches a bottom of the lowest electronic

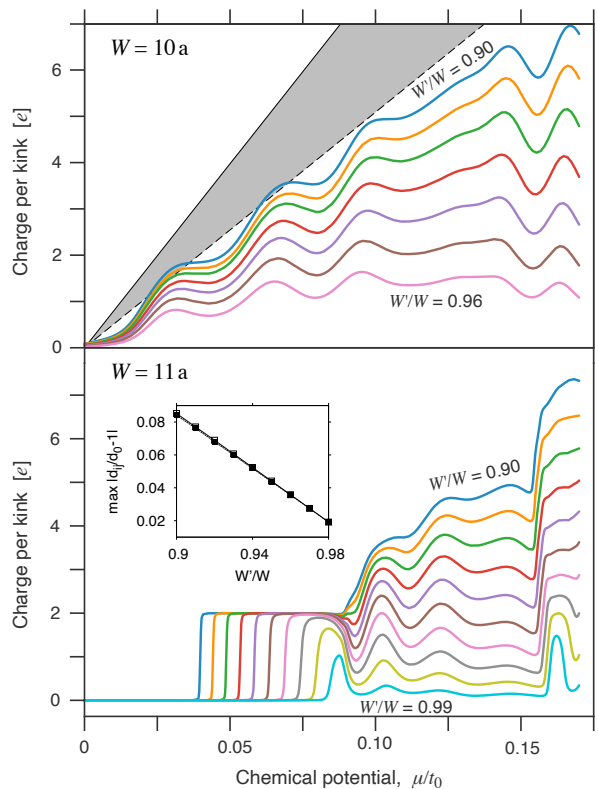


Figure 10: Charge pumped per each kink (or antikink) transition as a function of the chemical potential for (top) $W = 10a$ and (bottom) $W = 11a$. The bond lengths are optimized for $\beta = 3$. The ratio W'/W is varied between the lines with the steps of 0.01; the maximal and minimal W'/W are specified at each plot. Shaded area (top) marks the total charge available for pumping, approximated by Eq. (22) with $L_1 \leq L_{\text{eff}} \leq L_1 + W_\infty$. Inset (bottom) shows maximal absolute bond distortion, as a function of W'/W , for $W = 10a$ (open symbols) and $W = 11a$ (closed symbols); lines in the inset are drawn to guide the eye only.

subband [corresponding to the first conductance step in Fig. 9(d)]. For higher μ , the picture becomes qualitatively similar to this for a metallic case, with $\Delta Q(\mu)$ systematically growing with μ and degreasing with W'/W . Noticeably, the plateau with $\Delta Q \approx 2e$ is well-developed starting from moderate bucklings, $W'/W \approx 0.95$. For $W'/W \approx 0.9$, deviation from the quantum value in the plateau range is of the order of $|\Delta Q - 2e| \sim 10^{-4} e$, and can be attributed to the finite-size effects. Some stronger deviations may appear in a more realistic situation due to the finite-temperature and non-adiabatic effects, which are beyond the scope of this work.

In both (metallic and insulating) cases, the stability of numerical integration in Eq. (21) substantially improves for the lead offsets $L_s \gtrsim 5a$ (being comparable with the kink size), for which parts of the ribbon attached to the leads, together with a section between the leads, are (almost) uniformly buckled for either $y_0 \approx 0$ or $y_0 \approx L$.

In Fig. 10, we also display maximal bond distortions for different bucklings (see the *inset*), showing that local deformations $|\delta d_{ij}| < 0.1 d_0$ for all $0.9 \leq W'/W < 1$.

V. CONCLUSIONS

We have demonstrated, by means of computer simulations of electron transport, that buckled graphene nanoribbon with a topological defect (the *kink*) moving along the system may operate as adiabatic quantum pump. The pump characteristic depend on whether the ribbon is metallic or insulating. In the former case, even for moderate bucklings (with relative bond distortions below 10%) the kink strongly suppresses the current flow, and shifts the electric charge when moving between the leads attached to the system sides. In turn, the charge pumped per cycle is not quantized. For insulating ribbon, there are electronic states localized near the kink (with energies lying within the energy gap) which can be utilized to transport a quantized charge of $2e$ per kink transition (with the factor 2 following from spin degeneracy), providing a candidate for the quantum standard ampere.

Remarkably, the current suppression, and subsequent effects we have described, are visible after the bond lengths optimization for the Su-Schrieffer-Heeger model is performed, introducing significantly stronger bond distortions than the classical (a molecular-dynamics-like) model optimization. Therefore, electron-phonon coupling appears to be a crucial factor for utilizing the moving kink for adiabatic quantum pumping in buckled graphene ribbons.

Acknowledgments

We thank Tomasz Romańczukiewicz and Krzysztof Rościszewski for discussions. The work was supported by the National Science Centre of Poland (NCN) via Grant No. 2014/14/E/ST3/00256. Computations were partly performed using the PL-Grid Infrastructure.

-
- [1] M. M. Benameur, F. Gargiulo, S. Manzeli, G. Autés, M. Tosun, O. V. Yazyev, and A. Kis, *Nat. Commun.* **6**, 8582 (2015).
- [2] Z. H. Khan, A. R. Kermany, and F. Iacopi, *J. Phys. D: Appl. Phys.* **50**, 053003 (2017).
- [3] M. I. Katsnelson, *Graphene: Carbon in Two Dimensions*, (Cambridge University Press, Cambridge, 2012), Chapter 1.
- [4] J.-L. Tsai and J.-F. Tu, *Mater. Des.* **31**, 194 (2010).
- [5] A. Derras-Chouk, E. M. Chudnovsky, D. A. Garanin, and R. Jaafar, *J. Phys. D: Appl. Phys.* **51**, 195301 (2018).
- [6] M. A. H. Vozmediano, M. I. Katsnelson, and F. Guinea, *Phys. Rep.* **496**, 109 (2010).
- [7] E. Prada, P. San-Jose, and H. Schomerus, *Solid State Comm.* **151**, 1065 (2011).
- [8] M. Wakker and M. Blaauboer, *Phys. Rev. B* **82**, 205432 (2010).
- [9] P. San-Jose, E. Prada, H. Schomerus, and S. Kohler, *Appl. Phys. Lett.* **101**, 153506 (2012).
- [10] Y. Jiang, T. Low, K. Chang, M. I. Katsnelson, and F. Guinea, *Phys. Rev. Lett.* **110**, 046601 (2013).
- [11] E. Grichuk and E. Manykin, *Eur. Phys. J. B* **86**, 210 (2013).
- [12] B. Abdollahipour and E. Moomivand, *Physica E* **86**, 204 (2017).
- [13] M. Fujimoto, H. Koschke, and M. Koshino, *Phys. Rev. B* **101**, 041112 (2020).
- [14] Y. Zhang, Y. Gao, and D. Xiao, *Phys. Rev. B* **101**, 041410(R) (2020).
- [15] D. Suszalski and A. Rycerz, e-print [arXiv:2002.08507](https://arxiv.org/abs/2002.08507) (unpublished).
- [16] Yu. V. Nazarov and Ya. M. Blanter, *Quantum Transport: Introduction to Nanoscience*, (Cambridge University Press, Cambridge, 2009), Chapter 1.
- [17] J. P. Pekola, O. P. Saira, V. Maisi, A. Kemppinen, M. Möttönen, Y. A. Pashkin, and D. Averin, *Rev. Mod. Phys.* **85**, 1421 (2013).
- [18] N.-H. Kaneko, S. Nakamura, and Y. Okazaki, *Meas. Sci. Technol.* **27**, 032001 (2016).
- [19] W. Poirier, S. Djordjevic, F. Schopfer, and O. Thévenot, *C. R. Physique* **20**, 92 (2019).
- [20] D. B. Newell, F. Cabiati, J. Fischer, K. Fujii, S. G. Karshenboim, H. S. Margolis, E. de Mirandés, P. J. Mohr, F. Nez, K. Pachucki, T. J. Quinn, B. N. Taylor, M. Wang, B. M. Wood, and Z. Zhang, *Metrologia* **55**, L13 (2018).
- [21] P. J. Mohr, B. D. Newell, B. N. Taylor, and E. Tiesinga, *Metrologia* **55**, 125 (2018).
- [22] R. D. Yamaletdinov, V. A. Slipko, and Y. V. Pershin, *Phys. Rev. B* **96**, 094306 (2017).
- [23] R. D. Yamaletdinov, T. Romańczukiewicz, and Y. V. Pershin, *Carbon* **141**, 253 (2019).
- [24] G. Dresselhaus, M. S. Dresselhaus, and R. Saito, *Physical Properties Of Carbon Nanotubes*, (World Scientific, Singapore, 1998), Chapter 11.
- [25] R. Peierls, *Quantum Theory of Solids*, (Oxford University Press, Oxford 1955), Chapter V.
- [26] S. Plimpton, *J. Comp. Phys.* **117**, 1 (1995); see also: <http://lammps.sandia.gov>.
- [27] Interactions between carbon atoms are described using the standard two-body, three-body, four-body (dihedral), and Lennard-Jones potential energy terms, see Ref. [22]. Periodic boundary conditions in y -direction are not applied in this case.
- [28] T. Kariyado and X. Hu, *Sci. Rep.* **7**, 16515 (2017).
- [29] O. Gröning, S. Wang, X. Yao, et al., *Nature* **560**, 209 (2018).
- [30] The corresponding value of kinetic energy per site is $(N_{\text{at}})^{-1} \langle T \rangle = -1.5746 t_0$ (with $N_{\text{at}} \approx \frac{2}{3} N_b$); see e.g.: L. M. Martelo, M. Dzierzawa, L. Siffert, D. Baeriswyl, *Z. Phys. B* **103**, 335 (1997).
- [31] A. Rycerz, in *Recent Advances in Graphene Research*, P. Nayak (ed.), InTech DOI:10.5772/64240 (2016) pp. 91-110; e-print [arXiv:1604.03783](https://arxiv.org/abs/1604.03783).
- [32] L.D. Landau and E.M. Lifschitz, *Theory of Elasticity* (Pergamon Press, Oxford, 1959).
- [33] Some scalar fields, modifying the electrostatic potential energy by $\delta V = g(u_{xx} + u_{yy})$, may also appear in the kink area (see Ref. [6]) but they are neglected in our analysis, since the coupling constant is not determined precisely (various works report $g \approx 4 - 20$ eV); also, the effective electrostatic potential barrier cannot substantially alter the current blocking (or the electron trapping) mechanism due to Klein tunnelling.
- [34] C. W. Groth, M. Wimmer, A. R. Akhmerov, and X. Waintal, *New J. Phys.* **16**, 063065 (2014); see also: <https://kwant-project.org>.
- [35] R. Landauer, *IBM J. Res. Dev.* **1**, 233 (1957).
- [36] M. Büttiker, Y. Imry, R. Landauer, and S. Pinhas, *Phys. Rev. B* **31** 6207 (1985).
- [37] Eq. (22) follows from the dispersion relation for lowest subbands in the metallic case (with opposite group velocities),

$E_{\pm}^{(1)} = \pm \hbar v_F k_y$; the contribution from higher subbands may be suppressed due to mismatching group velocities.

Oświadczenie współautora artykułów wchodzących w skład rozprawy doktorskiej mgr. Dominika Suszalskiego pt. "Relativistic charge and energy transport phenomena in graphene nanostructures"

Jestem współautorem sześciu publikacji stanowiących rozprawę doktorską:

1. D. Suszalski, G. Rut, and A. Rycerz, *Lifshitz transition and thermoelectric properties of bilayer graphene*, Phys. Rev. B 97, 125403 (2018), pp. 1–10.
2. D. Suszalski, G. Rut, and A. Rycerz, *Thermoelectric properties of gapped bilayer graphene*, J. Phys.: Condens. Matter 31, 415501 (2019), pp. 1–8.
3. D. Suszalski, G. Rut, and A. Rycerz, *Mesoscopic valley filter in graphene Corbino disk containing a p-n junction*, J. Phys. Mater. 3, 015006 (2020), pp. 1–17.
4. D. Suszalski, G. Rut, and A. Rycerz, *Conductivity scaling and the effects of symmetry-breaking terms in bilayer graphene Hamiltonian*, Phys. Rev. B 101, 125425 (2020), pp. 1–10.
5. D. Suszalski and A. Rycerz, *Adiabatic quantum pumping in buckled graphene nanoribbon driven by a kink*, Acta Phys. Polon. B, accepted (2020), pp. 1–7.
6. A. Rycerz and D. Suszalski, *Graphene disk in a solenoid magnetic potential: Aharonov-Bohm effect without a two-slit-like setup*, Phys. Rev. B 101, 245429 (2020), pp. 1–6.

Mój wkład w wymienione publikacje polegał (we wszystkich przypadkach) na opracowaniu koncepcji i planu badań, wykonaniu oszacowań analitycznych częściowo wyjaśniających wyniki numeryczne D.S., oraz redakcji tekstu. Rola D.S. w pracach 1.–5. była wiodąca, w przypadku 6. wkład pracy autorów oceniam jako równy.

Adam Rycerz
Kraków, 27 lipca 2020

Oświadczenie o współautorstwie

Jestem współautorem czterech artykułów wchodzących w skład pracy doktorskiej mgr. Dominika Suszalskiego:

1. D. Suszalski, G. Rut, A. Rycerz, *Lifshitz transition and thermoelectric properties of bilayer graphene*, **Phys. Rev. B** **97**, 125403 (2018).
2. D. Suszalski, G. Rut, A. Rycerz, *Thermoelectric properties of gapped bilayer graphene*, **J. Phys.: Condens. Matter** **31**, 415501 (2019).
3. D. Suszalski, G. Rut, A. Rycerz, *Mesoscopic valley filter in graphene Corbino disk containing a p-n junction*, **J. Phys. Mater.** **3**, 015006 (2020).
4. D. Suszalski, G. Rut, A. Rycerz, *Conductivity scaling and the effects of symmetry-breaking terms in bilayer graphene Hamiltonian*, **Phys. Rev. B** **101**, 125425 (2020).

Mój wkład w pierwszej pracy polegał na przeprowadzeniu części obliczeń numerycznych potrzebnych do wyznaczenia gęstości nośników oraz przewodnictwa fononowego. Brałem również udział w wyznaczeniu analitycznego przybliżenia liczby otwartych kanałów.

Na potrzeby drugiego artykułu wyznaczyłem numerycznie termoprzewodnictwo układu na bazie dwuwarstwy grafenowej z pojedynczym złączem.

W pracy trzeciej brałem udział w przeprowadzaniu symulacji przewodnictwa dysku Corbino ze złączem p-n w zewnętrznym polu magnetycznym. Dodatkowo, wyznaczyłem analityczną postać przewodnictwa nieskończonej płaszczyzny grafenowej ze złączem p-n.

W ostatniej pracy, w oparciu o przygotowany na potrzeby wcześniejszych prac kod mgr. Suszalskiego, opracowałem numerycznie przewodnictwo dwuwarstwy grafenowej z uwzględnieniem czynników łamiących symetrię elektron-dziura.

Przy powstawaniu prac brałem udział w kształtowaniu ostatecznej treści artykułów oraz opracowaniu części grafik.

Kraków, 27.07.2020

Grzegorz Rut